# STATE OF THE CLIMATE IN 2006

# AFFILIATIONS (ALPHABETICAL BY AUTHOR)


1. Aceituno, Patricio, Universidad de Chile, Santiago de Chile, Chile
2. Achberger, Christine, Institutionen för Geovetenskaper, Göteborgs Universitet, Göteborg, Sweden
3. Adams, Neil, Antarctic Meteorological Section, Australian Bureau of Meteorology, Hobart, Tasmania, Australia
4. Ambenje, Peter G., Kenyan Meteorological Department, Nairobi, Kenya
5. Arguez, Anthony, NOAA/NESDIS National Climatic Data Center, Asheville, North Carolina
6. Armstrong, Richard L., CIRES National Snow and Ice Data Center, University of Colorado, Boulder, Colorado
7. Baringer, Molly O., NOAA/OAR Atlantic Oceanographic and Meteorological Laboratory, Physical Oceanography Division, Miami, Florida
8. Barreira, Sandra, Argentine Navy Meteorological Service, Argentine Hydrographic Service, Buenos Aires, Argentina
9. Baum, Bryan, Space Science and Engineering Center, University of Wisconsin—Madison, Madison, Wisconsin
10. Belitskaya, Valentina Davydova, National Meteorological Service-NWC, Mexico City, Mexico
11. Bell, Gerald D., NOAA/NWS/NCEP Climate Prediction Center, Camp Springs, Maryland
12. Bell, Michael, International Research Institute for Climate and Society, Palisades, New York
13. Bengtsson, Lennart, Max-Planck Institute for Meteorology, Hamburg, Germany
14. Bidegain, Mario, University of Republic, Montevideo, Uruguay
15. Bissolli, Peter, German Meteorological Service, Department of Climate Monitoring, Offenbach, Germany
16. Blake, Eric, NOAA/NWS/NCEP National Hurricane Center, Miami, Florida
17. Boudet Roco, Dagne, Instituto de Meteorología, La Habana, Cuba
18. Bourassa, Mark, Center for Ocean–Atmospheric Prediction Studies, The Florida State University, Tallahassee, Florida
19. Box, Jason E., Byrd Polar Research Center, The Ohio State University, Columbus, Ohio
20. Bromwich, David H., Byrd Polar Research Center, The Ohio State University, Columbus, Ohio
21. Bulygina, Olga N., All-Russian Research Institute of Hydrometeorological Information, Obninsk, Russia
22. Burgess, Stuart M., National Institute of Water and Atmospheric Research, Ltd., Wellington, New Zealand
23. Camacho, Jose Luis, Centro Internacional para la Investigación del Fenómeno de El Niño, Guayaquil, Ecuador
24. Camargo, Suzana J., International Research Institute for Climate and Society, The Earth Institute at Columbia University, Palisades, New York
25. Carrión Romero, Ana M., Instituto de Meteorología, La Habana, Cuba
26. Chelliah, Muthuvel, NOAA/NWS/NCEP Climate Prediction Center, Camp Springs, Maryland
27. Chen, Deliang, Institutionen för Geovetenskaper, Göteborgs Universitet, Göteborg, Sweden
28. Christy, John C., University of Alabama in Huntsville, Huntsville, Alabama
29. Coelho, Caio A. S., CPTEC/INPE, Center for Weather Forecasts and Climate Studies, Cachoeira Paulista, Brazil
30. Cutié Cansino, Virgen, Instituto de Meteorología, La Habana, Cuba
31. Diamond, Howard J., NOAA/NESDIS National Climatic Data Center, Silver Spring, Maryland
32. Douglas, Arthur, Creighton University, Omaha, Nebraska
33. Dutton, Geoff S., NOAA/OAR Earth Systems Research Laboratory, Global Monitoring Division, Boulder, Colorado
34. Elkins, James W., NOAA/OAR Earth Systems Research Laboratory, Global Monitoring Division, Boulder, Colorado
35. Evan, Amato T., Cooperative Institute for Meteorological Satellite Studies, University of Wisconsin—Madison, Madison, Wisconsin
36. Feely, Richard A., NOAA/OAR Pacific Marine Environmental Laboratory, Seattle, Washington
37. Fetterer, Florence, CIRES National Snow and Ice Data Center, University of Colorado, Boulder, Colorado
38. Fogt, Ryan L., Byrd Polar Research Center, The Ohio State University, Columbus, Ohio
39. Fonseca Rivera, Cecilia, Instituto de Meteorología, La Habana, Cuba
40. Garcia-Herrera, Ricardo F., Universidad Complutense Madrid, Madrid, Spain
41. Gierach, Michelle M., University of South Carolina, Columbia, South Carolina
42. Gill, Stephen, NOAA/NOS Center for Operational Oceanographic Products and Services, Silver Spring, Maryland
43. Gleason, Karin L., NOAA/NESDIS National Climatic Data Center, Asheville, North Carolina
44. Goldenberg, Stanley B., NOAA/OAR Atlantic Oceanographic and Meteorological Laboratory, Miami, Florida
45. Goni, Gustavo, NOAA/OAR Atlantic Oceanographic and Meteorological Laboratory, Physical Oceanography Division, Miami, Florida
46. Guttman, Nathaniel B., NOAA/NESDIS National Climatic Data Center, Asheville, North Carolina
47. Halpert, Michael S., NOAA/NWS/NCEP Climate Prediction Center, Camp Springs, Maryland
48. Heidinger, Andrew K., NOAA/NESDIS Center for Satellite Applications and Research, Cooperative Research Program, University of Wisconsin—Madison, Madison, Wisconsin
49. Heim, Richard R., Jr., NOAA/NESDIS National Climatic Data Center, Asheville, North Carolina
50. Henriquez, Maximiliano, Institute of Hydrology, Meteorology and Environmental Studies (IDEAM), Bogotá, Columbia
51. Hernández Souza, Marieta, Instituto de Meteorología, La Habana, Cuba
52. Higgins, Wayne, NOAA/NWS/NCEP Climate Prediction Center, Camp Springs, Maryland
53. Horvitz, Andy, NOAA National Weather Service, Silver Spring, Maryland

54. Hovsepyan, Anahit, Armenian State Hydrometeorological and Monitoring Service, Yerevan, Armenia
55. Hughes, Paul J., Center for Ocean-Atmospheric Prediction Studies, The Florida State University, Tallahassee, Florida
56. Hurtado, Gonzalo, Institute of Hydrology, Meteorology and Environmental Studies (IDEAM), Bogotá, Columbia
57. Jaimes, Ena, National Meteorological and Hydrological Service of Peru (SENAMHI), Lima, Perú
58. Janowiak, John E., NOAA/NWS/NCEP Climate Prediction Center, Camp Springs, Maryland
59. Jezek, Kenneth, Byrd Polar Research Center, The Ohio State University, Columbus, Ohio
60. Johnson, Gregory C., NOAA/OAR Pacific Marine Environmental Laboratory, Seattle, Washington
61. Kabidi, Khadija, Direction de la Météorologie Nationale, Rabat, Morocco
62. Kadi, Mohammed, African Center for Meteorological Applications for Development, Niamey, Niger
63. Kennedy, John J., Hadley Centre for Climate Change, Met Office, Exeter, United Kingdom
64. Khoshkam, Mahbobeh, Islamic Republic of Iran Meteorological Organization, Tehran, Iran
65. Korshunova, Natalia N., All-Russian Research Institute of Hydrometeorological Information, Obninsk, Russia
66. Kruger, Andries, South African Weather Service, Pretoria, South Africa
67. Landman, Willem A., South African Weather Service, Pretoria, South Africa
68. Landsea, Chris W., NOAA/NWS/NCEP National Hurricane Center, Miami, Florida
69. Lapinel Pedroso, Braulio, Instituto de Meteorología, La Habana, Cuba
70. Lawrimore, Jay H., NOAA/NESDIS National Climatic Data Center, Asheville, North Carolina
71. Levinson, David H., NOAA/NESDIS National Climatic Data Center, Asheville, North Carolina
72. Levy, Joel M., NOAA/OAR Climate Program Office, Silver Spring, Maryland
73. L'Heureux, Michelle, NOAA/NWS/NCEP Climate Prediction Center, Camp Springs, Maryland
74. Li, Wei, National Climate Center, China Meteorological Administration, Beijing, China
75. Liu, Hongxing, Department of Geography, Texas A&M University, College Station, Texas
76. Lubin, Dan, Scripps Institution of Oceanography, University of California, San Diego, La Jolla, California
77. Lumpkin, Rick, NOAA/OAR Atlantic Oceanographic and Meteorological Laboratory, Physical Oceanography Division, Miami, Florida
78. Lyman, John M., NOAA/OAR Pacific Marine Environmental Laboratory, Seattle, Washington
79. Mahowald, Natalie M., National Center for Atmospheric Research, Boulder, Colorado
80. Majstorovic, Zeljko, METEOBIH, Federal Meteorological Institute, Sarajevo, Bosnia and Herzegovina
81. Marengo, José A., CPTEC/INPE Center for Weather Forecasts and Climate Studies, São Paulo, Brazil
82. Martínez, Rodney, Centro Internacional para la Investigación del Fenómeno de El Niño, Guayaquil, Ecuador
83. Massom, Robert A., Australian Antarctic Division and Antarctic Climate and Ecosystems CRC, University of Tasmania, Hobart, Tasmania, Australia
84. Maue, Ryan N., Center for Ocean–Atmospheric Prediction Studies, Florida State University, Tallahassee, Florida
85. Meinen, Christopher S., NOAA/OAR Atlantic Oceanographic and Meteorological Laboratory, Physical Oceanography Division, Miami, Florida
86. Menne, Matthew J., NOAA/NESDIS National Climatic Data Center, Asheville, North Carolina
87. Merrifield, Mark. A., University of Hawaii at Manoa, Honolulu, Hawaii
88. Mitchum, Gary T., University of South Florida, College of Marine Science, St. Petersburg, Florida
89. Mo, Kingste C., NOAA/NWS/NCEP Climate Prediction Center, Camp Springs, Maryland
90. Monaghan, Andrew, Byrd Polar Research Center, The Ohio State University, Columbus, Ohio
91. Morison, James, Polar Science Center, Applied Physics Laboratory, University of Washington, Seattle, Washington
92. Mullan, Brett, National Institute of Water and Atmospheric Research, Ltd., Wellington, New Zealand
93. Mumba, Zilore, African Center for Meteorological Applications for Development, Niamey, Niger
94. Newman, Paul A., NASA Goddard Space Flight Center, Greenbelt Maryland
95. Nghiem, Son V., NASA Jet Propulsion Laboratory, California Institute of Technology, Pasadena, California
96. Njau, Leonard, African Center for Meteorological Applications for Development, Niamey, Niger
97. Norte, Federico, National Program of Meteorology, Mendoza, Argentina
98. Oberman, Naum G., MIREKO Company, Syktyvkar, Russia
99. Obregón, André, Laboratory for Climatology and Remote Sensing (LCRS), Faculty of Geography, University of Marburg, Marburg, Germany
100. Oludhe, Christopher, University of Nairobi, Nairobi, Kenya
101. Overland, James E., NOAA/OAR Pacific Marine Environmental Laboratory, Seattle, Washington
102. Pabón, José Daniel, Universidad Nacional de Colombia, Bogotá, Colombia
103. Paredes, Daniel, Universidad Complutense Madrid, Madrid, Spain
104. Pasch, Richard, NOAA/NWS/NCEP National Hurricane Center, Miami, Florida
105. Patricio, Domingos Mosquito, Instituto Nacional de Meteorologia (INAM), Observation and Network Department, Mozambique
106. Pérez Fernández, Joel, El Centro del Agua del Trópico Húmedo para América Latina y el Caribe, Panama City, Panama

107. Pérez Suárez, Ramón, Instituto de Meteorología, La Habana, Cuba
108. Perovich, Donald K., ERDC Cold Regions Research and Engineering Laboratory, Hanover, New Hampshire
109. Peterson, Thomas C., NOAA/NESDIS National Climatic Data Center, Asheville, North Carolina
110. Pezza, Alexandre B., The University of Melbourne, Melbourne, Victoria, Australia
111. Phillips, David, Environment Canada, Toronto, Ontario, Canada
112. Proshutinsky, Andrey, Woods Hole Oceanographic Institute, Woods Hole, Massachusetts
113. Przybylak, Rajmund, Nicolaus Copernicus University, Toruń, Poland
114. Quintana, Juan, Dirección Meteorológica de Chile, Santiago, Chile
115. Rahimzadeh, Fatemeh, Atmospheric Science and Meteorological Research Center (ASMERC), Tehran, Iran
116. Rajeevan, Madhavan, National Climate Centre, India Meteorological Department, Pune, India
117. Ramirez Obando, Patricia, Regional Committee for Hydraulic Resources (CRRH/SICA), San José, Costa Rica
118. Ramos, Alexandre, CGUL, IDL, Universidade de Lisboa, Lisbon, Portugal
119. Razuvaev, Vyacheslav N., All-Russian Research Institute of Hydrometeorological Information, Obninsk, Russia
120. Remer, Lorraine A., NASA Goddard Space Flight Center, Greenbelt, Maryland
121. Revadekar, Jayashree, Indian Institute of Tropical Meteorology, Pune, India
122. Reynolds, Richard W., NOAA/NESDIS National Climatic Data Center, Asheville, North Carolina
123. Richter-Menge, Jacqueline A., ERDC Cold Regions Research and Engineering Laboratory, Hanover, New Hampshire
124. Rigor, Ignatius G., Polar Science Center, Applied Physics Laboratory, University of Washington, Seattle, Washington
125. Robinson, David A., Department of Geography, Rutgers–The State University of New Jersey, Piscataway, New Jersey
126. Rolph, Jeremy J., Center for Ocean–Atmospheric Prediction Studies, The Florida State University, Tallahassee, Florida
127. Romanovsky, Vladimir E., Geophysical Institute, University of Alaska, Fairbanks, Fairbanks, Alaska
128. Rusticucci, Matilde, University of Buenos Aires, Buenos Aires, Argentina
129. Sabine, Christopher L., NOAA/OAR Pacific Marine Environmental Laboratory, Seattle, Washington
130. Salinger, M. James, National Institute of Water and Atmospheric Research, Ltd., Newmarket, Auckland, New Zealand
131. Sanchez-Lugo, Ahira M., NOAA/NESDIS National Climatic Data Center, Asheville, North Carolina
132. Scambos, Ted A., CIRES National Snow and Ice Data Center, University of Colorado, Boulder, Colorado
133. Schnell, Russell C., NOAA/ESRL Global Monitoring Division, Climate Monitoring and Diagnostics Laboratory, Boulder, Colorado
134. Sensoy, Serhat, Turkish State Meteorological Service, Ankara, Turkey
135. Shiklomanov, Alexander I., University of New Hampshire, Durham, New Hampshire
136. Simonelli, Silvia, National Program of Meteorology, Mendoza, Argentina
137. Smith, Shawn R., Center for Ocean–Atmospheric Prediction Studies, The Florida State University, Tallahassee, Florida
138. Subrahmanyam, Bulusu, University of South Carolina, Columbia, South Carolina
139. Thiaw, Wassila M., NOAA/NWS/NCEP Climate Prediction Center, Camp Springs, Maryland
140. Trewin, Blair C., National Climate Centre, Australian Bureau of Meteorology, Melbourne, Victoria, Australia
141. Trigo, Ricardo M., CGUL, IDL, Universidade de Lisboa, Lisbon, Portugal
142. Turner, John, British Antarctic Survey, Cambridge, United Kingdom
143. Ulke, Graciela, Universidad de Buenos Aires, Buenos Aires, Argentina
144. Viale, Maximiliano, National Program of Meteorology, Mendoza, Argentina
145. Walker, Donald, Institute of Arctic Biology, University of Alaska, Fairbanks, Fairbanks, Alaska
146. Walsh, John, International Arctic Research Center, Fairbanks, Alaska
147. Wang, Lei, Department of Geography, Texas A&M University, College Station, Texas
148. Wang, Ling, China Meteorological Administration, Beijing, China
149. Wanninkhof, Rik, NOAA/OAR Atlantic Oceanographic and Meteorological Laboratory, Ocean Chemistry Division, Miami, Florida
150. Waple, Anne M., NOAA/NESDIS National Climatic Data Center (STG, Inc.), Asheville, North Carolina
151. Watkins, Andrew B., National Climate Centre, Australian Bureau of Meteorology, Melbourne, Victoria, Australia
152. Weller, Robert A., Woods Hole Oceanographic Institute, Woods Hole, Massachusetts
153. Whitewood, Robert, Environment Canada, Ottawa, Ontario, Canada
154. Willis, Joshua K., NASA Jet Propulsion Laboratory, Pasadena, California
155. Woodworth, Philip L., Proudman Oceanographic Laboratory, Liverpool, United Kingdom
156. Xie, Pingping, NOAA/NWS/NCEP, Climate Prediction Center, Camp Springs, Maryland
157. Ye, Dianxiu, National Climate Center, China Meteorological Administration, Beijing, China
158. Yu, Lisan, Woods Hole Oceanographic Institute, Woods Hole, Massachusetts
159. Zhu, Yanfeng, Beijing Climate Center, China Meteorological Administration, Beijing, China

# TABLE OF CONTENTS

## ABSTRACT—A. Arguez

The State of the Climate in 2006 report summarizes the year's weather and climate conditions, both globally and regionally. In addition, the year is placed into a long-term climatological context. Furthermore, notable events are also discussed.

Overall global temperatures were fifth or sixth warmest on record, depending on the dataset, continuing an upward trend in temperatures. Many countries and regions experienced their record warmest year (or tied for warmest), including Spain, the Netherlands, the United Kingdom, and China, as well as parts of Australia and Canada. In many regions, the warmth in 2006 is statistically indistinguishable from the record warmth in 1998. However, 1998 was influenced by the unprecedented warming associated with the record 1997/98 El Niño, whereas 2006 was marked by a 2005/06 La Niña that transitioned into a weak-to-moderate 2006/07 El Niño.

Consistent with the warming, sea ice extent in both polar regions reached record or near-record minima. In addition, Antarctic ozone concentrations reached an all-time minimum. Also, carbon dioxide measurements increased in the atmosphere by 2.3 parts per million (ppm) in 2006 to reach a global average of 381.1 ppm.

In the global oceans, sea levels were above average for ~80% of the ocean. The global mean sea level anomaly change of +6 mm from 2005 was the highest increase since the altimeter record began in 1993. Relative sea level change was also the highest ever recorded. Significant heat flux and current anomalies were observed in the regions of the 2006 El Niño and Indian Ocean dipole mode event.

Despite the warmth around the globe, tropical cyclone counts were near average. However, Tropical Cyclone Larry made landfall in northern Australia as one of the most intense storms in decades. Following the record Atlantic hurricane season of 2005, the 2006 season was very quiet.

## 1. INTRODUCTION—A. Arguez, A. M. Waple, and A. M. Sanchez-Lugo

On the heels of 2005's record-breaking weather events, 2006 was also a year of records. This was especially the case over the polar regions, where the largest Antarctic ozone hole on record occurred in 2006. Sea ice extent in the Antarctic reached records at times for both maximum and minimum extent, and in the Arctic, scientists observed the second lowest sea ice extent on record (lowest 2005). These record events came as attention to the polar regions gained greater focus, thanks in large part to the International Polar Year, in which an unprecedented effort is underway to monitor the Arctic and Antarctic from March 2007 through March 2009.

Several countries had their warmest year on record in 2006. These included, but were not limited to, China, the United Kingdom, Spain, and the Netherlands. Also, parts of Australia reported record warmth, while Canada and the United States experienced their second-warmest year on record. There was a transition between La Niña in the first half of the year to a weak-to-moderate El Niño in the latter half. While some regions had temperature and precipitation anomalies consistent with typical ENSO (see the appendix for a complete list of acronym expansions) impacts in their regions, it is noteworthy that the record warmth experienced over many parts of the world was not the result of a strong El Niño, as was the case in 1998. Record rainfall over parts of eastern Africa brought widespread damage to the region in 2006, while Australians were "Larried," as some Aussies referred to the destruction left behind by Tropical Cyclone Larry, including the near decimation of the banana crop.

This summary highlights the most salient weather events and overall climate conditions of 2006, which include noteworthy weather events (e.g., floods, tropical cyclones, tornadoes, and heat waves), assessment of temperature and precipitation anomalies, and reports on some of the primary features of the global climate system: the Indian monsoon, the Siberian high, the Kuroshio and the Gulf Stream (western boundary currents in the North Pacific and North Atlantic Oceans, respectively), the ITCZ, various jet streams, etc. To the greatest extent possible, the conditions in 2006 are placed in historical context to provide perspective on variations and change that have occurred through time. The data and analyses contained herein represent the best available as of early 2007; values are susceptible to updates by the source agencies, although it is not expected that any key findings would be materially affected.

This is the 17th annual State of the Climate report, the 11th year the report has been included in *BAMS,* and the second year it appears as a special supplement. NOAA/NCDC has been responsible for the report's publication for seven years, although the report is truly an international effort. For 2006, over 150 scientists from around the world participated, as NCDC continued to focus on widening international participation. As part of this effort, special "country spotlight" sidebars are included in the report, highlighting the 2006 climate events in six countries: Morocco, Mozambique, Cuba, Armenia, Turkey, and Bosnia and Herzegovina. A determined effort has been made to ensure that all participants are duly acknowledged. In particular, authorship is noted for individual sections. In addition to authors, numerous reviewers and other facilitators have made

the publication possible; these individuals are also listed in the acknowledgments section.

With every new State of the Climate report, new topics and special features are incorporated. For 2006, the following new sections are included: cloudiness, aerosols, global winds, ocean salinity, and ocean color. These additions represent a marked increase in the number of "essential climate variables" covered by the report. Our ability to observe global climate elements has been dramatically increased by satellite observations, and this improvement will likely continue as new instruments are placed in orbit. Also new for 2006 are sections on teleconnections and blocking, the Atlantic ITCZ, and a significantly augmented treatment of the Antarctic. The Australian tropical cyclone season also is discussed in a special sidebar.

The following is an executive summary of the report's five main sections.

*Section 2: Global climate*

- Continued global warmth marked 2006. The 10 warmest years on record have all occurred since 1995, with 2006 ranking fifth or sixth warmest in the 1880–2006 record, depending on the dataset analyzed. All datasets agree that global surface temperatures continue to warm, with the rate of global temperature rise increasing from around 0.06°C decade$^{-1}$ over the past century to nearly 0.18°C decade$^{-1}$ for the last 30 years.
- Northern Hemisphere snow cover extent was again below average for spring, and was near to slightly above average for winter in 2006.
- Global precipitation was above average in 2006 for the third consecutive year. Precipitation has increased globally since the start of the twentieth century, with the greatest increases in the mid- and high latitudes of the Northern Hemisphere.
- The concentration of carbon dioxide in the atmosphere increased by 2.3 ppm in 2006 to reach a global average of 381.1 ppm. The average rate of rise is 1.6 ppm yr$^{-1}$ since 1980; however, since the year 2000, this has increased to 2.1 ppm yr$^{-1}$. Prior to the Industrial Revolution, the atmospheric concentration was around 280 ppm.

*Section 3: Global oceans*

- Annual mean SLA was above the 1993–99 baseline average for nearly 80% of the ocean. The global mean SLA change of +6 mm from 2005 was the highest increase since satellite altimeter measurements began in 1993. Relative sea level change was also the highest ever recorded.
- Significant heat flux anomalies were observed in the regions of the 2006 El Niño and Indian Ocean dipole mode event.

*Section 4: The Tropics*

- There were a near-average number of major (very strong) tropical cyclones worldwide. Certain basins were more active than normal, for example, the eastern tropical Pacific. The tropical Atlantic had near-average activity, though in sharp contrast to 2005 there were few landfalls.
- A transition occurred from La Niña in the first quarter of the year to El Niño conditions during the last quarter of the year.

*Section 5: The Poles*

- Springtime ozone depletion over the Antarctic in 2006 was, by a small margin, the most severe ever recorded, reaching an average late-September extent of 27.4 million km$^2$. At the South Pole itself, ozone depletion reached 99% in early October, the most on record.
- Both the record minimum and record maximum sea ice extents relative to the 1979–2006 period were included in 2006 (the period of accurate satellite observations).
- Seasonal minimum sea ice extent in the Northern Hemisphere (typically occurring in September) was again near record low levels. The September rate of sea ice decline is now near 9% decade$^{-1}$, equating to a loss of over 60,000 km$^2$ of ice extent per year.

*Section 6: Regional climates*

Numerous noteworthy climate events occurred in 2006 on the regional scale (Fig. 1.1).

- Africa: Precipitation was generally above average over much of sub-Saharan Africa. Flooding caused substantial loss of life and property, including over eastern Africa, which had been grappling with a multiyear drought before the deluge. Flooding also wreaked havoc in Nigeria, Malawi, and Algeria. Temperatures were above average for most of the continent.
- North America: Canada and the United States experienced one of their two warmest years on record. Heavy rainfall fell over the Northwest, Great Lakes, and New England regions of the United States, while much of the interior faced intense drought conditions. Mexico was warmer than normal and slightly wetter than average.
- Central America and the Caribbean: Much of the region was dry and warm. The lack of rain was

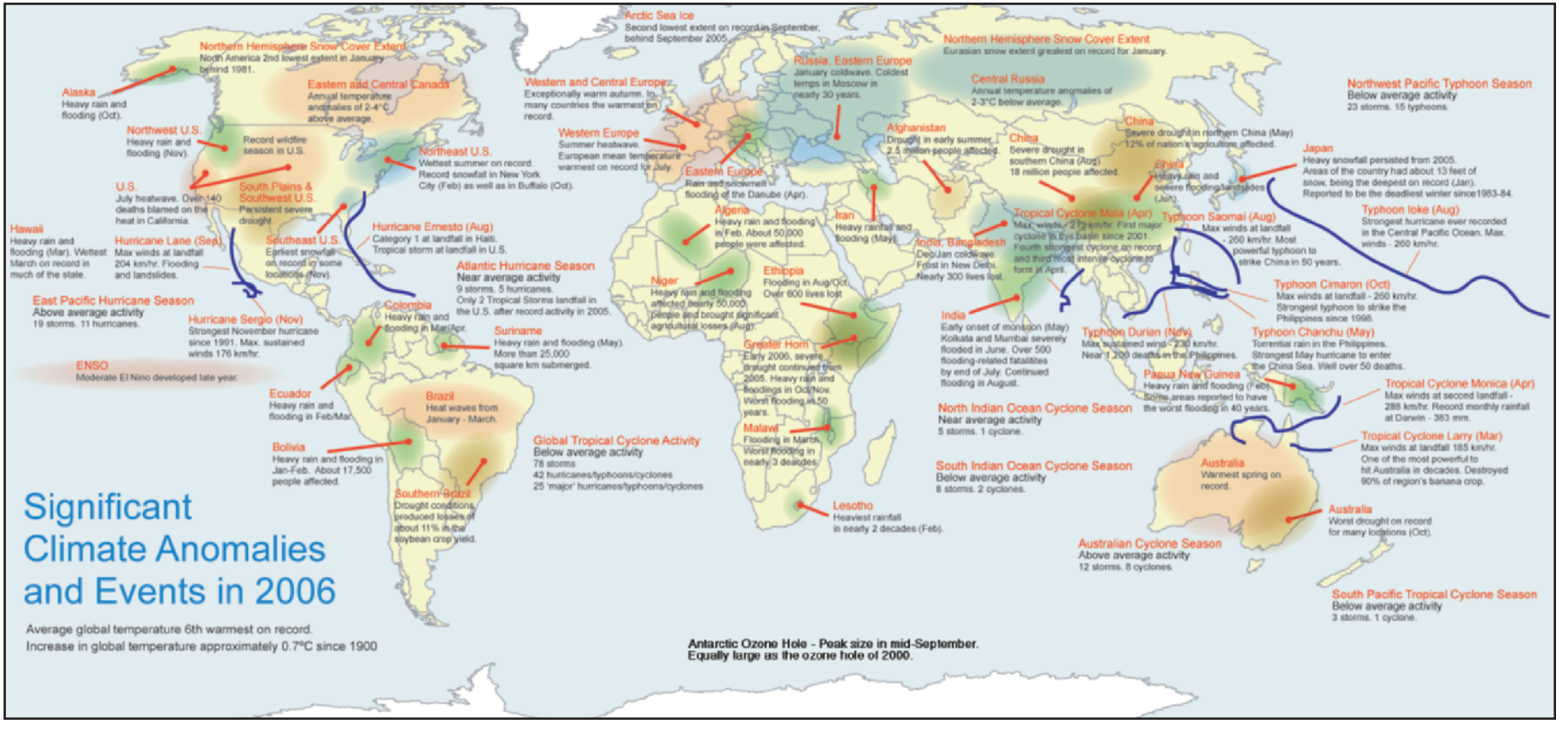


**Fig. 1.1. Geographical distribution of notable climate anomalies and events occurring around the planet in 2006.**

attributable in part to the lack of tropical cyclones impacting the region, as well as the emergence of El Niño late in the year.

- South America: The overall weather conditions varied from very wet to very dry. However, the year was warm throughout most of the continent. Classical ENSO teleconnections, as well as modulation by the MJO, were observed.
- Asia: Russian temperatures were anomalously warm, especially in December when records were broken, including in Moscow. However, January was very cold across the country. China experienced its warmest year on record and rainfall deficits. The Indian monsoon onset commenced in the fourth pentad in May. Heat waves struck parts of South Asia in May and June.
- Europe: Europe was unusually warm, with new high-temperature records set in many countries. A summer heat wave and a very warm autumn contributed to this warmth.
- Oceania: Parts of Australia were the warmest on record. Many locations were impacted by severe drought and tropical cyclones, including TC Larry, which was one of the strongest storms to hit Australia in decades.

## 2. GLOBAL CLIMATE—A. Horvitz, Ed.

### a. *Overview*—A. Horvitz

Anomalous warmth continued at the surface and throughout the troposphere in 2006. The global annual average surface temperature in 2006 ranked as either the fifth or sixth highest, depending on the dataset used. Worldwide, land surface temperatures ranked as fourth highest on record according to NOAA/NCDC, and SSTs ranked as the fifth highest. The annual global mean low- to midtroposphere anomaly for 2006 was the third to fifth warmest (depending on the dataset) since records began in 1958.

Global land surface precipitation was above average in 2006 with an annual anomaly 34.0 mm (3.0%) above the 1961–90 mean. Over the tropical Pacific, weak El Niño conditions developed during mid-2006 and lasted through the rest of the year. However, the coupling between the warmer-than-normal SST and the atmosphere did not materialize fully and no discernable ENSO signature was evident in the precipitation anomaly pattern. The 12-month running means of NH snowfall extent were below the long-term average throughout the year, continuing the trend since the late 1980s. The preliminary globally averaged atmospheric $CO_2$ mole fraction in 2006 was approximately 2.3 ppm greater than the 2005 global annual mean.

New to 2006, this section also provides a summary for global cloudiness, aerosols, and global winds. Also included is a report on teleconnection patterns and blocking reflecting large-scale changes in the atmospheric wave and jet stream patterns, which influence temperature, rainfall, storm tracks, and jet stream location and intensity over vast distances.

### b. *Global temperature*

#### 1) Surface temperature—M. J. Menne and T. C. Peterson

The global annual average surface temperature in 2006 ranks as either the fifth or sixth highest according to analysis conducted independently at institutions in the United States and United Kingdom. As shown in Fig. 2.1, the global value for 2006 ranks as the fifth highest on record according to NOAA/NCDC and NASA's GISS, and as the sixth highest according to the University of East Anglia Climate Research Unit (CRU)/Met Office (MO) Hadley Centre estimate. Calculated as a linear trend, the rates of temperature change since 1901 are 0.064°, 0.066°, and 0.073°C decade$^{-1}$ for the NOAA/NCDC, NASA GISS, and CRU/MO analyses, respectively. However, the temperature change is not linear, and the rise from 1979 to 2006 is approximately 0.17°C decade$^{-1}$ according to all three sources (Fig. 2.2).

All three global temperature analyses combine air temperature data over land with SST. The NOAA/NCDC surface temperature analysis is described in Smith and Reynolds (2005), the NASA GISS analysis is described in Hansen et al. (2001), and the CRU/MO (HadCRUT3) analysis is described in Brohan et al. (2006). Because the analyses make use of different data reconstruction and interpolation approaches, they differ most in regions with sparse data. Where data are plentiful and for global averages the three

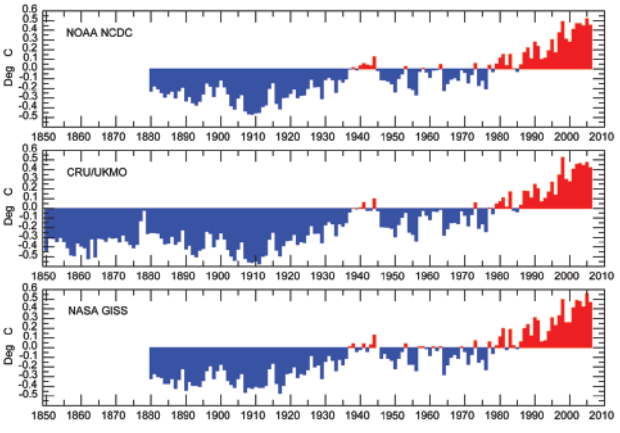


**Fig. 2.1. Annual global surface temperature departures from the 1961–90 average. [Source: NOAA/NCDC, CRUHadCRUT3, and NASA GISS.]**

analyses agree well with each other and with the other historical "global" temperature time series shown in Fig. 2.3. While the underlying data sources for all the time series differ widely, the high degree of trend consistency among them, since 1901, increases the confidence that the changes they depict are robust (Sommerville et al. 2007).

Worldwide, surface air temperatures over land rank as the fourth highest on record according to the NOAA/NCDC record, and SSTs ranked as the fifth highest (not shown). Warming has occurred in both land temperatures and SST. As might be expected given the heat capacity of oceans, land temperatures have risen at over twice the ocean rate since 1979 (about 0.30°C decade$^{-1}$ versus 0.12°C decade$^{-1}$).

The geographic distribution of annual temperature anomalies is shown in Fig. 2.4. Regionally, 2006 temperatures were the highest or near highest on record in the United States, Canada, China, the United Kingdom, Spain, and the Netherlands, as well as parts of Australia. These events are discussed in detail in the regional climate sections (see section 6).

2) Upper-air tropospheric temperatures—J. C. Christy

The temperature variations of three broad atmospheric layers, the low to midtroposphere (LT; surface to 300 hPa), the midtroposphere to lower stratosphere (MT; surface to 70 hPa), and the upper troposphere to lower stratosphere (LS; 150–20 hPa) are monitored by two observing systems—radiosondes and satellites. Three radiosonde-based products are available—HadAT2 (Thorne et al. 2005), based on about 650 stations; RATPAC (Free et al. 2005), based on 85 stations; and RAOBCORE (version 1.4; Haimberger 2007), based on about 1100 stations. Satellite products for LT, MT, and LS are from the UAH (Christy et al. 2003; Spencer et al. 2006; version 5.2 LT, version 5.1 MT; and LS) and RSS (Mears et al. 2003; Mears and Wentz 2005; version 3.0). An MT dataset from UMD (Vinnikov et al. 2006) is also included. "Annual" is defined as the period from December through November (otherwise known as the meteorological year).

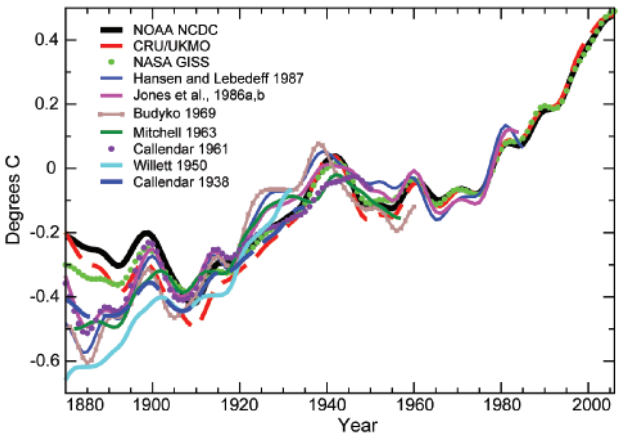


**Fig. 2.3. "Global" temperature time series: Callendar (1938): global—based on land stations; Willett (1950): global—based on land stations; Callendar (1961): 60°N to 60°S—based on land stations; Mitchell (1963): global—based on land stations; Budyko (1969): Northern Hemisphere—based on land stations and ship reports; Jones et al. (1986a,b): global—based on land stations; Hansen and Lebedeff (1987): global—based on land stations. The NOAA/NCDC, CRU/MO, and NASA GISS time series are expressed as anomalies from the 1961–90 mean (°C). Each of the other time series was originally presented as anomalies from the mean temperature of a specific, but differing base period. To make them comparable, the historic time series have been adjusted such that the mean of their last 30 yr is identical to the equivalent period in the NOAA/NCDC anomaly time series. All series have been smoothed using a 13-point filter.**

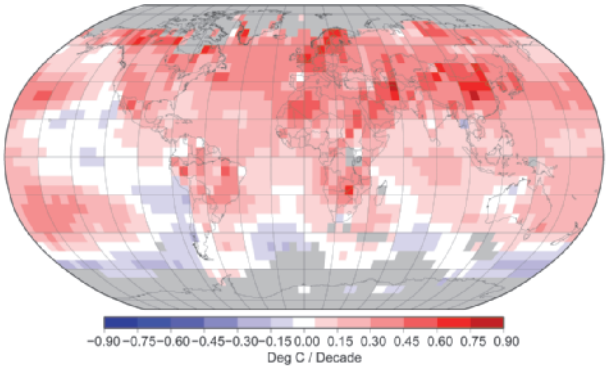


**Fig. 2.2. Pattern of linear surface temperature trends 1979–2006 according to the NOAA/NCDC analysis. Gray areas indicate data-sparse regions.**

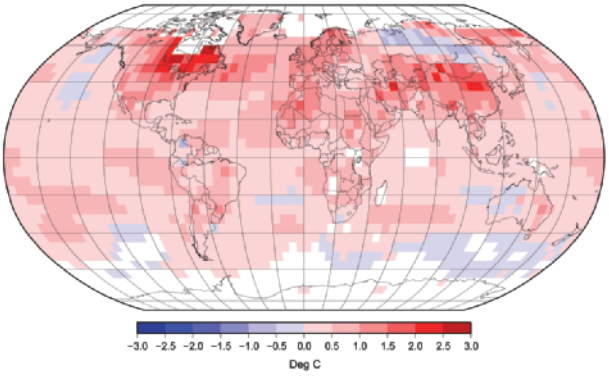


**Fig. 2.4. Geographic distribution of temperature anomalies in 2006. Departure from the 1961–90 average. [Source: NOAA/NCDC.]**

**Table 1. Linear trends (°C decade$^{-1}$) of global and tropical (20°S–20°N) anomalies for 1958–2006. In parentheses are trends for 1979–2006.**

| | HadAT2[1] | RATPAC[1] | RAOBCORE[1] | UAH[3] | RSS[3] | UMd[3,4] |
|---|---|---|---|---|---|---|
| Global LT | +0.15(+0.17) | +0.15 (+0.16) | +0.14(+0.16) | (+0.14) | (+0.19) | |
| Tropical LT | +0.12 (+0.09) | +0.14 (+0.12) | +0.13 (+0.12) | (+0.08) | (+0.18) | |
| Global MT | +0.09 (+0.07) | +0.08 (+0.04) | +0.10 (+0.12) | (+0.05) | (+0.13) | (+0.21) |
| Tropical MT | +0.09 (+0.02) | +0.08 (+0.03) | +0.13 (+0.12) | (+0.06) | (+0.14) | (+0.21) |
| Global LS | −0.35 (−0.54) | −0.43[2] (−0.70)[2] | −0.30 (−0.40) | (−0.44) | (−0.32) | |
| Tropical LS | −0.34 (−0.55) | −0.50[2] (−0.72)[2] | −0.24 (−0.34) | (−0.38) | (−0.31) | |

[1] Radiosonde datasets are characterized by more limited coverage with few data south of 50°S latitude and little in oceanic areas.

[2] The use of the 100–50-hPa layer as an approximation for the satellite LS layer leads to slightly more negative trends because the temperature trend below 100 hPa, which makes up a portion of the LS signal, is positive but not included in the 100–50-hPa layer.

[3] UAH coverage is 85°S–85°N, RSS 70°S–85°N. UMd MT covers 82.5°S–82.5°N. Since less warming has been observed in the high southern latitudes, their inclusion tends to reduce "global" trends, for example, the UAH "global" LT trend is 0.02°C decade$^{-1}$ more positive if limited to 50°S–85°N.

[4] Through 2005 only.

The annual global mean LT anomaly for 2006 was the third to fifth warmest among the datasets since records began in 1958 (Fig. 2.5), about 0.2°C cooler than the warmest year of 1998. All datasets are consistent with global trend values of +0.16 ±0.03°C decade$^{-1}$ since 1979 and +0.14 ±0.01°C decade$^{-1}$ since 1958 (Table 1). Note that the datasets are constructed using independently developed methodologies. Because none of these datasets claim precision better than ±0.05°C decade$^{-1}$, this level of agreement is very encouraging, providing a relatively confident assessment of global LT trends.

A more visual interpretation of long-term change suggests a relatively large increase in global temperatures around 1977 and another shift to warmer temperatures associated with the 1997/98 ENSO (Seidel and Lanzante 2004). Since 1977 no seasonal anomaly has dipped below −0.4°C, and since 2000 none has dipped below the 1979/88 mean.

Regionally, the largest 2006 positive anomaly magnitudes occurred in the Arctic (not shown), where the most positive trends since 1979 are also found, because both UAH and RSS measure a trend greater than +0.4°C decade$^{-1}$ poleward of 60°N.

A similar picture is indicated for the MT layer (not shown), which includes some stratospheric influence. The rankings for 2006 place it from the third to the ninth warmest among the datasets; however, the magnitude of the temperature differences in this range is not significant. Linear trends are more negative than for the LT layer because of the influence of the cooling stratosphere (Table 1).

The QBO shifted to the westerly or warm phase in 2006 and thus, tropical stratospheric temperatures (LS) were warmer than those in 2005 by about +0.6°C. Globally, the 2006 annual anomaly ranked from being the coldest to the seventh coldest, with both satellite datasets ranking 2006 as the second coldest. In particular, the south polar region was exceptionally

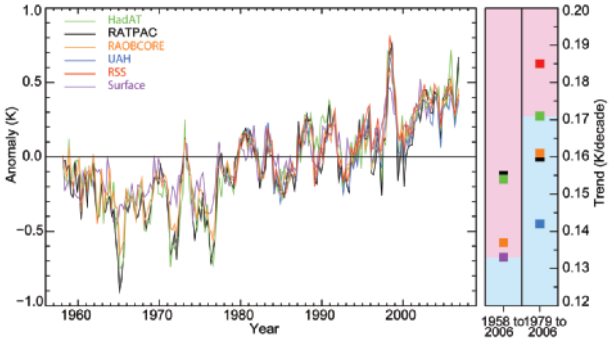


**Fig. 2.5. Time series of seasonal anomalies of the LT, with respect to 1979–88. Trend values for two periods, beginning in 1958 and in 1979, are plotted on the right. The background color of the right panels indicates the LT trend relative to the surface trend (HadCRUT3) as being more positive (lavender) or negative (light blue). [Source: H. Tichner, Hadley Centre.]**

cold in autumn (SON) 2006, countering a series of recent warm temperatures for that season (see 2005 report). Linear trends are more variable among the datasets and indicate that considerably more analysis is needed to understand the differences and give better estimates of confidence. Even so, all indicate significant cooling over the period (Table 1), though since about 1995 the global trends have not been remarkable (Fig. 2.6).

### c. *Hydrologic cycle*

#### 1) Global precipitation

##### *(i) Over land*—J. H. Lawrimore and D. H. Levinson

Global precipitation anomalies determined from land-based gauges were analyzed on both an annual and a seasonal basis using data from the GHCN (Peterson and Vose 1997). Anomalies from 1900 to 2006 were determined from the GHCN dataset with respect to the 1961–90 mean using those stations with a minimum of 25 years of data during the 30-year base period (Vose et al. 1992). Highlights of selected regional precipitation anomalies are also included below, with additional regional details provided in section 6.

Global land surface precipitation was above average in 2006, with an annual anomaly that was 34.0 mm (3.0%) above the 1961–90 mean (Fig. 2.7a). It was the eighth wettest year since reliable global records began in 1900. On a seasonal basis only JJA was drier than average. It was the fourth wettest DJF and the second wettest boreal spring (MAM) on record (Figs. 2.7b and 2.7c, respectively). The DJF and MAM anomalies were +16.7 (+6.5%) and +13.9 (+4.7%) mm, respectively.

Precipitation patterns consistent with the presence of La Niña conditions in early 2006 were evident in some areas of the world (Ropelewski and Halpert 1987). In January, above-normal precipitation occurred in much of the Maritime Continent, northern Australia, and western Pacific. Precipitation was also above average in parts of southern Africa. Also consistent with La Niña was above-average winter rain and snowfall in the northwestern United States, while precipitation and snowpack in the southwest United States were at near-record to record low levels. In April, enhanced rainfall persisted in the western equatorial Pacific from Queensland, Australia, through much of Indonesia, even as the weak La Niña episode ended. Additional details on ENSO conditions are available in section 4b.

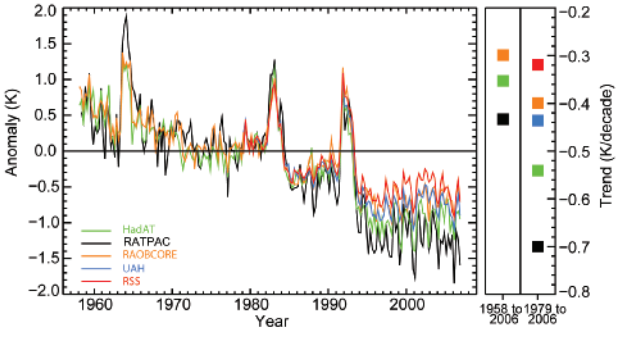


**Fig. 2.6. As in Fig. 2.5, but for the LS, and no surface comparison. Warming events follow major volcanic eruptions: Agung (1963), El Chichón (1982), and Mt. Pinatubo (1991). [Source: H. Tichner, Hadley Centre.]**

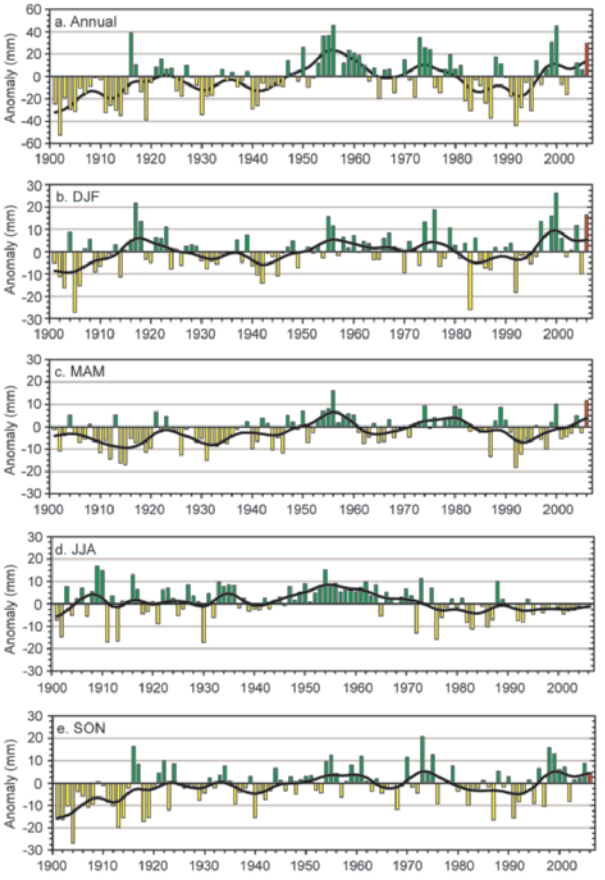


**Fig. 2.7. Time series of annual and seasonal global land surface precipitation anomalies over the period 1900–2006, based on observations from the Global Historical Climatology Network dataset (Vose et al. 1992): (a) annual, (b) December 2005–February 2006, (c) March–May, (d) June–August, and (e) September–November. The precipitation anomalies were calculated (mm) with respect to the 1961–90 base period mean: green bars = positive anomalies, yellow bars = negative anomalies, and red bar = 2006 anomaly. In addition, the black line in each time series denotes the smoothed annual or seasonal values using a 13-point binomial filter.**

Precipitation during JJA was 2.4 mm (0.6%) below average, which is a drier-than-average pattern that has occurred in all but 8 of the past 30 such seasons (Fig. 2.7d). The southwest monsoon season was near average in total rainfall on the Indian subcontinent, but periods of heavy rain resulted in record 24-h rainfall totals in some locations. Heavy rains also fell in parts of Africa. In much of Niger, the heaviest rainfall in decades led to significant agricultural losses with tens of thousands of people affected in August. Heavy rain also caused devastating floods in Ethiopia in the same month (see section 6b).

While JJA has largely been drier than average in recent decades, much of the past decade has been wetter than average during SON, and 2006 was no exception (Fig. 2.7e). Precipitation was 7.7 mm (2.4%) above average, making this the 8th out of the past 10 SONs that were wetter than average for the globe. A long-lasting drought in the Greater Horn of Africa ended with heavy rainfall and reports of the worst flooding in 50 years from October through early December. The worst-hit areas were in Ethiopia, Kenya, and Somalia, where some stations received more than six times their average monthly rainfall.

Conversely, severe drought continued in eastern Australia in late 2006, as the rapid onset of El Niño conditions in late August and September exacerbated unusually dry conditions that had been present throughout much of the year. For many areas of Australia, the lack of adequate rainfall in 2006 compounded longer-term dry conditions, with large regions not having yet recovered from the droughts of 2002/03 and 1997/98 (Nicholls 2004). Dry conditions have now persisted for 5–10 years in many areas, and for almost three decades in southwestern portions of western Australia.

Other areas of the world also have had an increasing incidence of drought over the past three decades. The percentage of the world affected by severe drought more than doubled from approximately 10%–15% in the early 1970s to approximately 30% by 2002 (Dai et al. 2004). Almost half of this increase has been linked to rising surface temperatures. The increase in global surface temperature of near 0.18°C decade$^{-1}$ since the mid-1970s (section 2bi) is thought to have increased the evaporation of moisture from many land areas. One significant consequence has been that even though decreasing trends in precipitation at regional scales were a factor associated with increasing drought coverage in some areas, the increase in areas affected by severe drought occurred even while precipitation increased in most regions of the world (Dai et al. 2004).

For global land areas as a whole, total annual precipitation increased at a rate of 0.59% decade$^{-1}$ since the mid-1970s and 0.19% decade$^{-1}$ since the start of the twentieth century. The largest increases have been in the high latitudes of the NH. Although there has been large decadal variability and periods of decreasing precipitation trends during the past century, the monotonic trend averaged within the 55°–85°N latitude band from 1900 to 2006 was approximately +1.2% decade$^{-1}$. During the same period precipitation increased at a rate of 0.4% decade$^{-1}$ in the midlatitudes of the NH (30°–55°N) and 0.25% decade$^{-1}$ in the midlatitudes of the Southern Hemisphere. A decreasing trend near 0.4% decade$^{-1}$ occurred from 10° to 30°N. This in part reflected large negative trends over western and eastern Africa, where rainfall decreased at a rate near 0.8% decade$^{-1}$.

*(ii) Precipitation over oceans*—P. Xie and J. E. Janowiak

Real-time monitoring of global oceanic precipitation is conducted at NOAA's Climate Prediction Center (CPC) using the "CAMS-OPI" dataset (Janowiak and Xie 1999). By combining the gauge observations of precipitation collected and archived by CPC via the CAMS (Ropelewski et al. 1985) with the satellite-based OPI (Xie and Arkin 1998), the CAMS-OPI database provides monthly precipitation estimates over global land and ocean. Several large-scale anomalies, discussed below, were observed in 2006 (Fig. 2.8, bottom panel).

The mean precipitation amount over the entire global oceans during 2006 was 2.812 mm day$^{-1}$, which is equivalent to a freshwater influx of 1026.4 kg m$^{-2}$. Maximum annual precipitation rates of over 9 mm day$^{-1}$ were observed over the tropical western Pacific where the ITCZ merges with the SPCZ (near the equator and 150°E). Relatively light precipitation was recorded over the oceanic dry zones in the southeast Pacific, the northeast Pacific off the coast of the southwestern United States, the southeast Atlantic, the tropical North Atlantic near western Africa, and the southeastern Indian Ocean.

Over the tropical Pacific, weak (and at times moderate) El Niño conditions developed during mid-2006 and lasted through the rest of the year. However, coupling between the warmer-than-normal SST (see section 3b) and the atmosphere did not materialize fully, and no discernable ENSO signature was seen in the precipitation anomaly pattern. In fact, the precipitation pattern in the tropical Pacific was more characteristic of La Niña conditions. These include greater-than-normal rainfall east of the Maritime Continent and over the ITCZ and SPCZ, and less-

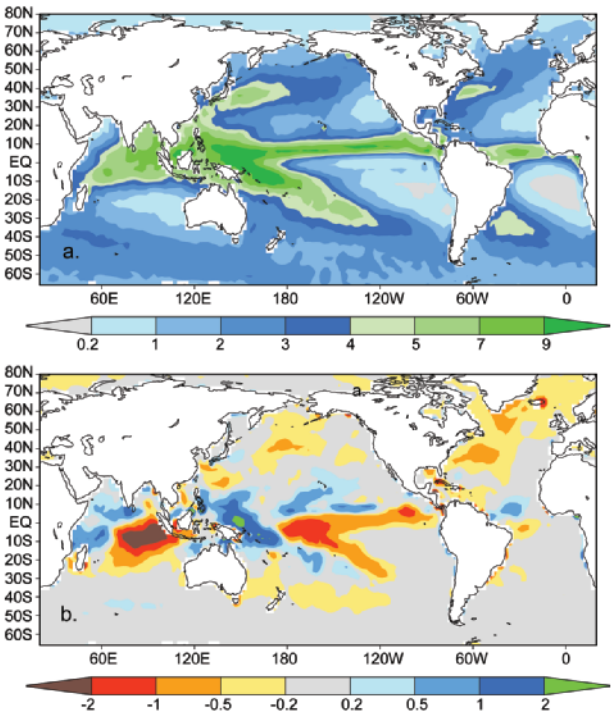


**Fig. 2.8. Annual mean total precipitation (mm day$^{-1}$, upper) and annual mean precipitation anomaly [mm day$^{-1}$, bottom] for 2006 as observed by the gauge–satellite merged dataset of CAMS-OPI (Janowiak and Xie 1999). Precipitation anomalies were calculated using 1979–95 as the base period.**

than-normal rainfall over much of the central and eastern near-equatorial Pacific (Fig. 2.8). In contrast, a time–longitude diagram of near-equatorial precipitation anomalies (Fig. 2.9) showed a steady eastward progression of positive rainfall anomalies beginning in June 2006 that coincided with the developing El Niño conditions. However, the eastward movement was restricted to the area from 160°E to about 170°W.

Over the Indian Ocean, the precipitation distribution during 2006 was characterized by a large negative anomaly over the eastern portion of the basin between the equator and 20°S. This anomaly was associated with a cold water mass that developed during the second half of the year. In contrast, the western portion of the Indian Ocean experienced wetter-than-normal conditions that included the entire Arabian Sea southward to Madagascar. This anomaly pattern is indicative of the positive phase of the Indian Ocean dipole pattern (Baquero-Bernal et al. 2002).

The lower-than-normal rainfall over the Caribbean Sea and the Gulf of Mexico (Fig. 2.8) may have been associated with the relatively inactive hurricane season. Elsewhere, weak negative precipitation anomalies were observed over the northwestern Atlantic Ocean during most of 2006.

### 2) Snow—D. A. Robinson

Annual SCE over NH lands averaged 24.9 million km$^2$ in 2006; this is 0.6 million km$^2$ less than the 37-yr average and ranks 2006 as having the 27th most extensive cover of record. This evaluation considers snow over the continents, including the Greenland ice sheet. The SCE in 2006 ranged from 47.7 million km$^2$ in January to 2.2 million km$^2$ in August. Monthly snow extent values are calculated at the Rutgers–The State University of New Jersey Global Snow Laboratory from weekly SCE maps produced by NOAA meteorologists, who rely primarily on daily visible satellite imagery to construct the maps.

Hemispheric SCE was above the long-term mean in January, February, and October, but close to or below the mean in all other months. Thus, the 12-month running means of NH extent were below the long-term average throughout the year (Fig. 2.10). This has almost exclusively been the situation since the late 1980s. Eurasian SCE was somewhat above the long-term average in 2006 and ranked as the 17th

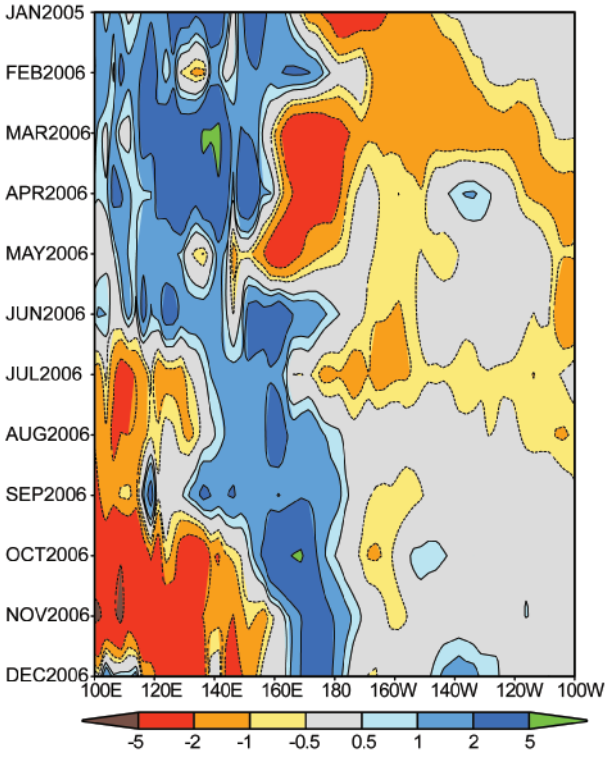


**Fig. 2.9. Time–longitude section of precipitation anomaly averaged over the tropical Pacific (10°S–10°N) as observed by the CAMS-OPI (Janowiak and Xie 1999). Precipitation anomalies were calculated using 1979–95 as the base period.**

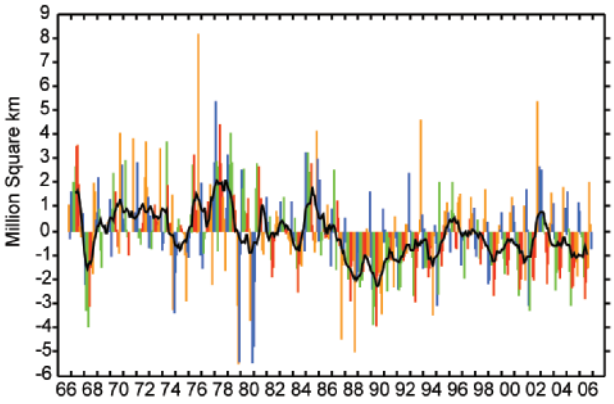


**Fig. 2.10. Anomalies of monthly snow cover extent over Northern Hemisphere lands (including Greenland) between November 1966 and December 2006. Also shown are 12-month running anomalies of hemispheric snow extent, plotted on the seventh month of a given interval. Anomalies are calculated from NOAA snow maps. Mean hemispheric snow extent is 25.5 million km$^2$ for the full period of record. Monthly means for the period of record are used for nine missing months between 1968 and 1971 in order to create a continuous series of running means. Missing months fall between June and October; no winter months are missing.**

most extensive cover of the satellite era. North American SCE was much below average, ranking 36th, the second least extensive.

As is common, 2006 SCE showed significant variability on temporal and spatial scales. For instance, hemispheric SCE ranked in the top 10 in January and October, while totals ranked in the lowest 10 from May through September, as well as in December. January's anomaly was positive as a result of Eurasian extent being the second largest of record, despite North America ranking 39th, or second least extensive. October's high ranking was the result of extensive cover over both continents, following a late spring, summer, and early fall, when both continents ranked quite low. Spring and summer snow cover continues to be less extensive in the second half of the satellite record than in the first half (Fig. 2.11). Lower-than-average North American SCE was first noted in North America in April, while it was not until June that Eurasian cover fell to well below average extent. Fall and winter SCE continue to show considerable year-to-year variability, however there are no apparent trends.

Over the contiguous United States, January SCE was the second lowest on record, while April and November ranked in the top 10 lowest. Meanwhile, October SCE was the 14th largest. Alaskan cover ran close to average from January through summer's end, and then fell well below average during the fall.

### 3) Cloudiness—A. Heidinger, A. Evan, and B. Baum

Cloudiness in 2006 was dominated by La Niña at the beginning of 2006, and by El Niño at the end of the year. The dataset used in this analysis of global cloudiness is based on 25 years of data (1982–present) from the series of AVHRR imagers on the NOAA polar-orbiting platforms, and is known as the AVHRR PATMOS-x (information available online at http://cimss.ssec.wisc.edu/clavr/patmosx.html).

Figure 2.12 is a map of boreal winter cloudiness (January–March) for 2006 in which the climatological mean based on the PATMOS-x record for the same months has been subtracted. Inspection of this figure shows that the enhanced Pacific trade flow results in a reduction in cloudiness across the equatorial eastern Pacific that is caused by cooler-than-normal SSTs. Also present is an increase in cloud amount in the Indonesian region, consistent with the characteristic warming of ocean temperatures that occurs during a La Niña event. A slight cooling across the Indian

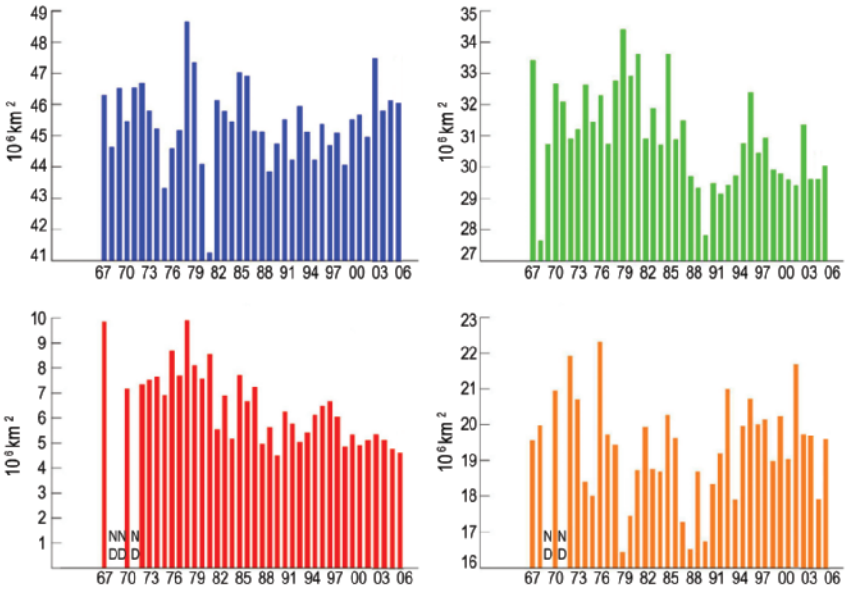


**Fig. 2.11. Seasonal snow cover extent over Northern Hemisphere lands (including Greenland) between winter (December–February) 1966–67 and fall (September–November) 2006. Calculated from NOAA snow maps.**

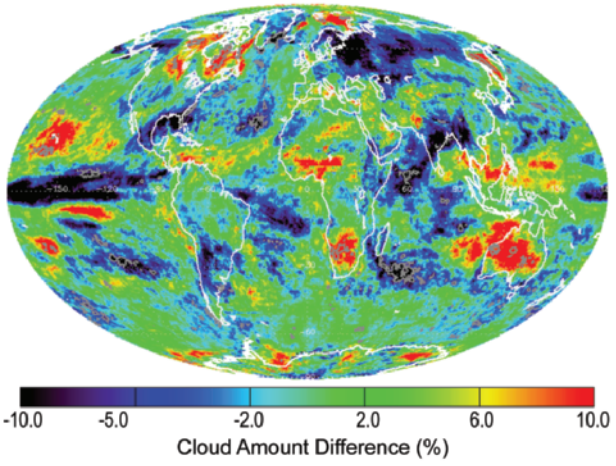


**Fig. 2.12. Map of boreal winter (January–March) absolute cloud amount differences (%) between the observations in 2006 and the climatological winter mean based on the period from 1982 to 2006.**

Ocean and the observed reduction in cloud amounts during this period is also consistent with the negative phase of an ENSO period.

Figure 2.13 provides similar analysis, but for the boreal fall of 2006, consisting of the cloud amount for October, November, and December. There is a sharp reversal of cloud patterns across the equatorial Pacific associated with the onset of an El Niño event. The easing of the easterly trade flow and the subsequent eastward migration of warmer sea surface temperatures results in the pattern of increased cloudiness along the eastern equatorial Pacific, a drastic decrease in cloudiness from northern Australia to Southeast Asia, and an increase in cloudiness across the Indian Ocean. While the departure from the mean state is more than a 10% reduction in cloudiness in these regions, this anomaly (and that of the La Niña state) is not statistically significant at the 95% confidence level, and is by no means impressive when compared to cloud amount anomalies during much stronger ENSO events.

The year 2006 also featured an increase in high-level cloudiness across much of southern Africa. This anomaly was more prevalent and statistically significant in a map of annual mean high cloud anomalies (Fig. 2.14). These anomalies in high cloud amounts are consistent with a strong monsoon observed toward the beginning of 2006 that stretched across the region.

*d. Trace gases and aerosols*

1) Carbon dioxide—E. J. Dlugokencky and R. C. Schnell

The $CO_2$ emitted from fossil fuel burning is partitioned into the following three mobile reservoirs: atmosphere, oceans, and terrestrial biosphere. One result of fossil fuel combustion has been that atmospheric $CO_2$ has increased from about 280 ppm at the start of the industrial revolution to more than 380 ppm today. Roughly half of the emitted $CO_2$ remains in the atmosphere and the remainder has gone into the following two sinks: oceans and the land biosphere (which includes plants and soil carbon).

Currently, more than 7 Pg (Pg = 1015 g) of carbon is emitted into the atmosphere by fossil fuel combus-

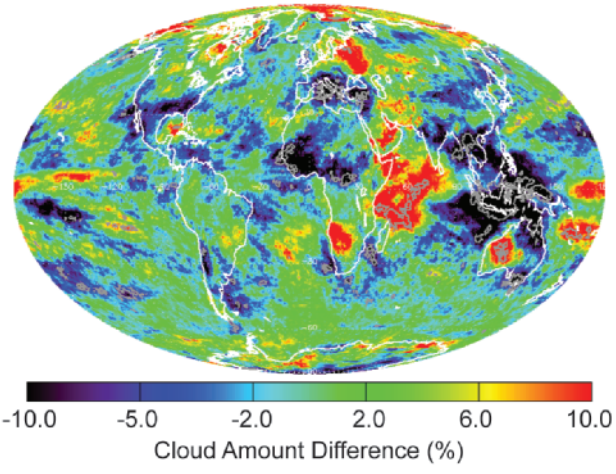


**Fig. 2.13. Map of boreal fall cloudiness (October–December) absolute cloud amount differences (%) between the observations in 2006 and the climatological mean for the boreal fall based on the period from 1982 to 2006. The data are provided by the AVHRR PATMOS-x project.**

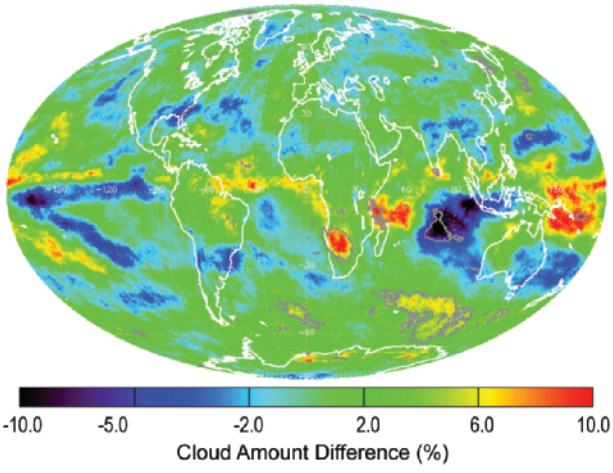


**Fig. 2.14. Difference (%) between the mean 2006 high cloud amounts and the climatological mean high cloud amounts (1982–2006). There are regions where the anomaly is a statistically significant departure from the mean state, notably in the Indian Ocean and over South Africa.**

tion each year. During the 1990s, net uptake by the oceans was estimated as 1.7 ±0.5 Pg $yr^{-1}$ and by the land biosphere as 1.4 ±0.7 Pg $yr^{-1}$ (Prentice et al. 2001). The gross fluxes between the atmosphere and oceans, and the atmosphere and terrestrial biosphere (photosynthesis and respiration), are on the order of 100 Pg $yr^{-1}$. Interannual variations in the atmospheric increase of $CO_2$ (see Fig. 2.15, based on Conway et al. 1994) are because of small changes in these net fluxes, not because of variations in fossil fuel emissions. Most attempts to explain the interannual variability of the atmospheric $CO_2$ increase have focused on short-term climate fluctuations (e.g., ENSO and post–Mt. Pinatubo cooling), but the mechanisms, especially the role of the terrestrial biosphere, are not well understood. To date, about 5% of conventional fossil fuels have been combusted. If combustion were stopped today, after a few hundred years, 15% of the total carbon emitted would remain in the atmosphere and the remainder would be in the oceans.

The preliminary globally averaged atmospheric $CO_2$ mole fraction in 2006 was 381.1 ppm, which is ~2.3 ppm greater than the 2005 global annual mean. While there has been an average annual increase of 1.6 ppm $yr^{-1}$ since 1980, the average rate of increase since 2000 has been 2.1 ppm $yr^{-1}$. This suggests that the fraction of $CO_2$ emitted from fossil fuel combustion that remains in the atmosphere may be increasing.

NOAA ESRL launched the "Carbon Tracker" (information online at www.ersl.noaa.gov/gmd/ccgg/carbontracker), a new tool that uses observations and a state-of-the-art model to keep track of time-dependent emissions and the uptake of atmospheric $CO_2$ from both natural and anthropogenic processes. For the period from January 2001 to December 2006, Carbon Tracker estimated that the uptake of carbon by North American ecosystems averaged –0.65 ± 0.75 Pg C $yr^{-1}$; this can be compared to the total North American fossil fuel emissions of 1.9 Pg C $yr^{-1}$.

### 2) Methane—E. J. Dlugokencky and R. C. Schnell

The $CH_4$ contribution to anthropogenic radiative forcing, including direct and indirect effects, is about 0.7 W $m^{-2}$ (about half that of $CO_2$). Changes in the burden of $CH_4$ feed back into atmospheric chemistry, affecting the concentrations of OH and $O_3$. The increase in $CH_4$ since the preindustrial era is responsible for ~½ of the estimated increase in background tropospheric $O_3$ during that time. Changes in OH concentration affect the lifetimes of other greenhouse gases, such as the replacement refrigerants (HCFCs and HFCs).

High-precision measurements of atmospheric $CH_4$ provide climate modelers with current and past rates of $CH_4$ increase, and they are also useful in constraining the global $CH_4$ budget and how it is changing with time. This "top-down" approach can determine total global emissions to within ±10%, but background atmospheric observations alone cannot effectively quantify emissions from individual sources. A recent surprise in the global $CH_4$ budget was the report that vegetation can be a significant source of atmospheric $CH_4$, even under aerobic conditions (Keppler et al. 2006). Our inability to identify this source before now shows the limitations of observations, particularly in the Tropics, for quantifying weakly emitting, diffuse sources.

In Fig. 2.15b, $CH_4$ mole fractions from the NOAA observatory at Mauna Loa, Hawaii, are plotted as a

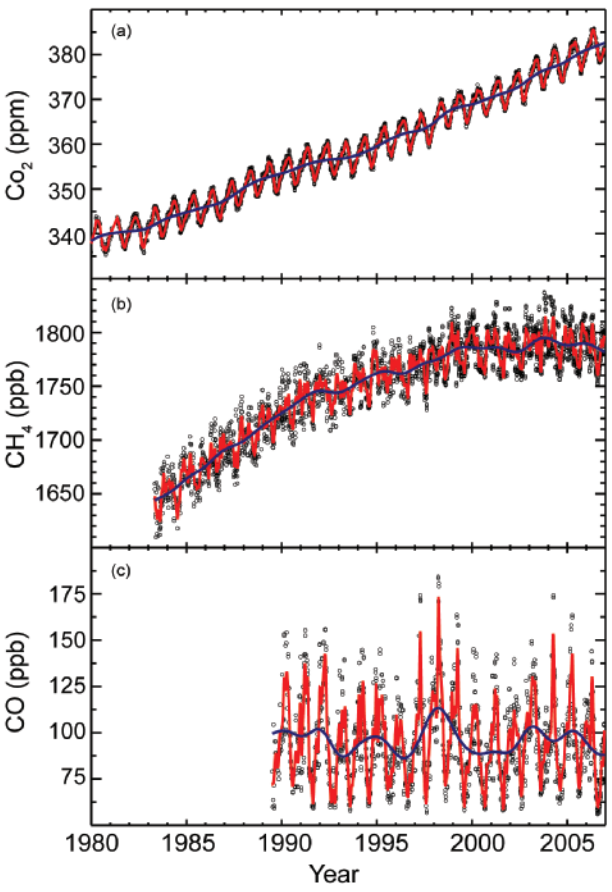


**Fig. 2.15. Trace gas mole fractions (black symbols) determined from samples collected at the NOAA/ESRL Mauna Loa Observatory (MLO) for (a) $CO_2$ (T. J. Conway, NOAA), (b) $CH_4$ (E. J. Dlugokencky, NOAA), and (c) CO (P. C. Novelli, NOAA). In all panels, the solid blue line is the deseasonalized trend and the red line is a smooth curve fitted to the black symbols. Current trends at MLO are available online (www.cmdl.noaa.gov/ccgg/trends/; additional plots can be found at www.cmdl.noaa/ccgg).**

function of time. During more than 20 years of measurements $CH_4$ has increased by nearly 10%, but the rate of increase has slowed in recent years. A large increase in 1998 and a smaller one in 2003 were likely the result of climatic conditions that resulted in increased emissions from biomass burning and natural wetlands. Otherwise, atmospheric $CH_4$ has remained nearly constant (Dlugokencky et al. 2003). Possible causes for the recent lack of growth in atmospheric $CH_4$ burden are decreased emissions from natural wetlands because of widespread drought in the Tropics (Bousquet et al. 2006), and a change in the $CH_4$ sink because of increased lightning (Fiore et al. 2006); but, the exact causes are still unclear. Our preliminary global annual $CH_4$ average for 2006 of 1775.4 ppb is only 3 ppb greater than that observed in 1999.

3) Carbon monoxide—E. J. Dlugokencky and R. C. Schnell

Unlike $CO_2$ and $CH_4$, CO does not strongly absorb terrestrial infrared IR radiation, but it still impacts climate through its chemistry. The chemistry of CO affects OH (which influences the lifetimes of $CH_4$ and HFCs) and tropospheric $O_3$ (itself a greenhouse gas), so emissions of CO can be considered equivalent to emissions of $CH_4$ (Prather 1996). Current emissions of CO may contribute more to radiative forcing over decadal time scales than emissions of anthropogenic $N_2O$ (Daniel and Solomon 1998).

The CO mole fractions from Mauna Loa are plotted as a function of time in Fig. 2.15c and show little trend over the period of these measurements (Novelli et al. 2003). Superimposed on the flat trend are significant increases during 1997/98, and again in 2002/03, which were likely the result of tropical (Langenfelds et al. 2002) and boreal biomass burning (Kasischke et al. 2000). Because the lifetime of CO is relatively short (a few months), the anomaly quickly disappeared and CO returned to pre-1997 levels shortly afterward. In 2005, CO levels are comparable to those found in the early 2000s.

The preliminary globally averaged CO mole fraction in 2006 was 82.1 ppb, which is 1.1 ppb less than the 2005 global annual mean and 13.5 ppb lower than 1998, which had a large contribution from CO emitted by biomass burning.

4) Decreases in ozone-depleting gases and their replacements—S. A. Montzka and R. C. Schnell

Long-lived halocarbons affect the radiative balance of the atmosphere because they efficiently absorb terrestrial IR radiation. Halocarbons containing Br and Cl also influence the radiative atmospheric balance indirectly through their destruction of stratospheric $O_3$ (see section 5c).

Because of concerns over stratospheric $O_3$ depletion, the production of many halocarbons has been restricted in recent years. The international phase-out of human-produced halocarbons was brought about through amendments and revisions to the 1987 Montreal Protocol on Substances that Deplete the Ozone Layer. As a result of these efforts, mixing ratios of many ozone-depleting gases have been declining at the Earth's surface in recent years; this decline continued in 2006 (Fig. 2.16). It is now apparent from the NOAA/ESRL/GMD measurements from around the globe that tropospheric mixing ratios of CFC-12, the longest lived and most abundant human-made ozone-depleting gas in the atmosphere, peaked within the last few years and now has begun to decrease.

The NOAA/ESRL/GMD data show that mixing ratios of some halogenated gases continue to increase globally (Fig. 2.16). The most rapid increases are observed for HCFCs and HFCs, which are chemicals commonly used as replacements for CFCs, halons, and other ozone-depleting gases. Although HCFCs contain Cl and deplete $O_3$ with a reduced efficiency compared to that of CFCs, HFCs do not participate in ozone-destroying reactions.

Increases in HCFCs have slowed notably in recent years; by mid-2006, the Cl in the three most abundant HCFCs amounted to 227 ppt, or 8.4 % of all Cl carried by long-lived halocarbons. Mixing ratios of HFC-134a (1, 1, 1, 2-tetrafluoroethane), the most abundant HFC in the global background atmosphere, increased nonlinearly in the 1990s during the period of early production and use. From 2001 to 2006, however, it has increased in the global troposphere at a fairly constant linear rate of 4.3 ppt $yr^{-1}$. Concern over increases in HFCs stems in large part from the fact that these gases are efficient absorbers of infrared radiation.

The influence of these disparate trends on future levels of stratospheric $O_3$ can be gauged roughly from a sum of Cl and Br in long-lived halocarbons, provided the enhanced efficiency for Br to destroy $O_3$ is considered [note that this efficiency factor has been updated here to 60 based upon a reanalysis appearing in the latest WMO Scientific Assessment of Ozone Depletion (Cunnold et al. 2007)]. This sum is expressed here as EECl (Fig. 2.16), and is derived from surface-based measurements. EECl provides an estimate of the ozone-depleting power of trace gases a few years in the future, when air at the Earth's surface will have become mixed into the midlatitude stratosphere where the $O_3$ layer resides. A second metric,

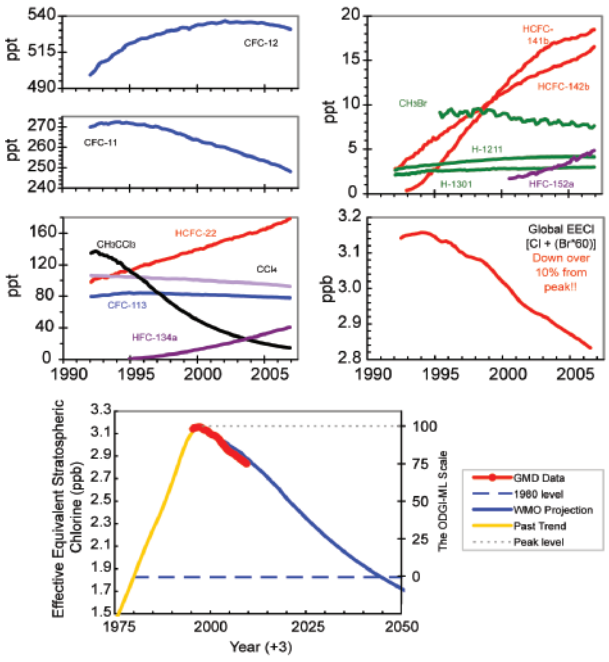


**Fig. 2.16. Changes in global mean tropospheric mixing ratios (ppt, or pmol mol$^{-1}$) of the most abundant CFCs, HCFCs, HFCs, chlorinated solvents, and brominated gases. These global changes are calculated from atmospheric measurements made at remote sites in both the Northern and Southern Hemisphere (from the NOAA/ESRL/GMD cooperative air sampling network). The middle-right hand panel shows secular changes in atmospheric EECl (in ppb or nmol mol$^{-1}$), which is an estimate of the ozone-depleting power of atmospheric halocarbons. EECl is derived from observed mixing ratios of ozone depleting gases appearing in the other 4 panels, and it is derived from the sum of [Cl + (Br × 60)] contained in these gases. The bottom panel shows the recent changes in EESC observed by the NOAA/GMD global network relative to the secular changes observed in the past, including the level observed in 1980 when the ozone hole was first observed, and a projected future. The Ozone Depleting Gas Index for midlatitudes is derived (right-hand axis) from rescaling EESC. EESC is derived from EECl by simply adding 3 yr to the time axis to represent the lag associated with mixing air from the troposphere to the middle stratosphere, where the ozone layer resides. [Source: S. A. Montzka, J. H. Butler, G. Dutton, D. Mondeel, and J. W. Elkins, NOAA/GMD.]**

ECl, provides an estimate of the ozone-depleting power of trace gases in the near future for the stratosphere over the polar regions (not shown).

The observations indicate that the EECl and ECl content of the lower atmosphere has declined fairly steadily since the peak in 1994 to 2006 at a mean rate of 27–29 ppt yr$^{-1}$. Scenarios projecting future halocarbon mixing ratios have been derived elsewhere based upon full compliance with the fully amended and revised Montreal Protocol and our understanding of the atmospheric lifetimes of these gases (Cunnold et al. 2007). These analyses suggest that it will take 40–60 years for EECl and ECl to decline to the levels present in 1980, which is before $O_3$ depletion was first observed. This 1980 level is notable, given that one might expect nearly full recovery of stratospheric $O_3$ once atmospheric EECl or ECl returns back to this level. The time scale for $O_3$ recovery will depend upon other factors as well, however, such as stratospheric temperatures and atmospheric aerosol loading. Nonetheless, the declines in EECl from 1994 to the present represent a significant drop in the atmospheric EECl burden; as of 2006 EECl had declined 20% of the way back down to the 1980 level (lower panel of Fig. 2.16).

Progress toward EECl returning to the abundance in 1980 can now be readily assessed with the NOAA ODGI (online at www.cmdl.noaa.gov/odgi/). This index is derived from EECl and ECl data for the midlatitude and Antarctic stratosphere. The index is scaled so that a value of 100 represents the EECl or ECl abundance at its peak, and 0 represents the 1980 level (the level at which no ozone depletion is expected, assuming constancy in all other variables). In 2005, the ODGI-Midlatitudes was 76.7, indicating that the abundance of ozone-depleting substances have decreased nearly 25% of the way toward the levels that were present in 1980 (Fig. 2.16). Less progress is evident for Antarctica; ODGI-Antarctica was 87.6 in 2005, which suggests halocarbon abundances have declined slightly over 12% of the way down to 1980 levels.

Changes in the direct radiative influence of long-lived halocarbons can be estimated from observed changes in atmospheric mixing ratios with knowledge of trace-gas radiative efficiencies. Such an analysis suggests that the direct radiative forcing of these gases was still increasing in 2005, though at a much slower rate than observed from 1970 through 1990.

### 5) The combined influence of long-lived trace gases on the radiative balance of the atmosphere—S. A. Montzka and R. C. Schnell

Changes in the abundance of long-lived trace gases have a direct and indirect influence on the energy balance of the atmosphere. The direct radiative influence of a trace gas is directly proportional to its atmospheric abundance and how efficiently it absorbs infrared radiation in specific regions of the electromagnetic radiation spectrum (its radiative

forcing). High-precision measurements of $CO_2$, $CH_4$, $N_2O$, CFC-12, and CFC-11 (the major greenhouse gases), along with 10 minor greenhouse gases obtained from the NOAA global air sampling network, have been used to calculate the overall change in the direct radiative climate forcing arising from the sum of all of these long-lived gases (Hofmann et al. 2006) (Fig. 2.17). This forcing is calculated by considering changes in the abundances of these gases since 1750. By mid-2005, the increases in the abundances of all of these gases above 1750 levels amounted to an additional radiative forcing to the atmosphere totaling approximately 2.6 W $m^{-2}$. Changes in the abundance of $CO_2$ since 1750 accounted for nearly two-thirds of this enhanced radiative heating.

The NOAA AGGI has been developed based upon the radiative forcing calculated from these NOAA measurements (Hofmann et al. 2006). The index is a ratio of radiative forcing from all of these gases (based upon changes since 1750) relative to the radiative forcing calculated from these gases for 1990, the Kyoto Protocol baseline year. By 2005, the AGGI was 1.215, indicating that the direct radiative forcing arising from increases in the abundance of these trace gases had increased by 21.5% from 1990 to 2005 (Fig. 2.17). Increases in the atmospheric abundance of $CO_2$ accounted for over 75% of the observed increase in the AGGI from 1990 to 2005.

### 6) Nitrous oxide and sulfur hexafluoride—J. W. Elkins and G. S. Dutton

Nitrous oxide and $SF_6$ are strong infrared-absorbing greenhouse gases and are measured on the same gas chromatographic instrument channel at all of NOAA's Earth System Research Laboratory baseline observatories. Molecules of $N_2O$ and $SF_6$ in the atmosphere are 296 and 22,200 times more effective infrared absorbers per molecule compared to $CO_2$ over a 100-year time horizon, respectively. However, the concentrations of $N_2O$ and $SF_6$ are just over 1000 and 60 million times lower than the atmospheric $CO_2$ concentration, respectively. At the end of 2006, the mean atmospheric concentrations of $N_2O$ and $SF_6$ were 320 ppb and 6 ppt, respectively, as shown in Fig. 2.18. The current climate forcing relative to the beginning of the industrial revolution (1750) for $N_2O$ and $SF_6$ is 0.16 and 0.002 W $m^{-2}$, respectively. While the climate forcing from $SF_6$ is small, it has a longer lifetime (500–3500 yr) than $N_2O$ (100 yr). Atmospheric $N_2O$ also affects stratospheric $O_3$ because it is the source gas for stratospheric NO. Stratospheric NO contributes to the NOx catalytic sink for stratospheric $O_3$ loss, which is dominant between 25 and 40 km.

Another striking feature of these greenhouse gases is their almost linear growth rate over their full atmospheric records (Fig. 2.18). Atmospheric $N_2O$ and $SF_6$ are growing at 0.77 ppb $yr^{-1}$ and 0.22 ppt $yr^{-1}$, respectively. Atmospheric $N_2O$ has both natural and manmade sources, where the manmade sources (fertilizer usage, catalytic reduction of fossil fuel emissions, by-products of chemical processes, etc.) account for about 30% of total emissions. Whereas $SF_6$ is produced solely by man, its usage is now considered essential as an insulator for the distribution of electric power (95%) with minor usage in atmospheric tracer studies. There are biennial and short-term changes in the atmospheric growth rates of $N_2O$ and $SF_6$ that are greater than ±25%. These changes are related to varying source strengths on the ground, in transport, and as destruction in the upper atmosphere. The decline in the growth rate of $SF_6$ after 1996 is most likely the result of voluntary recovery of $SF_6$ by utility companies and elimination of the use of $SF_6$ as a compressed gas in automobile tires, and the switch to the use of other gases or materials for bladders in the soles of athletic shoes.

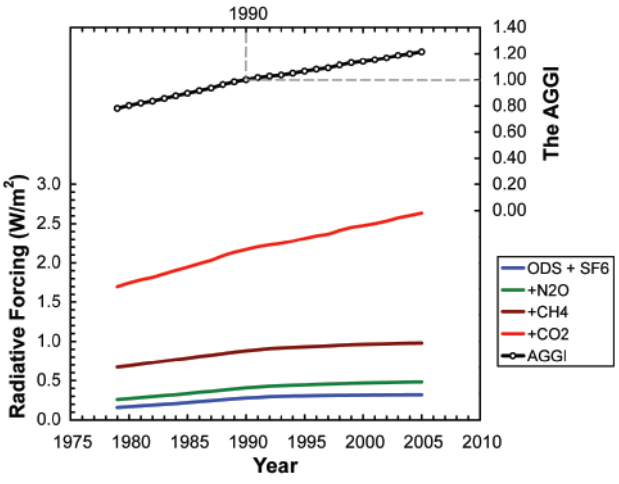


**Fig. 2.17. The direct radiative forcing arising from increases in the abundance of long-lived trace gases in the atmosphere since 1750 and the Annual Greenhouse Gas Index (Hofmann et al. 2006). The colored lines indicate the radiative forcing from different subsets of gases including ozone-depleting substances and $SF_6$ (indicated as "ODS+$SF_6$"), the additional contribution of $N_2O$ (indicated as "+$N_2O$"), the additional contribution of $CH_4$ (indicated as "+$CH_4$"), and the additional contribution of $CO_2$ (indicated as "+$CO_2$"). The total direct radiative forcing from all these gases is equivalent to the line indicated as "+$CO_2$." Also shown is the NOAA AGGI, which is calculated from the total direct radiative forcing normalized to 1990, the baseline year of the Kyoto Protocol.**

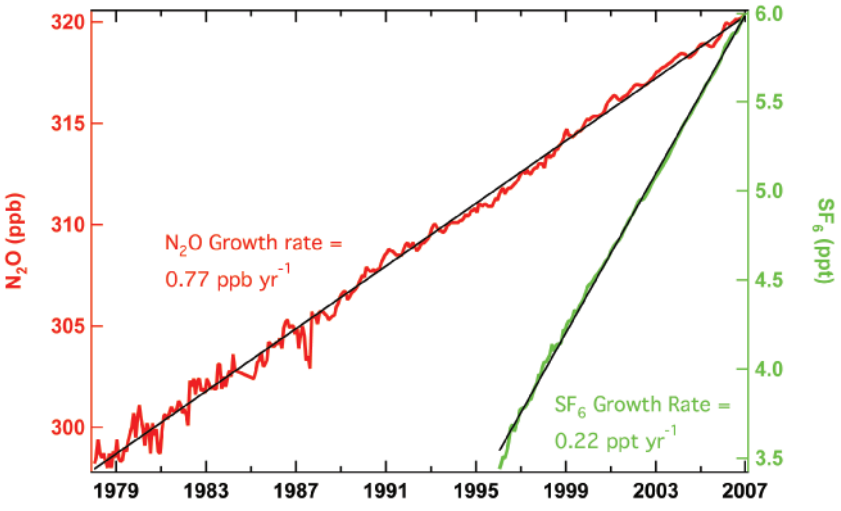


**Fig. 2.18. The global atmospheric concentration of $N_2O$ versus time from flasks (1977–87) and in situ gas chromatographs (1988–2006) at NOAA/ Earth System Research Laboratory baseline stations at Pt. Barrow, Alaska; Niwot Ridge, Colorado; Mauna Loa, Hawaii; American Samoa; and South Pole is shown in red. The global trend for atmospheric $SF_6$ from flasks (1996–99) and in situ gas chromatographs (2000–06) is shown in green. Calculated linear regression lines are shown in black. [Source: J. W. Elkins and G. S. Dutton, NOAA/ESRL.]**

7) Aerosols—A. T. Evan, N. M. Mahowald, and L. A. Remer

The global aerosol system in 2006 was both typical and atypical of long-standing patterns. Figure 2.19 shows the annual mean AOD at 550 nm, calculated from daily MODIS 10-km retrievals (Remer et al. 2005). The AOD is a measure of the extinction of shortwave radiation, and its global distribution is roughly equally divided between dust, sulfates, and carbonaceous aerosols, even though dust and sea salt dominate the aerosol mass loading. This is because sulfates and carbonaceous species are much more efficient in terms of light extinction (Tegen et al. 1997). Note that the standard MODIS algorithm does not retrieve either over clouds, or over snow, ice, sunglint, or bright desert surfaces. Thus, the aerosol distribution of Fig. 2.19 is biased toward summer retrievals in high-latitude and cloud-free high pressure systems.

For long time series analysis, we use data from longer-flying satellites, for example, the AVHRR, since the MODIS data record begins in 2000. Here we use the 870-nm AOD (Ignatov and Stowe 2002a,b) and dust fraction (Evan et al. 2006) products from the Pathfinder Atmospheres Extended dataset (online at http://cimss.ssec.wisc.edu/clavr/patmosx.html). This dataset applies a new calibration technique to the AVHRR imagers (Heidinger et al. 2002), making it more apt for studying long-term changes. However, aerosol activity over land and in the presence of clouds is not detectable and therefore must be inferred either by over-water clear-sky retrievals or by comparison with MODIS retrievals. We also include output from a reanalysis-driven transport model that includes mineral aerosol source and deposition algorithms (Mahowald et al. 2003).

*(i) Saharan and Sahelian output*

While some of the aerosols produced from this region include carbonaceous aerosol from biomaburning, biofuels, and urban sources, mineral dust provides the bulk of the mass exported over the Atlantic Ocean. Mineral aerosols from west and central Africa have been shown to account for ~50% of the global dust loading (Luo et al. 2004) and, therefore, are responsible for ~20% of the global aerosol optical thickness (Tegen et al. 1997). Figure 2.20 is a plot of the changes in annual mean dust concentration observed in Barbados (Prospero et al. 2003) and seen by the AVHRR for the western North Atlantic (0°–30°N, 10°–60°W). According to the AVHRR dust product, loadings over the western North Atlantic were below the climatological mean for 2006 (this was also found to be true over the Mediterranean). However, this low level of activity is not statistically significant and reflects a

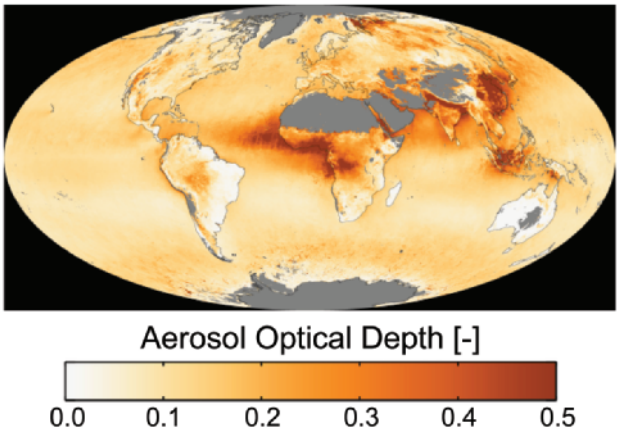


**Fig. 2.19. Map of global mean AOD values at 550 nm from the MODIS for 2006. Regions in gray denote missing values.**

downward trend in the data over the last 20 years. Additionally, a strong downward trend in dust is not seen in the Barbados data, which show an increase in dustiness from the mid-1960s through the early 1980s, and then a leveling off of dustiness. This disagreement may simply result from comparing dust-frequency satellite data of model output averaged over a large area, with concentration amounts from a point source. Model output also corroborates a decline in dust activity for 2006, with amounts for January–October below the climatological mean (1979–2005). The 2006 annual mean AOD for this region from MODIS is the lowest of all seven years in the MODIS record.

*(ii) India*

The Indo-Gangetic Plain in India consistently shows elevated AOD that is a combination of locally produced pollution from urban/industrial aerosol, biofuel, and biomass burning during the winter months, and transported desert dust from both the Arabian and Thar Deserts in the premonsoon and summer months. The MODIS AOD shows that 2006 was typical in terms of mean annual AOD, according to the seven years of available data.

*(iii) China and the Yellow Sea*

Eastern China and the surrounding Yellow Sea contained some of the heaviest aerosol loading in 2006, and is one of the few areas in the AVHRR data to show a statistically significant departure (increase) from the mean state in 2006. It is probable that dust from the upwind deserts (whose activity peaks during boreal spring) and urban/industrial aerosols from nearby population centers contribute to these higher-than-normal aerosol concentrations. The MODIS data show a strong increase in fine-mode aerosol amounts in the summer of 2006, as well as an increase in coarse-mode aerosol during April and May. This suggests that the elevated aerosol amounts may result from increases in dust aerosol during the spring and urban/industrial aerosol or transported biomass burning smoke during the summer. However, the increases in 2006 are corroborated neither by the model output, which shows near-normal activity for 2006 in this region, nor by observations made at Midway Island (Prospero et al. 2003).

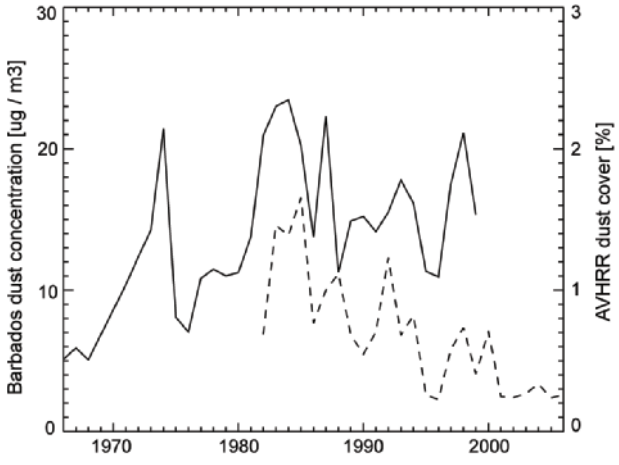


**Fig. 2.20. Annual mean time series of soil dust over the North Atlantic. The solid line represents annual mean dust concentrations observed in Barbados for the years of 1966–99. The dashed line is the annual mean dust cover as seen by the AVHRR imager over the western North Atlantic (0°–30°N, 10°–60°W) for the years of 1982–2006.**

*(iv) Indonesia*

Aerosol optical thickness maps of the areas surrounding Indonesia show above-average aerosol loadings for the boreal summer and fall that are statistically significant. These elevated levels of aerosols are likely the result of smoke from biomass burning. October 2006 has the highest single monthly mean value of AOD in the entire 7-yr MODIS record for this region. It is probable that the positive-phase ENSO event and the accompanying decrease in precipitation are key factors in this increase of aerosol loadings (van der Werf et al. 2004). An analysis of aerosol values for the bodies of water surrounding the Indonesian islands reveal a similar (but much greater) response during the ENSO event of 1997.

*(v) Eastern Europe, the boreal forests, and the Arctic*

The MODIS AOD dataset shows high aerosol loading over eastern Europe, Siberia, and the adjoining Arctic Ocean. These aerosols were produced by the biomass burning of agricultural lands and boreal forests in Russia during May, transported across Scandinavia and into the Arctic (Stohl et al. 2006). The MODIS picture is slightly misleading. Because of snow and ice cover, MODIS retrievals are possible only in a limited part of the year. An aerosol event that occurs in the short summer season will be exaggerated in the annual mean values calculated from the MODIS retrievals. The 2006 Siberian smoke season is the second strongest in the 7-yr MODIS record, exceeded only by the 2003 season. In contrast, boreal forest smoke that was prevalent in North America in 2002 (Quebec, Canada) and 2004 (Alaska) is mostly absent in 2006. Interannual boreal fires and the aerosols they produce are almost entirely dependent on natural causes that include precipitation and

humidity patterns, soil moisture left from winter snow cover, and lightning strikes. However, forest management practices also play a part.

*(vi)Amazon basin*

One of the more interesting aerosol stories of 2006 was the sudden decrease of biomass-burning aerosol in the Amazon basin, noted in Fig. 2.19 by annual mean AOD values of less than 0.25. The drought in 2005 created one of the heaviest smoke seasons on record in the Amazon. In 2006, continued drought in the beginning of the season threatened a repeat of the previous year. A combination of enforced fire regulations changed cultural practices, and an early onset of the rain in the latter part of the season cut the seasonal mean AOD values to roughly half of what they had been in 2005 (Koren et al. 2007, manuscript submitted to *Environ. Res. Lett.*).

e. *Global winds*—M. A. Bourassa, R. N. Maue, S. R. Smith, P. J. Hughes, and J. Rolph

1) Ocean surface winds

Wind speeds for ice-free regions for the period from July 1999 to 2006 are obtained using the SeaWinds scatterometer on the QuikSCAT satellite. Technically, this instrument also responds to changes in the air–sea temperature difference; however, variability resulting from temperature is usually relatively small compared to changes in wind speed. Monthly averaged speeds are determined for January 2000 through December 2006. The range of anomalies in 2006 is large, similar to that of 2003 and 2004, and much greater than that of 2000, 2001, and 2005. The month-to-month changes in 2006 are also relatively large. Note that an increase in wind speeds is typically associated with a greater rate of transfer of energy from the ocean to the atmosphere. For low–wind speeds regions, such a change would result in only an ~1 W $m^{-2}$ change in the rate of heat transfer. For high–wind speeds regions, the change could exceed 5 W $m^{-2}$, which integrated over a month is a very large extra input of energy to the atmosphere.

*(i) Tropics*

Some regional changes (Fig. 2.21) in wind speeds are steadier than suggested in the global average. The El Niño–related atypical position of the SPCZ is evident in the last half of the year. Similarly, from June onward there are greater wind speeds in the western Pacific Ocean warm pool and increased westward winds in the eastern central Pacific Ocean. There are also changes in the subtropical North Atlantic related to an eastward displacement of the Bermuda high, which could have contributed to the reduction in the number of landfalling tropical cyclones. Increased wind speeds in the western subtropical Atlantic Ocean in September and October are indicative of greater vertical wind shear, which would also tend to inhibit the strengthening of tropical cyclones.

*(ii) Northern oceans*

Monthly anomalies in the NH show westerlies that are stronger than usual for most of the year and possibly shifted farther north than usual. Wind anoma-

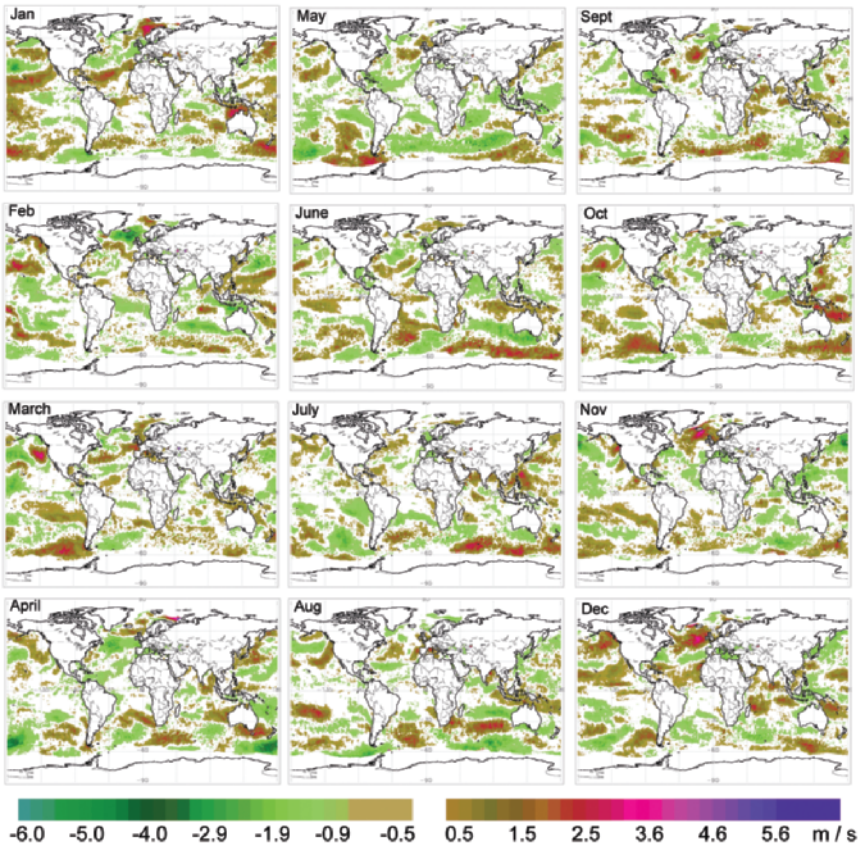


**Fig. 2.21. Regional wind speed anomalies for January–December 2006.**

lies in the Gulf of Alaska are indicative of stronger westerly-to-southwesterly flow that lasted from May into October. Late in the year, the North Atlantic was dominated by a strong Icelandic low (November and December). This resulted in stronger winds throughout the ocean between Greenland and Europe. An anomalous ridge near the eastern seaboard of the United States during the same months is apparent in negative wind anomalies and the resulting warm start to the 2006/07 winter.

*(iii) Southern Ocean*

There are also long periods of increased wind in the Southern Ocean. The most notable location is south of Australia (May–July, September–December). Examination of daily wind fields shows that some of these greater wind speeds are associated with offshore flow from the eastern Antarctic ice dome. They may be an indicator of stronger katabatic wind flow from the interior of Antarctica. These katabatic flows may not be directly responsible for the higher over-ocean winds, but they have been shown to increase convergence and cyclogenesis in the circumpolar trough. The result would be an increase in wind speeds.

2) Land surface winds

Monthly wind speed anomalies (Fig. 2.22) with respect to the long-term mean (1968–96) were calculated from data obtained from the NCEP–NCAR reanalysis (Kalnay et al. 1996). The oceanic wind

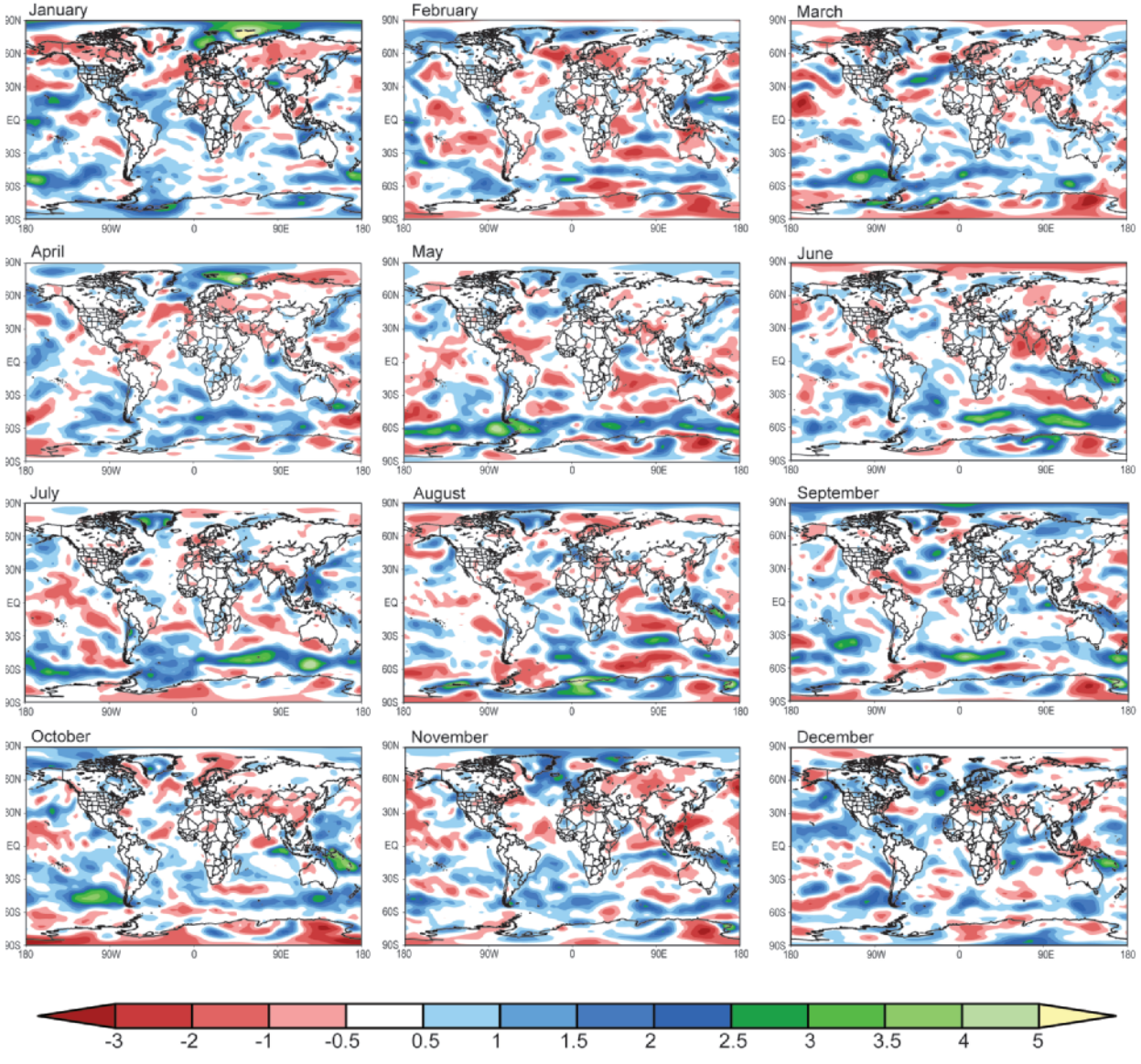


**Fig. 2.22. Global monthly mean wind speed anomalies obtained from NCEP–NCAR reanalysis for January–December 2006 (m $s^{-1}$).**

speed anomalies are qualitatively similar to the QuikSCAT-derived wind speeds over the oceans and ice edges especially in the polar regions. Differences in spatial resolution between the two datasets (QuikSCAT: ~0.25° versus NCEP–NCAR: ~2.5°) explain the difference in magnitudes. It is important to note that QuikSCAT winds are not assimilated into the reanalysis product.

The wind speed anomaly patterns over most of the world's landmasses are small or inconsistent from month to month, with relatively small magnitudes compared with the adjacent ocean. Stronger-than-normal wind speeds persisted over the Arctic, including Greenland, Alaska, and Siberia throughout winter. For the remainder of the year, Greenland experienced above-average winds. Notable small-magnitude negative wind speed patterns persisted over the Indian subcontinent during spring and early summer. In the Southern Hemisphere, there is evidence of considerable wind speed anomalies of both signs over Antarctica, possibly a result of varying cyclolysis regions and katabatic wind regimes. The austral spring over the tip of South America also experienced stronger-than-normal wind speeds.

*f. Teleconnection patterns and blocking*—W. Higgins and M. L'Heureux

Teleconnection patterns are recurrent and persistent large-scale patterns of pressure and circulation anomalies that span large geographical areas. They reflect large-scale changes in the atmospheric wave and jet stream patterns, and influence temperature, rainfall, storm tracks, and jet stream location and intensity over vast distances. Thus, they are often responsible for abnormal weather patterns occurring simultaneously over regions separated by great distances. Although these patterns typically last from several weeks to several months, they can sometimes be prominent for consecutive years or longer, reflecting an important part of both the interannual and interdecadal variability of the atmospheric circulation. The focus of this section is on the NAO, PNA, and WP teleconnection patterns. Monthly index values for the NAO, PNA, and WP teleconnection patterns over the last few years are shown in Fig. 2.23. The NOAA/CPC provides daily and monthly time series for other NH teleconnection patterns and details about the analysis procedure used to obtain them (information online at www.cpc.ncep.noaa.gov/data/teledoc/telecontents.shtml).

Atmospheric blocking is characterized by an interruption or splitting of the normal westerly flow around a ridge of high pressure into two separate branches over a considerable longitudinal extent. Common characteristics include easterly flow to the south of the blocking ridge and pronounced meridional flow both upstream and downstream of the blocking ridge. As a consequence, the normal eastward progression of synoptic disturbances is obstructed, leading to episodes of prolonged extreme weather conditions. On intraseasonal time scales the persistent weather extremes can last from several days up to a few weeks, often accompanied by significant temperature and precipitation anomalies. Preferred areas for atmospheric blocking, especially during the NH cold season, include the North Pacific and northeastern Atlantic.

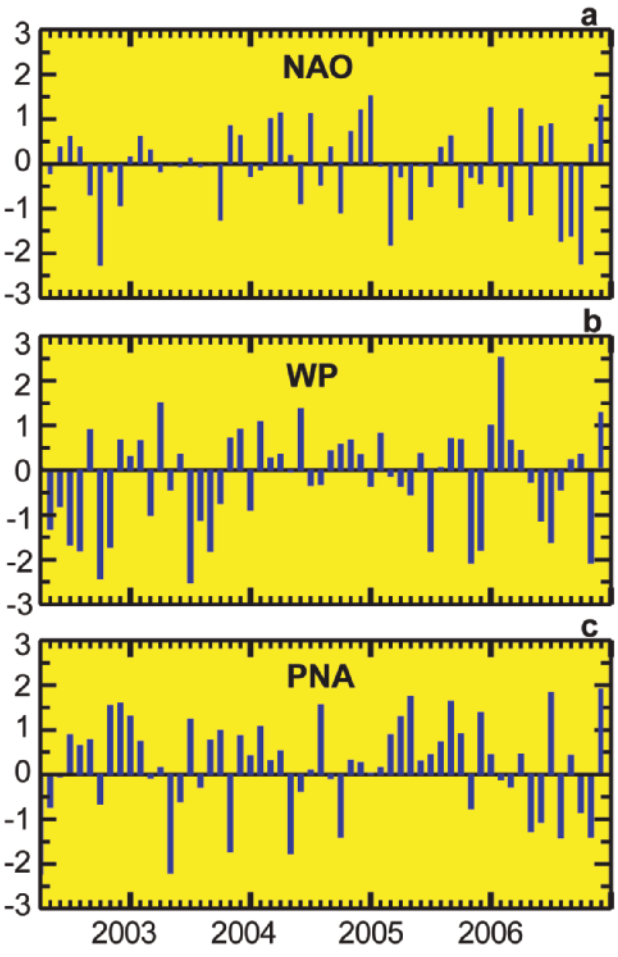


**Fig. 2.23. Standardized time series of the monthly (a) NAO, (b) WP, and (c) PNA teleconnection indices for the period 2003–06. The teleconnection patterns are calculated from a RPCA applied to monthly standardized 500-hPa height anomalies during 1950–2000. The anomalies are standardized by the base period monthly means and standard deviations. Additional discussion on how the teleconnection indices are calculated is found online at www.cpc.ncep.noaa.gov/data/teledoc/telecontents.shtml. [Source: CPC.]**

NOAA/CPC routinely monitors atmospheric blocking and is involved in continuing research to better understand its role in the global climate system. The procedure used to identify blocking is based on the blocking index of Tibaldi and Molteni (1990), modified from that of Lejenas and Okland (1983). The index calculation, together with current conditions, blocking outlooks, and blocking composites, is readily available from the CPC Web site (www.cpc.ncep.noaa.gov/products/precip/CWlink/MJO/block.shtml).

#### 1) Description of teleconnection patterns

The NAO is a metric of the meridional pressure gradient over the North Atlantic Ocean (see Hurrell 1995; Barnston and Livezey 1987), and is highly correlated with the AO (e.g., Wallace 2000; Thompson and Wallace 1998). The most conspicuous attribute of the PNA is a "wave train" of action centers that stretch from the subtropical North Pacific to Florida, with intermediate action centers near the Aleutians and in central Canada (see Wallace and Gutzler 1981). ENSO is related to a PNA-like pattern in the extratropics. El Niño (La Niña) tends to be associated with the positive (negative) phase of the PNA pattern.

The West Pacific pattern consists of a north–south dipole of anomalies, with one center located over the Kamchatka Peninsula and another broad center of the opposite sign covering portions of southeastern Asia and the western subtropical North Pacific. A third anomaly center is located over the eastern North Pacific and southwestern United States. Strong positive or negative phases of this pattern reflect pronounced zonal and meridional variations in the location and intensity of the entrance region of the Pacific jet steam. The positive phase is associated with above-average precipitation in all seasons over the high latitudes of the North Pacific, and below-average precipitation extending across the central North Pacific toward the west coast of North America; the opposite is true for the negative phase.

#### 2) Recent monthly teleconnection index values

For 2006 as a whole, both the NAO and PNA were dominated by the negative phase, though there were notable monthly excursions into the positive phase (e.g., the PNA during July 2006). The WP pattern was generally positive during early 2006, with strong negative excursions during NH summer and during November 2006. During February 2006, the 500-hPa circulation pattern in the extratropics featured a pronounced north–south dipole of height anomalies across the western and central North Pacific, which reflected a strong positive phase (+2.5) of the WP teleconnection pattern (Fig. 2.23b). The 500-hPa circulation pattern during August–October 2006 featured positive height anomalies over Greenland and the polar region, and negative height anomalies from the north-central United States to the United Kingdom; and over central Siberia. The eastern third of the United States tended to be colder than normal, especially in September and October, consistent with the strong negative values of the NAO index (Fig. 2.23a). During October, the NAO index value was –2.2, and for the August–October season, the NAO index value was –1.9. The October 2006 value (–2.2) was the most extreme since the October 2002 value (–2.3), when temperatures across the northern and eastern United States were also significantly below normal.

The NH 2005/06 winter was dominated by the negative phase of the NAO for the first time since 2000/01 (not shown). On the other hand, the PNA continued in its positive polarity for the fourth consecutive winter season (Fig. 2.24). Since 1995, the PNA has tended to be in the positive phase; 2006 was a bit of an exception in that the PNA index was negative during six calendar months.

#### 3) Description of blocking episodes and links to major climate anomalies during 2006

Two examples that relate exceptional blocking events to extreme weather conditions during 2006

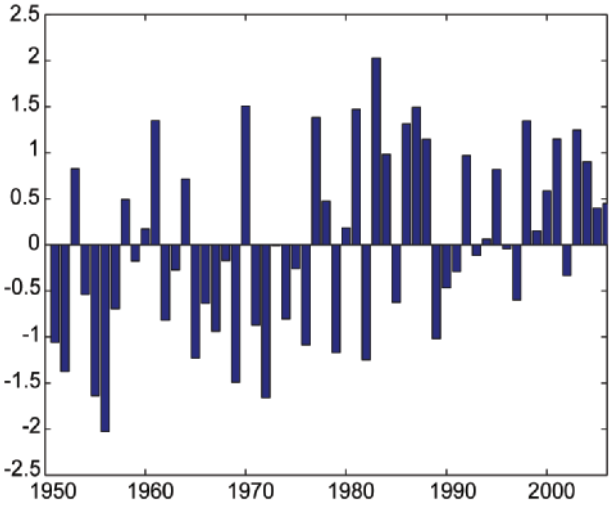


**Fig. 2.24. Standardized time series of the PNA teleconnection indices for the period December–March 1950–2006. The labeling convention is such that 2005 indicates DJFM 2005/06. The procedure used to calculate the teleconnection patterns is briefly described in the caption to Fig. 2.23.**

are presented below. The latter event was associated with the negative polarity of the WP teleconnection pattern.

*(i) Excessive rainfall in New England during May 2006*

Record rainfall fell over portions of New England (specifically northeastern Massachusetts, southern New Hampshire, and southern Maine) during 12–15 May 2006, resulting in flooding in the region comparable to the most extreme events during the last 70 years. Rainfall totals at some locations exceeded 12 feet.

The blocking conditions developed in the beginning of May 2006 when a block formed in the vicinity of Scandinavia. As is quite often the case, the blocking ridge shifted westward with time (retrograde motion) at high latitudes, passing over Greenland (20°–50°W) during 6–12 May and over eastern Canada (60°W–90°) during 12–15 May (Fig. 2.25). The low-level (850 hPa) wind during 12–15 May (Fig. 2.26a) shows a cyclonic circulation covering the entire eastern United States. The persistent very strong southeasterly flow of moist Atlantic air over central New England contributed greatly to the excessive rainfall totals observed in the region (Fig. 2.26b). Situations like this one often feature a "training" effect in which precipitating clouds move over the same area along the direction of the mean flow, resulting in excessive rainfall and flooding.

*(ii) Excessive rainfall in the Pacific Northwest during November 2006*

A strong upper-level ridge, which dominated the Gulf of Alaska and west coast of North America during October 2006, weakened late in the month. It was replaced by a persistent blocking pattern that devel-

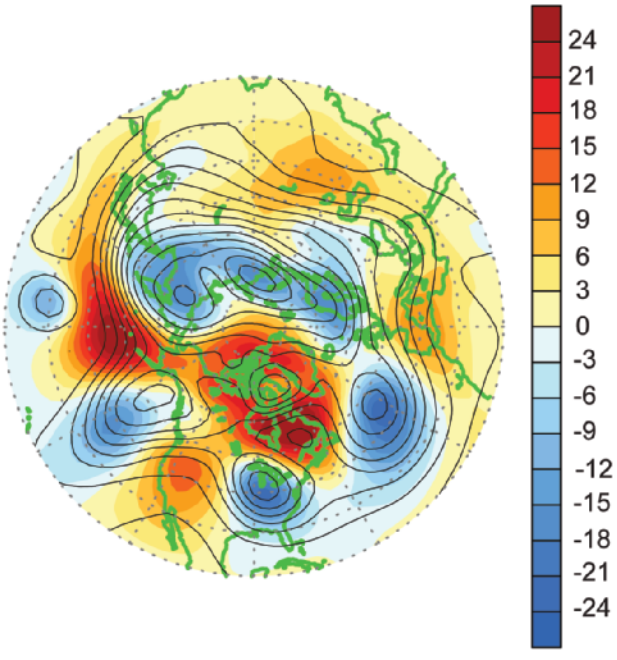


**Fig. 2.25. Mean 500-hPa height (contours, contour interval 60 m) and height anomalies (shading, units are decameters) for 12–15 May 2006. Anomalies are departures from the 1979–95 base period means. The blocking ridge axis is indicated by the dotted white line, and the flanking trough axes are indicated by dashed white lines.**

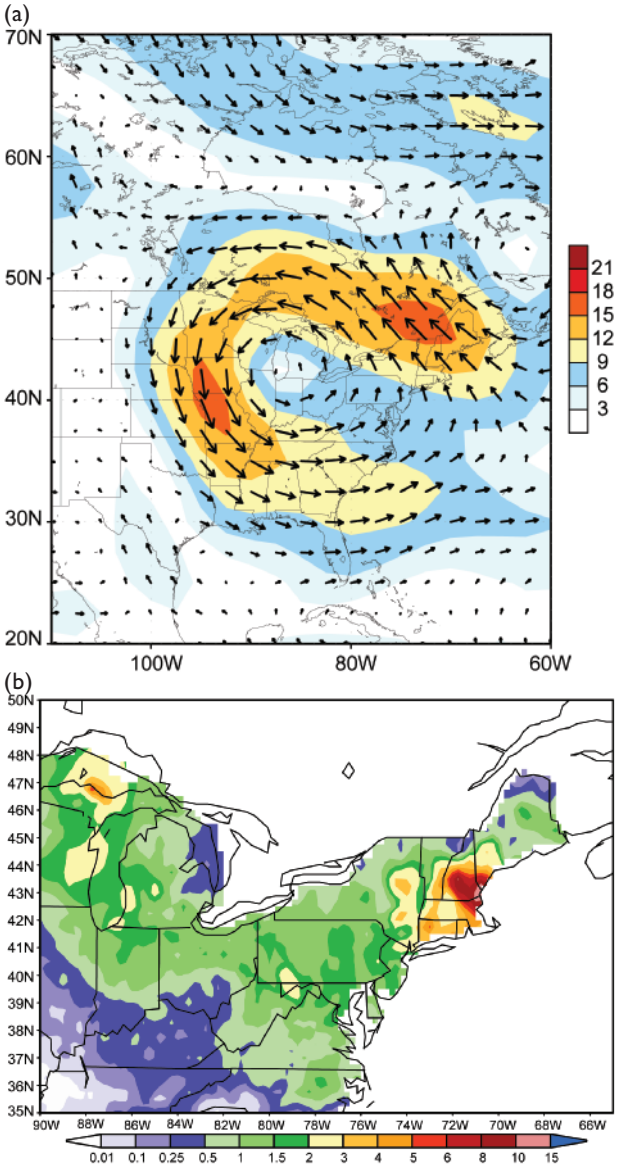


**Fig. 2.26. (a) Mean 850-hPa wind vectors and wind speed (shading). Units: m $s^{-1}$. (b) Total precipition (in.) for the period 12–15 May 2006.**

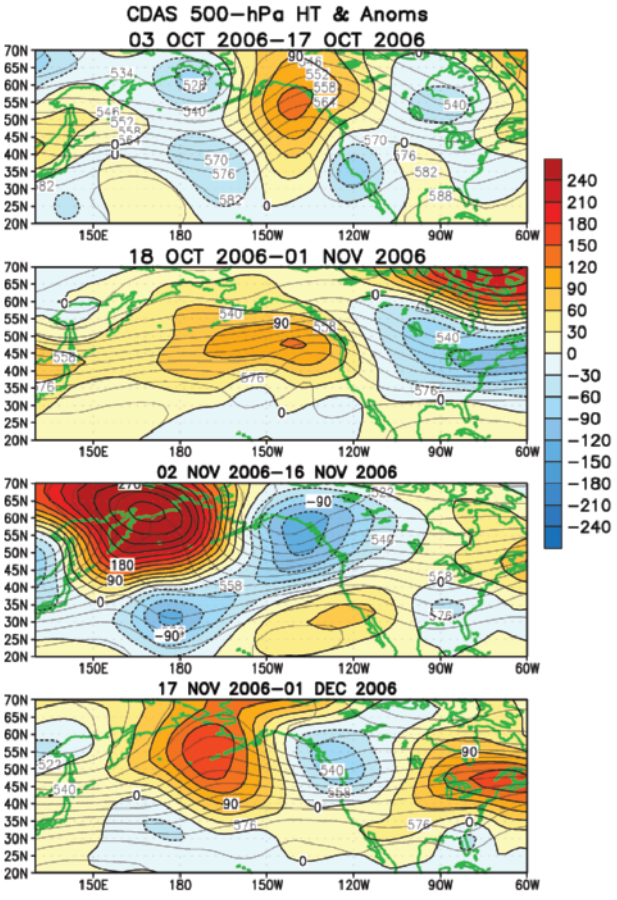


**Fig. 2.27. 500-hPa heights (dm) and anomalies (m) over the North Pacific and North America during the 2-week periods indicated on each panel.**

oped over the high latitudes of the west-central North Pacific in early November (Fig. 2.27). The northern and southern branches of the Pacific jet stream recombined over the eastern North Pacific, contributing to a series of strong storms that resulted in remarkably wet and cold conditions in the Pacific Northwest, western Canada, and portions of Alaska during the first half of November 2006. This pattern projected very strongly on the negative phase of the WP teleconnection pattern during November 2006 (Fig. 2.23b).

It is important to note that the conditions during November 2006 were related to midlatitude variability, with little or no connection to the developing El Niño conditions in the tropical Pacific. In particular, these events occurred in advance of the development of El Niño–related enhanced convection near and to the east of the international date line, which typically leads to atmospheric coupling and an eastward shift of the subtropical ridges and the North Pacific jet stream during the NH winter.

## 3. GLOBAL OCEANS—J. M. Levy, Ed.

### *a. Overview*—J. M. Levy

As the global ocean observing system matures, climatologies of essential climate variables are growing more robust, as are observations of anomalous departures that shed light on the evolving behavior of the coupled ocean–atmosphere system. Year 2006 exhibited numerous anomalies of interest:

- Global SST anomalies were primarily positive, notably so in boreal summer in the North Atlantic and in the latter part of the year in the central and eastern equatorial Pacific, associated with the 2006 El Niño.
- The mean of latent plus sensible heat flux was similar to that in 2005; total flux in both years was at the high end of a long-term upward trend that started in 1977/78. Significant heat flux anomalies were observed in the regions of the 2006 El Niño and Indian Ocean dipole mode event.
- Global sea surface salinity anomalies accentuated climatological patterns: freshwater regions were fresher and salty regions were saltier. The subpolar North Atlantic and Nordic Seas were anomalously salty in 2006.
- Dramatic westward surface current anomalies associated with the development of El Niño were observed late in the year in the tropical Pacific Ocean, while the seasonal reversal of currents was particularly pronounced on the equator in the Atlantic Ocean. Exchange of water between the South and North Atlantic Oceans was weaker than normal.
- The MOC in the North Atlantic was a bit low, albeit within a standard deviation of the historical annual mean. However, there is no indication of a systematic trend in MOC transport.
- Annual mean SLA was above the 1993–99 baseline average for nearly 80% of the ocean. The global mean SLA change of +6 mm from 2005 was the highest increase since the altimeter record began in 1993. Relative sea level change was also the highest ever recorded. There were an anomalously high number of extreme sea level events.
- Global ocean carbon uptake in 2005 (about 2.2 Pg C $yr^{-1}$) was near average for the past decade. Interannual variability over the past decade has been about ±0.2 Pg C $yr^{-1}$. Atlantic Ocean anthropogenic $CO_2$ uptake continues to exceed Pacific Ocean uptake.
- Global annual average ocean color anomalies were not markedly different from those observed in the satellite record over the past decade. However, anomalies in the Niño-3.4 region were indicative

of a 2006 El Niño that was stronger (considerably weaker) than that of 2002/03 (1997/98).

*b. Temperature*

1) Sea surface temperature—R. W. Reynolds

SSTs for 2006 are shown as monthly fields interpolated from the weekly 1° OI analyses of Reynolds et al. (2002). All results presented here are depicted as anomalies defined as differences from a 1971–2002 climatological base period described by Xue et al. (2003).

The yearly average and standard deviation of the monthly anomalies are shown in Fig. 3.1. The anomalies are primarily positive resulting from overall global warming relative to the climatological base period. Three features dominate 2006. First, the average shows a strong positive anomaly signal in the North Atlantic and North Pacific between roughly 40° and 65°N. This is due to a boreal summer positive anomaly, which also occurred in 2003–06. However, in 2006, the summer anomaly in the Pacific was relatively weak compared with 2003–05. Second, in 2005 there was also a strong positive anomaly of roughly 1°C in the tropical North Atlantic (0°–30°N) while in 2006 it was smaller. Finally, a weak El Niño began to be evident in June (see section 4).

The zonally averaged monthly anomaly is shown for the Atlantic between 80°W and 20°E for 2000–06 in Fig. 3.2. Strong positive summer anomalies are shown north of 40°N beginning in 2003. The anomaly signals were the oceanic response to summer heat waves that helped reduce summer ice cover in the Arctic. The 2003 European summer heat wave corresponded to an especially strong positive SST anomaly. In addition, the 2005 spring and summer tropical North Atlantic positive anomalies are evident between 5° and 20°N in the figure and were smaller in 2006. The smaller anomalies in 2006 may partly explain the lower number of 2006 Atlantic hurricanes compared to 2005.

2) Heat content—G. C. Johnson, J. M. Lyman, and J. K. Willis

Storage and transport of heat in the ocean are central to such aspects of climate as El Niño (e.g.,

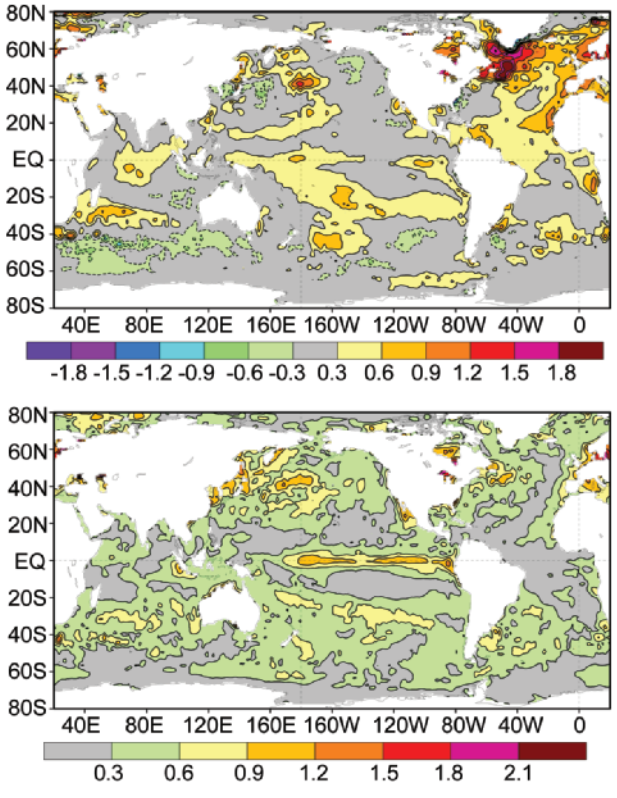


**Fig. 3.1. Mean (top) and standard deviation (bottom) of monthly SST anomalies for 2006 on a 1° spatial grid. The anomalies are computed relative to a 1971–2000 base period. The contour interval is 0.3°C; the 0 contour is not shown. AVHRR satellite data are used.**

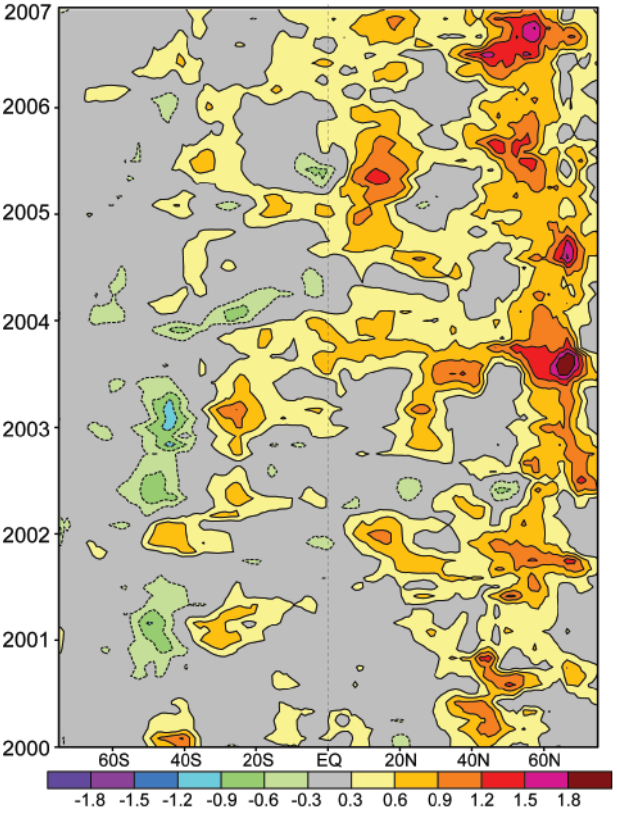


**Fig. 3.2. Zonally averaged monthly SST anomalies for January 2000 through December 2006 for the Atlantic. The contour interval is 0.3°C; the zero contour is not shown. The anomalies are computed relative to a 1971–2000 base period.**

Zebiak 1989), the North Atlantic Oscillation (e.g., Curry and McCartney 2001), hurricane seasons (e.g., Emanuel 2005), and global change (e.g., Levitus et al. 2005; Hansen et al. 2005). Here we discuss an estimate of upper (0–750 m) OHCA estimated from a combination of in situ temperature profiles with satellite altimetry sea surface height data for the period of 1 January–31 December 2006 (Fig. 3.3), analyzed following Willis et al. (2004), but relative to a 1993–2006 baseline. Data from Argo floats with a recently detected systematic bias in reported pressure values have been removed from the estimates discussed here. Details of the fields analyzed here may change after more real-time data are subject to delayed-mode scientific quality control.

The 2006 combined OHCA map (Fig. 3.3) shows eddy and meander variability down to the 100-km mapping scales, as does, to a greater extent, the difference between the 2006 and 2005 combined OHCA maps (Fig. 3.4). There is a great deal of small-scale spatial variability in OHCA fields associated with the western boundary currents in every gyre, as well as the Antarctic Circumpolar Current. The difference in combined OHCA maps between 2006 and 2005 (Fig. 3.4) illustrates the large year-to-year variability in ocean heat storage, with changes reaching or exceeding the equivalent of an 80 W $m^{-2}$ magnitude surface flux. Ocean advection likely plays a significant role in many of these changes.

Large-scale patterns are also evident in OHCA for 2006 (Fig. 3.3), and for its difference from 2005 (Fig. 3.4). One of the prominent patterns is along the equatorial Pacific, where there is a band of high heat content in 2006, which is also seen as a heat gain since 2005. This pattern is consistent with the onset of El Niño in 2006. There is also a band of high OHCA along 10°N from the western Pacific to about 160°W. In addition, there is a band of high OHCA that reaches from 150°E on the equator to at least 120°W and about 25°S.

The combined OHCA map for 2006 (Fig. 3.3) is high in the subpolar North Atlantic (except for seas just northeast of Iceland) and low in the subtropical North Atlantic. This pattern dynamically implies a decreased strength of the North Atlantic Current, and is probably related to decadal changes in the North Atlantic Oscillation Index (e.g., Curry and McCartney 2001). This climate index was lower in 2006 than during the baseline period; it has trended lower from 1993 to 2006.

In the equatorial Indian Ocean, OCHA is low in the east and high in the west (Fig. 3.3), with interannual variations (Fig. 3.4) apparently contributing to this pattern. The southern subtropics of the Indian Ocean are generally high in OCHA, but changes since 2005 (Fig. 3.4) do appear to be a dominant contributor to this pattern.

In 2006, OHCA is high in the Southern Oceans in a belt located north of the Antarctic Circumpolar Current (Fig. 3.3), especially east of New Zealand in the South Pacific and between 30° and 45°S in the South Atlantic, but less perceptible in the south Indian Ocean. This change has recently been studied on decadal time scales in the South Pacific (Roemmich et al. 2007) and appears to be related to changes in the wind stress field associated with an increase in the Antarctic Oscillation index. This index reached a peak in 1999, fell into a shallow valley in 2002, and has been near neutral since then. Consistent with this neutrality, there is relatively little large-scale trend of OHCA between 2005 and 2006 in this region (Fig. 3.4), with smaller spatial scale changes of vary-

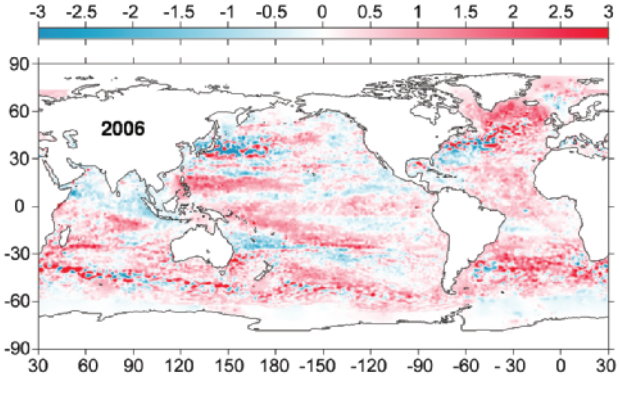


**Fig. 3.3. Combined satellite altimeter and in situ ocean temperature data upper (0–750 m) ocean heat content anomaly OHCA (J $m^{-2}$) map for 2006.**

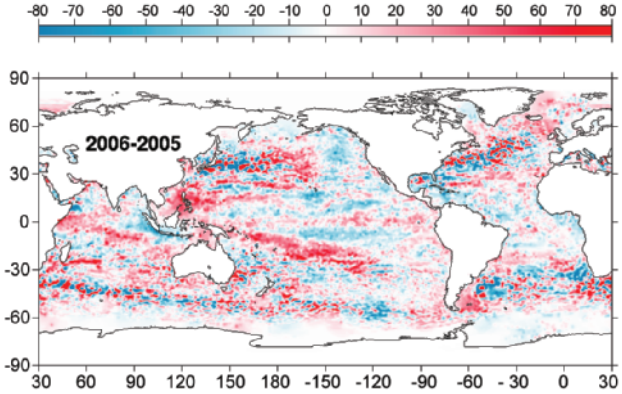


**Fig. 3.4. The difference of 2006 and 2005 combined OHCA maps expressed as a local surface heat flux equivalent (W $m^{-2}$).**

ing sign predominating in the subpolar regions of the Southern Hemisphere.

Finally, given the potential link between hurricane intensity and warm ocean waters (e.g., Emanuel 2005), we discuss tropical Atlantic patterns in OHCA. There was a record North Atlantic hurricane season in 2005 and a much weaker one in 2006 (see section 4). This change is consistent with decreases in OHCA from 2005 to 2006 in the Gulf of Mexico, in the Caribbean, and to a lesser extent around 10°N across much of the tropical North Atlantic (Fig. 3.4). This area had an increase in OHCA and hurricanes between 2004 and 2005 (Shein et al. 2006).

### 3) Global ocean heat fluxes—L. Yu and R. A. Weller

Latent heat (evaporation) and sensible heat fluxes are the primary mechanism by which the oceans release much of the absorbed solar energy back to the atmosphere. These ocean-to-atmosphere heat transfers are a cooling mechanism for the oceans but a source of heating for the atmosphere. The cooling and heating change the temperature gradients and energize the circulations in the ocean and atmosphere, which in turn affect air–sea temperature and humidity contrasts and modify the magnitudes of the ocean heat fluxes.

The estimates for the global LHF + SHF in 2006 (Fig. 3.5) were produced by the OAFlux project (Yu and Weller 2007) at the WHOI. The flux estimates are accurate within 8 W $m^{-2}$. On an annual mean basis, the largest absolute ocean heat losses occur over the regions associated with major WBCs and their extensions, the most noted of which are the Kuroshio off Japan, the Gulf Stream off the United States, and the Agulhas Current off the African coast. The magnitude of annual mean LHF + SHF in these regions exceeds 250 W $m^{-2}$, and is produced largely during the fall-to-winter seasons by strong winds and cold and dry air masses coming from the land. The secondary heat loss maximum (~180 W $m^{-2}$) is located over the broad subtropical southern Indian Ocean, where the large air–sea heat exchanges are sustained by the strong southeast trade winds during the boreal summer monsoon months (June–September).

Compared to the annual mean LHF + SHF in 2005 (Fig. 3.5), the heat fluxes in 2006 showed changes over all global basins, with the magnitude of the deviation within 50 W $m^{-2}$. Among all of the changes, two features in the tropical oceans are the most interesting. The first change is the increased LHF + SHF in the eastern and central equatorial Pacific Ocean concurrent with the development of a mild El Niño. In late 2006, SSTs were 2°–3°C above normal across much of the region. The increased evaporative heat loss is observed in regions of the El Niño warm SST anomalies. Variation of ocean heat fluxes in the tropical Pacific on ENSO time scales is a dominant interannual signal in the OAFlux multidecade time series (e.g., Yu and Weller 2007). The second feature is characterized by the east–west asymmetry in the 2005/06 difference anomalies in the tropical Indian Ocean. A positive IOD mode event occurred in 2006, with cold SST anomalies off the west coasts of Sumatra and Java and warm SST anomalies across the central and western parts of the basin. The IOD SST pattern is almost a mirror image of the El Niño SST in the Pacific. However, the changes in the flux patterns of these two basins did not mirror each other in 2006. The colder eastern Indian Ocean enhanced sea-to-air heat fluxes, while the warmer western Indian Ocean reduced the heat fluxes. This means that positive SST anomalies in the El Niño region correlated with positive heat flux anomalies, but positive SST anomalies in the Indian Ocean correlated with negative heat flux anomalies. The sign of the flux changes was opposite to the sign of the SST anomalies in the two basins, which suggested differ-

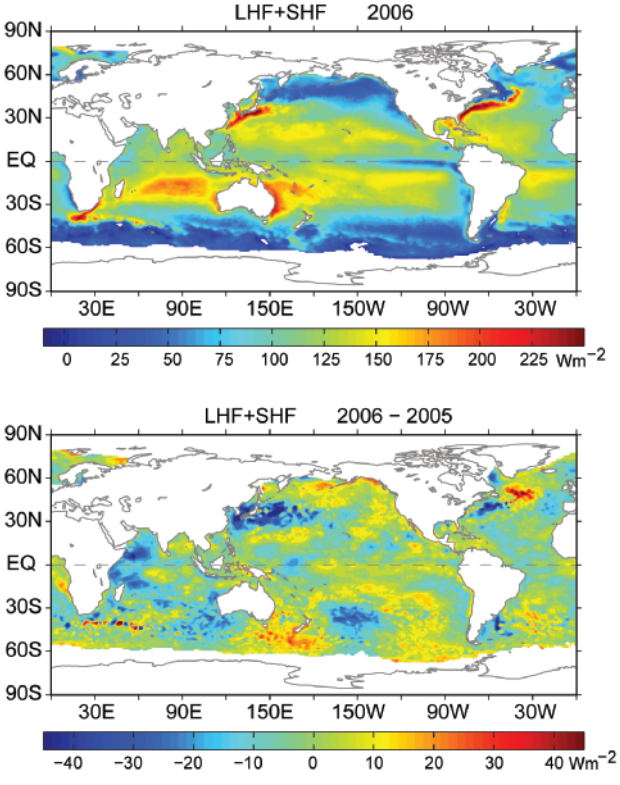


**Fig. 3.5. (top) Annual mean latent plus sensible heat fluxes in 2006. The sign is defined as upward (downward) positive (negative). (bottom) Differences between the 2006 and 2005 annual mean latent plus sensible heat fluxes.**

ent feedback mechanisms were at work. Scientists are working to determine if the SST–flux relationship in the Pacific suggests a response of the atmosphere to the oceanic forcing, and if the SST–flux relationship in the Indian Ocean implies an atmospheric forcing for the ocean.

Outside of the Tropics, the influence of eddy-scale structures is evident in the 2-yr difference map. Nevertheless, the difference anomalies are most pronounced in the vicinity of the two WBCs, that is, the Kuroshio and the Gulf Stream, and their extensions. For the former, there were negative LHF + SHF anomalies over almost the entire region; while for the latter, there were negative flux anomalies south of the Gulf Stream extension and positive anomalies north of the current. A colder sea surface coupled to slightly weakened wind speed appears to be the cause of the reduced LHF + SHF in these regions. It may be worth noting that the SSTs in the Kuroshio and its extension are generally lower than normal during the ENSO warm phases (White and He 1986). The connection between lower SST and less oceanic heat loss is another indication of the response of the atmosphere to oceanic forcing.

The long-term context of the change in ocean heat fluxes in 2006 is shown in the plot of year-to-year variations of the globally averaged annual mean from 1958 to 2006 (Fig. 3.6). The 2006 mean of LHF + SHF was at a similar level to the 2005 mean. However, the two recent years are located at the high end of a long-term upward trend that started in 1977/78. Since then, LHF + SHF have increased by about 9 W $m^{-2}$, from a minimum at ~99 W $m^{-2}$ in 1977 to a maximum at ~108 W $m^{-2}$ in 2003. The magnitude of the variability is dominated primarily by LHF. SHF is about one order smaller than LHF, and the change in SHF is also small (less than 2 W $m^{-2}$ over the entire 50-year analysis period). Nonetheless, the trend in SHF is very different from that in LHF: the downward trend in SHF lasted until the late 1980s, followed by a few abrupt jumps in the early 1990s. Since 2000, SHF has tended downward.

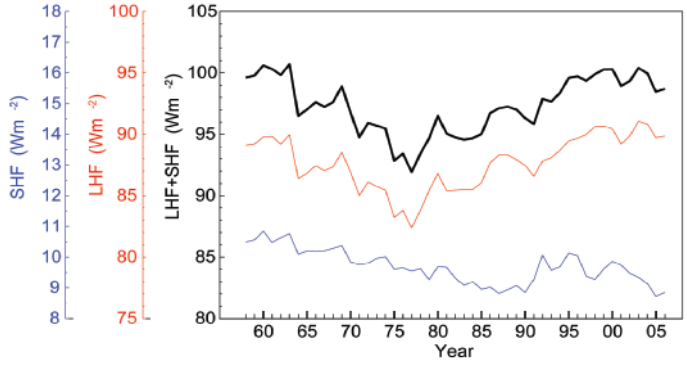


**Fig. 3.6. Year-to-year variations of globally averaged annual mean latent plus sensible heat flux (black), latent heat flux (red), and sensible heat flux (blue).**

*c. Sea surface salinity*—G. C. Johnson and J. M. Lyman

Ocean storage and transport of freshwater are intrinsic to many aspects of climate, including the global water cycle (e.g., Wijffels et al. 1992), El Niño (e.g., Maes et al. 2006), and global climate change (e.g., Held and Soden 2006). Regional studies of decadal freshwater variability are possible in well-sampled regions like the North Atlantic (e.g., Curry and Mauritzen 2005). In addition, zonal averages of long-term global trends of salinity in each ocean basin have been analyzed (Boyer et al. 2005). In situ ocean salinity data have traditionally been too sparse and their reporting too delayed for an annual global perspective of ocean freshwater and its complement, salinity. However, the rapidly maturing Argo array of profiling floats (Roemmich et al. 2004) is remedying this situation. Argo data are used here to present annual average SSS analyses for 2006 and 2005, the first years with near-global Argo coverage. Remote sensing of SSS by satellite is planned for 2009 (information online at http://aquarius.nasa.gov/).

Here the shallowest near-surface (< 25 m) salinity data flagged as good from each available Argo profile for the years in question were subjected to a statistical check to discard outliers. The remaining data were then cast as differences from a climatological mean surface salinity field from the WOA based on historical data reported through 2001 (WOA 2001; Boyer et al. 2002). The resulting anomalies were then mapped, essentially assuming a Gaussian covariance function with 6° latitude and longitude decorrelation length scales and a signal-to-noise variance ratio of 2.2 (Bretherton et al. 1976).[1]

SSS patterns are fairly well correlated with surface freshwater flux, the sum of evaporation, precipitation, and river runoff (e.g., Behringer et al. 1998). In each ocean basin, subtropical salinity maxima centered near 20° or 25° in latitude are signatures of the predominance of

[1] While some delayed-mode scientific controlled (final) Argo data are available for the 2005/06 time period, many real-time (preliminary) Argo data were used in both years. The real-time estimates of SSS made here could change after all the data have been subject to careful scientific quality control.

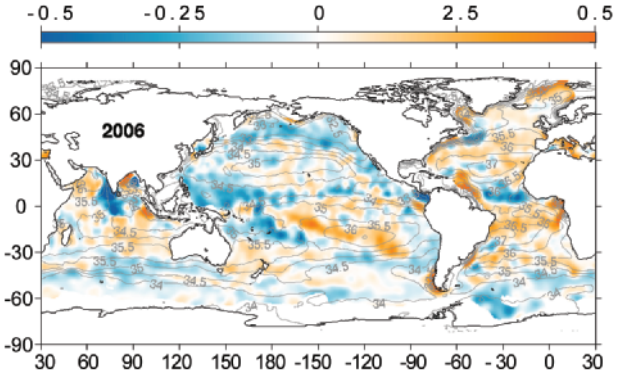


**Fig. 3.7. Map of the 2006 annual surface salinity anomaly estimated from Argo data (colors in PSS-78) with respect to a climatological salinity field from WOA 2001 (gray contours at 0.5 PSS-78 intervals). White areas are either neutral with respect to salinity anomaly or are too data poor to map. While salinity is often reported in practical salinity units it is actually a dimensionless quantity reported on the PSS-78.**

evaporation over precipitation. Conversely, in most regions where climatological surface salinities are relatively fresh, precipitation generally dominates over evaporation. The 2006 anomalies from WOA 2001 (Fig. 3.7) reveal some large-scale patterns. In 2006 the regions around the climatological salinity maxima are mostly salty with respect to WOA 2001. In many of the climatologically fresh regions, 2006 values appear fresher than those of WOA 2001, including most of the ACC near 50°S, the subpolar gyre of the North Pacific, and the ITCZ over the Atlantic and Pacific Oceans (including the SPCZ).

These patterns may suggest an increase in the hydrological cycle (more evaporation in drier locations, and more precipitation in rainy areas), as depicted in simulations of global warming. These simulations do suggest that this signal might be discernible during the last two decades of the twentieth century (Held and Soden 2006). Any increase in the hydrological cycle would certainly result in changes of local SSS values, but not alter the global average salinity by itself. Most of these patterns observed in 2006 (Fig. 3.7) are not reflected in the 2005–06 differences (Fig. 3.8), suggesting that these anomalies have evolved over longer-than-interannual time scales; although, without global coverage prior to 2005, it is difficult to determine the time scale. However, there are alternate explanations. It is possible that the climatology, being based on relatively sparse data distributions in many parts of the oceans, may tend to underestimate regional extrema that the well-sampled Argo array can better resolve. Also, some of these patterns might be explained by interannual shifts in ocean features such as the ACC or atmospheric features such as the ITCZ.

For example, the subpolar North Atlantic and Nordic Seas are relatively salty, both in 2006 (Fig. 3.7) and in 2005 (not shown), with relatively small changes between these two years (Fig. 3.8). This salty anomaly is inconsistent with an increase in the strength of the hydrological cycle. However, the pattern may have less to do with local evaporation and precipitation fields and more with northward spread of saltier waters from the south. The salty anomaly in this region is consistent with a stronger influence of subtropical gyre waters in the northeastern North Atlantic in recent years and a reduced extent for the subpolar gyre (Hátún et al. 2005).

There are evidently some rather large anomalies in the equatorial and North Indian Ocean. The Bay of Bengal and much of the Arabian Sea appear to be anomalously salty, while the ocean to the south and east of India appears to be fresh (Fig. 3.7). The changes appear to be interannual, as reflected in the large changes in anomaly between 2005 and 2006 in this region (Fig. 3.8).

One last feature of interest in the 2006 salinity field is the anomalously salty water located in the region of the fresh Amazon River plume (Fig. 3.7). The influence of this plume would normally be apparent in the relatively fresh conditions to the north and west of the mouth of the Amazon River (near the equator) that reach as far north as Puerto Rico. The salty anomaly in this region in 2006 may be explained by the reduced freshwater flow from the Amazon into the ocean during a record drought in the Amazon River basin in 2005 (Shein et al. 2006), with some time delay for hydrological and oceanic processes. The change in salinity between 2005 and 2006 (Fig. 3.8) shows that this salty anomaly is limited to 2006.

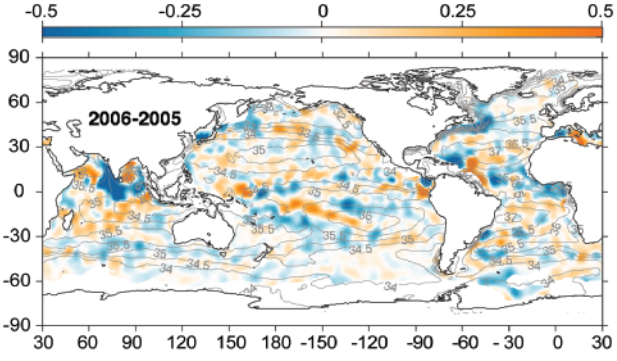


**Fig. 3.8. The difference of 2006 and 2005 surface salinity maps estimated from Argo data (colors in PSS-78 $yr^{-1}$). Other details follow Fig. 3.7.**

*d. Circulation*

1) Surface current observations—R. Lumpkin and G. Goni

Near-surface currents are measured in situ by satellite-tracked drifting buoys and acoustic point-measuring meters on ATLAS moorings.[2] In September 2005, the drifter array reached its target goal of 1250 drifters worldwide, becoming the first fully realized component of the GCOS-92. During 2006, surface currents were well sampled except in the far northern Pacific, in the southwest Pacific between 20° and 40°S, from 150°E to the date line, for the Arabian Basin of the Indian Ocean, and for the extreme Southern Ocean south of 55°S.

Weekly maps of absolute surface currents and geostrophic current anomalies for 2006 were calculated from a synthesis of in situ observations, near-real-time AVISO data gridded altimetry, and NCEP operational winds (Niiler et al. 2003). Anomalies are defined with respect to the 1993–98 mean.

In 2006, the most dramatic surface current anomalies were associated with the development of El Niño conditions late in the year in the Pacific Ocean basin. Anomalies elsewhere in the World Ocean were caused either by energetic mesoscale (60–90-day period) variations or by displacements of currents from their typical positions, or were associated with the seasonal reversals of currents in the Tropics.

*(i) Pacific Ocean*

Annual mean anomalies (Fig. 3.9) were most prominently organized in a coherent pattern in the western tropical Pacific Ocean, associated with the 2006 El Niño. Seasonal mean anomalies (Fig. 3.10) show a typical seasonal reversal of the equatorial surface current from January through June. During July, eastward anomalies began developing in the eastern (145°–170°E) equatorial Pacific (Fig. 3.11). By August, these anomalies had reached 70 cm $s^{-1}$ at 160°E to the date line. In September, eastward anomalies of ~40 cm $s^{-1}$ were seen at 120°–140°W. The largest eastward anomalies of 50 cm $s^{-1}$ were seen in October at 160°E to the date line. These anomalies also propagated eastward while weakening to +25 cm $s^{-1}$ in November. Anomalies in December were small.

*(ii) Indian Ocean*

The tropical Indian basin exhibited a band of anomalously eastward flow along 25°–30°S, immediately south of westward anomalies. This is the band where the westward SEC encounters Madagascar and is deflected southwestward to join the Agulhas Current system flowing southward against Africa's west coast. The anomaly pattern suggests that the SEC was displaced to the north of its climatological position. Seasonally averaged anomalies (not shown) were associated with monsoon-driven changes in the tropical basin and the complex pattern of mesoscale anomalies in the Agulhas Return Current. The eastward equatorial jet was prominent in April–June, but not in October–December.

*(iii)Atlantic Ocean*

The seasonal reversal of western tropical Atlantic Ocean currents (cf. Lumpkin and Garzoli 2005) was prominent in 2006. Anomalously strong westward anomalies were seen on the equator in July–September, reversing to eastward anomalies in October–December. This reversal is typical, but was more ener-

[2] Drifter data are distributed by NOAA/AOML's Global Drifter Program at the Drifter Data Assembly Center Web site (www.aoml.noaa.gov/phod/dac/dacdata.html). Moored current meter data are distributed by NOAA/PMEL's Tropical Atmosphere–Ocean Project at www.pmel.noaa.gov/tao. Altimetric time series of transports may be viewed at www. aoml.noaa.gov/phod/satprod. NCEP data are provided by the NOAA–CIRES Climate Diagnostics Center, Boulder, Colorado (www.cdc.noaa.gov). AVISO altimetry is produced by the CLS Space Oceanography Division as part of the Environmental and Climate EU ENACT project and with support of CNES.

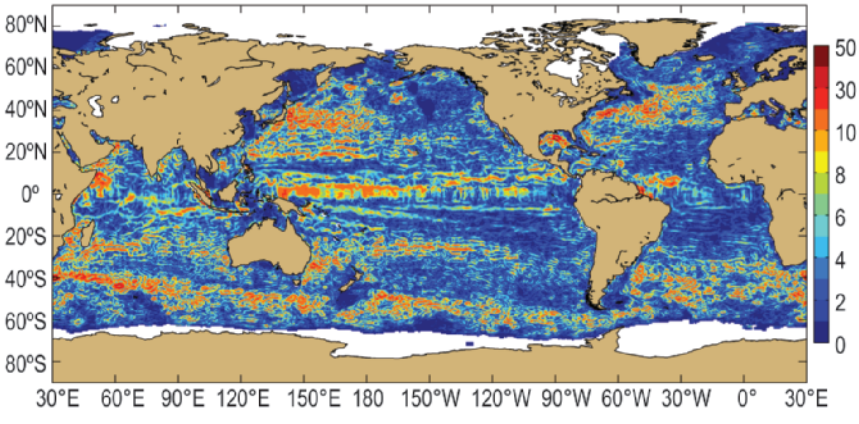


**Fig. 3.9. Amplitude (cm $s^{-1}$) of 2006 averaged surface current anomalies, with respect to the 1993–98 mean.**

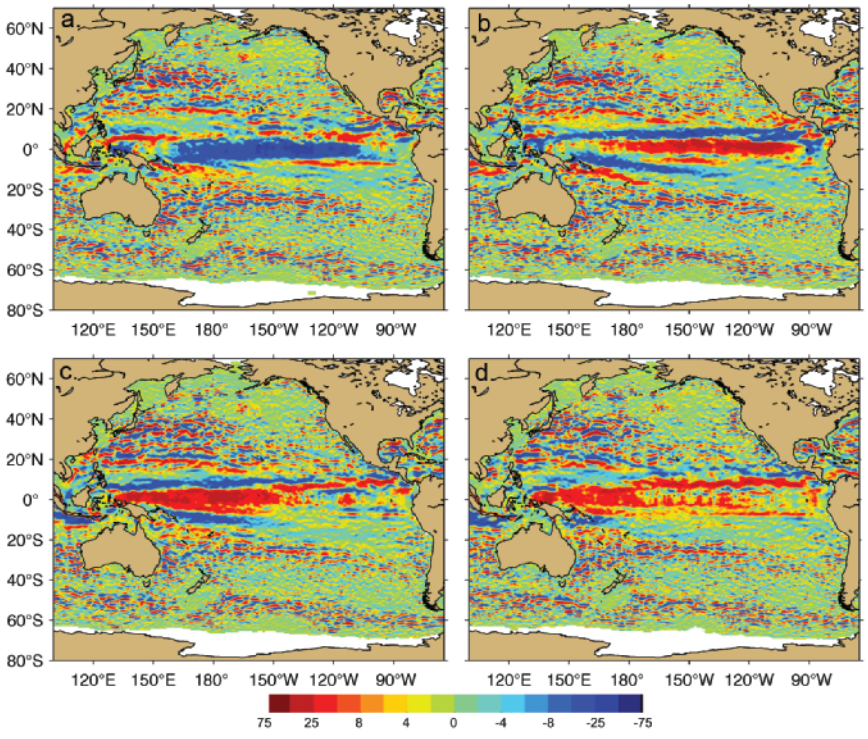


**Fig. 3.10. Pacific seasonal anomalies of zonal current (positive = eastward) during (a) January–March, (b) April–June, (c) July–September, and (d) October–December 2006.**

getic and dramatic in 2006. Anomalies elsewhere were associated with intense mesoscale features in the Gulf Stream, Brazil/Malvinas Confluence off the Brazilian coast, and the Agulhas retroflection west of the southern tip of Africa. Averaged over 2006, the Gulf Stream axis was close to its climatological position. Late in 2006, the Gulf Stream developed a dramatic pattern of alternating meanders at 50°–65°W.

Satellite altimetry observations indicate that the Agulhas Current, which runs southward against Africa's southeast coast, was somewhat larger than average during 2006. This current can serve to connect the Indian and Atlantic Oceans by transferring salty, tropical Indian water into the South Atlantic via Agulhas rings shed from the current. However, the number of rings shed in 2006, as revealed by altimetry, was lower than average. Thus, unless the few rings that were shed were unusually deep, the South Atlantic Ocean may reveal fresh anomalies in Argo-derived salinity maps for early 2007.

The NBC runs northward along the Brazilian coast, carrying South Atlantic water past the equator before it abruptly leaves the coast and flows eastward across the Atlantic. Rings shed by the NBC continue northwestward, and carry a large fraction of the upper-water exchange from the South Atlantic to the North Atlantic. This pathway is thus a critical part of the upper limb of the MOC in the Atlantic.

The space–time diagram of sea height residual (sea height anomaly with the annual cycle removed) along the pathway of NBC rings (not shown) reveals that five rings are shed by the NBC during 2006, which is approximately the historical mean. However, most of these rings did not enter the Caribbean Sea. The time series of geostrophic transport of the Yucatan Straits (not shown), connecting the Caribbean Sea to the Gulf of Mexico, indicates that the transport decreased during 2006. This is significant, because the flow through the Yucatan Straits feeds the Loop Current–Florida Current–Gulf Stream system. Consistently, the Florida Current transport, measured by an undersea cable running from South Florida to the Bahamas, decreased slightly from its historical average of 30–32 million tons $s^{-1}$ in mid-October to around 28 million tons $s^{-1}$ by the end of the year. Such anomalies are common in the record.

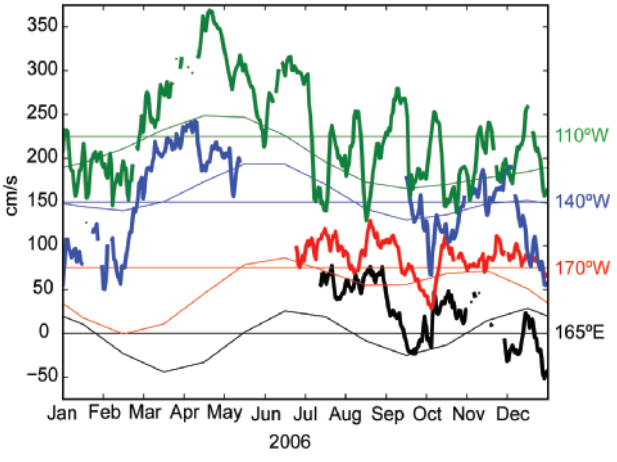


**Fig. 3.11. Near-surface zonal current anomalies (daily averages) measured at equatorial TAO moorings. Time series east of the date line have been displaced vertically; the zero line for each is indicated by a horizontal line. Seasonal climatology at each site is indicated by thin curves.**

### 2) The Meridional Overturning Circulation and oceanic heat transport—M. O. Baringer and C. S. Meinen

The component of the ocean circulation associated most with long-time-scale variability in heat redistribution is the MOC, sometimes referred to as the "thermohaline circulation." The MOC is a global circulation cell wherein surface waters in the high latitudes are cooled, thereby becoming denser; this dense water sinks and flows toward the equatorial regions. In tropical and subtropical regions around the world these waters eventually mix with other waters, becoming less dense, and they return to the sea surface to ultimately flow toward the higher latitudes and complete the cell. This circulation simultaneously transfers a significant amount of heat to the higher latitudes. The primary locations where deep convection occurs are in the northern North Atlantic and in the subpolar ocean around Antarctica, while the upwelling of new surface waters is spread broadly around the globe.

The strengths of the overturning circulations in different basins are directly related to the strength of the heat transport; warm water flowing north in the upper layers and returning southward as cold water at depth represents a net poleward heat transport in the Northern Hemisphere. There are several available estimates of the averaged global mass and heat transport based on inverse model calculations (Lumpkin and Speer 2007; Ganachaud and Wunsch 2003; Talley 2003;). Historical estimates of the state of the MOC have come from either cross-basin hydrographic sections or specific point measurements of the water property changes in the deep ocean. These water property measurements have been used to infer the state of the MOC using a variety of analytical techniques. Currently, observing systems capable of quantifying changes in the complete MOC are at fledgling stages that at best observe only one component (e.g., a specific current or ocean layer) of the MOC at discrete locations.

The MOC is generally thought of as a basin-wide phenomenon, however at 26°N in the Atlantic the bulk of the warm upper limb of the MOC is thought to be carried in the Florida Current through the Straits of Florida (with a smaller contribution being carried by the Antilles Current east of the Bahamas), while the majority of the cold lower limb is believe to be carried to the south in the DWBC just east of the Bahamas. Fluctuations in the Florida Current show a clear negative correlation with the atmospheric phenomenon known as the NAO; however, while the NAO has been tending to decrease over the past 20 years, the Florida Current transport shows no corresponding long-term trend through 2006 (Fig. 3.12). The annual mean transport observed in 2006 (31.3 Sv[3]) falls within the lowest quartile of historical annual mean transports from the cable, however this transport is still well within one standard deviation from the long-term mean of 32.1 Sv. Given the statistical standard error of the mean of 1 Sv for the year, 2006 cannot be termed as an unusual year in terms of the Florida Current transport. Additional information can be found in Baringer and Meinen (2006).

In a recent article, Bryden et al. (2005) postulate a 30% reduction in the MOC transport between the 1950s and the present day. However, that analysis is based on a very limited dataset (essentially five "snapshot" hydrographic sections). In contrast, a comparison of moored observations near the Southeast Newfoundland Ridge in the early 1990s and early 2000s finds no trend in the DWBC transport (Schott et al. 2004), and a subsequent study at 26°N comparing transports from moored instruments in the late 1980s and 2004/05 finds no indication of a systematic trend either (Meinen et al. 2006). Furthermore, the latter study finds evidence of significant baroclinic and barotropic variability at time scales that could be aliased by "snapshot" hydrographic sections such as those used in Bryden et al. (2005).

Other recent work using cross-basin hydrographic sections along 48°N in the Atlantic suggest conflicting conclusions relative to the state of the ther-

[3] Sv is a Sverdrup or $10^6$ m$^3$ s$^{-1}$, a unit commonly used for ocean volume transports.

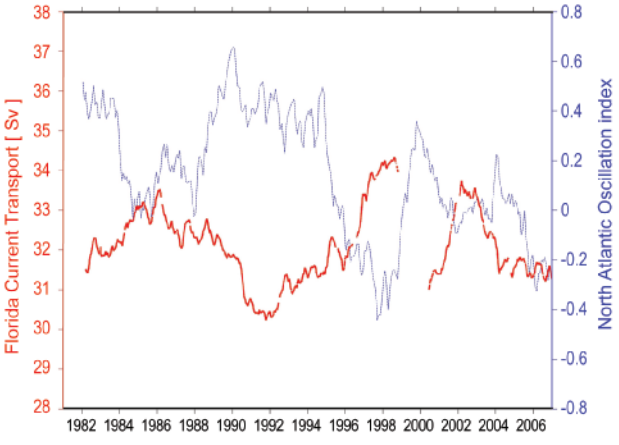


**Fig. 3.12. Florida Current transport (red solid) as measured by the NOAA-funded submarine cable across the Florida Straits, along with the North Atlantic Oscillation index produced by the NOAA National Centers for Environmental Prediction (blue dashed).**

mohaline circulation. In particular, Koltermann et al. (1999) show large variability of the MOC that, they conclude, is related to the strength of Labrador Sea Water production, with larger (smaller) MOC transport corresponding to less (more) Labrador Sea Water export. More recently, these data have been reanalyzed to formally test the hypothesis that the MOC circulation is steady. Lumpkin et al. (2007) find that a steady MOC over the same time period could not be ruled out based on the uncertainty in determining the barotropic circulation.

Clearly, additional work needs to be done to understand the full range of time scales associated with MOC variability and the improvement of error estimates attached to these estimates. The programs in place in 2006 are an excellent first step toward the development of an integrated measurement system. However, much work remains to fully monitor the Atlantic MOC system, as well as the global overturning circulation system.

e. *Sea level*—M. A. Merrifield, S. Gill, G. T. Mitchum, and P. L. Woodworth

Global sea level variability during 2006 is summarized using measurements from the complementary satellite altimeter and tide gauge observing systems. Here we use SLA data (1993–99 base) from the multimission, 1/4° gridded product available from the French Aviso program (online at www.aviso.ceanobs.com/). Because 2006 satellite orbit corrections are still being applied, the 2006 SLA analysis period is taken as October 2005 through September 2006. We also used RSL data (1993–99 base) from The GLOSS (Woodworth et al. 2003), a network of nearly 300 coastal tide gauges. The SLA is used to assess global mean sea level change and RSL is used to summarize coastal sea level variability for 2006.[4]

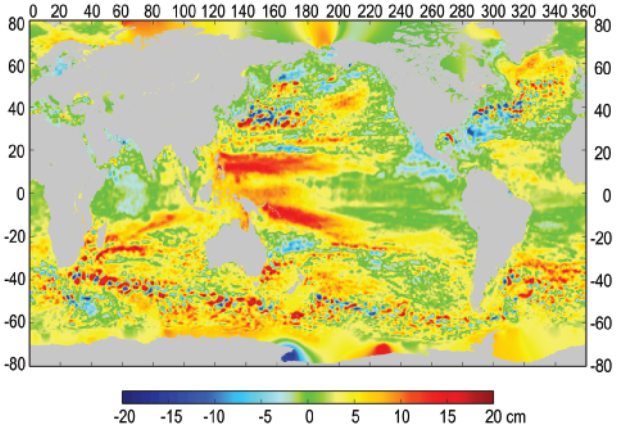


**Fig. 3.13. Annual average SLA for 1 Oct 2005–30 Sep 2006.**

Annual mean SLA in 2006 was above the 1993–99 baseline average for nearly 80% of the ocean surface (Fig. 3.13). Bands of high SLA (10–20 cm) occurred in the western tropical Pacific east of the Philippines, extending southeastward from the Solomon Islands along the South Pacific convergence zone. These bands also were the areas of the highest positive increase relative to the 2005 annual mean. A notable pattern in the eastern equatorial Pacific that was most evident after the averaging period used to construct Fig. 3.13 was a weak El Niño event with ~10 cm positive sea level anomalies in December 2006.

The spatially weighted, global mean SLA for 2006 was the highest annual mean (computed from October through September of each year) since the beginning of the altimeter record in 1993. Global mean SLA was 6 mm higher in 2006 than 2005, an increase larger than the global sea level rise rate of $2.8 \pm 0.4$ mm yr$^{-1}$ estimated over altimeter data from 1993 to 2003 (Leuliette et al. 2004). The increasing global mean level is attributed primarily to large SLA increases south of 20°N, especially between 40° and 30°S and near the equator (Fig. 3.14a), and in longitude bands encompassing the Indo-Pacific (100°–240°E) and the Atlantic (310°E–360°) (Fig. 3.14b). Detailed global maps of SLA trends are available online at http://sealevel.colorado.edu/.

Changes in relative sea level, including vertical land motion contributions, are examined using available RSL data from 2006 (Fig. 3.15). This provides an assessment of sea level change as experienced at the coast, but is not a measure of global mean sea level change, which is best addressed using the SLA dataset. The annual RSL average for 2006 was the highest over the collective record, which begins in at least 1980 for the majority of stations, and in the early twentieth century for ~10% of stations. The station mean RSL increased by 2.9 mm in 2006 from 2005, about one-half the global mean SLA increase over the same period. The station mean RSL

[4] The altimeter products were produced by Ssalto/Duacs and distributed by Aviso, with support from CNES (www.aviso.oceanobs.com). The Aviso dataset used is listed as the Gridded Sea Level Anomalies DT-MSLA "Ref," multimission product. Tide gauge data were obtained from the University of Hawaii Sea Level Center (http://uhslc.soest.hawaii.edu). SLA is corrected for atmospheric pressure, the RSL time series is not.

rise rate is 2.3 mm $yr^{-1}$ since 1993, the time span of the SLA data, and 1.9 mm $yr^{-1}$ since 1975.

Extreme sea levels during 2006, associated with storms and other nontidal variability, is characterized by the average of the 5% largest daily averaged RSL values at each station. The highest extreme values occurred at high-latitude stations resulting from winter storms, with sporadic high values at low-latitude stations presumably resulting from isolated storm events (Fig. 3.15a). To determine how anomalous the extremes were during 2006, the percentage of years at each station with extreme values less than 2006 is depicted in Fig. 3.15b. For the majority of stations, the 2006 extremes were in the 90th percentile or higher (e.g., Europe, the east coast of North America, the South Pacific). The year 2006 was an anomalously high year for extreme sea levels in part because of rising sea levels. If the percentiles are computed after removing mean sea level trends at each station, 2006 is seen as a less anomalous year in the South Pacific, although values around North America and North Europe remain high (Fig. 3.15c). The increase in the 2006 percentiles for some Alaskan and Canadian stations (Fig. 3.15c) is due to the correction for negative rates of RSL change.

*f. Global ocean carbon cycle*—C. L. Sabine, R. A. Feely, and R. Wanninkhof

1) Air–sea carbon fluxes

Seasonal-to-interannual variability in the ocean $CO_2$ sink is being investigated by studying the $CO_2$

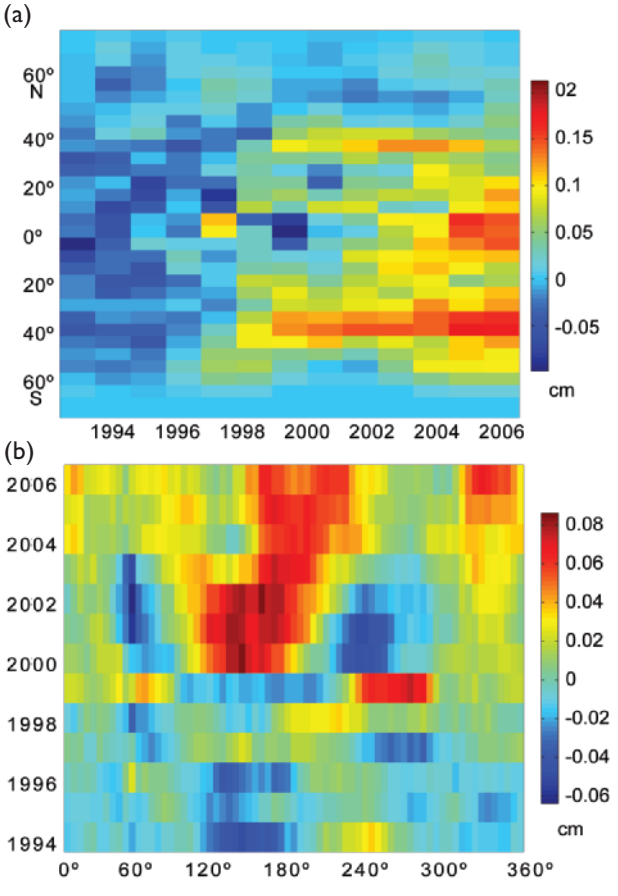


**Fig. 3.14. (a) Time vs latitude plot of annual mean SLA averaged over longitude and weighted by the percentage of total ocean surface area covered. (b) Longitude vs time plot of annual mean sea level averaged over latitude and weighted by the percentage of total ocean surface area covered.**

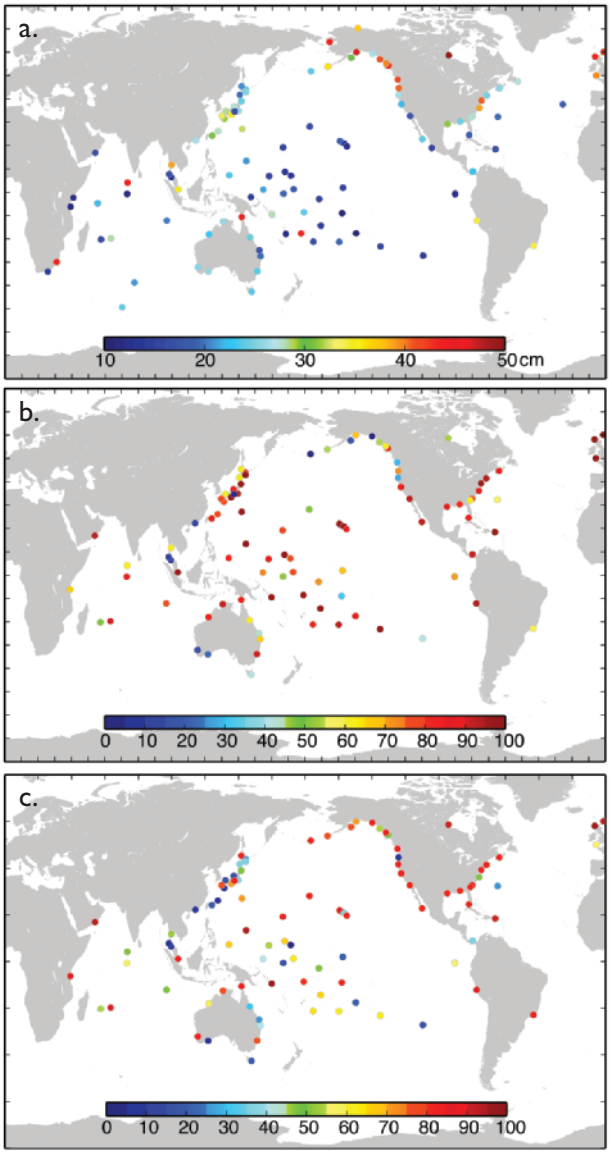


**Fig. 3.15. (a) Average of the highest 5% of daily sea level values during 2006. (b) Percentage of years at each station with extreme values less than in 2006. (c) Same as (b), but with the trend of mean sea level first removed from each time series.**

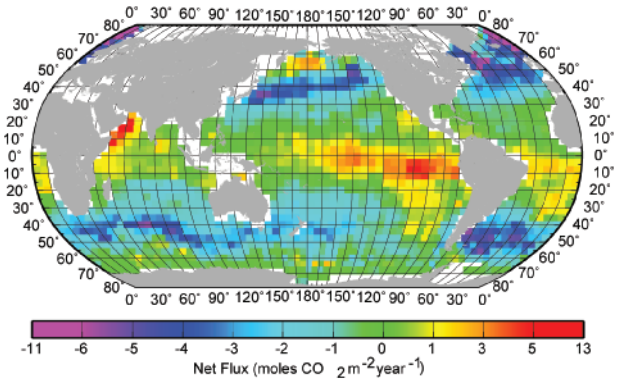


**FIG. 3.16. Mean annual net air–sea flux for $CO_2$ (moles $CO_2$ $m^{-2}$ $yr^{-1}$) for the reference year 1995. Red–yellow areas indicate that the ocean is a source for atmospheric $CO_2$, and blue–purple areas indicate that the ocean is a $CO_2$ sink. From Takahashi et al. (2002).**

flux across the air–sea interface. Carbon dioxide flux is calculated from measurements of surface water and atmospheric $pCO_2$, together with wind speed. The climatological monthly distribution of $pCO_2$ in global surface water has been calculated with a spatial resolution of 4° × 5° (Takahashi et al. 2002). Fewer than 30% of the monthly pixels have direct observations. In general, the tropical regions are a net source of $CO_2$ to the atmosphere and the high latitudes are a net sink for $CO_2$ (Fig. 3.16). The published value for the net air–sea flux indicates a net ocean uptake of 2.2 Pg C for the reference year of 1995, but this estimate was later corrected for a systematic error in the wind speeds to give a net global ocean uptake of 1.5 Pg C for the reference year of 1995 (Sabine et al. 2004a). The contemporary $CO_2$ uptake of 1.5 Pg C $yr^{-1}$ combined with the estimated preindustrial ocean source of 0.6 Pg C $yr^{-1}$ implies an anthropogenic $CO_2$ uptake estimate (1.5 + 0.6 = 2.1 Pg C $yr^{-1}$) that is consistent with other independent estimates (Sabine et al. 2004a).

The $CO_2$ climatology has been used extensively as a baseline for placing regional flux estimates into a global context and as a constraint for global biogeochemistry and inverse models. However, developing seasonal-to-annual estimates of net air–sea $CO_2$ fluxes to evaluate the changing role of the ocean in the global carbon cycle resulting from climate change remains a formidable task. The large spatial and temporal variability in surface water $pCO_2$ still requires interpolation approaches to determine a meaningful global flux estimate or "flux map." Making flux maps directly from observations representing shorter time frames, however, will require a continued expansion of the observing network.

As a first step for assessing the interannual variability in air–sea $CO_2$ fluxes, we have taken the empirical approach of Lee et al. (1998) and Park et al. (2006) together with global monthly estimates of SST and a high-resolution wind speed assimilation product (online at http://podaac-www.jpl.nasa.gov/products/product079.html) to develop monthly estimates of global air–sea $CO_2$ flux between 1995 and 2005. To execute the scheme, surface water $pCO_2$–SST relationships were determined for each 4° × 5° pixel from least squares linear fits of the monthly climatological $pCO_2$ (Takahashi et al. 2002) and SST values for the following three periods: January–April, May–August, and September–December. In much of the world's ocean, except in the South Indian and Southern Oceans, the correlations between $pCO_2$ and SST are quite robust ($r^2 = 0.70 \pm 0.3$, number of pixels = 1314). These relationships are then applied to the interannual SST anomalies relative to 1995 to evaluate the change in $pCO_2$ for each pixel relative to the $pCO_2$ climatology. For the equatorial Pacific Ocean, one of the best-studied regions for seasonal and interannual $CO_2$ flux variability (e.g., Chavez et al. 1999; Cosca et al. 2003; Feely et al. 1995, 2006), empirical relationships between surface water $pCO_2$ and SST, rather than climatological values, are used to estimate $pCO_2$. Here we use the formulations of Cosca et al. (2003) to estimate $pCO_2$ for the equatorial Pacific between 5°N and 5°S. The air–sea flux is then calculated for each 4° × 5° pixel using the derived surface water $pCO_2$ estimates; the global atmospheric $CO_2$ mole fraction obtained from NOAA's Environmental Science and Research Laboratory (GLOBALVIEW-CO2 2006), converted to $pCO_2$ using the climatological SLP; and the wind speed gas exchange parameterization of Wanninkhof (1992). Validation of the approach at the few time series sites available shows good correspondence in the sign of the year-to-year changes between observations and this empirical approach, and an agreement in magnitude of better than 40%.

Figure 3.17 shows the interannual variability in the net annual air–sea $CO_2$ gas exchange from 1995 to 2005 relative to the 10-yr mean. The period from 1995 to 1998 was a period of generally negative anomalies indicating increased uptake by the oceans. The effect of the 1997/98 El Niño with decreased outgassing in the equatorial Pacific, which translates into net increased oceanic uptake, is clearly apparent (Feely et al. 2006). This is followed by three years of reduced uptake. The 2005 uptake appears to be very close to that of the 10-yr average. Overall, the implied interannual variability of the ocean uptake is about

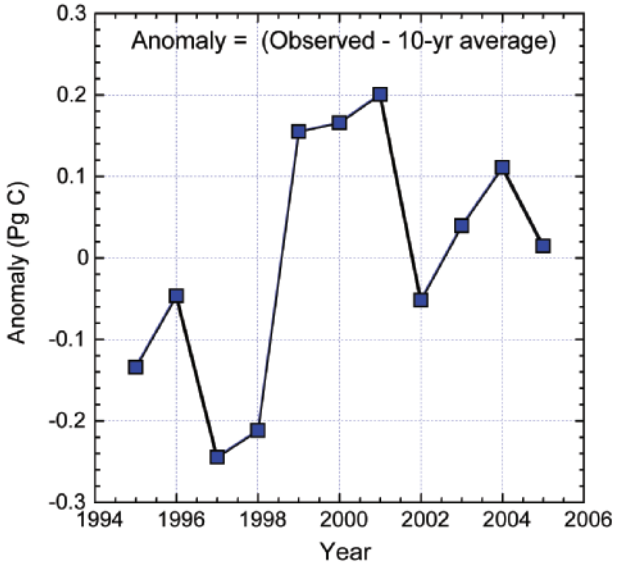


**Fig. 3.17. Interannual variability in the net annual global air–sea $CO_2$ gas exchange from 1995 to 2005 relative to the 10-yr mean. Negative values indicate increased ocean uptake.**

10% of the climatological value, consistent with previous ocean model–based estimates, including Park et al. (2006).

There are significant uncertainties in the seasonal flux map calculations based on several factors, including the assumptions that go into the fits, the quality of the empirical fits, uncertainties in the reanalysis products, and uncertainties in the wind speed relationship for gas exchange. This approach does not fully account for the biological effects on surface water $pCO_2$. Despite these shortcomings, these first estimates of interannual variability provide a useful tool for assessing the changing role of the ocean in global climate change and for comparison with models. Extension of the global surface ocean $CO_2$ network will facilitate the development of improved regional algorithms that will lead to more accurate flux maps.

### 2) Subsurface carbon inventory

An analysis of approximately 73,000 carbon measurements from 95 research cruises run as part of the WOCE and the JGOFS in the 1990s has provided the first global assessment of DIC distributions with sufficient accuracy and coverage to evaluate the change in ocean carbon resulting from the accumulation of anthropogenic $CO_2$ (Feely et al. 2001; Wallace 2001). Using these measurements, Sabine et al. (2004b) estimated that the ocean accumulated approximately 118 Pg C between 1800 and 1994 accounting for 48% of the $CO_2$ released from burning fossil fuels over this same time period (Fig. 3.18). The highest column inventories are observed in the North Atlantic and in a band around the Southern Hemisphere because these are regions where surface waters are sinking and moving anthropogenic $CO_2$ into the ocean interior (Fig. 3.18).

Although the WOCE/JGOFS data were used to determine the total accumulation of carbon in the ocean since preindustrial times, this one time global survey could not provide information on how ocean carbon inventories have evolved over time or how the storage has varied geographically over different time periods. To elucidate decadal variability and temporal evolution, the U.S. CLIVAR/CO2 Repeat Hydrography Program has identified 19 hydrographic sections distributed around the global ocean that will be reoccupied approximately every 10 years. The program started in 2003 with three cruises in the North Atlantic that were repeats of select WOCE/JGOFS cruises. Each year, one to three cruises are run in different locations with a goal of completing the first global resurvey by 2012.

The repeat hydrography strategy presents at least two major challenges for interpreting the measurements. First, it will take about a decade to survey enough of the oceans to draw robust inferences about the global patterns of decadal variations in the oceanic anthropogenic $CO_2$ sink. Second, some of the assumptions (e.g., steady-state circulation and biology) that appeared to be reasonable for the Sabine et al. (2004b) 200-year inventory assessment do not hold true for shorter time scales. New techniques must be developed for isolating the anthropogenic signal from the natural variations in ocean circula-

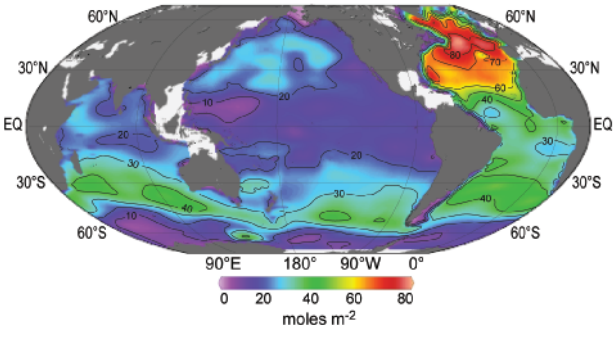


**Fig. 3.18. Column inventory of anthropogenic $CO_2$ (mol $m^{-2}$) that has accumulated in the ocean between 1800 and 1994. High inventories are associated with deep water formation in the North Atlantic and intermediate and mode water formation between 30° and 50°S (Sabine et al. 2004b).**

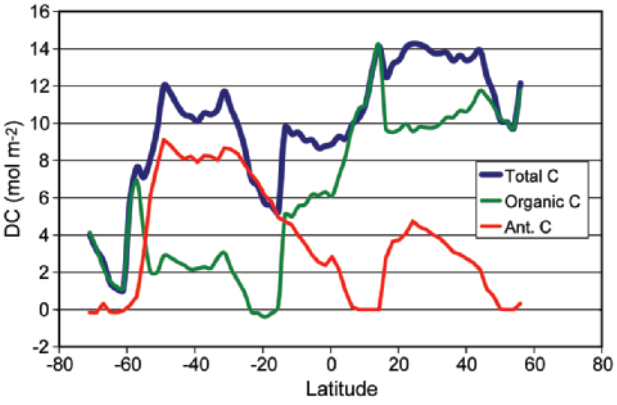


**FIG. 3.19. Column inventories of the change in total DIC resulting from variations in the apparent decomposition rate of organic matter, and the change in DIC from the accumulation of anthropogenic $CO_2$ as a function of latitude along 152°W between 1991 and 2006.**

tion and biological particle decomposition rates that affect the interior carbon distributions on interannual-to-decadal time scales. Indeed, natural ocean variations can be the same order of magnitude as the anthropogenic changes and can either mask or enhance the anthropogenic signal.

Ocean carbon changes have been evaluated for ocean cruises that have reoccupied a Pacific north–south section along 152°W from Antarctica to Alaska in 2005 and 2006, approximately 15 years after the WOCE/JGOFS cruises. The total DIC column inventory changes along the section ranged from less than 2 mol C $m^{-2}$ in the high-latitude Southern Ocean to greater than 14 mol C $m^{-2}$ in the North Pacific (Fig. 3.19). This total DIC change, however, reflects both the uptake of anthropogenic $CO_2$ from the atmosphere and carbon changes resulting from natural variations in ocean physics and biogeochemistry. Separating these two components using newly developed methodologies reveals that in the North Pacific, the natural variations account for up to 83% of the total DIC change, leaving a rather modest anthropogenic $CO_2$ component (Fig. 3.19).

A full global assessment of ocean DIC changes cannot be made until the resurvey of the oceans is completed in the next few years. However, each updated ocean section provides incremental insight into how carbon uptake rates are evolving spatially and temporally. Table 3.1, updated in this report to reflect the 2005/06 Pacific cruises, summarizes the current best estimates of anthropogenic $CO_2$ accumulation along representative north–south cruise tracks in the Atlantic and Pacific Oceans. The North Atlantic shows the largest increase, consistent with the long-term accumulation of Sabine et al. (2004b), illustrating the importance of North Atlantic Deep Water formation as a mechanism for transporting anthropogenic $CO_2$ into the ocean interior. The formation of mode and intermediate waters in the Southern Hemisphere also contributes to the substantial DIC increases in the South Atlantic and South Pacific. The North Pacific shows a relatively modest increase because of the lack of deep water formation and restricted intermediate water formation in that region. The Indian Ocean is being surveyed in 2007/08, so accumulation rates are not yet available.

To place these regional measurements in a global perspective, indirect approaches for estimating the current ocean storage of anthropogenic $CO_2$ suggest a global ocean uptake of approximately 2.2 Pg C $yr^{-1}$ (e.g., Bopp et al. 2002; McNeil et al. 2003; Matsumoto et al. 2004). If this carbon were distributed evenly over the entire global ocean area ($335.2 \times 10^9$ $km^2$), it would imply an average column inventory increase of ~0.55 mol C $m^{-2}$ $yr^{-1}$. The cruises completed thus far in the Atlantic and Pacific Oceans tend to bracket this average and suggest that the current patterns of ocean carbon storage are similar to the patterns observed in the long-term accumulation (Fig. 3.18). As additional cruises in the Atlantic and Pacific Oceans are evaluated, improved uptake estimates that consider the spatial variability within a basin will be generated.

*g. Global ocean color and phytoplankton*—M. M. Gierach and B. Subrahmanyam

Ocean color is a measure of chlorophyll-a (a pigment within phytoplankton) at the ocean surface and is considered an indicator of phytoplankton biomass. Ocean color can potentially illustrate the distribution

**TABLE 3.1. Estimates of ocean column inventory changes in anthropogenic carbon (mol C $m^{-2}$ $yr^{-1}$) over the last decade.**

| | Atlantic Ocean (along 25°W) | Pacific Ocean (along 152°W) | Indian Ocean (along 90°E) |
|---|---|---|---|
| Northern Hemsphere | 0. 63 | 0. 25 | * |
| Southern Hemisphere | 0. 75 | 0. 41 | * |

*Indian Ocean cruises are scheduled for 2007–08.

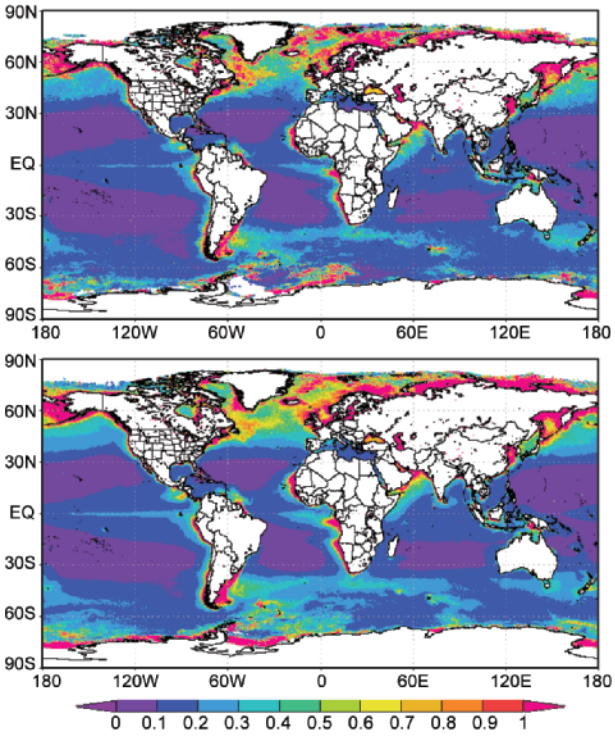


**Fig. 3.20. Global time-averaged chlorophyll-a concentration (mg $m^{-3}$) plots for (top) January–December 2006 and (bottom) September 1997–December 2005. Images generated by NASA's Giovanni (giovanni.gsfc.nasa.gov).**

of nutrients and changes in stratification and circulation within oceanic basins. Marine phytoplankton influence the global pattern of the SST, density, and associated flows by heat release to the upper-ocean environment. Therefore, the patterns of biological production shown through ocean color can demonstrate climate changes, such as ENSO and monsoons.

Prior to the launch of satellites, global ocean color (i.e., chlorophyll-a concentration or phytoplankton biomass) datasets were nonexistent. This issue has since been eliminated with instruments such as SeaWiFS, which provides the longest historical record among all ocean color sensors. The ~9-year SeaWiFS dataset provides a means to assess the seasonal and interannual variability of ocean color on global scales. The data product used here is the NASA Goddard OBPG monthly global 9-km product, acquired using the GES-DISC Interactive Online Visualization and Analysis Infrastructure (Giovanni). The time period analyzed is from September 1997 through December 2006.

Global chlorophyll concentrations in 2006 exhibit some difference from the long-term average, but the significance of the anomalies is difficult to assess (Fig. 3.20). Low concentrations are observed in the center of ocean gyres, whereas high concentrations are detected in ocean margin waters, in equatorial upwelling regions, in river deltas, at latitudinal belts greater than approximately 40°N/S, and within the southern subtropical convergence zone (Yoder and Kennelly 2003; Behrenfeld et al. 2001). However, the elevated levels associated with riverine input should be given special consideration because the signature observed could be a result of either detritus, colored dissolved organic matter, or suspended particulate matter within the water column (Joint and Groom 2000).

Peak chlorophyll concentrations occur during spring and fall, while minimums occur during winter and summer (Yoder and Kennelly 2003; Miller 2004). Typically, the Tropics have low annual productivity, whereas the temperate and polar regions exhibit high productivity (Garrison 2005). However, phytoplankton blooms are observed in the eastern tropical Atlantic during boreal summer resulting from multiple mechanisms, one of which is the intensification of the southeast trade winds (Pérez et al. 2005). The temperate zone undergoes two peaks in phytoplankton biomass (i.e., phytoplankton blooms; Garrison 2005). The larger of these is observed during boreal spring and the smaller during boreal fall. In comparison, polar regions experience only one peak in phytoplankton biomass, which is observed during boreal summer (Garrison 2005).

A globally averaged time series of chlorophyll-a concentrations from September 1997 to December 2006 reveals low concentrations during boreal winter and an occasional dip in concentration around boreal summer (not shown). Peak chlorophyll-a concentrations are observed primarily during boreal spring (May), with an occasional increase in concentration during boreal fall. Analysis of chlorophyll-a concentration anomalies from September 1997–December 2006 depict above-normal concentrations of approximately 0.021 mg $m^{-3}$ in August 1998 and approximately 0.034 mg $m^{-3}$ in July 2005 (Fig. 3.21). The August peak in 1998 is a direct result of the strong 1998–2001 La Niña event that took place in the equatorial Pacific, whereas the peak in July 2005 is a combination of a highly active biological summer season in the eastern tropical Atlantic and northern polar region. Note that the depicted chlorophyll anomalies are the differences between the monthly standard mapped image product and the monthly climatology standard mapped image product from OBPG, where the climatology data are derived by time binning the monthly binned files from September 1997 through August 2006, and are mapped to

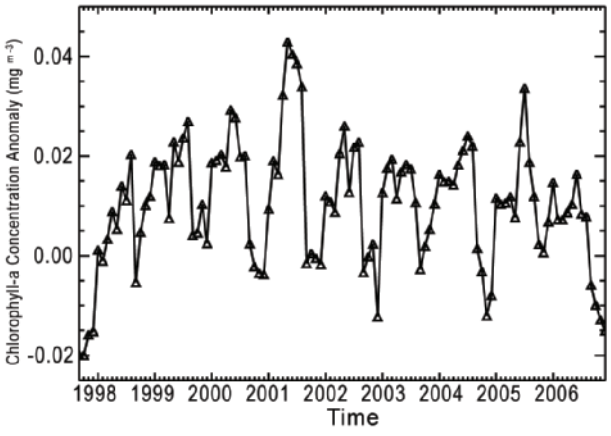


**Fig. 3.21. Global area-averaged chlorophyll-a concentration anomalies (mg $m^{-3}$) for September 1997–December 2006.**

an equidistant cylindrical projection with 9-km resolution at the equator. Each month is derived from nine years of monthly bins (online at http://reason.gsfc.nasa.gov/OPS/Giovanni/Readme_climate_seawifs.shtml).

Other anomalies to highlight are the above-normal chlorophyll concentration of approximately 0.043 mg $m^{-3}$ in May 2001 and below-normal concentration of approximately –0.02 mg $m^{-3}$ in the boreal fall of 1997 (Fig. 3.21). The below-normal concentrations in 1997 are a direct result of the extremely strong 1997/98 El Niño event. The peak in May 2001 is attributed to the negative state of the NAO. When the NAO index is negative, phytoplankton biomass and productivity in the North Atlantic have higher-than-mean conditions because of enhanced winter mixing of subtropical waters (Yoder and Kennelly 2003; Follows and Dutkiewicz 2002).

El Niño and La Niña events alter the previously described seasonal cycle of phytoplankton stocks in the Northern Hemisphere. Peak concentrations are observed during boreal summer in La Niña events and minimal concentrations occur during boreal fall in El Niño events. Several studies have been conducted in regard to the central/eastern equatorial Pacific chlorophyll decrease during the 1997/98 El Niño and the increase during the subsequent La Niña (Murtugudde et al. 1999; Chavez et al. 1998, 1999; Wilson and Adamec 2001; Ryan et al. 2002). Each of these studies illustrate that during a La Niña event, trade wind intensification prompts thermocline and nutricline shoaling, which increases the nutrient flux to the surface layer, generating intense phytoplankton blooms; conversely, during an El Niño event the thermocline and nutricline deepen, which impinges upwelling and reduces the supply of nutrients into the euphotic zone, thereby limiting chlorophyll production.

The year 2006 marked the beginning of the 2006/07 El Niño event. Both the 1997/98 and 2002/03 El Niños exhibited their lowest chlorophyll concentrations during the month of December. For the 2006/07 El Niño it is yet to be known at the time of writing whether peak below-normal concentrations do in fact occur in December. However, it is safe to say, based upon the available chlorophyll data, that the 2006/07 El Niño is stronger (in terms of its effects on chlorophyll) than the 2002/03 El Niño (with a below-normal concentration of approximately –0.031 mg $m^{-3}$ in December 2006 in the Niño 3.4-region compared to approximately –0.024 mg $m^{-3}$ in December 2002), but is less intense than the strong El Niño of 1997/98, which had a below-normal concentration of approximately –0.09 mg $m^{-3}$ in December 1997 in the Niño 3.4-region.

## 4. THE TROPICS—H. J. Diamond

### *a. Overview*—H. J. Diamond

This Tropics section consists of global input on the following three primary topics: 1) ENSO and the tropical Pacific, 2) TC activity for the 2006 season in seven basins (the Atlantic, northeast Pacific, northwest Pacific, North and South Indian, South Pacific, and Australia), and 3) ITCZ behavior in the Pacific and Atlantic basins.

The year was characterized by a transition from La Niña conditions in the first quarter of the year to El Niño conditions during the last quarter of the year. Regarding TC activity, the 2006 Atlantic season was much different than the 2005 season as follows: the number of storms dropped from 28 in 2005 to 10 in 2006, the northeast Pacific was a bit more active than in 2005, and the Australian basin had several strong storms.

### *b. ENSO and the tropical Pacific*—G. D. Bell and M. S. Halpert

#### 1) Overview

El Niño and La Niña episodes represent opposite phases of ENSO. These episodes are often defined from a time series of area-averaged SST anomalies in the Niño-3.4 region (called the Niño-3.4 index), which spans the central and east-central equatorial Pacific between 5°N–5°S and 170°–120°W. During 2006, this index showed below-average SSTs associated with La Niña during January–March, followed by a return to near-average temperatures and ENSO-neutral conditions during April–July (Fig. 4.1). El Niño conditions developed during August and

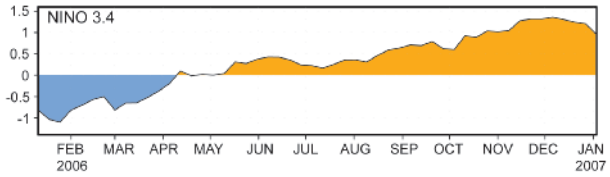


**Fig. 4.1. Time series of the Niño-3.4 region SST anomaly index.**

September, with Niño-3.4 temperatures increasing to more than +1.2°C above average during November and December.

The surface and subsurface temperature anomaly patterns show the changes across the central and east-central equatorial Pacific during 2006 (Fig. 4.2). Between December–February 2005/06 and September–November 2006, anomalies warmed 2°–3°C across much of the region (Figs. 4.2a,b), and subsurface temperature anomalies warmed 3°–6°C (Figs. 4.2c,d). This warming is associated with increased depths of the 20°C isotherm (thick black line), which approximates the center of the oceanic thermocline.

The strong coupling between surface and subsurface temperature anomalies is a well-known characteristic of both El Niño and La Niña, and reflects their link to changes in thermocline depth (Figs. 4.3a,b). During La Niña, stronger-than-average tropical easterly winds in the lower atmosphere produce increased upwelling, which leads to shallower thermocline depths and cooler ocean temperatures. Conversely, weaker-than-average tropical easterlies during El Niño result in decreased upwelling, which leads to increased thermocline depths and warmer waters. The transition from La Niña to El Niño during 2006 was indeed accompanied by a significant weakening of the 850-hPa equatorial easterlies, which were stronger than average early in the year (blue shading) and generally weaker than average after May (orange shading, Fig. 4.3c).

The development of El Niño also followed a sharp transition in the overall distribution of anomalous convection during May and June across the equatorial Pacific (Fig. 4.4). This transition mainly featured a westward shift in the area of suppressed convection (brown shading) from the date line to the western Pacific. However, enhanced convection near the date line did not become established until mid-September, which coincided with a significant warming of the central and east-central equatorial Pacific. This anomalous tropical convection led to several well-known El Niño impacts, including 1) below-average rains across northeastern Australia, Indonesia, and the western tropical Pacific, 2) fewer Atlantic hurricanes and more East Pacific hurricanes than in recent years, 3) above-average temperatures across the northern half of the United States during November–December, and 4) stormier- and wetter-than-average conditions across the southeastern United States during November–December.

### 2) The MJO and Kelvin wave activity

Low-frequency variability in the Tropics is strongly influenced by the MJO (Madden and Julian 1971, 1972, 1994), a tropical disturbance that modulates tropical convection and atmospheric circulation patterns with a typical period of 30–60 days. The MJO tends to be most active during ENSO-neutral years, and can produce ENSO-like anomalies (Mo and Kousky 1993; Kousky and Kayano 1994). The low- (850 hPa) and upper- (200 hPa) level equatorial zonal winds, tropical convection, and both sea surface and subsurface temperature anomalies exhibited considerable intraseasonal variability during 2006 in association with the MJO.

The MJO is indicated in a time–longitude section by continuous propagation of

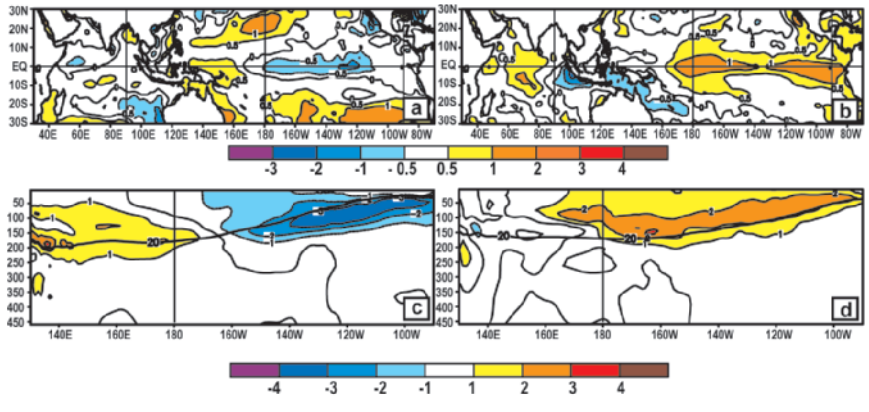


**Fig. 4.2. Seasonal SST anomalies (top) and depth–longitude section of subsurface temperature anomalies (bottom) for (a), (c) DJF 2005/06 and (b), (d) SON 2006. The 20°C isotherm (thick black line) is also plotted in panels (c), (d). SST anomalies are departures from the 1971–2000 adjusted OI climatology (Smith and Reynolds 1998). The subsurface analysis is based on data derived from an analysis system that assimilates oceanic observations into an oceanic GCM (Behringer et al. 1998), and anomalies are departures from the 1981–2000 base period means.**

the 200-hPa velocity potential anomalies around the globe (Fig. 4.5). During April–December, several periods of MJO-related suppressed convection (brown shading, see Fig. 4.4) and anomalously weak low-level tropical easterly winds were evident over the western tropical Pacific. These conditions can initiate oceanic equatorial Kelvin waves, which are eastward-propagating gravity waves featuring downwelling in the mixed layer at their leading edge and upwelling in their wake (Zhang et al. 2001). A typical eastward propagation rate for these waves is roughly 10° of longitude per week.

Four major Kelvin waves occurred during April–December, with the amplitude of each wave exceeding that of its predecessor. Prior to and during El Niño's development, these waves acted to significantly modulate the upper-ocean heat content across the central and east-central equatorial Pacific. The warming associated with the downwelling phase of a particularly strong Kelvin wave during September prompted NOAA to report that El Niño had developed. This was followed during November and December by an even stronger Kelvin wave and additional warming.

### c. *Tropical cyclones*

#### 1) Seasonal activity overview—H. J. Diamond and D. H. Levinson

Averaged across all basins, the tropical storm season of 2006 (2005/06 in the Southern Hemisphere) had a below-normal (1981–2000 base) number of tropical storms, fewer HTC, but a greater number of major HTCs than average. Globally, 78 TS (> 33 kt) were recorded, with 42 becoming HTCs, and of these 26 attained major/intense (> 95 kt) status (compared to an average of 97, 55, and 25 storms, respectively). While 2005 was a more active season overall, the number of major HTCs in both 2005 (28) and 2006 (26) were similar.

The 2006 season was near average in three basins (Atlantic, North Indian, and southwest Pacific), slightly above average in two basins (northeast Pacific and Australian), and slightly below average in two basins (northwest Pacific and South Indian). As a result of El Niño conditions described earlier in the section, the Atlantic season was notable (e.g., no landfalling hurricanes in the United States versus seven in 2005). The highlight of the Australian season was the occurrence of three Australian category

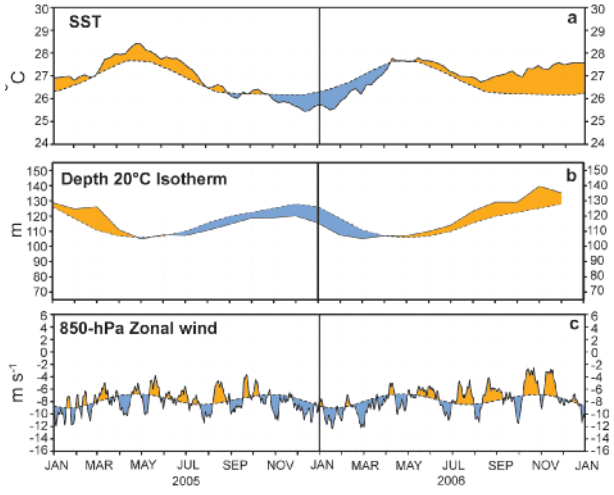


**Fig. 4.3. Monthly time series of (a) SST (°C), (b) the depth of the 20°C isotherm (m), and (c) 850-hPa zonal wind speed (m s$^{-1}$), over the central and east-central equatorial Pacific. Values were averaged over the region bounded by 5°N–5°S and 180°–100°W. Five-day and (solid line) climatological values (1979–95; dashed line) are shown, as are positive (orange) and negative (blue) anomalies relative to the 1979–95 base period.**

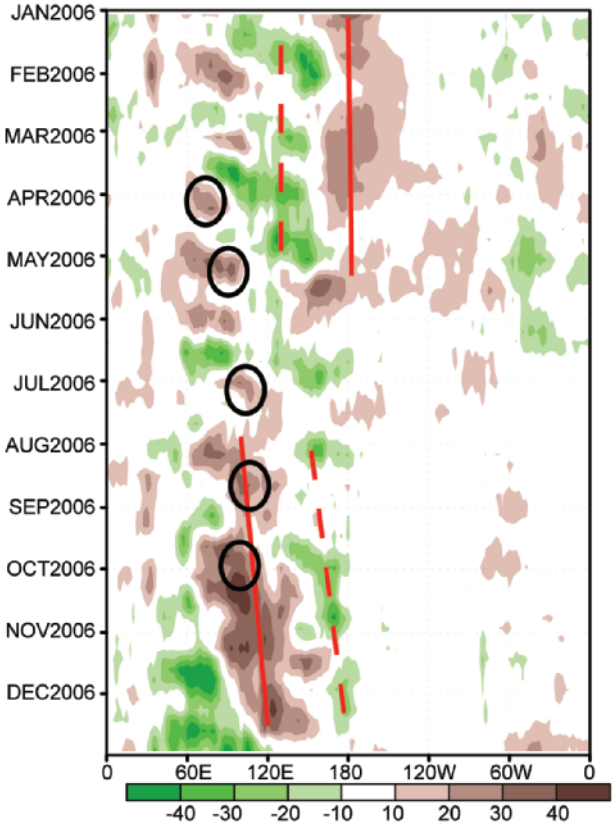


**Fig. 4.4. Time–longitude section of OLR anomalies (W m$^{-2}$) during 2006. Solid (dashed) red lines indicate main areas of suppressed (enhanced) convection. Black circles indicate suppressed convection associated with initiation of equatorial oceanic Kelvin waves. Anomalies are based on 5-day average values, and are departures from the 1979–95 base period pentad means. A 1–2–1 smoother was applied to the data.**

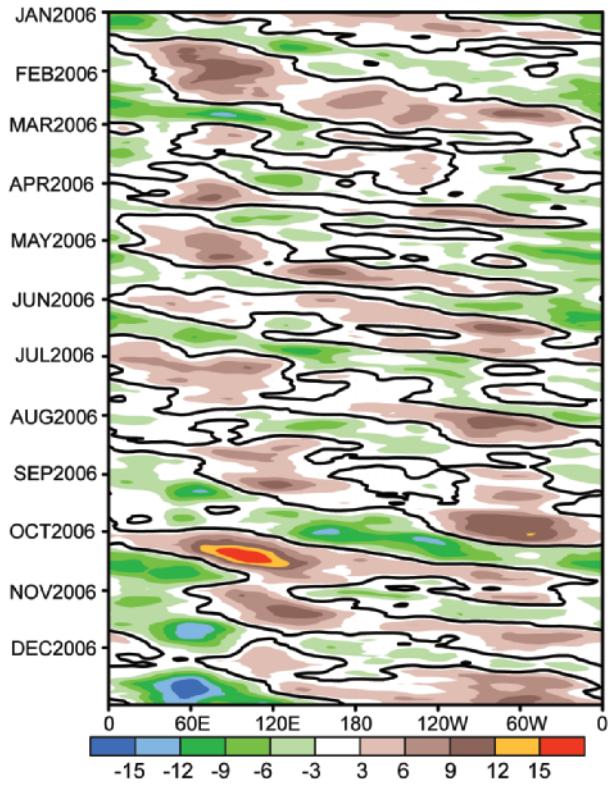


**Fig. 4.5 Time–longitude section (5°N–5°S) of daily 200-hPa velocity potential anomalies during 2006. The shading interval is 3 × $10^6$ $m^2$ $s^{-1}$, and the thick solid contour is the zero line. Green (brown) shading is indicative of anomalous upper-level divergence (convergence). Anomalies are departures from the 1971–2000 base period daily means, and are plotted using a 5-day running-mean smoother.**

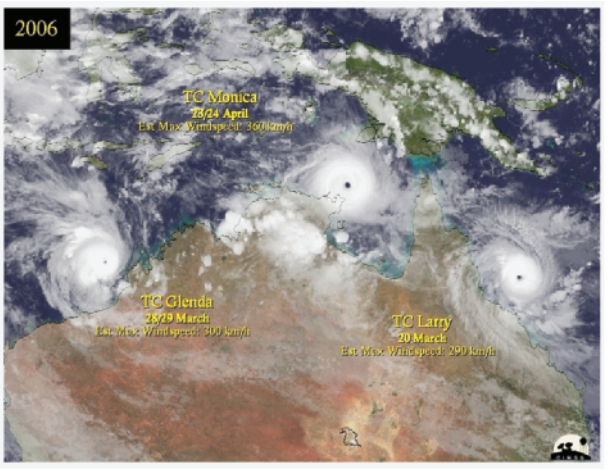


**Fig. 4.6. Satellite montage of Australian category 5 landfalling tropical cyclones. [Source: C. Velden, University of Wisconsin—Madison, CIMSS.]**

5 storms (Fig. 4.6), one of which was the strongest TC in Queensland since 1918, and one that was the strongest TC ever observed in the Northern Territory (see sidebar: An Australian Season of Extremes: Yes, We Have No Bananas).

2) Atlantic basin—G. D. Bell, E. Blake, C. W. Landsea, M. Chelliah, R. Pasch, K. C. Mo, and S. B. Goldenberg

The 2006 Atlantic hurricane season produced 10 TSs, five Hs, and two MHs [categories 3–5 on the Saffir–Simpson scale (Simpson 1974)]. These values are slightly below the 1950–2000 averages of 11 TSs, 6 Hs, and 2.5 MHs.

A widely used measure of seasonal activity is NOAA's ACE Index (Bell et al. 2000). The ACE Index accounts for the combined strength and duration of TCs during the season. The 2006 ACE Index was 90% of the 1950–2000 median value (87.5 × $10^4$ $kt^2$), indicating a near-normal season (Fig. 4.7). This value is well below the three previous seasons, which averaged 247% (Bell et al. 2005) and less than one-third of the record high (284%) seen in 2005 (Bell et al. 2006).

The reduced activity during 2006 reflects the competing influences of two dominant climate factors. The first dominant factor is El Niño, which suppressed activity during September and October through anomalous upper-level convergence and sinking motion across the Caribbean Sea. Anomalous circulation features not related to El Niño accentuated this signal at times, and also contributed to the reduced activity. The second dominant climate factor was the set of ongoing oceanic and atmospheric conditions that have been conducive to above-normal hurricane seasons since 1995, which remained strong during the climatological peak months ASO of the season.

El Niño's suppressing influence on Atlantic hurricane activity is well documented (Gray 1984; Tang and Neelin 2004; Bell and Chelliah 2006), and is clearly evident during the current active hurricane era that began in 1995. During 1995–2006, 9 of 12 hurricane seasons were in the above-normal tercile, defined as ACE larger than 117% of the median. The three exceptions are all El Niño years (1997, 2002, and 2006).

The large-scale El Niño signal during ASO 2006 is evident in the patterns of anomalous 200-hPa velocity potential and streamfunction. In the Tropics velocity potential anomalies are related to the upper-level divergent circulation and anomalous convection. Negative velocity potential anomalies across the central and east-central equatorial Pacific reflect the El Niño–related enhanced convection and anomalous

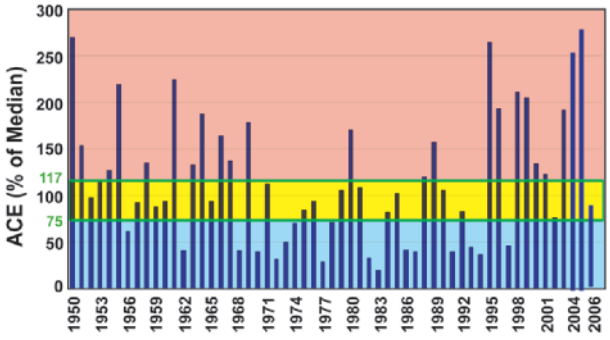


**Fig. 4.7. NOAA's ACE Index expressed as percent of the 1951–2000 median value ($87.5 \times 10^4$ kt$^2$). ACE is a wind energy index, and is calculated by summing the squares of the 6-hourly maximum sustained wind speed in knots (Vmax$^2$) for all periods while the system is a tropical storm, subtropical storm, or hurricane. Season types are indicated by the background shading, with pink, yellow, and blue indicating NOAA's classifications for above-, near-, and below-normal seasons, respectively.**

upper-level divergence. Positive values over both the western Pacific/Indonesia region and the Caribbean Sea reflect compensating anomalous upper-level convergence and suppressed convection. Another characteristic El Niño signature is anomalous upper-level ridges (positive streamfunction anomalies in the NH, and negative streamfunction anomalies in the SH) in the subtropics of both hemispheres flanking the region of enhanced convection over the central equatorial Pacific. However, this feature was not evident until October.

El Niño's typical impacts over the western tropical Atlantic Ocean and Caribbean Sea include increased vertical wind shear between 200 and 850 hPa and anomalous sinking motion in the middle and upper atmosphere. During ASO 2006, El Niño appears to have suppressed TC activity mainly by contributing to anomalous upper-level convergence and sinking motion across the Caribbean Sea. This suppressing influence was particularly notable during September and October, when only one TC developed over the Caribbean Sea despite low wind shear (< 8 m s$^{-1}$) (Fig. 4.8a) and anomalously warm SST. During September, the same conditions, but with no anomalous sinking motion, led to the formation of several hurricanes and major hurricanes over the central and eastern tropical Atlantic Ocean.

SST anomalies during ASO were positive throughout the North Atlantic (Fig. 4.9a). For the entire MDR, which encompasses the tropical Atlantic Ocean and Caribbean Sea (Goldenberg and Shapiro 1996), area-averaged SSTs during ASO were 0.68°C above average, the second warmest in the historical record dating back to 1871 (Fig. 4.9b). The reduced activity despite this anomalous warmth is consistent with previous findings, indicating that local atmospheric circulation anomalies, rather than local SST anomalies, are the dominant contributor to seasonal fluctuations in Atlantic hurricane activity (Shapiro and Goldenberg 1998; Bell and Chelliah 2006).

The vertical wind shear pattern during ASO 2006 primarily reflected anomalously weak shear (relative to the period 1971–2000) throughout the MDR in association with the ongoing active hurricane era (Fig. 4.8a). A modest El Niño–related increase in wind shear was evident over the western Caribbean Sea, but only when the departures are calculated relative to the current active era (Fig. 4.8b).

As with the 200-hPa streamfunction anomalies, there is little indication that El Niño affected the vertical wind shear prior to October. Even then, there is little evidence that the increased shear contributed to the shutdown in activity. For example, the main suppressing influence from strong vertical shear (> 8 m s$^{-1}$) occurred in August, prior to the time when El Niño began affecting this field. During September and October, the shear was quite weak across the Caribbean Sea, and was, therefore, not a suppressing factor.

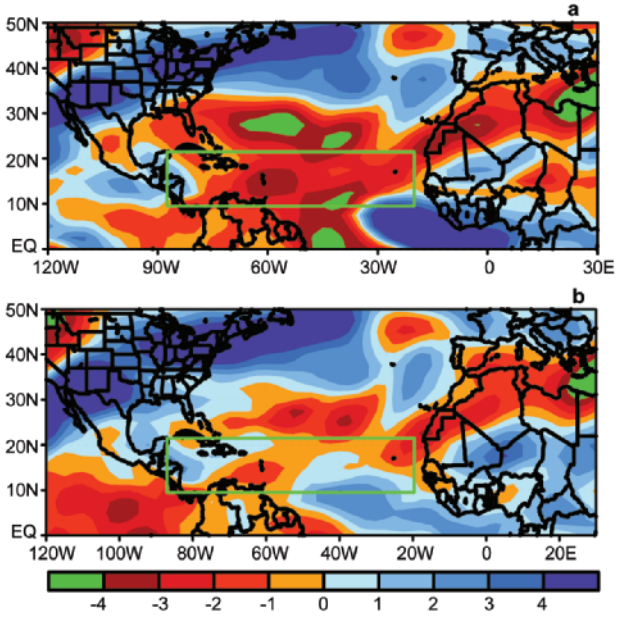


**Fig. 4.8. August–October 2006: Anomalous strength of the total 200–850 hPa vertical wind shear, calculated with respect to (a) the 1971–2000 and (b) the 1995–2005 period monthly means. Red shading indicates below-average strength of the vertical shear. Green box denotes the main development region.**

Although El Niño appears to be the primary cause for the reduced TC activity, highly variable circulation features not linked to El Niño also helped to suppress the activity. For example, during August increased vertical wind shear associated with an enhanced midoceanic trough led to reduced activity across the central MDR. During September, a deep trough near the U.S. east coast contributed to an anomalous sinking motion over the Gulf of Mexico. During October, an enhanced upper-level ridge over the south-central United States and western Gulf of Mexico contributed to the anomalous sinking motion over the Gulf of Mexico and accentuated the sinking motion over the Caribbean Sea. These conditions resulted in the third earliest end (following 1983 and 1993) to seasonal activity since routine daily satellite coverage began in 1966.

It is not clear why the El Niño signal was manifested mainly in the upper-level divergence and vertical motion fields, as opposed to the 200–850-hPa vertical wind shear, as is typical for most episodes. Also, while it is possible that the MJO (see section 4bii) may have accentuated the vertical motion patterns (e.g., Mo 2000), no such influence was evident during August and September. However, it is possible that the strong MJO signal in October contributed to the suppressed convection and lack of TC activity across the western Caribbean Sea in that month.

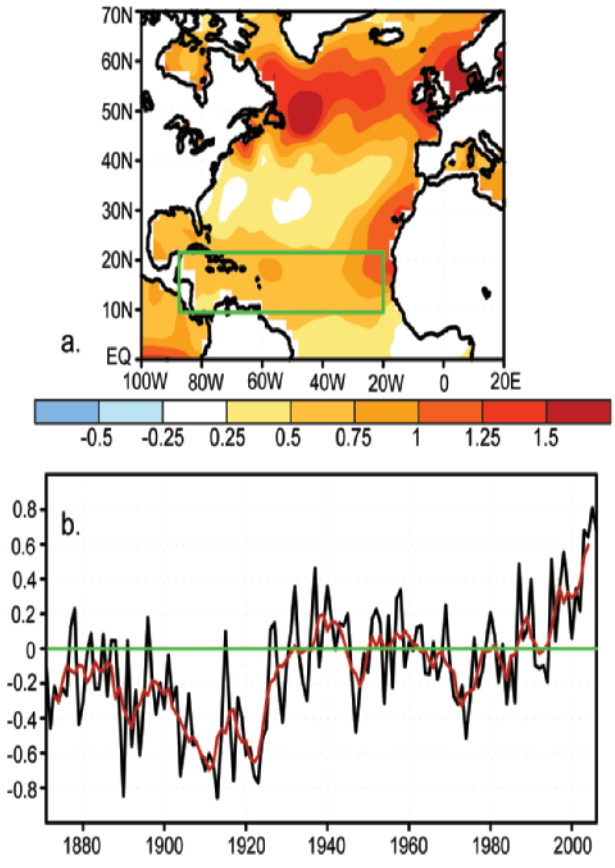


**Fig. 4.9. (a) SST anomalies (°C) during August–October 2006, and (b) time series of area-averaged SST anomalies for the main development region [green boxed region shown in (a)]. Red line in (b) shows the corresponding 5-yr running mean. Anomalies are departures from the 1971–2000 period monthly means.**

Only three Atlantic tropical storms—Alberto, Beryl, and Ernesto—struck the continental United States during 2006. Also, this was the first year since 2001 that no hurricanes struck the continental United States. This represents a sharp drop in strikes compared to the preceding four years (2002–05), when an average of seven named storms and three hurricanes per season struck the continental United States. In September (four of the five 2006 hurricanes formed in September), the deep trough near the U.S. east coast was critical in steering hurricanes out to sea long before they reached the coast. The overall suppression of activity over the western part of the Atlantic basin, in part resulting from El Niño, also contributed to fewer U.S. strikes.

Despite the reduced activity, key oceanic and atmospheric features continued to reflect the ongoing active Atlantic hurricane era. A main contributing factor to this active era is the tropical multidecadal signal, which reflects the leading modes of tropical convective rainfall variability occurring on multidecadal time scales (Bell and Chelliah 2006). The ongoing warm phase of the Atlantic multidecadal mode (Goldenberg et al. 2001), indicated by a continuation of above-average SSTs in the North Atlantic (Fig. 4.9b), is one important aspect of the tropical multidecadal signal. Some of this persistent anomalous warmth has also been linked to increasing global temperatures over the last 100 years (Santer et al. 2006).

Other very important and interrelated aspects of the tropical multidecadal signal and the ongoing active hurricane era that were also in place during 2006 included 1) an enhanced West African monsoon system (Landsea and Gray 1992) and suppressed convection in the Amazon basin, 2) enhanced upper-level ridges in both hemispheres over the Atlantic Ocean, 3) reduced wind shear across the tropical Atlantic (Fig. 4.10a), 4) an enhanced tropical easterly jet at 200 hPa and reduced tropical easterlies at 700 hPa across the tropical Atlantic (Fig. 4.10b), and 5) increased cyclonic relative vorticity across the eastern MDR (Fig. 4.10c). In light of these conditions, there is no indication that the current active hurricane era has ended. Instead, the El Niño–related re-

duction in activity merely represents a short-term break (similar to the 1997 and 2002 El Niño years) in an ongoing string of active hurricane seasons that began in 1995.

### 3) East Pacific basin—D. H. Levinson

*(i) Overview of the 2006 season*

The hurricane season in the ENP basin officially begins on 15 May and continues through the end of November, with peak activity occurring in September. The ENP basin includes two subregions officially used by NOAA/NWS to issue warnings: the east Pacific warning area extends from the western coast of North America to 140°W, which is the responsibility of NOAA's National Hurricane Center in Miami, Florida, while the region between 140°W to the date line is the responsibility of NOAA/Central Pacific Hurricane Center collocated at the NWS Weather Forecast Office in Honolulu, Hawaii.

In 2006, the hurricane season in the ENP was above normal, with a total of 18 NSs, 10 Hs, and 6 MHs having developed in the basin, which was above the 1971–2000 climatology of 16.4 NSs, 9.6 Hs, and 4.8 MHs each year. In terms of landfalling TCs, the 2006 season was also above average with two hurricanes making landfall along the Pacific coast of Mexico, and one of these as a major hurricane. Over the period 1951–2000, 1.34 TSs, 1.3 Hs, and 0.3 MHs annually made landfall along Mexico's Pacific coast each year (Jauregui 2003).

*(ii) Comparison of the 2006 season with climatology*

Seasonal activity in 2006 was above normal compared with the climatological mean for the majority of indices. Figure 4.11 shows the seasonal variability of TC activity in the ENP basin covering the period 1970–2006. In terms of the number of NSs, which is the total number of TCs that reached at least minimal

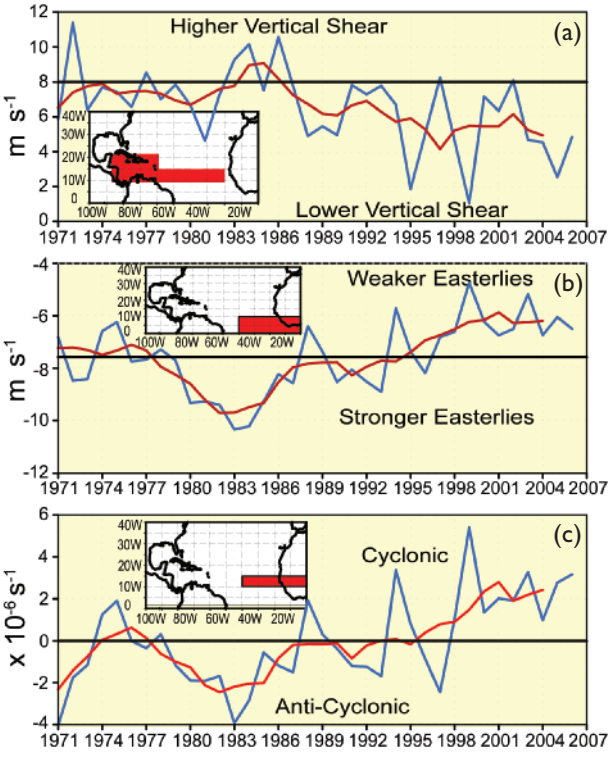


**Fig. 4.10. August–October seasonal time series showing area-averaged values for key regions of (a) magnitude of the 200–850-hPa vertical shear of the zonal wind (m $s^{-1}$), (b) 700-hPa zonal wind (m $s^{-1}$), and (c) 700-hPa relative vorticity (x $10^{-6}$ $s^{-1}$). Blue curve shows unsmoothed 3-month values, and red curve shows a 5-point running mean of the time series. Averaging regions are shown in the insets.**

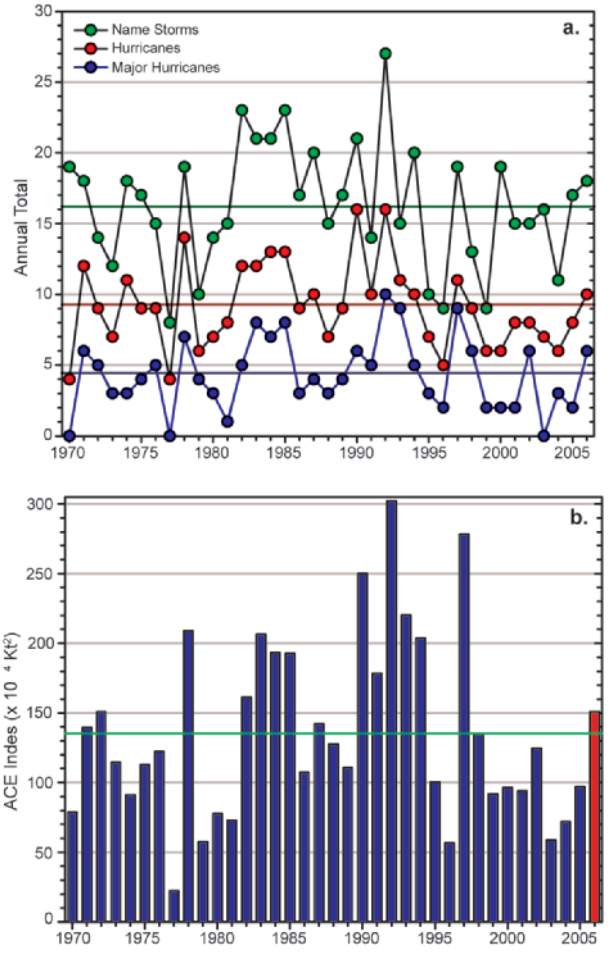


**Fig. 4.11. Seasonal tropical cyclone statistics for the east North Pacific Ocean over the period 1970–2006: (a) number of NSs, Hs, and MHs and (b) the ACE Index (x $10^4$ $kt^2$) with the seasonal total for 2006 highlighted in red. Both time series include the corresponding 1971–2000 base period means.**

tropical storm strength (sustained winds ≥ 34 kt), activity in the ENP basin has been near average since the mid-1990s, fluctuating between slightly above or below the long-term mean each year (Fig. 4.11a). However, in terms of H and MH, most seasons have been below normal since the mid-1990s. In fact, since 1995 NOAA has identified 7 of the 12 ENP seasons as being below normal, and only the 1997 and 2006 El Niño–influenced seasons as being above normal. This is in sharp contrast to higher activity seen during the preceding 1970–94 period, when only 6 of 24 (25%) hurricane seasons were below normal and 9 of 24 (38%) were above normal.

The ACE Index (Bell et al. 2000; Bell and Chelliah 2006) value for the ENP basin in 2006 was $150.68 \times 10^4$ kt$^2$, which was above both the long-term mean and median, and also at the upper end of NOAA's definition of a "near normal" season. Prior to the above-normal 2006 season, there had been a marked decrease in the ACE Index for the ENP basin beginning in 1995, with the only exception being the aforementioned 1997 hurricane season that corresponded with the last strong El Niño event in the Pacific Ocean. Another interesting aspect of the below-normal activity in the ENP since 1995 has been the inverse relationship to the observed increase in activity in the North Atlantic basin (Lander and Guard 1998), and the so-called Atlantic multidecadal mode (Landsea et al. 1998, 1999; Goldenberg et al. 2001; Bell and Chelliah 2006). Both the maximum wind speed and the mean maximum wind speed have had a slight decreasing trend in the last decade. More obvious has been the decrease in mean hurricane duration in the ENP basin, which was ~3.9 days in 2006, slightly below the 4–5 days during the most active years. The recent decade of low activity reached a minimum in 2003, and since that time there has been an increase in all indicators over the past three seasons.

In terms of the timing of activity in the ENP basin, the 2006 season was unusually slow to develop. After the formation of TS Aletta in late May, no named storms formed in June, which previously had only occurred once before (in 2004) during the period of reliable data. The below-normal activity continued into early July, because there were no TCs during the first half of the month; but, cyclogenesis increased dramatically during the second half of July as three hurricanes (MH Bud, H Carlotta, and MH Daniel) and one tropical storm (TS Emilia) developed. Above-normal activity persisted into August, with five hurricanes, three of which reached major hurricane strength (Ioke, Ileana, and John). Of note, MH Ioke, which officially developed in the central Pacific warning area, reached category 5 intensity and propagated westward past the date line into the West Pacific basin, becoming a super-TY during its life cycle. In September, one hurricane (Lane) and one tropical storm (Miriam) formed, as overall activity to this point of the season was near normal. However, both October and November were above average. Three named storms developed during October (TS Norman, TS Olivia, and H Paul), which normally has only two (on average 1 TS and 1 H), while November 2006 was the most active in the reliable historical record. Two named storms formed during the month (TS Rosa and H Sergio), and only in 1966 had there previously been two tropical storms during any November on record. The final TC of the season, H Sergio, was the most intense hurricane ever observed in November (category 2; maximum sustained winds ~95 kt) in the ENP basin, and it was also the longest-lived TC for the month, with a record 5.5 days at tropical storm strength or greater.

#### *(iii) Environmental influences on the 2006 eastern North Pacific hurricane season*

Previous studies have demonstrated that TC activity (both frequency and intensity) in the ENP basin is directly influenced by several large-scale environmental factors, including SSTs, vertical wind shear in the mid- and upper troposphere, the phase of the QBO in the tropical lower stratosphere, and the phase of ENSO in the equatorial Pacific region (Whitney and Hobgood 1997).

In 2006, above-normal vertical wind shear in the midtroposphere (200–850 hPa) was observed in the ENP basin during the first half of the season (June–August; see Fig. 4.12). Vertical wind shear anomalies exceeding 9 m s$^{-1}$ occurred in the ENP basin's MDR, which is the area between 10°–20°N and 90°–130°W off the coast of Mexico (green box in Fig. 4.12). Three-month-averaged wind shear anomalies exceeding 12 m s$^{-1}$ were also measured west of the Baja Peninsula. In addition to the increased vertical wind shear, the SSTs were near normal in the MDR during June and July, while warmer SSTs developed in August when an area from +0.5° to +1.0°C SST anomalies developed off the coast of the Baja Peninsula (Fig. 4.13). The situation changed dramatically during the latter half of the season, as the moderate El Niño formed in September; the midtropospheric wind shear anomalies weakened and SSTs increased in response to the developing warm event. As a result, warmer-than-normal SST anomalies persisted over the eastern half of the MDR during September and October (Fig. 4.13).

Variability of the tropical atmosphere on interannual time scales related to ENSO and the QBO has been shown to modulate seasonal activity, affecting both the intensity and frequency of TCs in the ENP basin (Whitney and Hobgood 1997). According to NOAA/National Hurricane Center, above-normal TC activity in the ENP basin typically occurs during El Niño years, while seasons with ENSO-neutral conditions tend to have less activity, and seasons with the lowest activity are typically associated with La Niña years. In contrast, utilizing data covering the period 1963–93, Whitney and Hobgood (1997) found only a marginal relationship between ENSO phase and ENP activity, although their results showed that TCs in El Niño years reach their maximum intensities slightly farther south and west than during non–El Niño years. Obviously, the strength and timing of the SST anomalies associated with ENSO warm events is an important aspect to this relationship. The moderate 2006/07 El Niño event developed during late August and early September, so the phase of ENSO was transitioning from a neutral to a warm event during the peak of the hurricane season, and was the major factor influencing the above-normal season in 2006.

*(iv) Impacts in 2006*

There were no landfalling tropical systems in the ENP during the first half of the season, although four systems impacted the Mexican coast (TS Aletta, TD 02E, H Daniel, and TS Emilia). Above-normal activity during the second half of the season in the ENP basin resulted in two landfalling hurricanes and rainfall impacts from the remnants of tropical storms.

The first landfalling hurricane of the season was MH John, which reached category 4 intensity before weakening and eventually making landfall at category 2 strength in southern Baja ~65 km northeast of Cabo San Lucas early on 2 September. John generated numerous impacts, including 280 mm of rain at San Jose de los Planes near the landfall location, the overflow of the Iguagil Dam in Comundu, coastal flooding in the Acapulco area, and an official total of five deaths directly attributed to the storm. Major Hurricane Lane came ashore at category 3 intensity with winds ~110 kt along the Peninsula de Guevedo in Sinaloa. Lane interacted with the coastal mountains, producing heavy rainfall, flooding, and mud-

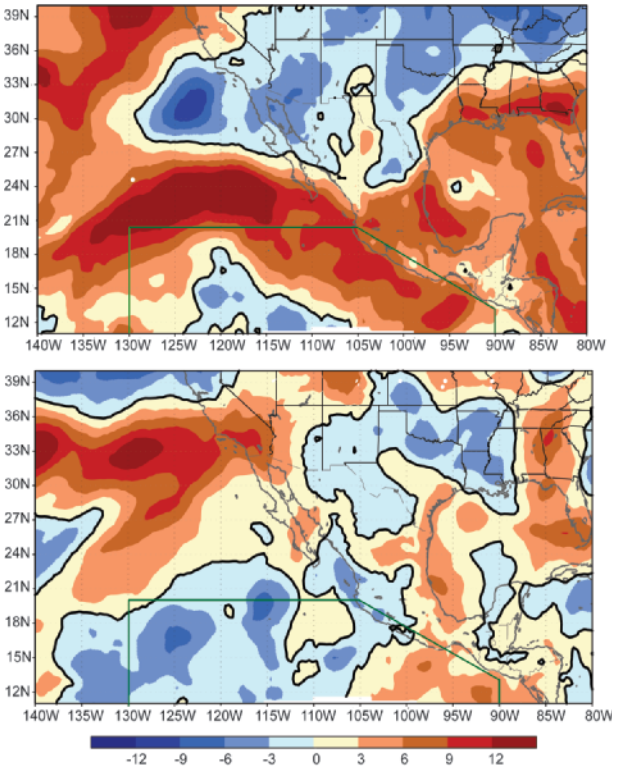


**Fig. 4.12. The 200–850 hPa vertical wind shear anomaly (m $s^{-1}$) averaged over the following periods: (top) June–August and (bottom) September–November 2006. The main development region for ENP hurricanes is the area delineated by the green polygon in both maps. [Source: NOAA NOMADS, NARR dataset, with anomalies determined relative to the 1979–2004 base period mean.]**

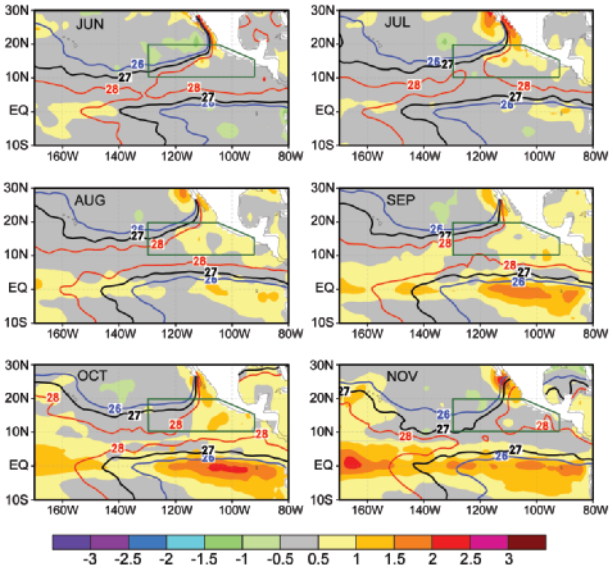


**Fig. 4.13. Monthly averaged SSTs calculated using NOAA's OI dataset (Reynolds and Smith 1994; Reynolds et al. 2002). Isotherms denote monthly averaged SSTs and shading represents SST anomalies (°C) for each month (June–November) of the hurricane season in 2006. The MDR for ENP hurricanes is the area delineated by the green polygon in each plot.**

slides over many areas along the Pacific Coast, with four fatalities directly attributed to this landfall. Hurricane Paul, which reached category 2 intensity on 23 October, resulted in four deaths associated with flooding.

#### 4) Western North Pacific basin—S. J. Camargo

In 2006, a total of 27 TCs (including 3 TDs) occurred in the western North Pacific. This was below the climatological (1970–2004) median of 31, matching the 25th percentile of the climatological distribution. In Fig. 4.14a the number of TSs, TYs, and super-TYs per year is shown. There were 24 TCs reaching TS intensity or higher, according to the JTWC preliminary reports, but two of them were not named (01W and 17W). The climatological median for NSs: TSs and TYs is 26; 24 NSs also match the 25th percentile of the climatological distribution. There were 15 TYs in 2006, which is slightly below the climatological median of 16. In contrast, the number of super-TYs in 2006 (7) was in the top quartile of the climatological distribution (median is four, 75th percentile is five). A high number of intense TYs is typical during El Niño years in the western North Pacific (Camargo and Sobel 2005). Since 1970, when the data are more reliable, only two other years had more super-TYs than in 2006, and they occurred in 1997 and 2002, both of which were El Niño years. Another typical characteristic of El Niño years is an above-normal occurrence of central Pacific hurricanes (Chu and Wang 1997; Clark and Chu 2002), with some of the central Pacific hurricanes moving into the western North Pacific, as was the case with H/super-TY Ioke in 2006.

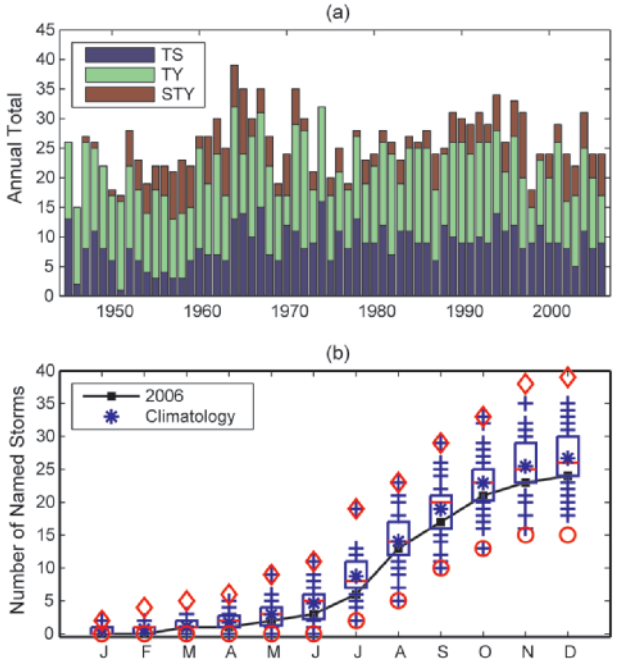


**Fig. 4.14. (a) Number of tropical storms, typhoons, and supertyphoons per year in the western North Pacific for the period 1945–2005. (b) Cumulative number of tropical storms with tropical storm intensity or higher per month in the western North Pacific: 2006 (black squares and line), and climatology (1970–2004) shown as box plots [interquartile range: box, median: red line, mean: blue asterisk, values in the top or bottom quartile: blue crosses, high (low) records in the 1945–2005 period: red diamonds (circles)]. [Source: 1945–2004 JTWC best-track dataset, 2005/06 JTWC preliminary operational track data.]**

The cumulative number of TCs per month climatologically and in 2006 are shown in Fig. 4.14b. The 2006 western North Pacific TC season started slowly in March with a TC that reached TS intensity (01W), but was given no name. The next TC (Chanchu) occurred in May and reached super-TY (≥ 130 kt maximum sustained winds) intensity. Tropical cyclone activity continued to be below normal in June and July, with one and three TCs, respectively, placing that period in the bottom quartile of the 1970–2004 climatological distribution for those months. In contrast, August was a very active month with eight TCs, which is slightly above the 75th percentile of the distribution of seven; four of these reached TY intensity, and two became super-TYs (Saomai and Ioke). September and October had a normal level of TCs, with five and four TCs, respectively, equal to the median of the climatological distribution for those months. November and December had two TCs, corresponding to the 25th and 75th percentiles of the climatological distribution for those months, respectively. The cumulative distribution (Fig. 4.14b) shows a slightly below-normal season throughout the year.

The ACE Index (Bell et al. 2000) was slightly above the climatological median in 2006, in spite of the low number of TCs, because of the high number of intense TYs in 2006 (see Fig. 4.15a). The seven super-TYs contributed to 64% of the ACE of the 2006 season; the largest contribution was from the very long lasting super-TY Ioke, which provided 17% of 2006 ACE and had the 15th highest ACE per storm value (in the top one percentile) of the historical record. The 2006 ACE per month is shown in Fig. 4.15b compared with the 1970–2004 climatology. In the months of May and September, values of ACE were in the top quartile of the climatology, due to the occurrence of super-TYs Chanchu (May), Ioke (August–September), and Yagi (September), and TYs Shansha and Xangsane (September).

The number of days with TCs that reached TS intensity or higher in 2006 was 132.25 (based on preliminary JTWC data), which was below the climatological median of 159 days, but slightly above the 25th percentile of the climatological distribution (128 days). There were 75.5 days with TYs in 2006, which was above the climatological median of 57.25 days, and very near the 75th percentile of the 1970–2004 distribution (76.4 days). There were 32.75 days with intense TYs (with sustained winds ≥ 96 kt) in the top quartile of the climatological distribution (75th percentile is 27.1 days). Figure 4.16 shows a scatterplot of the number of days with intense TYs and the Niño-3.4 index (Barnston et al. 1997) for July–October; note that for higher values of the Niño-3.4 index (El Niño years) there is a tendency for more days with intense TYs, as discussed in Camargo and Sobel (2005). Another typical characteristic of El Niño years is a tendency for long-lived TCs (Wang and Chan 2002; Camargo and Sobel 2005). In 2006, 7 of the 24 named TCs' lifetimes were longer than the median of the climatological distribution of 7.25 days. One super-TY, Ioke, had a very long lifetime of 16.25 days, which is in the top quartile of the climatological lifetime distribution. There were, however, many short-lived named TCs in 2006, nine of which had lifetimes in the bottom quartile of the climatological lifetime distribution.

A well-known influence of ENSO on western North Pacific TC activity is a southeast (northwest) shift of the mean genesis location within the region in El Niño (La Niña) years (e.g., Chan 1985; Chia and Ropelewski 2002). In 2006, the mean average genesis position of the NSs was 13.9°N, 139.8°E, which is slightly northwest of the climatological mean genesis position (12.8°N, 143.2°E; standard deviations: 1.9° latitude, 6.6° longitude). Therefore, the typical southeast shift of genesis in El Niño years did not occur in 2006. However, the mean track position of NSs was 18.8°N, 131.2°E, which is slightly east of the climatological mean position (19.0°N, 134.1°E), largely due to the contribution of the long-lived Ioke, with a track starting in the central Pacific.

The 2006 El Niño started late and was not very strong, attaining moderate strength in November after the peak TY season. Therefore, its influence on the TY season was not typical. In Fig. 4.17a the SST anomalies in the months of July–October (when the peak TY season occurs) are shown with a slightly positive SST anomaly in the central Pacific region.

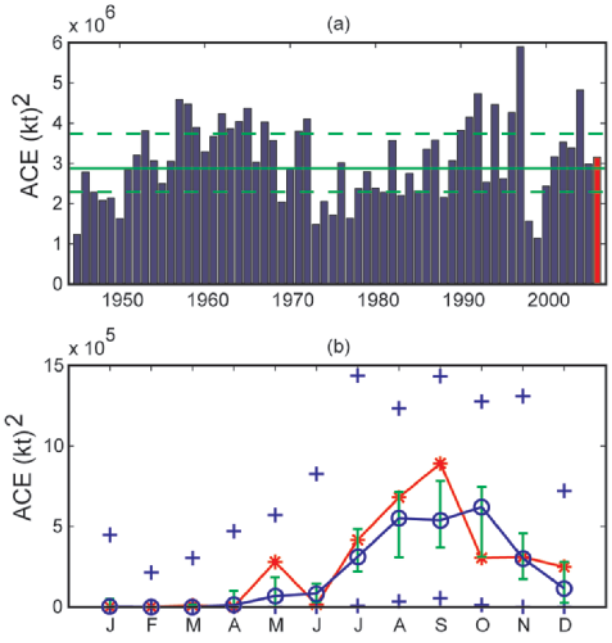


**Fig. 4.15. (a) ACE Index (x $10^4$ $kt^2$) per year in the western North Pacific for the years 1945–2006. The solid green line indicates the median for the 1970–2004 climatology, and the dashed green lines show the 25th and 75th percentiles. (b) ACE Index per month in 2006 (red line) and the median in the years 1970–2004 (blue line), where the green error bars indicate the 25th and 75th percentiles. In the cases of no error bars, the upper and/or lower percentiles coincide with the median. The blue plus signs (+) denote the maximum and minimum values during the period 1945–2006.**

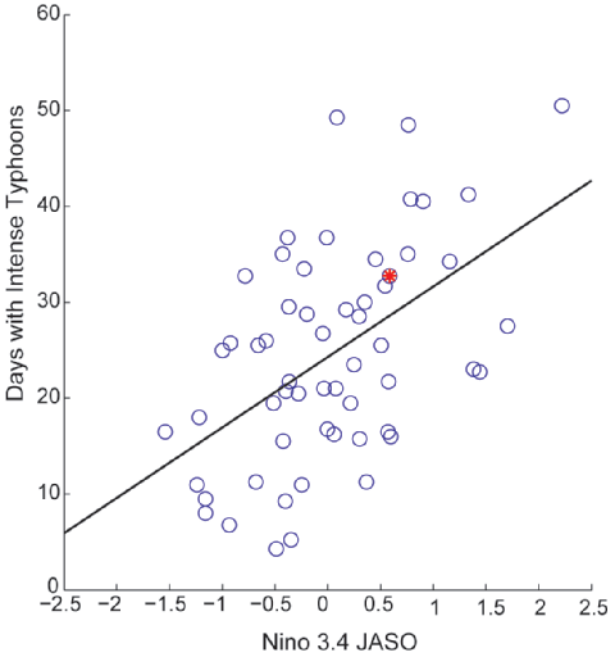


**Fig. 4.16. Scatterplot of number of days with intense typhoons and Niño-3.4 index (°C) for JASO in the period 1950–2006; the black line is the linear regression, the number of intense typhoons for 2006 is marked in red (r = 0.52).**

As shown in Chan and Liu (2004), the western North Pacific TY activity does not have a relationship with local SSTs. However, there is a relationship with large-scale dynamics associated with El Niño events, such as the extension of the low-level anomalous westerlies from the monsoon trough. In strong and typical moderate El Niño events, the anomalous westerlies extended throughout the western North Pacific (see, e.g., Camargo et al. 2007). In 2006, however, the anomalous westerlies were present just west of 150°E (Fig. 4.17b). There was no TC genesis in 2006 east of 150°E, with exception of TYs with more subtropical genesis locations and Ioke, with a genesis location in the central Pacific (Chan 2007).

Some interesting events occurred in the 2006 TY season. Super-TY Chanchu (8–18 May) attained that status in the South China Sea, a rare occurrence, with only two other TCs reaching that intensity in the area before: Ryan (1995) and Sally (1996). Chanchu was also the earliest system to become a super-TY in the South China Sea (Padgett 2007). Super-TY Saomai (4–14 August) made landfall in eastern China, and was the strongest TY to make landfall in China in the modern record (Padgett 2007). Super-TY Saomai, TS Bopha (6–10 August), and TY Maria (5–9 August) coexisted in the western North Pacific, contributing to a very busy month of August in the basin. Tropical storms Wukong (12–19 August) and Sonamu (13–16 August) formed in a large monsoon gyre. The monsoon gyre is an episodic event, occurring approximately once a year and lasting from two to three weeks, and often TCs are produced in the eastern periphery of the gyre (Lander 1994). Wukong and Saomai underwent a binary interaction, and the stronger Wukong absorbed Sonamu, similar to the case described in Lander (1995). The strongest TC in 2006 was super-TY Yagi, which did not affect any major land areas.

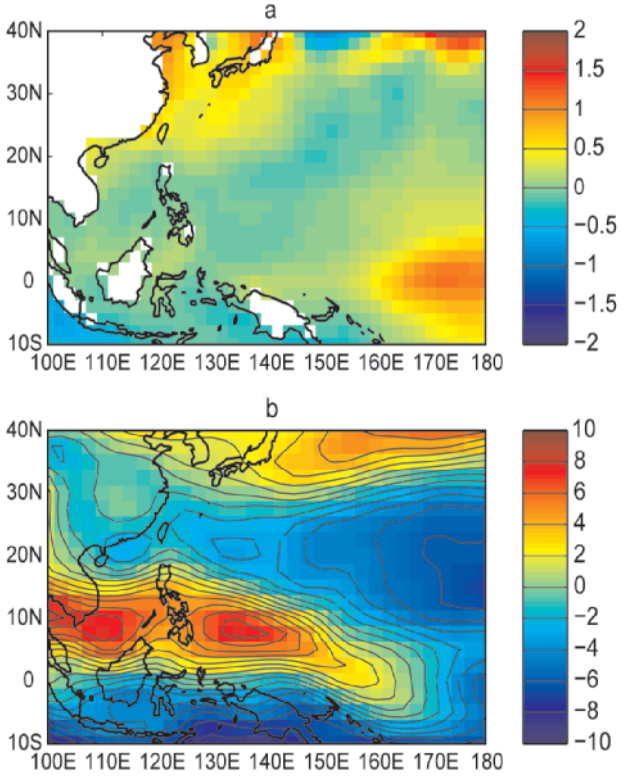


**Fig. 4.17. (a) SST anomalies (°C) from July to October of 2006. (b) Anomalous 850-hPa zonal winds (m $s^{-1}$) from July to October of 2006.**

The 2006 western North Pacific TY season was responsible for many fatalities and economic losses, primarily in the Philippines and China, with eight and four landfalls, respectively. Other countries affected by TCs in the 2006 season were Vietnam, Taiwan, Japan, and South Korea. Bilis (8–15 July), though only reaching TS intensity, was responsible for 672 deaths in China and over $2.5 billion (USD) in economic losses due to very heavy rain, flooding, and landslides. Bilis was soon followed by TYs Kaemi (8–16 July) and Prapiroon (28 July–5 August), which also struck China and caused more economic losses and resulted in over 100 deaths. Typhoon Xangsane (25 September–2 October) had significant impacts in the Philippines, where strong winds and heavy rainfall led to numerous mudflows and the death of over 200 people, before striking Vietnam where 71 deaths were reported. Typhoons Cimaron (26 October–6 November), Chebi (8–14 November), Durian (24 November–5 December), and Utor (7–14 December) all made landfall in the Philippines. Typhoon Durian was responsible for at least 720 deaths resulting from mudslides of volcanic ash, which covered houses in a large portion of Legazpi City.

### 5) Indian Ocean basins—K. L. Gleason

#### *(i) North Indian Ocean (NIO)*

The NIO TC season extends from April to December, with two peaks in activity during May–June and again in November when the monsoon trough is climatologically positioned over tropical waters in the basin. Tropical cyclones in the NIO basin develop in the Bay of Bengal and the Arabian Sea typically between 8° and 15°N latitude and are usually short lived and weak, quickly moving into the subcontinent. However, strong and "severe cyclonic storms,"[5] as

[5] The Bangladesh supercyclone of 1970 produced perhaps the greatest human fatality toll on record from a TC, where at least 300,000 people died, primarily from the associated storm surge in the low-lying deltas (Holland 1993).

illustrated by Neumann et al. (1993), can develop with winds greater than 130 kt.

Using reliable records from 1981 to 2000, a mean of nearly five NSs (sustained winds ≥ 34 kt), 1.6 TCs (sustained winds ≥ 64 kt), and one MTC (sustained winds ≥ 96 kt) form each year in the NIO. The 2006 TC season was near average with five NSs, one TC, and one MTC forming from January to December (Fig. 4.18a). Regarding the overall level of TC activity, the estimated ACE Index for the NIO basin in 2006 was nearly $14 \times 10^4$ kt$^2$, which was less than the 1981–2000 mean of $17 \times 10^4$ kt$^2$ (Fig. 4.18b). In fact, the annual ACE values in the NIO over the past seven years have all been below average, indicating a period of decreased activity. This most recent period of below-normal activity followed four active TC seasons with above-average ACE values during the late 1990s (Fig. 4.18b).

Severe TC Mala was the only TY-strength storm to form during 2006. Mala developed off the western tip of Sumatra on 24 April and tracked northwest into the central Bay of Bengal. By 25 April, Mala had intensified into the equivalent of a category 1 TC on the Saffir-Simpson scale and began to accelerate to the northeast. TC Mala continued to intensify over the next several days and with winds speeds over 185 km h$^{-1}$ (115 kt) on 28 April, attained peak intensity, and became the first major cyclone in the NIO since 2001. Shortly after attaining peak intensity, MCYC Mala weakened somewhat before making landfall over Myanmar on 29 April. The hardest hit area was near Yangon, with more than 100 buildings and numerous power lines damaged by the strong winds. Extreme storm surge and large waves caused severe structural damage. Heavy rainfall associated with Mala also caused flooding, which resulted in at least 22 fatalities in this region.

*(ii) South Indian Ocean*

The TC season in the SIO is typically active from December through April and officially extends from July to June, spanning across parts of two calendar years. The SIO basin extends south of the equator from the African coastline to 105°E, although most cyclones develop south of 10°S latitude. Cyclones in the SIO that remain east of 105°E are included in the Australian summary (see section 4c7). The vast majority of SIO landfalling TCs impact Madagascar, Mozambique, and the Mascarene Islands, including Mauritius. Due to a lack of historical record keeping by individual countries and no centralized monitoring agency, the SIO is probably the least understood of all TC basins (Atkinson 1971; Neumann et al. 1993). As a result of the disparate nature of the data in this region, the SIO historical statistics presented are incomplete, especially prior to the late-1970s.

Using reliable data from 1981 to 2000, the SIO averages 11.9 NSs, 6.2 TCs, and 2.8 MTCs each year. During the 2005/06 season (July 2005–June 2006), the SIO TC occurrences were below average with 9 NSs, 3 TCs, and 3 MTs (Fig. 4.19a). The estimated ACE Index for the SIO during 2005/06 was 55 $\times 10^4$ kt$^2$, which is slightly more than half of the 1981–2000 average of $107 \times 10^4$ kt$^2$ (Fig. 4.19b). The SIO ACE Index values over the last three years were below average and the 2006 ACE value was the fifth lowest value since 1980. During the 2005/06 season, the strongest TC in the SIO was MTC Carina with 130-kt sustained winds.

The first major TC in the southeast Indian Ocean formed east of 90° during mid-November 2005 and

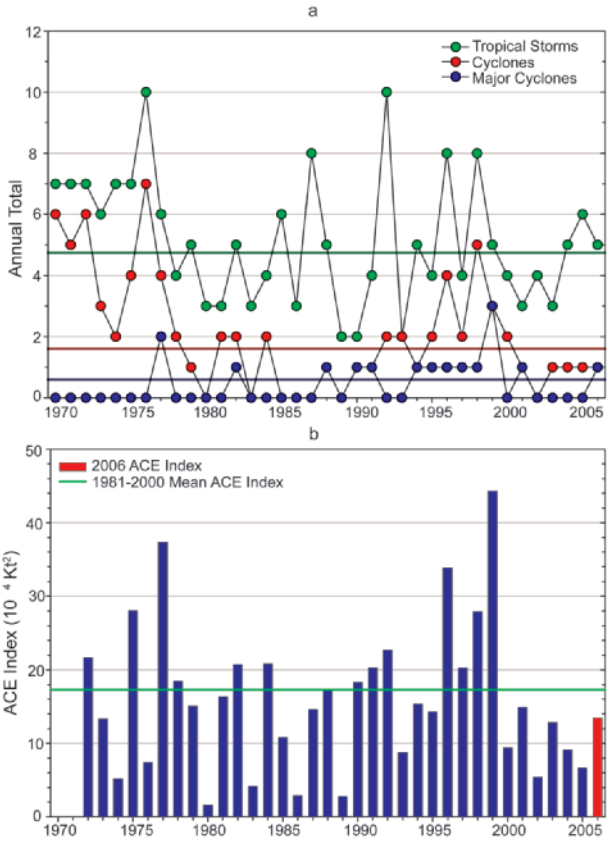


**Fig. 4.18. Annual tropical cyclone statistics for the North Indian Ocean over the period of 1970–2006: (a) number of tropical storms, cyclones, and major cyclones, and (b) the estimated annual ACE Index (x $10^4$ kt$^2$) for all tropical cyclones during which they were at least tropical storm or greater intensities (Bell et al. 2000). The 1981–2000 base period means are included in both (a) and (b). Note that the ACE Index is estimated due to a lack of consistent 6-h sustained winds for every storm.**

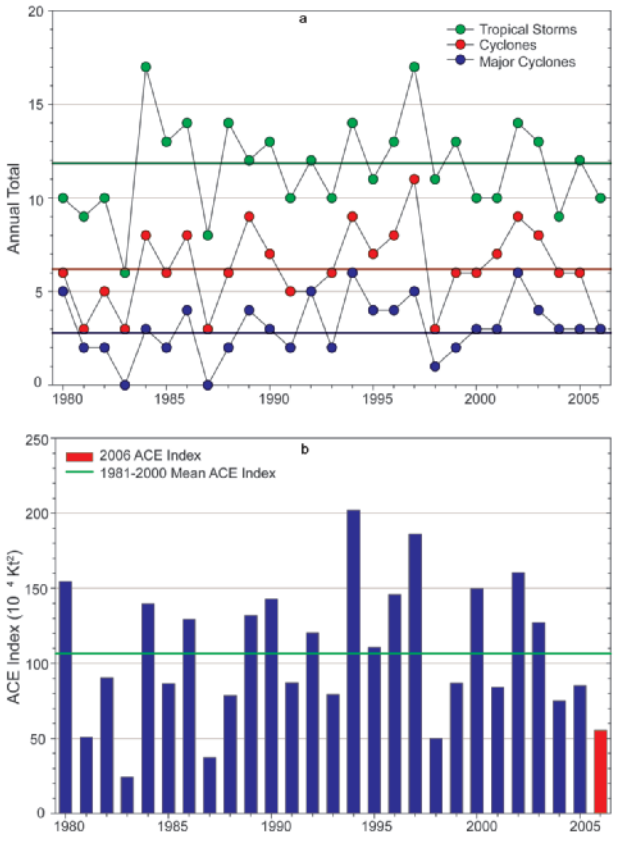


**Fig. 4.19. Same as Fig. 4.18, but for TCs in the South Indian Ocean over the period 1980–2006.**

was named Bertie. This storm gradually strengthened and was classified as a severe TC on 21 November. By the 23 November, Bertie entered the southwest Indian Ocean and was renamed Alvin. That same day, Bertie/Alvin reached peak intensity of 115 kt, which is the equivalent of a weak category 4 TC. The storm weakened shortly after attaining peak intensity and dissipated by the end of the month.

TC Boloetse formed off the eastern coast of Madagascar during late January 2006. Boloetse intensified into a tropical storm with sustained winds of 50 kt before making landfall near the village of Mananjary on 29 January. After crossing the island, Boloetse remerged and reorganized in the Mozambique Channel. Gaining intensity, this storm reached a peak intensity of 100 kt in early February, the equivalent of a category 3 cyclone on the Saffir–Simpson scale. Eventually, CYC Boloetse tracked southwest of Madagascar before it transitioned to being extratropical. Boloetse was the only TC that made landfall during the 2005/06 season.

The most intense TC in the SIO during the 2005/06 season was MTC Carina, which attained peak sustained winds of 130 kt. Carina developed in late February 2006 southeast of Diego Garcia in the central Indian Ocean and quickly strengthened into a moderate tropical storm. While remaining over open waters and among favorable conditions for development, Carina deepened and became a MTC as it moved to the southwest. On 28 February, MTC Carina neared category 5 strength on the Saffir–Simpson scale as it reached a peak intensity of 130 kt. Shortly after attaining this intensity, the storm entered an unfavorable environment with high wind shear and began to dissipate.

### 6) Southwest Pacific basin—M. J. Salinger and S. M. Burgess

The southwest Pacific experienced nine occurrences (east of 150°E) of TCs during 2006, equal to the average number normally expected for the region in a year (Fig. 4.20). There was also one occurrence that originated adjacent to the region, just west of 150°E. Many of the seasons' occurrences affected the region west of the date line, with the highest frequency of occurrences in the Coral Sea since at least 1999/2000 (Fig. 4.21). This was consistent with weak La Niña conditions in early 2006. There was an even spread of TCs throughout the period from January to March, and the most severe portion of the season was in April. Above-average SSTs combined with enhanced convection over the Coral Sea, and assisted in the development of TCs in that area of the basin. Seven of the southwest Pacific basin TCs (71%) reached H strength (sustained wind speeds of at least 118 km $h^{-1}$), and three major hurricane strength (sustained wind speeds of at least 168 km $h^{-1}$).

TC Tam was the first TC of the season, which occurred north of Fiji on 12 January, and tracked toward Tonga on 13 February, to pass west of Niue, with gale force winds. Urmil occurred on 15 January, and tracked well south of Niue with maximum sustained winds of 85 km $h^{-1}$. TC Jim occurred next, with sustained wind speeds of at least 155 km $h^{-1}$ (hurricane force). Jim was located in the

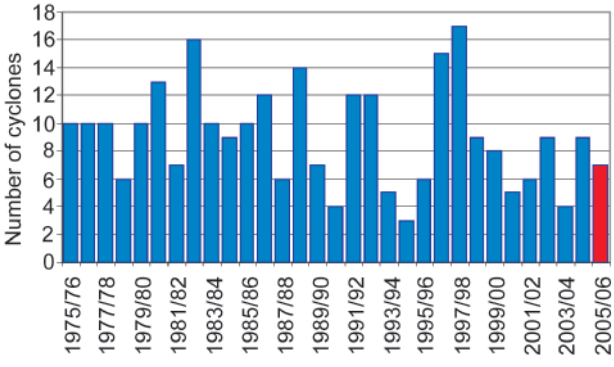


**Fig. 4.20. The number of southwest Pacific TCs for the 2005/06 season (solid red bar) compared to frequencies during the past 30 yr. For the 2006 calendar year there were nine.**

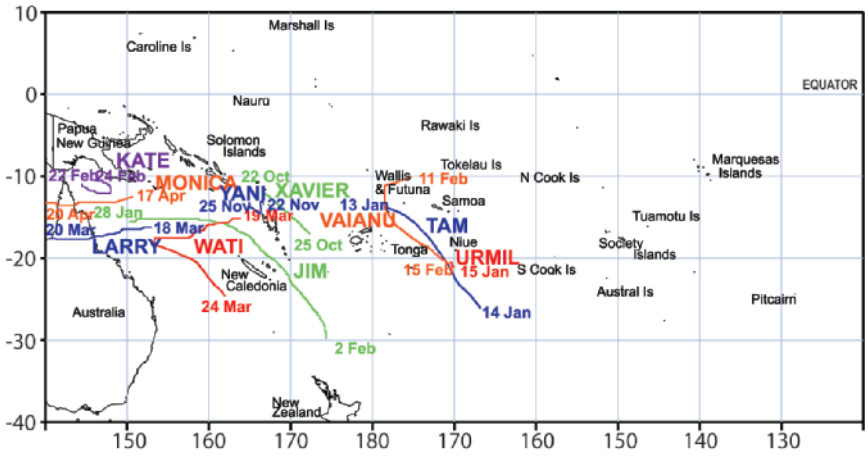


**Fig. 4.21. Southwest Pacific TC tracks for the 2005/06 season (including Monica).**

Coral Sea on 28 January, and later tracked southeast to pass between New Caledonia and Vanuatu. A mean speed of 154 km $h^{-1}$ (H force) was noted at Pekoa in northern Vanuatu on 31 January. TC Vaianu from 11 to 15 February produced sustained wind speeds of 140 km $h^{-1}$. Vaianu affected open waters near the Wallis and Futuna and Tongan Islands. TC Kate occurred from 24 to 25 February with sustained wind speeds of 90 km $h^{-1}$. Kate was fairly localized, occurring over the Coral Sea south of Papua New Guinea. The TCs in March were Larry (18–20 March) (see section 7) and Wati (19–24 March). TC Wati affected the open waters west of Vanuatu and New Caledonia, with estimated maximum wind speeds of 150 km $h^{-1}$. TC Monica (see section 7) was the last to affect the southwest Pacific in mid-April.

The 2006/07 season commenced unusually early, consistent with El Niño conditions later in the year, on 22 October. While not part of the TC season described in this section, we note that two named TCs for the 2006/07 season occurred prior to the end of calendar year 2006. TC Xavier occurred from 22 to 25 October, with estimated maximum sustained wind speeds reaching 215 km $h^{-1}$, and TC Yani from 22 to 25 November had estimated maximum sustained wind speeds of 120 km $h^{-1}$. Both occurred between the Solomon Islands and Fiji.

#### 7) Australian basin—A. B. Watkins

Weak La Niña–like conditions in the equatorial Pacific Ocean and warmer SSTs off the northern and eastern coasts of Australia contributed to the slightly above average 2005/06 TC season. A total of 12 TCs occurred in the Australian region between 105° and 160°E, 2 more than the long-term average of approximately 10. However, 3 of these 12 reached category 5 on the Australian scale, with TC Larry being the strongest cyclone to make landfall in Queensland since 1918, and TC Monica the strongest TC ever observed in the Northern Territory region. In the western Australian/Indian Ocean sector, seven TCs were recorded as follows: Bertie (category 4), Clare (3), Daryl (2), Emma (1), Floyd (4), Glenda (5), and Hubert (2); and in the Queensland/Pacific sector, Jim (3), Kate (2), Larry (5), and Wati (3); and in the Queensland and Northern Territory region: Monica (5).

For more information on the category 5 TCs in the Australian basin (Larry, Monica, and Glenda), please see the "An Australian Season of Extremes" sidebar.

### *d. Intertropical convergence zones*

#### 1) Pacific ITCZ—A. B. Mullan

Three convergence zones can be identified in the Pacific: the ITCZ in the NH at around 5°–10°N; its Southern Hemisphere counterpart, denoted separately here as SITCZ; and the SPCZ, which extends diagonally from around the Solomon Islands (10°S, 160°E) to near 30°S, 140°W. The SITCZ only occasionally extends eastward of about 160°W, and west of this point often merges with the SPCZ, making it difficult to separate the two features in the southwestern Pacific.

The year 2006 saw a weak La Niña event end in the first few months, followed by the development of a moderate El Niño by mid-September that peaked at the end of the year. La Niña conditions in March–April are known to promote the appearance of a "double ITCZ" (Lietzke et al. 2001; Zhang 2001), and Fig. 4.22 shows a striking example of this. The SITCZ convection for March 2006 is continuous from 85°W to west of the date line, is stronger than a rather broken northern ITCZ, and shows a clear separation from a weak SPCZ farther south. Similar convection patterns are evident in TRMM rainfall data for March 1999 and 2000 (also La Niña periods), although in those years the separation from the SPCZ is not as marked. As noted by Gu et al. (2005), there appears to be some competition between the two ITCZs as measured by rainfall, and the northern ITCZ is weaker at this time than the prominent SITCZ.

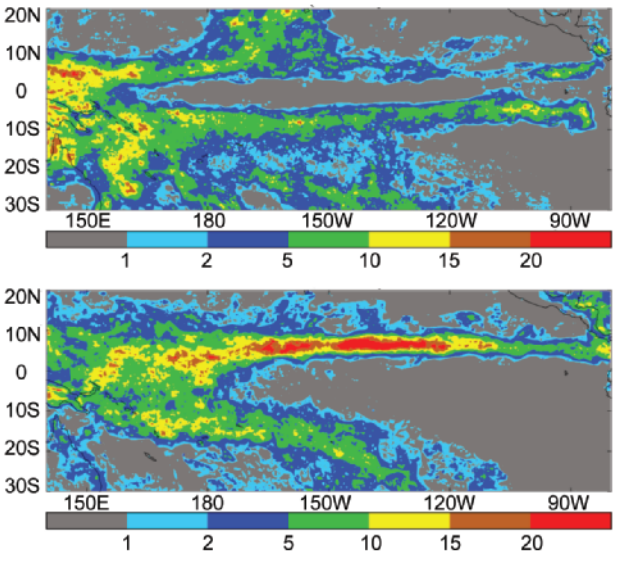


**Fig. 4.22. Average rainfall rate (mm day$^{-1}$) from TRMM 0.25° analysis for months of March (upper panel) and December (lower panel) 2006. Contours at uneven spacing of 1, 2, 5, 10, 15, and 20 mm day$^{-1}$.**

A more typical two–convergence zone pattern is seen in the rainfall rate for December 2006 (Fig. 4.22, lower panel). A prominent ITCZ is particularly active east of the date line, and the SPCZ is bowed northward near 150°W, both features characteristic of El Niño conditions. For the year as a whole, the TRMM rainfall data suggest that rainfall was close to the 1999–2005 average over much of the tropical Pacific, with the exception of enhanced convection in the SITCZ region. (See section 6hiii for further information on the SPCZ.)

The seasonal progression of convection through 2006 is shown in Fig. 4.23, where area-averaged rainfall rates have been calculated for the following three convergence zone regions: ITCZ (0°–15°N, 150°E–90°), SITCZ (0°–10°S, 150°–80°W), and SPCZ (0°–30°S, 150°E–90°). These boundaries are chosen after examination of the data to avoid the complications of the merging ITCZ and SPCZ in the far western tropical Pacific, and the orographic rainfall over Central America near 80°W. The SITCZ region is limited to the east of 150°W, even though at rare times (Fig. 4.22) the southern ITCZ is distinct from the SPCZ west of this point. In calculating the SPCZ area-averaged rainfall, the rainfall within the SITCZ part of the domain is set to zero. To place all three quite different domains on a more equal footing, the monthly area averages are normalized by the 1999–2005 annual average for each region. Thus, Fig. 4.23 shows both the climatological annual cycle (dotted lines) and the monthly progression during 2006 for comparison. Note that although the

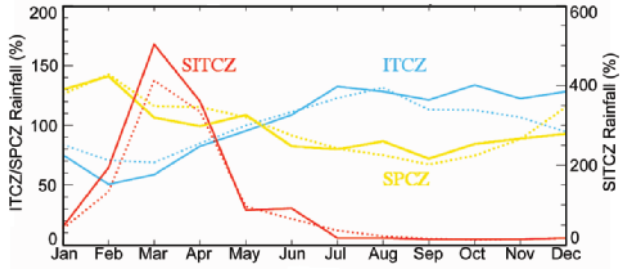


**Fig. 4.23. Area-averaged TRMM rainfall for the three convergence zone regions: ITCZ, 0°–15°N, 150°E–90°; SITCZ, 0°–10°S, 150°W–80°W; SPCZ, 0°–30°S, 150°E–90° (but excluding the SITCZ region). Monthly values are expressed as percentages of the 1999–2005 annual average. Solid lines show 2006 variation, and dotted lines the average variation over 1999–2005. Note the different ordinate scale (right-hand axis) for SITCZ.**

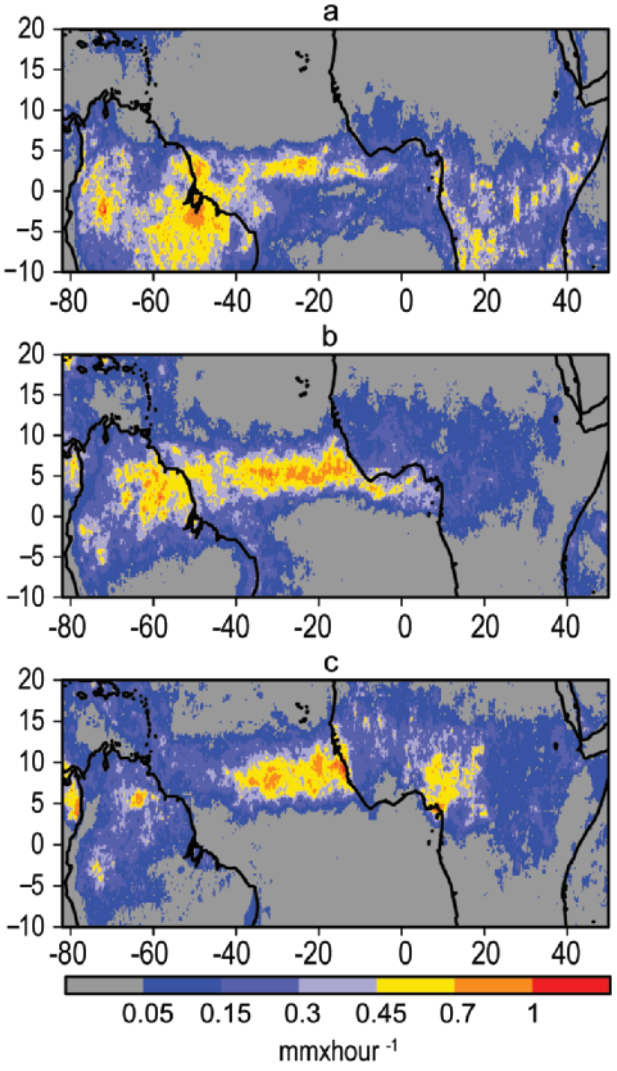


**Fig. 4.24. Average rainfall rate (mm h$^{-1}$) from high-resolution (0.25° latitude × 0.25° longitude) TRMM analysis for (a) April, (b) June, and (c) August 2006.**

## AN AUSTRALIAN SEASON OF EXTREMES: Yes, We Have No Bananas—

A. B. Watkins, H. J. Diamond, and B. C. Trewin

The 2005/06 TC season in Australia was only slightly above average when judged by TC frequency. When viewed in terms of intensity, it ranks as one of Australia's most extreme TC seasons on record. Of the 12 TCs of the season, 3 were Australian category 5, with 1 being the strongest to hit Queensland in nearly 90 years, and another being the strongest TC ever reported off the Northern Territory coast and one of the strongest ever in the Australian region. Although only one TC made landfall as category 5, each severe TC had impacts upon a different state or territory within Australia.

If you lived in Australia and craved a banana with your cereal, banana chips with lunch, or the occasional banana daiquiri, then 2006 was just not your year. When TC Larry blasted across the northern Queensland coast, it devastated the Australian banana crop, drastically limiting supply and raising prices Australia-wide by 400%–500%, arguably triggering a small rise in Australia's inflation rate.

TC Larry (Fig. 4.25) crossed the north Queensland coast near Innisfail on the morning of 20 March 2006. Larry reached category 5 intensity shortly before reaching the coast, but crossed as category 4. This was supported by a wind gust of 293.7 km $h^{-1}$ recorded on the eastern (leeward) slope of Mount Bellenden Ker at an elevation of approximately 1450 m, although by an instrument on a tower at nonstandard height. Worst affected was the town of Silkwood, where 99% of the houses suffered cyclone damage. In total, the immediate impact of the cyclone caused over $350 million Australian dollars of insured losses.

TC Larry destroyed between 80%–90% of the total Australian banana crop (Fig. 4.26). In addition to limiting supply, it served to synchronize the crop, which had been staggered through the year to ensure a constant supply and stable prices.

The second record TC of the season was severe TC Monica, which followed a very long track (Fig. 4.27) from the Coral Sea east of Queensland, crossing the Cape York Peninsula and then intensifying along the northern coast of the Northern Territory before making landfall north of Jabiru on 24 April. During its passage along the Northern Territory coast, it intensified into a category 5 system, and one of the most powerful cyclones witnessed in the Australian region and the strongest cyclone ever observed in the Northern Territory. Estimated wind speeds were in excess of 350 km $h^{-1}$ on both 23 and 24 April. There was evidence of a 5–6-m storm surge zone in Junction Bay.

Severe TC Glenda was a small but intense system that developed rapidly after moving off the northwest coast of Western Australia near Kimberley. Glenda reached category 5 intensity with estimated wind gusts to 300 km $h^{-1}$, but weakened as it approached the Pilbara coast. It weakened before finally crossing the coast near Onslow on 30 March as a marginal category 3.

The 2005/06 TC season in Australia was clearly one of its most intense on record. Fortunately, the strongest storms either missed heavily populated areas or reduced in intensity at just the right time, and hence, damage to property and loss of life was kept relatively low. However, in Queensland at least, the effect of a severe TC upon agriculture was devastating; an impact ultimately felt across the country.

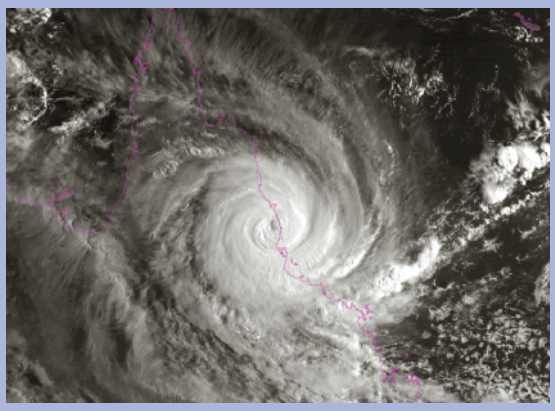

**Fig. 4.25. Tropical Cyclone Larry viewed just after landfall, 0730 Australian EST 20 Mar 2006.**

**Fig. 4.26. Damage to the banana crop as a result of Tropical Cyclone Larry.**

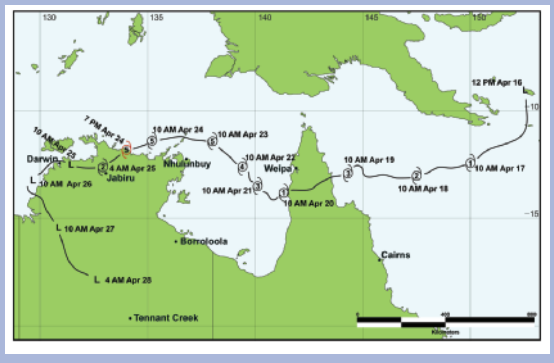


**Fig. 4.27. Track of TC Monica, the strongest TC ever recorded in the Northern Territory region.**

TRMM rainfall dataset begins in 1998, the long-term averages are taken from 1999 because extreme El Niño conditions in the first few months of 1998 distort the rainfall climatology in the SITCZ region.

Rainfall in the ITCZ is higher in the second 6 months of the year, and this climatological pattern was accentuated during 2006. Rainfall was lower than normal, particularly in February, and higher than normal in October through December 2006. This transition was also apparent in island rainfall records for the year. The islands of Micronesia in the western Pacific, which enter their dry season at the start of the calendar year, were very dry in some parts (e.g., the northern Marshall Islands) in the first quarter of 2006. South of the equator, rainfall in specific island groups was affected by the ENSO modulation of the SPCZ. The SPCZ was farther south than usual from January through May, as expected with La Niña, and farther north than usual in at least some months at the end of 2006 (e.g., December). However, in the area average of the SPCZ region plotted in Fig. 4.23, these local precipitation fluctuations average out and there is no marked pattern of precipitation anomalies through the year. As noted above, precipitation in the SITCZ region, which occurs mainly from February through April, was enhanced during 2006.

#### 2) Atlantic ITCZ—A. B. Pezza and C. A. S. Coelho

The Atlantic ITCZ is a narrow but well-organized convective region that oscillates between several degrees north of the equator during July–November and only a few degrees south of the equator in January–May (Waliser and Gautier 1993). The ITCZ is active all year-round, demarcating the transition from the southeasterly to the northeasterly Atlantic trade winds. A zonally oriented cloud band is usually observed over the Atlantic Ocean basin extending from the northeast coast of South America to the northwest coast of Africa. Convective activity with high rainfall rates well inland is generally triggered by the nearby passage of the ITCZ as observed over northern Amazon in 2006 (Fig. 4.24).

The positioning of the ITCZ modulates the rainy season of northern/northeastern South America and northwestern Africa. Some regions experience a bimodal monthly rainfall distribution with two peaks— one when the ITCZ is moving southward and the other when it is moving back northward. Its seasonal migration and high asymmetry are primarily driven by land–sea temperature contrast, low-level winds, moisture convergence, and the meridional SST gradient between the North and the South Atlantic (Nobre and Shukla 1996). Large-scale dynamics given by Kelvin wave propagation affecting the Walker circulation can also drive the ITCZ's interannual variability, because ENSO is one of the relevant mechanisms of seasonal influences (Münnich and Neelin 2005).

High-resolution TRMM data indicate that during 2006 the ITCZ reached its southernmost position in April (2.5°S) and its northernmost position in August and September (10°N), and was to the north of its monthly climatological mean position during a number of months, particularly during the second half of the year. As a result, most of the tropical South Atlantic presented less rainfall in 2006 than the 1998–2005 annual mean value. However, the 2006 ITCZ's annual mean position appears close to its climatological annual mean due to a high variability, with outbursts of southward displacement from late austral summer to early austral winter. TRMM also shows a double ITCZ (Liu and Xie 2002) during April, with a primary band of convective clouds around 3°N across the entire equatorial Atlantic, and a secondary band of clouds around 2.5°S (Fig. 4.24).

April featured the interaction and organization of the secondary ITCZ branch with continental convection over northern Brazil, resulting in a wider ITCZ to the west of 30°W. This interaction over northern Brazil was also noted in May and June (Fig. 4.24), decaying in July. The ITCZ became less active from September to December, with little rainfall observed in September around 7.5°N in the central North Atlantic and near the African coast. August was the most active month for the period from July to December, when some areas near the African coast experienced high rainfall rates (Fig. 4.24). Interaction with western Africa rain was irregular during the year, with areas of positive and negative precipitation anomalies observed over the western tip of the continent. The onset of a weak El Niño event in the Pacific during mid-2006 contributed to keeping most of the ITCZ convective activity to the north of the equator for the remainder of the year, with annual rainfall below average over most tropical South Atlantic and above average over the tropical North Atlantic.

## 5. THE POLES—F. Fetterer, Ed.

### *a. Arctic*—J. Richter-Menge, J. Overland, A. Proshutinsky, V. Romanovsky, R. Armstrong, J. Morison, S. Nghiem, N. Oberman, D. Perovich, I. Rigor, L. Bengtsson, R. Przybylak, A. Shiklomanov, D. Walker, and J. Walsh

#### 1) Overview

The permanent presence of sea ice, ice sheets, and continuous permafrost are unique features of the

polar regions. The Arctic is further distinguished because it sustains a human population in a harsh environment. These characteristics amplify the impact of global climate change on both the regional physical and societal systems. These impacts reach beyond the Arctic region. For instance, studies are underway to determine the extent to which the loss of sea ice cover and the conversion of tundra to larger shrubs and wetlands, observed to have occurred over the last two decades, have impacted multiyear persistence in the surface temperature fields, especially in the Pacific sector. In this report, we provide observations that indicate continuing trends in the state of physical components of the Arctic system, including the atmosphere, ocean, sea ice cover, and land (Richter-Menge et al. 2006). The temporal extent of the data provides a multidecadal perspective and confirms the sensitivity of the Arctic to changes in the global climate system.

In 2006 there continues to be consistent signs of a general warming in the Arctic region, most apparent in the relatively small extent of the winter and summer sea ice cover and increased greenness of the tundra. However, there are also indications of a possible deceleration in the rate of change in some geophysical parameters, driven by pronounced shifts in atmospheric circulation patterns. These atmospheric circulation patterns mark a return to patterns that predominated prior to the mid-1990s. Perhaps correspondingly, the most recent observations indicate that the upper-ocean salinity and temperature in the vicinity of the North Pole and in the Beaufort Sea have relaxed toward the climatological norms reported since the 1950s. In 2006 ocean temperatures cooled in the Bering Sea and there was a slight recovery in the extent of the summer sea ice cover. The persistence and impact of the moderating 2006 conditions represents an intriguing and significant puzzle with respect to the contemporary global climate system.

## 2) Atmosphere

### *(i) Circulation regime*

The annually averaged AO index in 2006 was slightly positive, continuing the trend of a relatively low and fluctuating index, which began in the mid-1990s (Fig. 5.1). This follows a strong, persistent positive pattern from 1989 to 1995. The current characteristics of the AO are more consistent with the characteristics of the period from the 1950s to the 1980s, when the AO switched frequently between positive and negative phases.

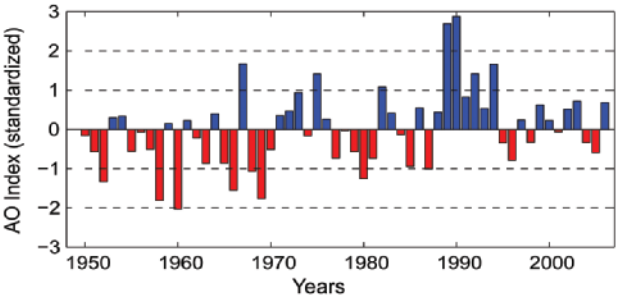


**Fig. 5.1. Time series of the annually averaged AO index for the period 1950–2006 based on data available online (www.cpc.ncep.noaa.gov). [Source: I. Rigor.]**

### *(ii) Surface temperatures and atmospheric circulation*

In 2006, the annual surface temperature over land areas north of 60°N was 1.0°C above the mean value for the twentieth century (Fig. 5.2). The surface temperature in this region has been consistently above the mean since the early 1990s. Figure 5.2 also shows warm temperatures in the 1930s and early 1940s, possibly suggesting a longer-term oscillation in climate. However, a detailed analysis shows different proximate causes for the 1930s compared to recent maxima. The early warm and cold periods are associated with intrinsic variability in high-latitude circulation patterns; while the recent warm temperatures appear to have an anthropogenic component (Johannessen et al. 2004; Wang et al. 2007).

In 2006 the regional hot spot of 3°–4°C in springtime temperature anomalies observed during 2000–05 shifted from the western Arctic (east Siberia, Alaska, and surrounding waters) to the eastern Arctic (Svalbard and the Barents Sea) (Fig. 5.3). Despite this shift, positive (warm) anomalies continue to remain over the entire Arctic. This pattern is in con-

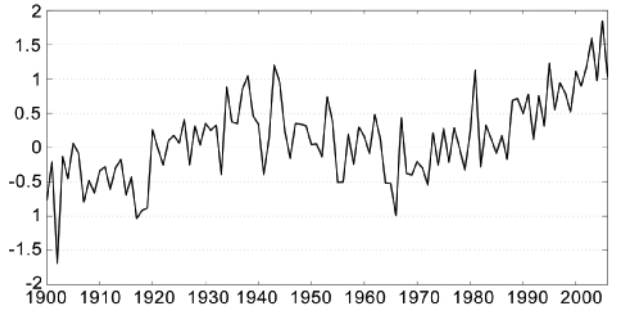


**Fig. 5.2. Arctic-wide and annually averaged surface air temperature anomalies (°C; 60°N–90°) over land for 1900–2006 based on the CRU TEM2V monthly data set. Anomalies are relative to the twentieth-century average.**

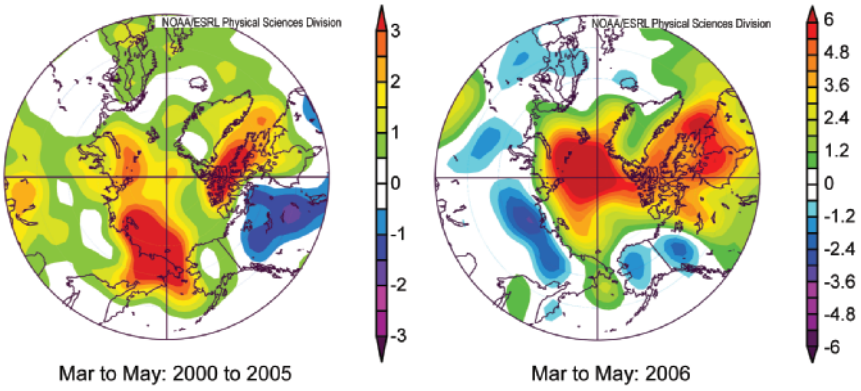


**Fig. 5.3. Near-surface March–May temperature anomaly composites (at the 1,000 mb geopotential height level) for 2006 in contrast to 2000–05. While the entire Arctic remained warm, the hot spot shifted from the western to the eastern Arctic. The figure is based on NOAA National Centers for Environmental Prediction (NCEP) reanalysis fields via the Climate Diagnostics Center (www.cdc.noaa.gov). Anomalies are relative to a 1968–96 base period.**

trast to the North America/Eurasia dipole patterns of anomalies associated with the two principal atmospheric circulation features of the twentieth century, the Pacific North American Pattern and the Arctic Oscillation/Northern Annular Mode/North Atlantic Oscillation (Quadrelli and Wallace 2004; Overland and Wang 2005).

*(iii) End of an era for the Bering Sea?*

Air and ocean temperatures in the Bering Sea cooled significantly in 2006 from the previous six-year period of relatively warm temperatures (Fig. 5.4) and reduced sea ice cover (Fig. 5.10), in concert with Arctic-wide changes (Fig. 5.3). Vertically averaged temperatures from an oceanographic mooring on the southeastern Bering Sea continental shelf (Stabeno et al. 2002) recorded temperatures in 2000–05 that were 2°C warmer than earlier years, with 2005 as having the warmest summer. Winter 2006 was cold (note the drop in temperature between fall 2005 and summer 2006), with a –0.2°C air temperature anomaly recorded at St. Paul Island for November–April. Although winter 2006 was cold, the spring ocean temperatures and ice extent in 2006 were near their climatological averages because the beginning fall 2005 temperatures were warm. Temperatures in fall 2006, in contrast, started cold and the weather pattern for November–December 2006 was also cold, with a –1.0°C anomaly for November–December. The 6-year period of sustained warm temperatures (2000–05) was sufficient to restructure the ecosystem away from Arctic conditions that favored bottom species, to favoring midwater fishes (Grebmeier et al. 2006). Because of the dramatic shift in ocean and ice conditions in 2006 and the beginning of 2007, the future state of the Bering Sea ecosystem is now less certain.

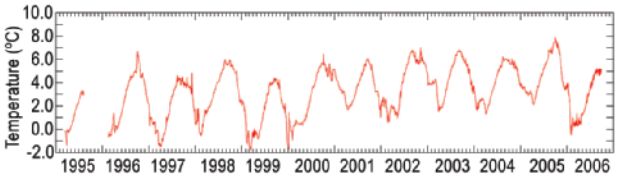


**Fig. 5.4. Ocean temperatures (°C) from a mooring on the southeastern Bering Sea continental shelf.**

3) Ocean

*(i) Surface circulation regime*

The circulation of the sea ice cover and ocean surface layer are closely coupled and are primarily wind driven. Data from satellites and drifting buoys indicate that the entire period of 2000–06 has been characterized by an anticyclonic circulation regime resulting from a higher sea level atmospheric pressure over the Beaufort Gyre, relative to the 1948–2005 mean, and the prevalence of anticyclonic winds. The sea surface atmospheric pressure at the North Pole together with the Arctic Oscillation index is a good indicator of the Arctic Ocean and atmosphere circulation regimes (Fig. 5.5). During high AO years, the low SLP dominates over the Arctic Ocean and the ice drift and ocean circulation are characterized by cyclonic (counterclockwise) motion. During low AO years, the high SLP prevails over the Arctic Ocean and sea ice and the ocean tends to circulate more in a clockwise sense. The dominance of the anticyclonic regime during the last decade of 1997–2006 is consistent with the AO index, which has exhibited relatively low and fluctuating values since 1996 (Fig. 5.5).

*(ii) Heat and freshwater content*

From 2000 to 2006, intensive investigations have been conducted in the vicinity of the North Pole (NPEO; online at http://psc.apl.washington.edu/northpole/) and in the western Arctic (BGOS; online at www.whoi.edu/beaufortgyre/index.html). Observations show that in the previous decade (1990s) the water temperature and salinity fields of the Arctic Ocean changed dramatically relative to the climatol-

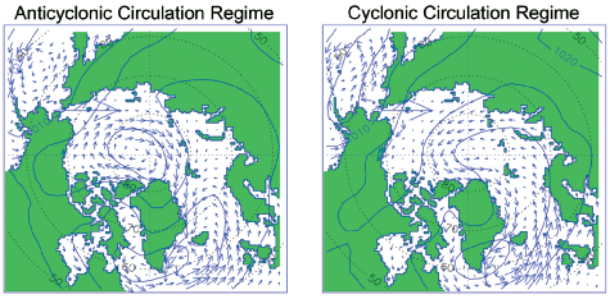


**FIG. 5.5. Idealized patterns of the dominant wind-driven circulation regimes of the Arctic Ocean. Two circulation regimes of surface waters (anticyclonic: left; cyclonic: right) are shown in blue arrows. In the cyclonic regime the clockwise circulation pattern in the Beaufort Sea region (the Beaufort Gyre) weakens, and the flow across the basin, from the Siberian and Russian coasts to the Fram Strait (the Transpolar Drift), shifts poleward. The cyclonic pattern dominated during 1989–96; the anticyclonic pattern has prevailed since 1997. Sea level atmospheric pressure patterns are shown by lines (hPa) (adopted from Proshutinsky and Johnson 1997).**

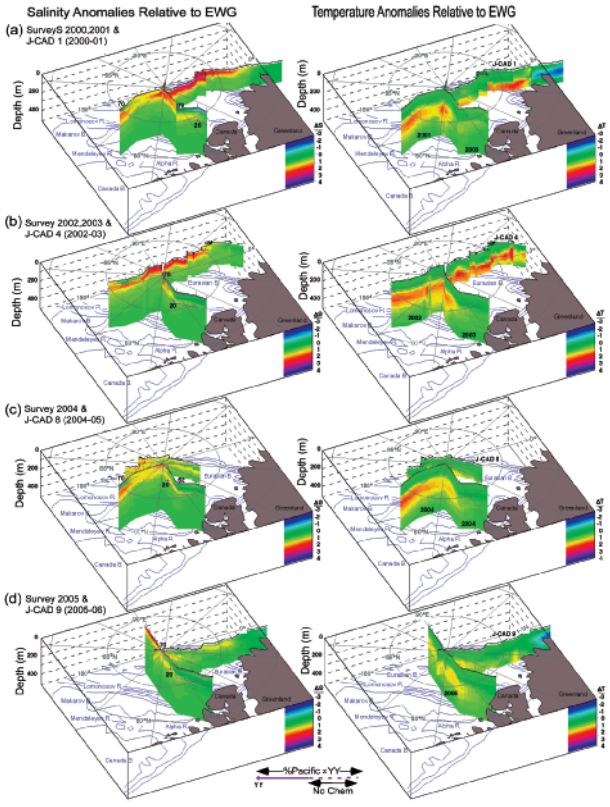


**FIG. 5.6. (left) Salinity and (right) temperature anomalies relative to EWG climatology along the NPEO surveys and J-CAD tracks for the years indicated on the temperature sections. Gray vertical lines mark survey station sites. Deep magenta lines (left) mark location of greater than 20% Pacific-derived water at 100–150 m. Surface lines mark greater than 70% Pacific-derived water in the surface layer (from Morison et al. 2006a).**

ogy of the Environmental Working Group atlas of the Arctic Ocean (Timokhov and Tanis 1997, 1998) where water temperature and salinity from observations were averaged and gridded for the decades of 1950, 1960, 1970, and 1980. Hydrographic data acquired at the North Pole in the 1990s show a strong increase in upper-ocean salinity and a large increase in Atlantic water temperature relative to EWG climatology average for all decades.

From 2000 to 2005, the oceanographic conditions in the North Pole region relaxed to near the pre-1990 climatology (Fig. 5.6). As characterized by average temperature and salinity anomalies relative to EWG climatology within 200 km of the North Pole, the change in the 1990s and the subsequent retreat to climatology are roughly consistent with a first-order response to the AO with a 5-year time constant and 3-year time delay (Morison et al. 2006a). Recent results indicate conditions in 2006 at the pole reverted to near 2004 conditions, but measurements of bottom pressure trends from 2002 to 2006 by GRACE suggest a return of oceanographic conditions over the entire Arctic Ocean to pre-1990s conditions (Morison et al. 2006b).

The western Arctic hydrography in the 1990s has also changed relative to climatology but, in opposition to the salinity increase at the North Pole, the salinity of the upper layer in the western Arctic was reduced. There are some indications that in the 2000s, relative to the 1990s, the salinity in this region has increased, but it is still significantly less than in EWG climatology. Since 2000, the temperature of the Pacific and Atlantic waters in the western Arctic is higher than in the 1990s and 0.8°–1.0°C higher than in EWG climatology.

The Beaufort Gyre is the major reservoir of freshwater in the Arctic Ocean. In 2000–06, the total freshwater content in the Beaufort Gyre has not changed dramatically relative to the climatology but there is a significant change in the freshwater distribution (Fig. 5.7, panels 3 and 4). The center of the freshwater maximum has shifted toward Canada and significantly intensified relative to the climatology. Significant changes were observed in the heat content of the Beaufort Gyre (Fig. 5.7, panels 1 and 2). It has increased relative to the climatology, primarily because of an approximately two-fold increase of the Atlantic layer water temperature (Shimada et al. 2004). The Pacific water heat content in the Beaufort Gyre

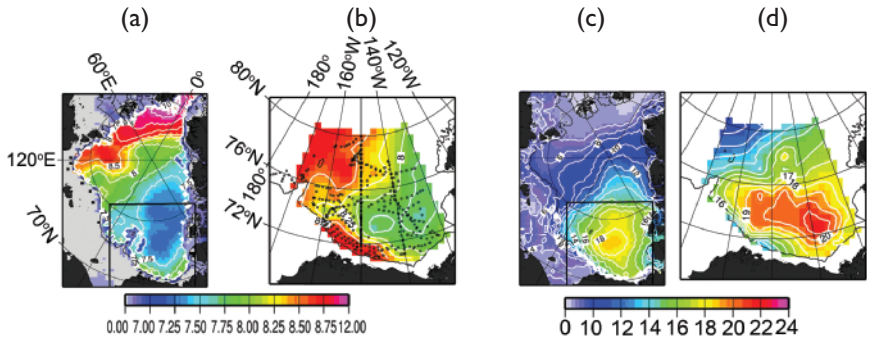


**Fig. 5.7. (a), (b) Summer heat ($10^{10}$ J m$^{-2}$) and (c),(d) freshwater (m) content. Panels (a) and (c) show heat and freshwater content in the Arctic Ocean based on 1980s climatology (Timokhov and Tanis 1997, 1998). Panels (b) and (d) show heat and freshwater content in the Beaufort Gyre in 2000–06 based on hydrographic surveys (black dots depict locations of hydrographic stations). For reference, this region is outlined in black in panels (a) and (c). The heat content is calculated relative to water temperature freezing point in the upper 1,000-m ocean layer. The freshwater content is calculated relative to a reference salinity of 34.8.**

region has also increased, and it is possible that the pronounced sea ice reduction in this region, observed in 2006 (see Fig. 5.8, right panel), resulted from heat being released from this layer (Shimada et al. 2006). It is speculated that the major part of these changes in the freshwater and heat content occurred in the 1990s, but there are not enough data to confirm this.

*(iii) Sea level*

Figure 5.9 shows sea level time series from nine coastal stations in the Siberian Seas. These stations are still operational in the Arctic with data from 1954 to 2006. There is a positive sea level trend along the Arctic coastlines. Proshutinsky et al. (2004) estimated that for 1954–89 the rate of sea level rise along Arctic coastlines (40 stations), corrected for the GIA, was 0.185 cm yr$^{-1}$. For the nine stations shown in Fig. 5.9 the rate for 1954–89, after correction for their GIA, was 0.194 cm yr$^{-1}$. Addition of 1990–2006 data increases the estimated rate of increase in sea level, beginning in 1954, to 0.250 cm yr$^{-1}$. The sea level time series correlates relatively well with the AO index and with the inverse of the SLP at the North Pole. Consistent with these influences, sea level dropped significantly after 1990 and reached a minimum in 1996/97 when the circulation regime changed from cyclonic to anticyclonic. In contrast, from 1997 to 2006 the mean sea level has generally increased in spite of the more or less stable behavior of the AO and SLP. At this point, because of the large interannual variability, it is difficult to evaluate the significance of the change in relative trends.

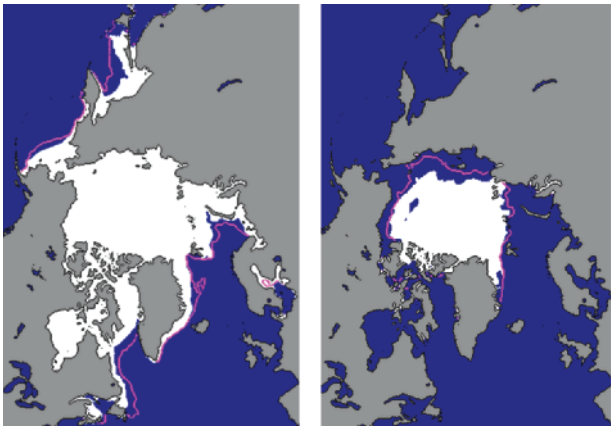

**Fig. 5.8. Sea ice extent in (left) March and (right) September 2006, when the ice cover was at or near its maximum and minimum extent, respectively. The magenta line indicates the median maximum and minimum extent of the ice cover, for the period 1979–2000. The March 2006 maximum extent marked a record minimum for the period 1979–2006. (Figures from the Sea Ice Index, online at nsidc.org/data/seaice_index.)**

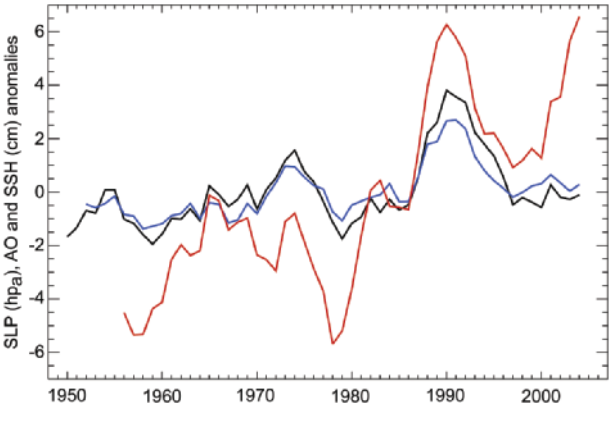


**Fig. 5.9. Annual mean sea level at nine tide gauge stations located along the Kara, Laptev, east Siberian, and Chukchi Sea coastlines (red). The blue line is the 5-yr running mean anomalies of the annual mean AO index (blue) multiplied by three. The black line is the sea surface atmospheric pressure (SLP) at the North Pole (from the NCEP–NCAR reanalysis data) multiplied by –1.**

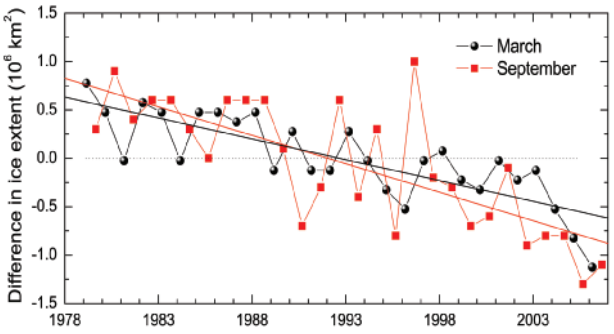


**Fig. 5.10. Time series of the difference in ice extent in March (maximum) and September (minimum) from the mean values for the time period 1979–2006. Based on a least-squares linear regression, the rate of decrease in March and September was 2.5% decade$^{-1}$ and 8.9% decade$^{-1}$, respectively.**

4) Sea ice cover

*(i) Extent and thickness*

Satellite-based passive microwave images of the sea ice cover have provided a reliable tool for monitoring changes in the extent of the ice cover since 1979. During 2006, the minimum ice extent, typically observed in September, reached 5.9 million km$^2$ (Fig. 5.8, right panel). This marked a slight recovery from the record minimum of 5.6 million km$^2$ for the period 1979–2006, observed in 2005. Consistent with the past several years, the summer retreat of the ice cover was particularly pronounced along the Eurasian and North American coastlines. A unique feature was the isolated region of open water apparent in the Beaufort Sea.

The maximum ice extent, typically observed in March, was 14.4 million km$^2$ and set a record minimum for the period 1979–2006 (Fig. 5.8, left panel). It is notable that in March 2006 the ice extent fell within the mean contour at almost every location. In comparison, the mean ice extent for March and September, for the period 1979–2006, is 15.6 and 6.8 million km$^2$, respectively.

To put the 2006 minimum and maximum ice extent into context, the time series of the variability of ice extent in March and September for the period 1979–2006 are presented in Fig. 5.10. In both cases, a negative trend is apparent with a rate of 2.5% decade$^{-1}$ for March and 8.9% per decade for September relative to the 1979 values. The summers of 2002–05 marked an unprecedented series of extreme summer ice extent minima (Stroeve et al. 2005).

Ice thickness is intrinsically more difficult to monitor. With satellite-based techniques (Laxon et al. 2003; Kwok et al. 2004) only recently introduced, observations have been spatially and temporally limited. Data from submarine-based observations indicate that the ice cover at the end of the melt season thinned by an average of 1.3 m between the period 1956–78 and the 1990s, from 3.1 to 1.8 m (Rothrock et al. 1999). Measurements of the seasonal ice cover do not indicate any statistically significant change in thickness in recent decades (Melling et al. 2005; Haas 2004; Polyakov et al. 2003).

*(ii) Perennial and seasonal ice*

The Arctic sea ice cover is composed of perennial ice (the ice located toward the center of the Arctic Basin that survives year-round) and seasonal ice (the ice around the periphery of the Arctic Basin that melts during the summer). Consistent with the diminishing trends in the extent and thickness of the cover is the observation of a significant loss of the older, thicker perennial ice in the Arctic (Fig. 5.11). Results from a simulation using drifting buoy data and satellite-derived ice concentration data to estimate the age distribution of ice in the Arctic Basin (Rigor and Wallace 2004) indicate that the March ice cover has experienced a significant decline in the relative amount of perennial ice over the period 1958–2006, from approximately 5.5 to 3.0 million km$^2$. While there is significant interannual variability, a general decrease in the amount of perennial ice appears beginning in the early 1970s. This trend appears to coincide with a general increase in the Arctic-wide, annually averaged surface air temperature, which also begins around 1970 (Fig. 5.2).

Results from a new technique employing data acquired by the NASA SeaWinds scatterometer on board the QuikSCAT have recently become available (Nghiem et al. 2005, 2006; Nghiem and Neumann 2007). In the half-decade of overlap, which begins in 2002 and represents the period of data reprocessed

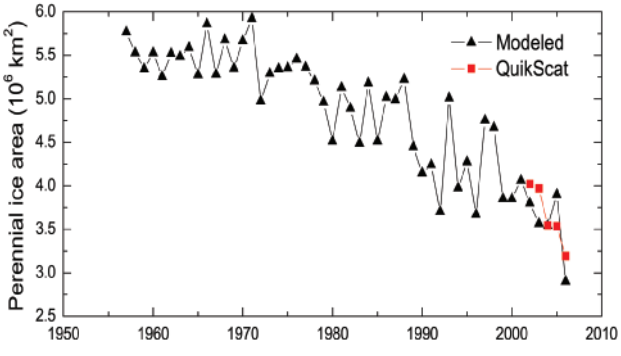


**Fig. 5.11. Time series of area of perennial sea ice extent in March estimated by a drift age model and satellite-derived ice concentration data and observed by QuikSCAT within the drift age model domain.**

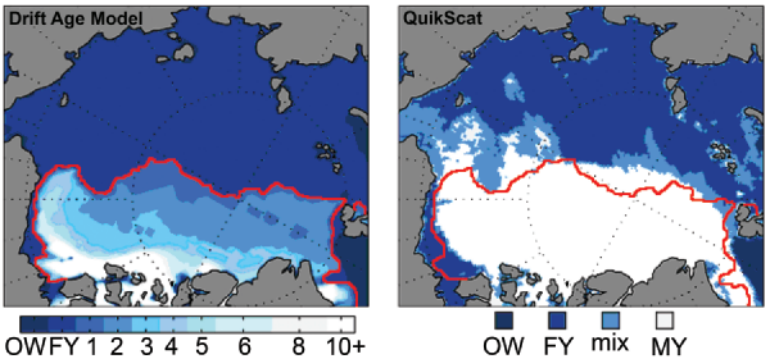


**Fig. 5.12. Comparison of sea ice distribution estimated using the drift-age model (March average, left panel) with QSCAT observations (21 Mar 2006, right panel). The red line in both panels indicates ice age older than one year (i.e., perennial ice) as estimated by the drift-age model.**

to date by the QSCAT project, the two products provide consistent estimates of perennial ice in March and suggest a precipitous decrease in the perennial ice extent in the last few years.

Figure 5.12 presents a comparison of the ice distribution derived from the drift age model and observed by QSCAT in March 2006. The two products provide strikingly similar results. Both indicate that the older, thicker ice is concentrated in the western Arctic Basin. This result is consistent with the dominant ice circulation patterns in the Arctic (see Fig. 5.5). Ice residence times are typically longer in the western Arctic in the region of the Beaufort Gyre. The eastern Arctic is dominated by the Transpolar Drift, which carries sea ice out of the Arctic basin via the Fram Strait.

A relatively younger, thinner ice cover, similar to the one that has developed in recent years, is intrinsically more susceptible to persistent atmospheric or oceanic warming. It is of crucial importance to observe whether the sea ice cover will continue its decline or recover under the recent, more neutral AO conditions, which have shown to be more conducive to ice growth.

### 5) Land

*(i) Vegetation*

The most convincing evidence of widespread change of vegetation in the Arctic comes from trends in tundra greenness as detected by satellites. The NDVI is a measure of greenness derived from reflectance of the surface in the red and near-infrared channels. If the climate warms, higher NDVI values might be expected to shift northward. Earlier global studies of NDVI changes indicated a general pattern of increased NDVI in the region between 40° and 70°N during the period 1981–99 (Myneni et al. 1997, 1998; Zhou et al. 2001; Lucht et al. 2002). Studies of the NDVI in the tundra area of northern Alaska indicate an increase of 17% in NDVI values in this region where the SWI measured at ground stations across northern Alaska has been increasing by 0.16°–0.34°C $yr^{-1}$ during the same period (Fig. 5.13) (Jia et al. 2003).

A more recent analysis indicates that different patterns of greening have occurred in the boreal forest and tundra areas of North America (Goetz et al. 2005). The NDVI has increased in tundra regions by an average of about 10% for all of North America, whereas the NDVI has declined in the boreal forest regions particularly during the past 10 years.

*(ii) Permafrost*

At the present time, there is no remote sensing technique to remotely and extensively monitor per-

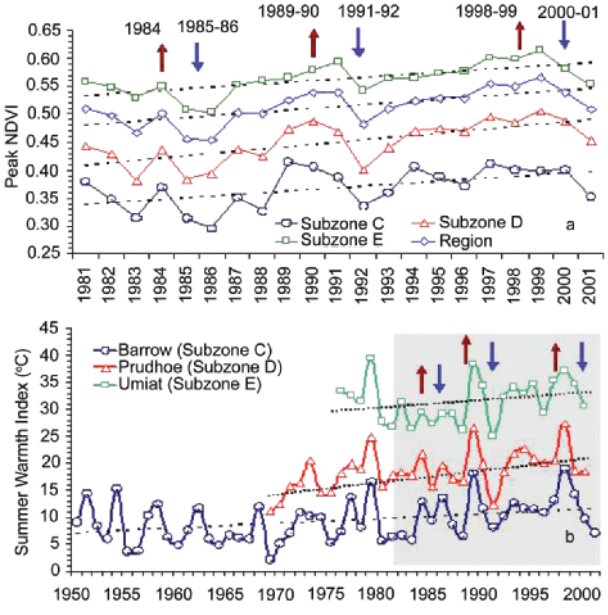


**Fig. 5.13. (a) Time series of peak NDVI derived from 8-km-resolution AVHRR data from 1981 to 2001 for bioclimate subzones and for the whole Arctic slope. (b) SWI over the past 22–50 yr at meteorological stations in each bioclimate subzone. Dashed lines are linear regressions. The shaded area in (b) highlights the period of SWI covered by the NDVI data in (a). The arrows show years of corresponding increases (red) and decreases (blue) in NDVI and SWI. From Jia et al. (2003).**

mafrost temperatures. Long-term permafrost temperature data are available only from a few clusters of stations, mostly in North America. However, the situation could improve as a result of implementing an INPO, which is the major goal of the IPY TSP project. Observations from the long-term sites show a general increase in permafrost temperatures during the last several decades in Alaska (Osterkamp and Romanovsky 1999; Romanovsky et al. 2002; Osterkamp 2003), northwest Canada (Couture et al. 2003; Smith et al. 2003), Siberia (Pavlov 1994; Oberman and Mazhitova 2001; Romanovsky et al. 2002; Pavlov and Moskalenko 2002), and northern Europe (Isaksen et al. 2000; Harris and Haeberli 2003). Uninterrupted permafrost temperature records for more than a 20-year period have been obtained by the University of Alaska Fairbanks along the International Geosphere–Biosphere Programme Alaskan transect, which spans the entire continuous permafrost zone in the Alaskan Arctic. All of the observatories show a substantial warming during the last 20 years. This warming was different at different locations, but was typically from 0.5° to 2°C at the depth of zero seasonal temperature variations in permafrost (Osterkamp 2005). In 2006, there was practically no change to the mean annual temperatures at the permafrost surface if compared to 2005 (Romanovsky et al. 2006). These data also indicate that the increase in permafrost temperatures is not monotonic. During the observational period, relative cooling has occurred in the mid-1980s, in the early 1990s, and additionally in the early 2000s. As a result, permafrost temperatures at 20-m depth experienced stabilization and even a slight cooling during these periods.

Very similar permafrost temperature dynamics were observed in the European north of Russia during the same period (Fig. 5.14). However, there is some lag in the soil temperature variations at the Alaskan sites compared to the Russian sites. This observation is similar to what was discovered in comparison with permafrost temperature dynamics in Fairbanks, Alaska, and Yakutsk, Russia (Romanovsky et al. 2007). Relative cooling has occurred in the Vorkuta region in the early and late 1980s and then in the late 1990s. The total warming since 1980 was almost 2°C at the Vorkuta site.

Data on changes in the ALT in the Arctic lowlands are less conclusive. In the North American Arctic, ALT experiences a large interannual variability, with no discernible trends. This is likely due to the short length of historical data records (Brown et al. 2000). A noticeable increase in the active layer thickness was reported for the Mackenzie Valley (Nixon et al. 2003). However, this positive trend was reversed into a negative trend at most of these sites after 1998 (Tarnocai et al. 2004). An increase in thickness of more than 20 cm between the mid-1950s and 1990 derived from historical data collected at the Russian meteorological stations was reported for the continuous permafrost regions of the Russian Arctic (Frauenfeld et al. 2004; T. Zhang et al. 2005). At the same time, reports from several specialized permafrost research sites in central Yakutia show no significant changes in the active layer thickness (Varlamov et al. 2001; Varlamov 2003). The active layer was especially deep in 2005 in interior Alaska. Around Fairbanks the 2005 active layer depth was the deepest observed in the past 10 years. Data from many of these sites show that the active layer developed during the summer of 2004 (one of the warmest summers in Fairbanks on record) and did not completely freeze during the 2004/05 winter. A thin layer just above the permafrost table was unfrozen during the entire winter. The active layer in the summer of 2006 was also one of the deepest on record at most of the observation sites in the Fairbanks area, even though the summer air temperatures were close to normal.

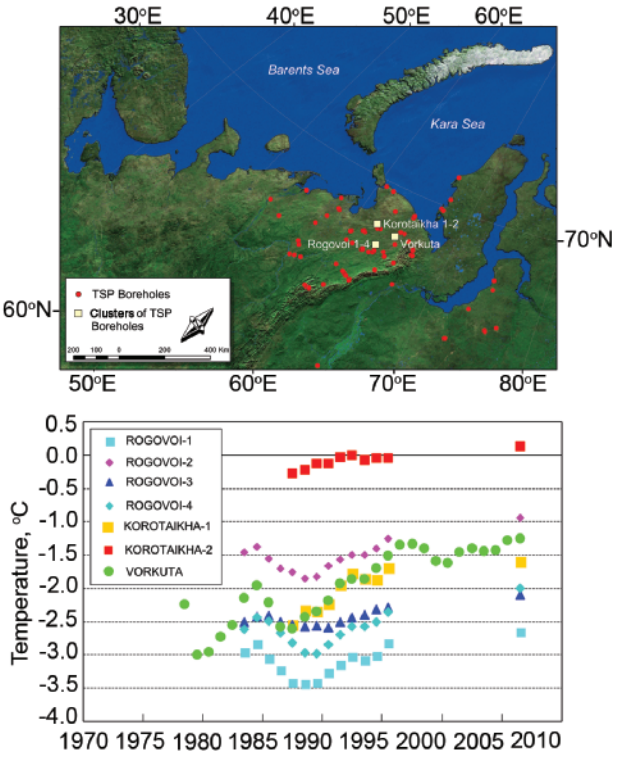


**Fig. 5.14. Top: Location of the long-term MIREKO permafrost observatories in northern Russia. Bottom: Changes in permafrost temperatures at 15-m depth during the last 20–25 yr (Oberman 2007).**

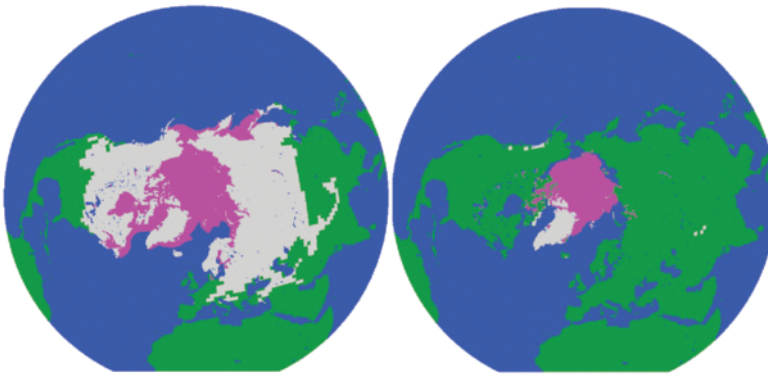

**Fig. 5.15. Mean snow cover extent (gray), 1966–2006, for (left) February and (right) August from the Northern Hemisphere EASE-Grid Weekly Snow Cover and Sea Ice Extent dataset (Armstrong and Brodzik 2005). The product includes climatologies of snow average conditions, probability of occurrence, and variance based on NOAA charts as revised by Robinson et al. (1993).**

*(iii) Snow extent*

As dicussed in section 2c(2), NOAA has produced snow extent charts since 1966 (Robinson et al. 1993; Frei and Robinson 1999). These charts were primarily derived from the manual interpretation of visible band imagery until 1999, when passive microwave and other data sources became available (Ramsay 1998; NOAA/NESDIS/OSDPD/SSD 2004, update 2006). Passive microwave data can enhance snow measurements based on visible data alone, sensing the surface through clouds and in darkness. However, passive microwave may not detect some areas of shallow snow that can be seen in visible band imagery. As a result, time series from the two sources can differ. Figure 5.15 shows mean snow cover for the 1966–2006 period. Figure 5.16 compares a microwave data–derived snow cover dataset (Armstrong and Brodzik 2001; Armstrong et al. 2005b) with NOAA snow extent data. Both show similar interannual variability and consistently indicate Northern Hemisphere maximum extents exceeding 40 million km$^2$. The NOAA time series indicates a decreasing trend of –2.0% decade$^{-1}$ (Brodzik et al. 2006). There is a decreasing trend of –0.7% decade$^{-1}$ in the microwave snow cover, although it is not significant at the 90% level. Both sources indicate a decreasing trend in snow cover in every month but November and December. The strongest seasonal signal occurs during May–August when both indicate significant decreasing trends. The western United States is among the regions with the strongest decreasing trends, supporting Groisman et al. (2004) and Mote et al. (2005) results using in situ observations. Shallow snow cover at low elevations in temperate regions is the most sensitive to temperature fluctuations and hence most likely to decline with increasing temperatures (IPCC 2007).

*(iv) Glaciers*

Glaciers and ice caps, excluding those adjacent to the large ice sheets of Greenland and Antarctica, can be found on all continents except Australia and have an estimated area between 512 and 540 × 103 km$^2$. The complicated and uncertain processes that control how fast glaciers move make it difficult to use changes in the areal extent of glaciers as a straightforward indicator of changes in climatic conditions. Further, many large collections of glacier photographs are available, but it is only in the last decade or so that remote sensing imagery has provided a means to monitor changes in the areal extent of glaciers. The Global Land Ice Measurements from Space glacier database project, with participation from more than 60 institutions in 28 nations, is working now on a baseline study to quantify the areal extent of existing glaciers (Armstrong et al. 2005a)

Mass balance measurements, or the difference between the accumulation and ablation, are a more direct method to determine the year-to-year "health" of a glacier. Changes in mass balance correspond to changes in glacier volume. These measurements are typically obtained from less than about 0.2% of the world's glaciers. Researchers have measured mass

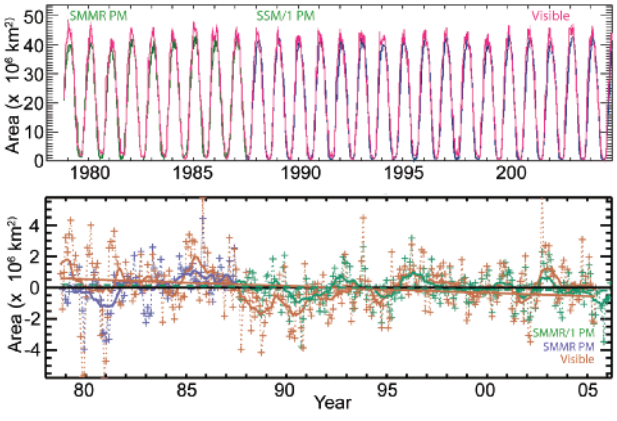


**Fig. 5.16. Time series of Northern Hemisphere SCA derived from passive microwave (green/blue) and visible (pink) sensors (top), and SCA departures from monthly means (bottom), from NOAA snow charts (orange) and microwave (purple/green) datasets.**

balance on more than 300 glaciers since 1946, although a continuous record exists for only about 40 glaciers since the early 1960s. Nevertheless, considerable compilation and analysis has occurred (e.g., Cogley 2005). These results indicate that in most regions of the world, glaciers are shrinking in mass. From 1961 to 2003, the thickness of "small" glaciers decreased approximately 8 m, or the equivalent of more than 6,000 km$^3$ of water (see http://nsidc.org/sotc/glacier_balance.html). Recent mass loss of glaciers and ice caps is estimated to be 0.51 ±0.32 mm SLE per year between 1961 and 2003 and 0.81 ±0.43 mm SLE per year between 1993 and 2003 (Dyurgerov and Meier 2006; online at http://nsidc.org/sotc/sea_level.html). The greatest mass losses per unit area are found in Patagonia, Alaska, and the northwest United States/southwest Canada. However, because of the corresponding large areas, the biggest contributions in total to sea level rise come from Alaska, the Arctic and the Asian high mountains.

*(v) River discharge*

The river discharge database R-ArcticNet (available online at www.R-Arcticnet.sr.unh.edu) was extended up to 2004 for 48 downstream river gauges. The last five years were characterized by an increase of total discharge to the Arctic Ocean mainly due to a contribution from Asian rivers. Mean 2000–04 discharge from Asia was 110 km$^3$ (5%) higher than over the previous 20 years. The mean discharge to the ocean from North America and Europe for 2000–04 was practically unchanged relative to 1980–99. A consistent increase in river discharge is observed from Eurasia for a longer time interval as well. Mean discharge over 2000–04 for the large Eurasian rivers was 3%–9% higher than the discharge over 1936–2004. Thus, the contemporary data further confirms the presence of a significant increasing trend in the freshwater discharge to the Arctic Ocean from Eurasia documented earlier by Peterson et al. (2002). The maximum total discharge of the six largest Eurasian rivers over 1936–2004 was observed in 2002, at 2080 km$^3$ yr$^{-1}$.

## b. Antarctic

### 1) Overview—T. Scambos

The Antarctic climate pattern and mean circulation is stabilized by the presence of the encircling Southern Ocean (for discussion here, the portions of the major oceans south of 50°S; definitions vary), and by the huge, roughly pole-centered ice plateau of the Antarctic continent. It is characterized by intense eastward-moving polar cyclonic systems and strong off-continent katabatic flow. Nevertheless, it is also strongly influenced by climate patterns to the north (e.g., ENSO; Bromwich et al. 2004a; Turner 2004), and it exhibits large circulation shifts that are correlated with changes to these broad temperate and tropical patterns. These changes in the atmospheric circulation in turn influence the formation and drift of Antarctic sea ice. The Southern Ocean sea ice cycle represents the third-largest annual change of the Earth's surface (after Northern Hemisphere leaf out, and seasonal northern snow cover), and its growth and retreat has a very large influence on heat and moisture transport to the atmosphere, as well as on the southern oceanic ecosystem.

The year 2006 continued the recent trend of warming in the peninsula and offshore west Antarctica, and a trend of moderate and shorter-duration anomalies in the SAM circulation index (Figs. 5.17 and 5.18). While annual averages for the high southern latitudes showed broad patterns of mildly warmer-than-average conditions, there were several anecdotal indications of a cool austral winter in 2006 (snow in South Africa; iceberg remnants off southern New Zealand). The annual mean SAM index was weakly positive, but there were several significant circulation shifts during the year. Sea ice trends were remarkable in that the year included both the record minimum and record maximum ice extents relative to the 1979–2006 period (the period of accurate satellite observations), possibly linked to the shifts in circulation pattern during the ice growth period. The extent of seasonal melt during the 2005/06 spring–summer period was quite low overall, but included an anomalously long melt event for the northeastern Ross Ice Shelf and Shirase Coast. While springtime

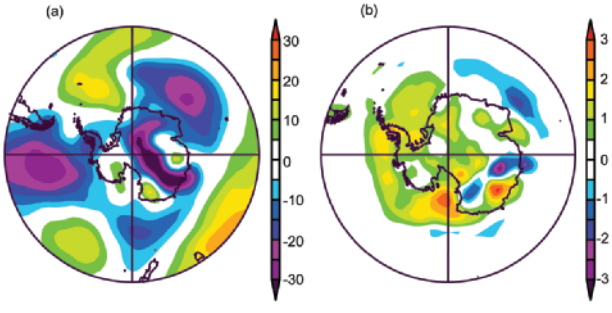


**Fig. 5.17. (left) Annual anomaly of 850-hPa geopotential height and (right) surface temperature for 2006 relative to the 1979–2005 period, from NCEP–NCAR reanalysis data. The 850-hPa value is inferred for high-altitude regions of the continent; however, this level best illustrates the near-surface and middle-troposphere patterns. [Source: NOAA/ESRL, generated online at www.cdc.noaa.gov.]**

ozone depletion reached record proportions by a small margin, it is still anticipated that detectable decreases in springtime ozone loss will occur by 2023.

### 2) Atmospheric circulation—R. L. Fogt, D. H. Bromwich, J. Turner, and S. Barreira

The year 2006 was dominated by strong changes in circulation reflecting changes in the SAM and the zonal wavenumber-3 pattern (Figs. 5.18 and 5.19). Here, the SAM index is based on the definition from the CPC (see www.cpc.noaa.gov/products/precip/CWlink/daily_ao_index/aao/aao.shtml) as the leading EOF of 700-hPa geopotential height anomalies south of 20°S. The year 2006 showed several significant SAM anomalies, particularly in May and August, when the SAM was more than one standard deviation above, and two standard deviations below, its 1979–2005 mean, respectively (Fig. 5.18). Overall, the year showed a mildly positive SAM index, continuing a trend toward positive mean SAM over the past several decades (Fig. 5.18, inset).

Based on an examination of monthly mean patterns, we divided the Antarctic 2006 climate into five multimonth periods (Fig. 5.18, top), and in Fig. 5.19 we examine their 850-hPa height and surface temperature anomalies. Strong geopotential height and pressure decreases across Antarctica, and corresponding rises in the southern midlatitudes, are seen for the May–June–July period (Fig. 5.19e), in association with the positive SAM index noted above. This led to warmer-than-average temperatures in the Weddell Sea by up to 6°C (Fig. 5.19f); and cooler temperatures over offshore Dronning Maud Land and Enderby Land (0°–60°E), again by 6°C. An abrupt shift to nearly opposite conditions, with opposing-sign temperature anomalies, occurred during the August–September period (Fig. 5.19h). This period also showed

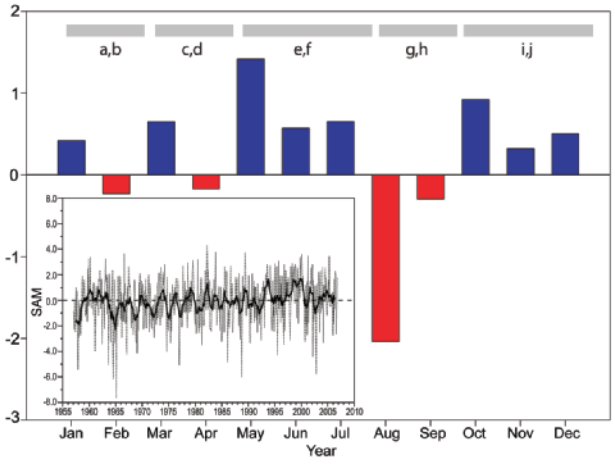


**Fig. 5.18. Monthly standard deviations of the SAM for 2006 relative to the 1979–2005 mean. Along the top, the periods of distinctive climate patterns examined in Fig. 5.19 are shown. Inset: Trends in monthly mean SAM index (dashed line) and running 12-month mean SAM, 1957–2006, from www.nerc-bas.ac.uk/icd/gjma/sam.html.**

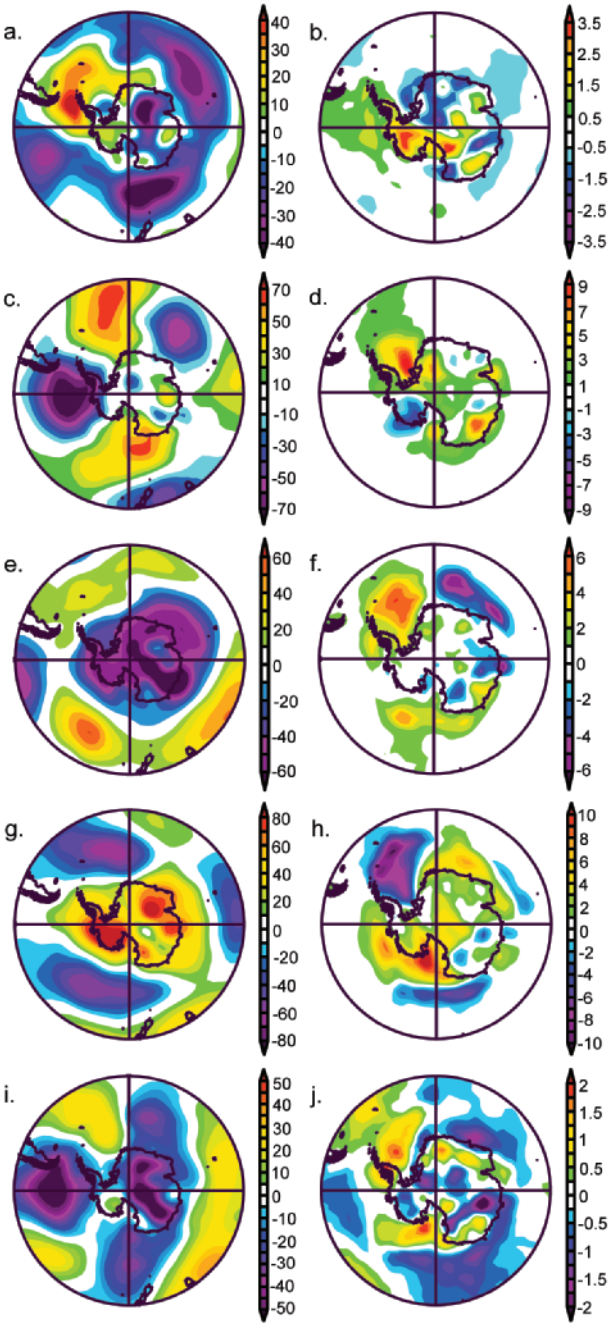


**Fig. 5.19. (left) 850-hPa geopotential height anomaly and (right) surface temperature anomaly (°C) relative to 1979–2005 climatology for five distinctive periods in 2006.**

intensely warm conditions (up to 10°C above mean) for the eastern Ross Sea and Ross Ice Shelf area.

The SAM has been characterized by high month-to-month variability since 2003. Notably, December 2006 initiated a mild El Niño event, which tends to produce positive height/pressure anomalies in the Amundsen–Bellingshausen Seas. However, Fig. 5.19i shows that a negative height anomaly was observed in this region during October–December, which suggests there was no significant climate teleconnection to the South Pacific from the late-onset 2006 El Niño at that time.

3) Surface and radiosonde observations—N. Adams, J. Turner, and T. Scambos

The patterns of circulation and temperature had a concurrent effect on surface weather observations during 2006 (Fig. 5.20). At the Australian bases [Casey (66.28°S, 110.52°E), Davis (68.58°S, 77.97°E), and Mawson (67.60°S, 62.87°E)], the large change in circulation and SAM index that occurred between July and August, and again between September and October, is clearly reflected in mean surface pressure anomaly shifts at those times. Temperature anomalies (warm in March–April, cooler generally in May–July) for the east Antarctic bases concur with the regional plots shown in Fig. 5.19. In the northeastern peninsula, surface observations from a number of stations operated by Argentina (Skvarca et al. 2006) indicate a very warm 2005/06 austral summer period, among the warmest during the preceding 30 years, during which extensive melt and melt ponding was observed. However, temperatures for the western peninsula were only slightly greater than the mean.

The long-term radiosonde record from these stations and several others has indicated that a midtropospheric, winter season warming has been taking place above the Antarctic in recent decades (Turner et al. 2006). At Syowa station on the coast of east Antarctica, temperatures at the 500-hPa level have risen by 0.7°C decade$^{-1}$ over the last 30 years. During 2006, however, the winter 500-hPa temperatures at Syowa were below average after near-record warm temperatures in 2005, 2003, and 2002.

4) Surface mass balance—A. Monaghan and D. Bromwich

Snowfall accumulation is the mass input to the Antarctic ice sheets, and is the net result of precipitation, sublimation/vapor deposition, drifting snow processes, and melt (Bromwich 1988). Of these, precipitation (almost entirely in the form of snowfall) is the dominant term of surface mass balance at regional and larger scales (Genthon 2004); only in relatively limited areas does ablation equal or exceed snow input, although recent remote sensing analyses suggest these may be more widespread than previously thought (firn "glaze" areas of near-zero accumulation; Scambos et al. 2006). Atmospheric models have been the primary means of assessing the variability of Antarctic snowfall for periods longer than a decade (e.g., Bromwich et al. 2004b). More recently, satellite radar altimetry (e.g., Davis et al. 2005) and other satellite-based techniques (e.g., Velicogna and

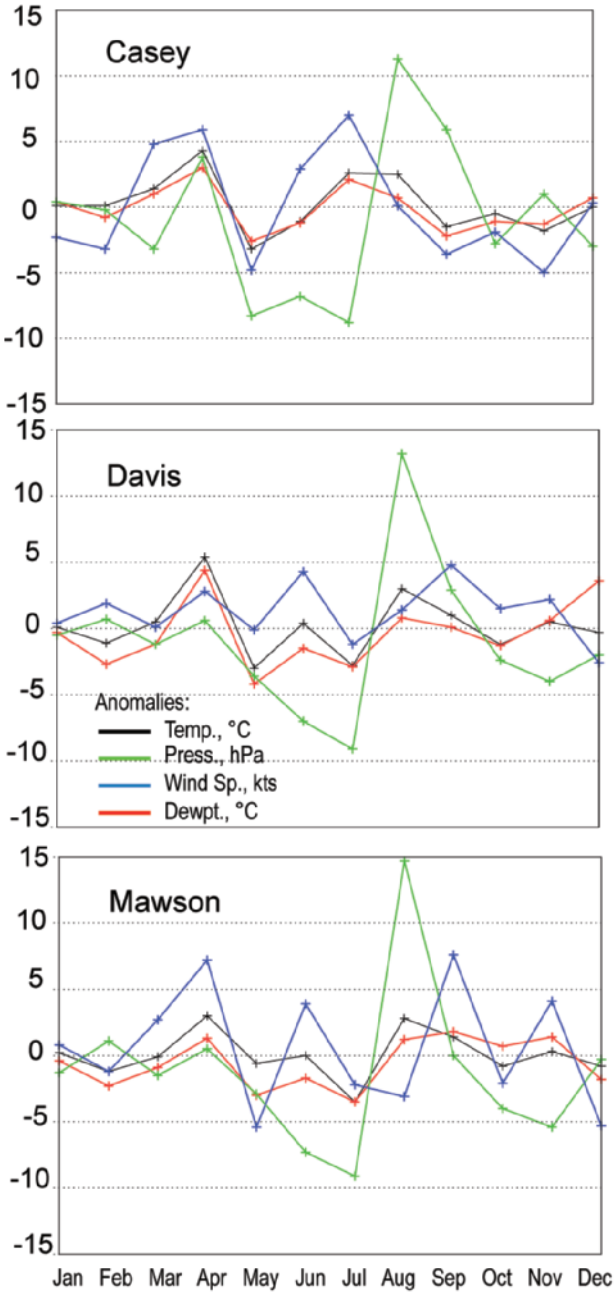


**Fig. 5.20. Monthly mean weather anomalies for the Australian Antarctic stations Casey, Davis, and Mawson.**

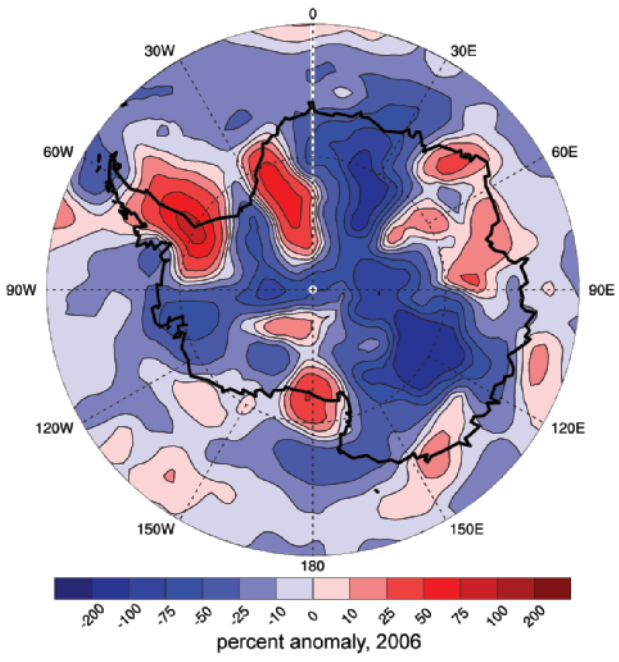


**Fig. 5.21. Detrended precipitation anomalies (% yr$^{-1}$) from NN2 for 2006 compared with the 1979–2006 mean.**

Wahr 2006) are increasingly being used to study surface and total ice sheet mass balance for periods of < 1 decade. The most recent model studies and observational data indicate there has been no trend in snowfall in recent decades (Van de Berg et al. 2005; Monaghan et al. 2006).

Precipitation fields from the NOAA/NWS/NCEP/DOE Reanalysis II (NN2; a successor to the NCEP–NCAR Reanalysis) are employed here to assess Antarctic snowfall for 2006. In recent studies (e.g., Bromwich et al. 2004b), snowfall trends in NN2 have been found to have an anomalous upward trend from 1979 onward, compared to other model-based records, snowstake measurements, and ice core records; however, the interannual variability of the snowfall is in very good agreement with other models (Monaghan et al. 2006). Therefore, a detrended NN2 record (linear mean trend subtracted) roughly approximates the "flat" trends that more accurate models predict. Using this we calculate a 2006 snowfall anomaly pattern compared to the 1979–2006 mean (Fig. 5.21).

In general, the anomaly over the continent interior is negative, and is positive over most of the Antarctic Peninsula and western Weddell Sea. Smaller positive trends over the Amery and northern Ross Ice Shelves suggest that the mean wavenumber-3 pattern (Fig. 5.17a) had a strong impact on precipitation. While the pattern of precipitation anomaly and circulation anomaly are consistent with a mildly positive SAM for 2006, the link between the SAM and precipitation is not as robust as the link for temperature (Genthon et al. 2003). Continentwide, the mean anomaly is small (–6%), with no month exceeding two standard deviations from the mean. The observed downward fluctuation would contribute an increase to sea level of approximately 0.30 mm for the year.

5) Sea ice extent and concentration—R. Massom, S. Barreira, and T. Scambos

Sea ice extent anomalies varied widely during the year, from record-low January and March extent (March was –18% relative to the 1979–2006 mean) to record highs of +4% for September and October, based upon analysis of monthly mean SSM/I-derived sea ice concentration data produced by the NSIDC Sea Ice Index project (Fig. 5.22; see Fetterer and

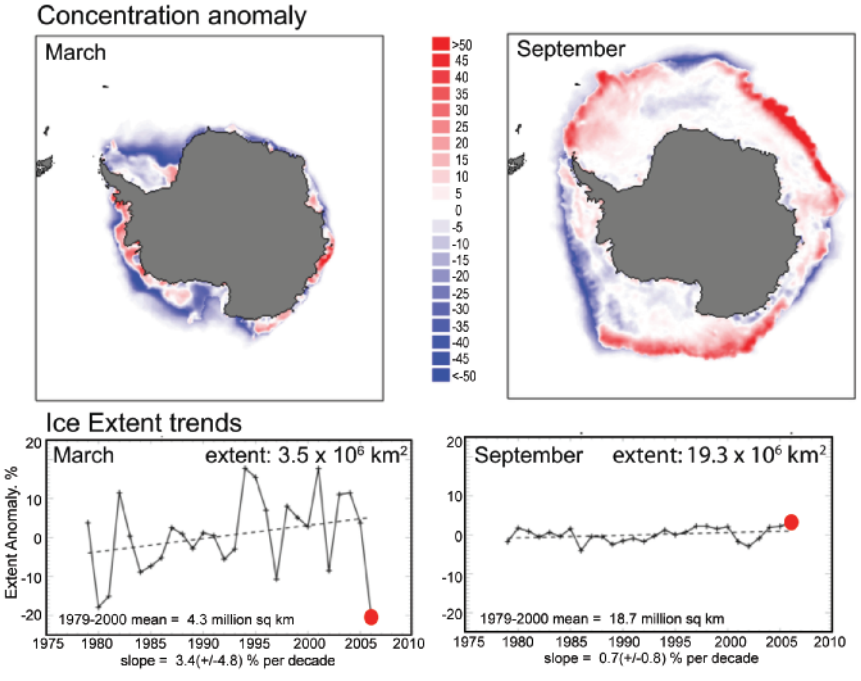


**Fig. 5.22. (top) Sea ice concentration anomaly (%) for March and September, 2006, and (bottom) trends in sea ice extent.**

Knowles 2004). However, by December 2006, sea ice extent was below average again. Strong regional variability is also apparent in ice extent and concentration anomalies. For the austral sea ice minimum period (February–March), the record low is primarily a result of greater-than-average March retreat in the Weddell Sea. This is likely a result of the intense warmth (up to 5°C above average) in the eastern Weddell in March, and a circulation pattern that favored southward and eastward wind-driven drift of the pack. In the autumn growth season, positive anomalies in the Amundsen Sea and western Indian Ocean sectors are balanced by negative anomalies in the South Atlantic (Weddell Sea) and Ross Sea/WPO sectors. The winter ice cover in August is characterized by major negative anomalies (indicative of wind-driven ice compaction) in the Bellingshausen–Amundsen Seas plus WPO sectors and a lesser negative anomaly skirting the Greenwich meridian. These are counterbalanced by equally large positive anomalies in the Weddell Sea, Ross Sea, and Indian Ocean sectors. This pattern persisted through September–October. In fact, the Indian Ocean sector experienced large positive extent and concentration anomalies from April through November. Locations of extent anomalies, and the overall record extent during the winter maximum, suggest an influence from the earlier positive SAM mode and strong positive wavenumber-3 anomaly, and the presence of lower-than-average temperatures near the winter ice edge (see Massom et al. 2006; Raphael 2004).

### 6) Seasonal melt extent and duration—H. Liu, Lei Wang, and K. Jezek

The extent, onset date, end date, and duration of snowmelt on the Antarctic Ice Sheet during the 2005/06 austral summer, and a time series spanning 1979/80 to the 2003/04 summers, have been derived using passive microwave remote sensing (Liu et al. 2005). The 25 season mean melt extent is 1.277 million km$^2$, or 9.34% of the continent's area. During the 2005/06 summer, melt extent, including all areas with at least one day of surface melting, was 1.009 million km$^2$, or 7.4% of the continent (Fig. 5.23). This is the second lowest extent during this period, after 1999/2000 (Liu et al. 2006). The 2005/06 melt season extended from 5 November to 4 March. Peak melt extent occurred on 7 January.

Extensive and continuous melt occurred on the ice shelves of the Antarctic Peninsula, and the Amery, Abbot, West, and Shackleton Ice Shelves. Melt areas are also scattered along the coasts of Wilkes Land and in glacial valleys in the Transantarctic Mountains. A brief but extensive surface melting occurred over the west Antarctic ice streams and Ross Ice Shelf in mid-December and again in January, coinciding with warm air temperature anomalies there during this time (Fig. 5.19b). Regionally, 2005/06 was a normal melt year for the Antarctic Peninsula, Amery Ice Shelf, Shackleton Ice Shelf, and West Ice Shelf, an extremely high melt year for the Ross Ice Shelf and Abbot Ice Shelf, and an extremely low melt year for the Ronne–Filchner Ice Shelf, and the ice shelves along the Queen Maud Land and Wilkes Land coasts.

### 7) 2006 austral springtime ozone depletion—P. A. Newman, B. J. Johnson, D. Lubin, S. J. Oltmans, and R. C. Schnell

Springtime ozone depletion in 2006 was by a small margin the most severe ever recorded as measured from the NASA Aura satellite's OMI. The ozone hole's area had an average late-September extent of 27.4 million km$^2$ (Fig. 5.24). The ozone hole area is estimated by integrating the area of observations with total ozone values less than 220 DU from the NASA TOMS instruments and the Aura OMI satellite instrument. A record-minimum column ozone abundance of 85 DU was recorded on 8 October over east Antarctica. This is consistent with the extremely cold temperatures in that same altitude range during this period (~ –85°C), which led to extensive PSC formation. Aura MLS observations revealed high ClO abundances (> 1 ppbv) filling nearly all of the polar vortex. While the 2006 ozone depletion was severe,

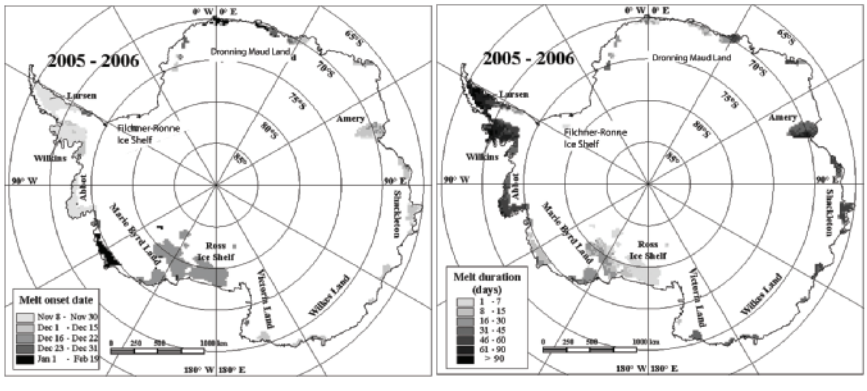


**Fig. 5.23. Melt onset date and melt season duration in days, for the 2005/06 melt season.**

it began about two weeks later than the mean of those years with comparable severity (Fig. 5.24a).

Information on the vertical structure of the ozone hole is provided by the NOAA/Earth System Research Laboratory Global Monitoring Division balloon-borne ozonesonde measurements (71 launches) at the Amundsen-Scott South Pole Station in Fig. 5.25. The total column of $O_3$ (blue line) is in Dobson units (and the 20–24-km stratospheric temperature (red line) illustrates the development of the $O_3$ hole over South Pole Station in 2006. The severity of $O_3$ depletion depends on wintertime stratospheric temperatures, the stability of the polar vortex, and active chlorine levels. The 2006 measurements showed some of the lowest $O_3$ amounts ever in the 21-year record at South Pole. Average total column of $O_3$ was 270 DU in July through mid-August before stratospheric $O_3$ began the now-typical, steady decline throughout September. Stratospheric temperatures remained colder than normal during that month. The total $O_3$ minimum of 93 DU at the South Pole (shown in Fig. 5.25c) was measured on 9 October, consistent with the satellite observations. This low value occurred about one week later than normal, and was the third lowest minimum observed since South Pole measurements began in 1986. The depletion was the largest ever observed within the primary $O_3$ layer from 14 to 21 km, dropping from 125 DU in late July to a record low of 1.2 DU (99% depletion) in early October. The polar vortex remained stable over the Antarctic for the final weeks of 2006, resulting in a slow recovery in stratospheric $O_3$. Significant amounts of ozone-enriched air transported from midlatitudes eventually reached the South Pole on 8 December, as shown in Fig. 5.25a and 5.25d, when total $O_3$ increased to 301 DU.

Despite its severity, the 2006 event does not necessarily signify a worsening of polar ozone depletion. Ozone depletion over Antarctica is highly sensitive to the dynamics of the winter stratospheric polar vortex, and this dynamical variability has yielded significant interannual variability in springtime ozone depletion over the past decade. For example, the weak and split polar vortex of 2002, accompanied by an anomalously warm stratosphere, led to a very mild springtime ozone depletion. During 2006, the polar vortex was much colder than average. These colder temperatures resulted from a weaker tropospheric planetary wave–driven warming of the stratosphere during the July–September period (related to the positive anomaly in 850-hPa level in Fig. 5.19g). Given these conditions, the severe 2006 ozone depletion is consistent with the decadally averaged abundance of anthropogenic ODS (mainly chlorofluorocarbons). ODS abundances have only recently started to decline in response to the Montreal Protocol; the rate of this decline is ~0.6% year$^{-1}$, not yet enough to reduce the severity of the springtime ozone depletion over Antarctica. According to models by Newman et al. (2006), ODS mitigation resulting from the Montreal Protocol should yield a decrease in Antarctic ozone depletion beginning

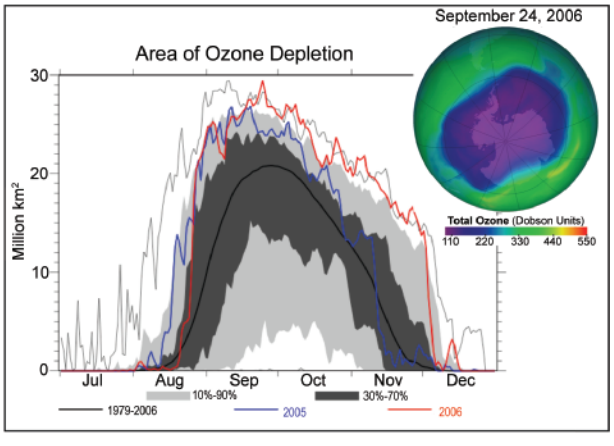


**Fig. 5.24. Ozone depletion for austral springtime period at South Pole, 2006 (red), 2005 (blue), maximum over the period 1979–2005 (gray line), and the climatological mean (black), with extent of ozone depletion as of 24 Sep 2006, the maximum area ever recorded (inset).**

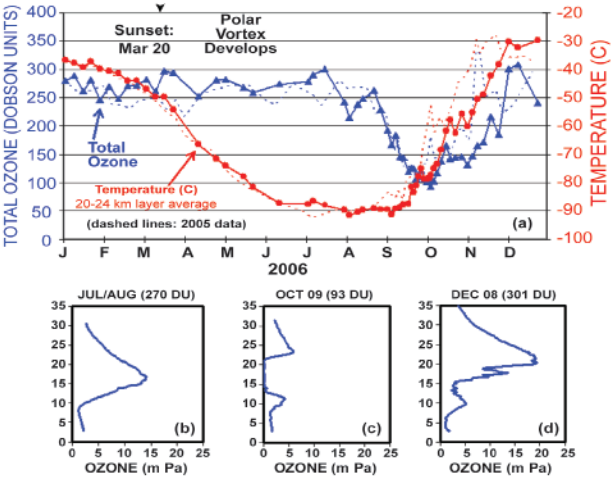


**Fig. 5.25. (a) Summary of South Pole total ozone in DU and stratospheric temperatures measured by ozonesondes during 2006. Dashed lines show the respective 2005 data. Three selected profiles of altitude versus ozone partial pressure (millipascals) are shown in the lower panels: (b)the July through mid-August average profile prior to the 2006 ozone hole, (c) the minimum total ozone, and (d) the postozone hole. [Source: B. Johnson and S. Oltmans, NOAA/ESRL/GMD.]**

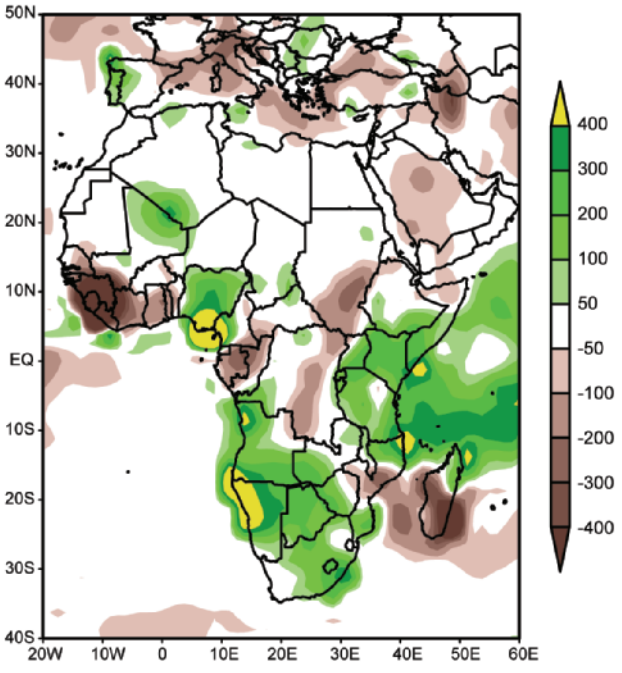


**Fig. 6.1. African 2006 annual precipitation anomalies (mm; 1979–2000 base) from the CAMS-OPI dataset (Janowiak and Xie 1999). [Source: NOAA/NCDC.]**

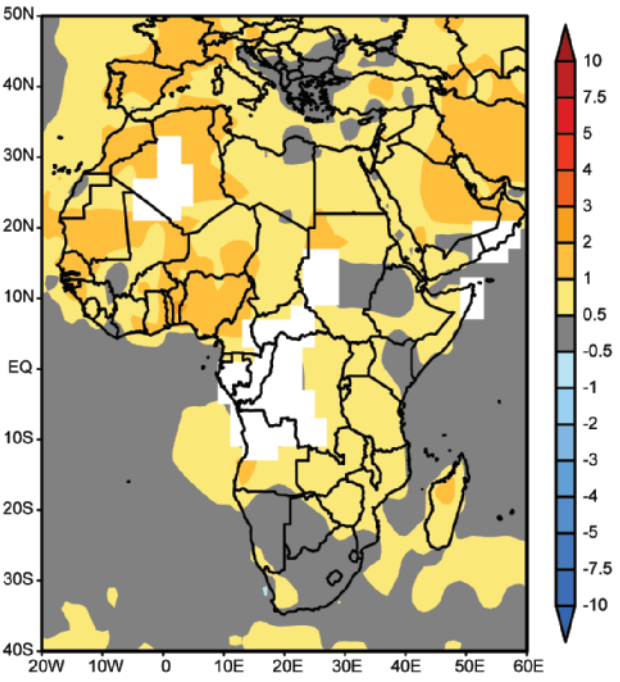


**Fig. 6.2. African 2006 annual temperature anomalies (°C; 1971–2000 base) from CAMS-OPI.**

around 2010, detectable at the 2σ level by 2023, and with a disappearance of the springtime ozone depletion phenomenon by 2070.

## 6. REGIONAL CLIMATES—A. Arguez, Ed.

### *a. Overview*—A. Arguez

While a holistic (global) view of the 2006 state of the climate is a worthwhile vantage point, much can also be gleaned by analyzing individual continents, countries, and subregions. This section represents such a "downscaling" approach, as 2006 weather conditions over smaller geographic areas are not only described and put in a historical context, but international and interregional contrasts are also brought to light. The section is divided into seven sections: Africa, North America, Central America and the Caribbean, South America, Asia, Europe, and Oceania. These regions are further subdivided into practical climate divisions. Country and regional names utilized in this section do not, in any shape or form, reflect any political bias or sympathy. In addition, please note that varying base periods are often utilized for the computation of climate anomalies.

### *b. Africa*—A. Arguez

Precipitation was generally above average over much of Sub-Saharan Africa in 2006 (Fig. 6.1). Several flood events and droughts occurred, causing substantial losses to human life and property. Most of Africa was slightly warmer than average for 2006 (Fig. 6.2). The following section discusses the state of the climate in four distinct regions: eastern Africa, northern Africa, southern Africa, and western Africa (including the Sahel).

#### 1) Eastern Africa—M. Bell, C. Oludhe, P. Ambenje, L. Njau, Z. Mumba, and M. Kadi

The GHA countries have experienced heavy rainfall leading to severe flooding (the worst in the region for 50 years), causing loss of life and property in the region from October to November 2006. The worst hit were parts in Ethiopia, Somalia, and Kenya. Flood waters from the Juba River in Somalia and the Tana River in Kenya combined to inundate a large region of northeastern Kenya. Several rivers burst their banks, washing away roads and destroying bridges.

Climatologically, the timing of the rainy seasons in East Africa is governed by the meridional migration of the ITCZ through the course of the year. Although the complex orography and presence of the East African lakes make the climate of the region quite complicated, three general regimes can be delineated. In the southern sector, central and southern Tanzania has a unimodal rainfall regime, with precipitation primarily between December and April. Northern and northeastern Tanzania, most of Kenya,

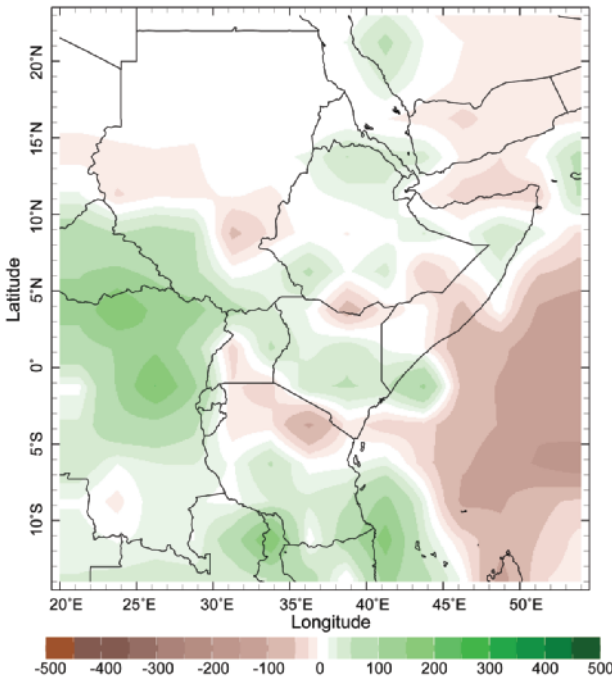


**Fig. 6.3. March–May 2006 precipitation anomalies (mm; 1979–2000 base) for East Africa using CMAP (Xie and Arkin 1997), v0610. [Source: NOAA/CPC.]**

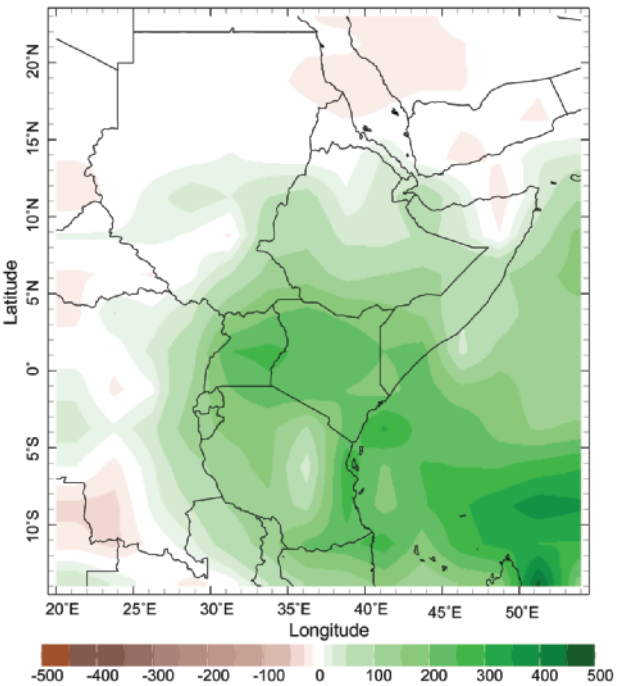


**Fig. 6.4. October–December 2006 precipitation anomalies (mm; 1979–2000 base) for East Africa from CAMS-OPI.**

southern and eastern Ethiopia, and most of Somalia comprise the equatorial sector, which generally exhibits a bimodal rainfall regime, with the "long rains" during March–May and the "short rains" during October–December. In the northern sector, which includes much of central and western Ethiopia, western Eritrea, and much of Sudan, the major rainy season occurs during the months of June–September. In addition to a peak in rainfall centered on July and August, areas of north-central Ethiopia, eastern Eritrea, and Djibouti also experience a climatological rainfall maximum during March–May.

East Africa experienced a dramatic shift from terrible drought at the beginning of the year to generally abundant precipitation that was accompanied by destructive flooding throughout the region. Although the March–May long rains (Fig. 6.3) brought above-normal rainfall to parts of Kenya and southern Somalia, areas of northern Tanzania, and portions of northern Kenya, southern and eastern Ethiopia, and central Somalia continued to experience precipitation deficits. However, the October–December short rains (Fig. 6.4) produced above-normal rainfall throughout the region.

*(i) Southern sector*

By the early months of 2006, below-normal rainfall in Tanzania during the previous year was causing significant food security and power supply problems. Approximately two-thirds of Tanzania's electrical power is produced by hydropower. By February 2006, water levels in the country's hydropower reservoirs were nearly too low to continue producing electricity. After extremely dry conditions in January, rain finally began falling somewhat consistently in February and March in central and southern Tanzania, which constituted a delay of several weeks for the start of the rainy season there.

In the final quarter of 2006, some significant early rainy season precipitation fell in October and November in central and southern Tanzania, and rainfall in December was well above average throughout the country. The heavy rains caused flooding in the regions of Shinyanga and Kigoma in northwestern Tanzania. The paths of Tropical Storm Anita and Cyclone Bondo brought them into the northern end of the Mozambique Channel during December, providing an additional source of moisture and rainfall, though neither made landfall on the continent.

*(ii) Equatorial sector*

The extreme drought in East Africa, which became very severe by early 2006 with the nearly complete failure of the October–December 2005 short rains (Oludhe et al. 2006), was centered on the border region of northeastern Kenya, southeastern Ethiopia,

and southern Somalia. Accumulated precipitation anomalies over the March–May 2006 long-rains season show near- to above-normal precipitation throughout much of Kenya, far southern Somalia, northeastern Uganda, and parts of southern Ethiopia. Below-normal precipitation is indicated in parts of north-central Kenya, southern Uganda, north-central Tanzania, eastern Ethiopia, and large parts of central and southern Somalia. Precipitation during the March–May long rains was only about 40%–70% of normal in these areas of Somalia (and in the neighboring Somali region of eastern Ethiopia, and parts of northern Kenya).

*(iii) Northern sector*

Rainfall in the highlands of central and western Ethiopia, much of Sudan, and western Eritrea started earlier than normal and remained plentiful throughout the June–September rainy season. In many areas of the northern sector, precipitation was more than 200% of normal. Heavy rainfall in July and August throughout most of Ethiopia resulted in deadly floods. In spite of some flood damage to crops, the above-normal June–September rainy season resulted in excellent crop production in Ethiopia and Sudan. A record cereal crop for 2006, estimated to be about 32% above the previous 5-year average, was forecast for Sudan.

2) Northern Africa—M. Bell

*(i) Temperature*

During 2006, annual mean temperature anomalies ranged from about 0.5° to 1.9°C above normal for most stations in North Africa. The warmest departures from the 1971–2000 mean were generally found along or just north of the Atlas Mountains across northern Morocco, Algeria, and Tunisia. Temperatures were generally cooler than normal in January and February 2006. Above-average temperatures returned to the region during March–May, but moderated somewhat during the course of the boreal summer through September. Above-normal temperatures again dominated in October and November.

*(ii) Precipitation*

The Mediterranean and Atlantic coastal area of North Africa receives the majority of its precipitation during October–April, largely from midlatitude cyclones and associated cold fronts. Mean annual rainfall totals decreased rapidly from about 700 mm at stations along the Mediterranean coast of Algeria and Tunisia to nearly zero in the interior of the Sahara Desert. In the Atlas Mountains of northern Morocco, Algeria, and Tunisia, cold-frontal passages can bring subfreezing temperatures and heavy rain or snow, occasionally causing floods and landslides.

For the year, annual precipitation amounts were above the 1971–2000 normal in a band extending just south of the Atlas Mountains from western Algeria northeastward into Tunisia, and at some locations along the Atlantic and Mediterranean coasts of Morocco and Algeria. Annual totals were generally below normal in Egypt, in interior Algeria, and in the Atlas Mountains of northern Algeria. Precipitation anomalies for the October 2005–April 2006 rainy season were above normal throughout the Canary Islands, Morocco, northern Algeria, northern Tunisia, and northwestern Libya. They were below normal in central Algeria, northwestern Libya, and northern Egypt (Fig. 6.6). After generally near-normal precipitation

## *COUNTRY SPOTLIGHT:* MOROCCO—K. Kabidi

During early 2006, Morocco recorded wet conditions with an average monthly rainfall much greater than the monthly long-term mean. Winter storm systems occurred during January and February, generating cold-air intrusion from the north and caused heavy rainfall that exceeded the monthly mean by more than 100%. For example, Rabat City recorded 173 mm during January, whereas the 1971–2000 monthly mean is only 82 mm. Several heat wave events occurred in late spring and during summer, punctuated by a +3°C temperature anomaly for the month of May in many parts of Morocco (Fig. 6.5). In addition, 2006 saw many Moroccan stations break wind speed records in summer, surpassing 100 km $h^{-1}$ in some instances.

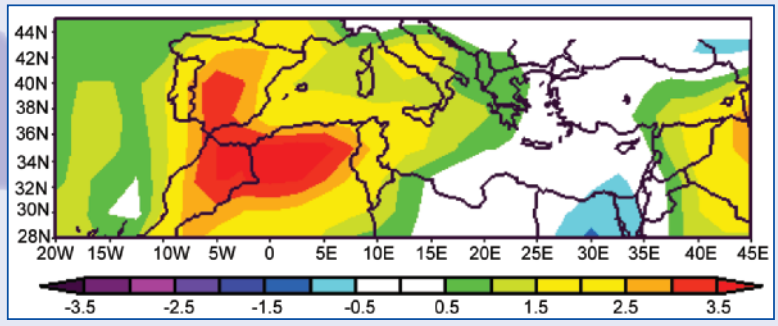


**Fig. 6.5. May air temperature anomalies over northwest Africa (°C).**

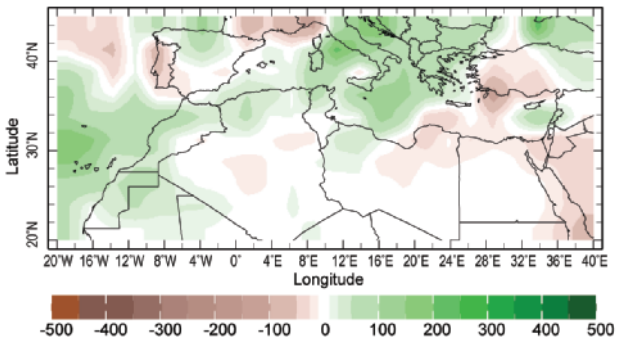


**Fig. 6.6. October 2005–April 2006 precipitation anomalies (mm; 1979–2000 base) for North Africa from CMAP.**

during October–December 2005, several extratropical cyclones brought abundant rainfall to most of North Africa during the first two months of 2006. However, the months of March and April were quite dry throughout the region, particularly in northern Algeria and Tunisia. To start the 2006/07 boreal winter rainy season, precipitation deficits affected northern Morocco, Algeria, and Tunisia in October and November. Above-normal precipitation returned to northern Algeria and Tunisia in December.

*(iii) Notable events*

During 7–13 February, a slowly propagating extratropical cyclone tracked eastward across the Canary Islands and Morocco, and into western Algeria, producing unusually heavy rainfall and destructive flooding. The heavy rains at Las Palmas/Gando Station on the Canary Islands contributed significantly to an October 2005–April 2006 precipitation total that was approximately 200% of the median for the rainy season. The storm also contributed heavily to a February 2006 total of 81 mm of precipitation at Tindouf Station in western Algeria; mean and median rainfall for February are 2.7 and 0.6 mm, respectively.

3) Southern Africa—A. Kruger, W. Landman, and W. Thiaw

*(i) Temperature*

Annual mean temperatures over southern Africa were generally very close to the 1971–2000 mean in the southern parts, but about 0.5°–1.0°C above the 1979–2000 average in the north. In an area in the northern part of Madagascar, temperatures were between 1° and 2°C above normal (Fig. 6.2). The near-normal temperature conditions in the southern parts is reflected by the mean temperature anomalies of 28 South African climate stations, which show that temperatures in South Africa were about 0.27°C above the 1961–90 mean, making 2006 only the 15th warmest year since 1961.

*(ii) Precipitation*

Overall, southern Africa received mostly normal to above-normal rainfall during 2006. The Namibian northern coastal area and adjacent interior experienced very high rainfall, which is very uncharacteristic of the region. In contrast, below-normal rainfall was experienced in central Mozambique and central and southern Madagascar, where it was very dry in the east (Fig. 6.1).

The rainy season for most of southern Africa extends from October to April, with most rainfall usually from December to March. ENSO plays a significant role in the variability of rainfall, and for the most part causes drier conditions during warm episodes and wetter conditions during cold episodes. In the 2006 late-summer rainfall season, SSTs in the Niño-3.4 region were on average about –0.7°C below normal (base period 1971–2000), probably playing a role in the above-normal rainfall experienced over most of southern Africa during late summer.

A surface trough got established over southern Angola, Namibia, and South Africa. Associated with this system, upper-air (500 hPa) cyclonic circulation resulted in high rainfall totals during the austral summer and autumn over the southern parts, including South Africa, Namibia, Botswana, and Angola. Such wet conditions may have been associated with the La Niña conditions observed during early 2006. Well-established cloud bands were reported, contributing to large rainfall anomalies, particularly over Namibia. Easterly waves contributed to rainfall over the eastern regions including Kenia, Tanzania, Mozambique, and parts of South Africa. In late autumn, the surface circulation became anticyclonic, but with some frontal activity that contributed to anomalously wet conditions over parts of South Africa, including regions that are predominantly summer rainfall areas. During austral spring (SON), surface and associated upper-air trough systems developed once again over the west, leading to wet conditions over large areas of the region. However, these systems weakened during the month of December in association with the establishment of El Niño, associate with dryness over the south and wetter conditions over eastern equatorial Africa.

*(iii) Circulation*

The low-level atmospheric circulation associated with the 2005/06 rainy season featured easterly winds

## *COUNTRY SPOTLIGHT:* MOZAMBIQUE—D. Patricio

Mozambique is situated on the southern part of the East African coast, generally between 10° and 27°S and between 30° and 41°E. The country has a climate with tropical characteristics due to its location, with a hot rainy season generally from October to April, and a milder dry season from May to September.

In the southern part of Mozambique, the average monthly rainfall ranges from 23 mm in August to 152 mm in January. The annual average rainfall is about 857 mm. The monthly normal average air temperature ranges from 18.7°C in July to 26.3°C in February, with an annual average air temperature of 23.0°C. In 2006, the minimum monthly rainfall was observed in July (14.4 mm) and the maximum in March (289.0 mm), with an annual total of 1067.1 mm (24.5% above normal). Concerning the average air temperature, the smallest monthly average was 20.1°C in July and the largest was 27.8°C in February. The annual average value was 23.8°C, corresponding to 0.8°C above normal.

In central Mozambique, the monthly mean rainfall varies from 16 mm in September to 221 mm in February, with average annual rainfall of about 1191 mm (Fig. 8). The monthly average air temperature ranges from 20.2°C in July to 27.0°C in January; the annual average air temperature is 24.4°C. In the case of 2006, the minimum monthly rainfall was observed in July (5.4 mm) and the maximum in March (322.7 mm), with an annual value of 919.5 mm (22.8% below normal). With regard to the average air temperature, the monthly minimum value was registered as 21.1°C in July and the maximum was 29.2°C in December. The annual average value of 25.4°C corresponds to 1.0°C above normal.

In northern Mozambique, the monthly mean rainfall ranges from 4 mm in September to 196 mm in January; the annual average rainfall is about 1017 mm. The normal monthly average air temperature ranges from 19.4°C in July to 24.4°C in November; the annual average air temperature is 22.5°C. For 2006, the smallest monthly rainfall was observed in September (2.4 mm), while the maximum was reported in March (259.9 mm). The annual total was 1122.3 mm (10.4% above normal). The coldest (warmest) monthly average temperature was registered as 20.8°C (28.0) in July (November). The annual average temperature was 24.5°C (2.0°C above normal).

Figure 6.7 depicts the temporal distribution of monthly total rainfall and average air temperature for year 2006, as well as for the normal period (1961–90). In 2006, the weather was strongly influenced by the ITCZ during summer in the center and north. In the south, cold fronts played a dominant role. The southern and central parts of Mozambique were affected by a tropical depression in January, and by tropical cyclone Boloetse in February.

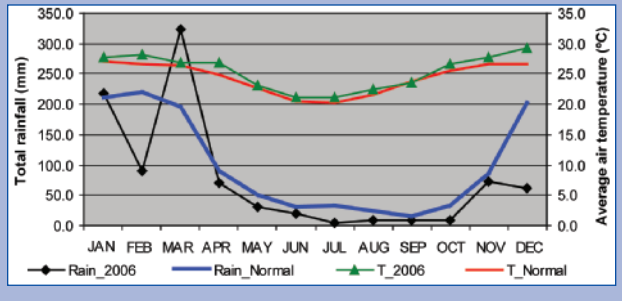


**FIG. 6.7. Time Series of monthly total rainfall (mm) and average air temperature (°C) for Mozambique in 2006 and the normals for the 1961–90 base period.**

that averaged about 4–8 m $s^{-1}$ from the east-central Indian Ocean westward into Madagascar and portions of interior southern Africa. This easterly flow was found along the equatorward flank of an enhanced Mascarene high pressure system and converged over interior southern Africa with a northeasterly flow that originated from the Bay of Bengal. The 500-hPa geopotential height exhibited strong intraseasonal variability in the circulation, but the presence of an anomalous trough was evident throughout the season. This anomalous trough was associated with a weak low-level anomalous cyclonic circulation across southern Africa and favored the intrusion of midlatitude disturbances. These contributed to higher-than-normal rainfall activity across southern Africa.

### 4) WESTERN AFRICA—W. Thiaw

*(i) Precipitation*

The 2006 rainy season once again featured above-normal rainfall across most of the Sahel (Fig. 6.8). Rainfall totals were slightly less than those in 2005, but exceeded 100 mm above the average over portions of southwestern Senegal, southern and northern Burkina Faso, southern Niger, and central Chad. Overall, the 2006 rainy season was the fourth wettest since 1968. However, despite the wet conditions, the rainfall season was marked by a late onset. As of July, most areas in central Senegal, southern Mauritania, western Mali, and Niger reported rainfall deficits with amounts only 50%–70% of the long-term climatological mean. An abrupt northward jump of the ITCZ in mid-July marked the onset of the rains in most areas in the Sahel. As of August 2006, cumulative rainfall totals were near or above average

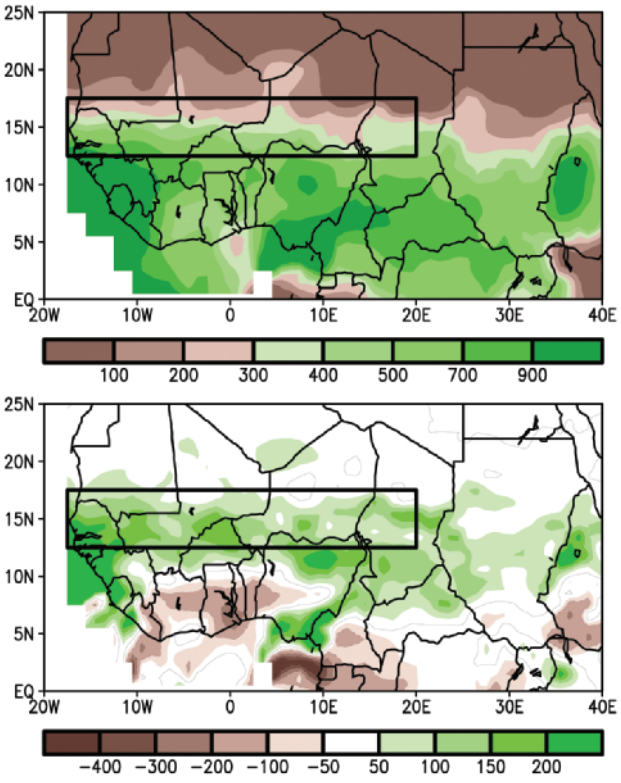


**Fig. 6.8. June–September 2006 (a) total rainfall and (b) anomalies (mm; 1971–2000 base) for western Africa. The boxed region denotes the approximate boundaries of the Sahel.**

across many areas in the Sahel. In the west, the formation of tropical depressions (some of them later developed into Atlantic tropical storms and hurricanes) along the coastlines of southern Senegal and Guinea, resulted in strong rainfall anomalies exceeding 200 mm. In contrast, seasonal rainfall totals across most of the Gulf of Guinea region were below normal. Rainfall deficits ranged between 100 and 300 mm across the central and southern areas of Benin, Togo, Ghana, most of the Cote d'Ivoire, and the eastern half of Guinea. The exceptions were the northern and southeastern areas of Nigeria, Liberia, and Sierra Leone, where rainfall totals exceeded 900 mm.

*(ii) Atmospheric circulation*

The above-average 2006 rainy season resulted from an enhanced West African monsoon in the latter part of the season. In August–September 2006, strong southwesterly winds at 925 hPa averaging 3–6 m $s^{-1}$ extended well northward into the Sahel region. This enhanced monsoonal inflow was also evident at 850 hPa with Atlantic westerly wind anomalies exceeding 3 m $s^{-1}$, contributing to a deep penetration of moist, unstable air well into the Sahel region. The enhanced monsoon was also associated with an anomalous low-level cyclonic circulation across the northern and central Sahel, characterized by enhanced cyclonic shear along the equatorward flank of the AEJ. The mean position of the AEJ across the western Sahel was at about 15°N.

*c. North America*

1) Canada—R. Whitewood and D. Phillips

The climate of Canada in 2006 was characterized by near-record temperatures (Fig. 6.9) and near-normal precipitation relative to the 1951–80 base period (Fig. 6.10). Extreme weather took a toll this year with several deaths and millions of dollars in property damage. British Columbia suffered the most in 2006, starting the year with a near-record number of days with precipitation, experiencing drought-like conditions through the summer, and concluding with some of the most powerful storms ever to hit the province.

*(i) Temperature*

Canada, as a whole, experienced its second warmest year—2.4°C above normal (Fig. 6.11), with 1998 remaining the warmest at 2.5°C above normal—since reliable nationwide records started in 1948. Most of Canada had temperatures at least 2°C above normal, with the northern territories experiencing the greatest anomaly of about 4°C. Only an area in northern British Columbia had near-normal temperatures. This marks the 10th straight year of above-normal temperatures, with 6 of the warmest 10 years occurring in the last 10 years. Over the period of record (1948–2006) the national trend is +1.3°C.

Nine of the eleven Canadian climate regions had temperatures that ranked among the 10 warmest, with three climate regions having their warmest year: two covering Nunavut (+3.4° and +2.3°C), and one covering northern Ontario and Quebec (+2.3°C). Three other regions experienced their second warmest year: the region covering much of the Northwest Territories (+3.2°C), Atlantic Canada (+1.8°C), and southern Ontario and Quebec (+1.8°C). Over the 59 years of record, all the climate regions show a positive trend, with the region covering much of the Northwest Territories showing the largest trend of +2.2°C, and the Atlantic Canada region the smallest trend of +0.3°C.

*(ii) Precipitation*

Nationally, 2006 was unremarkable with regard to precipitation totals, ranking 21st wettest, out of 59 years of nationwide records, 2.2% above the

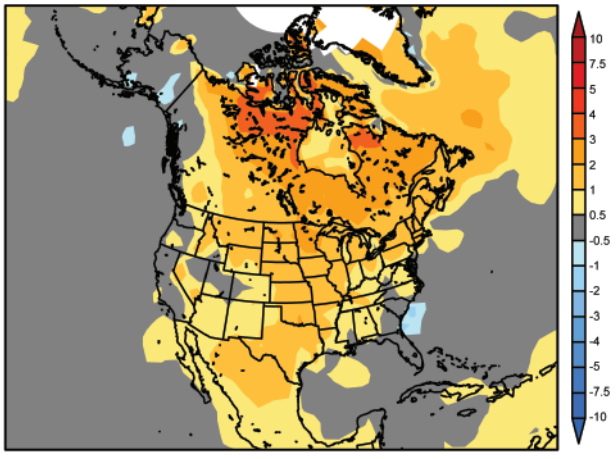


**Fig. 6.9. North American 2006 annual temperature anomalies (°C, 1971–2000 base) from CAMS-OPI.**

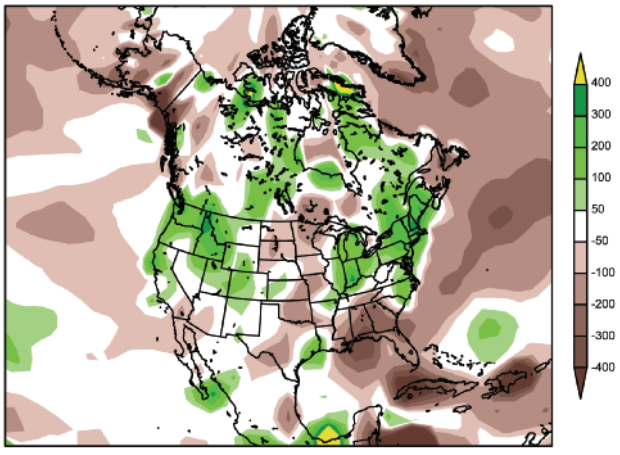


**Fig. 6.10. North American 2006 annual precipitation anomalies (mm, 1979–2000 base) from CAMS-OPI.**

1951–80 normal. This is in sharp contrast to 2005, which was the wettest on record, 13.4% above normal. Wetter areas of the country, those with more than 20% above normal, include the Arctic Islands, southwest British Columbia, central Saskatchewan, northern Manitoba and Quebec, and southern Ontario. Drier areas, those more than 20% below normal, include the western edge of the Northwest Territories, northern British Columbia, a few areas throughout Alberta, southern Manitoba, and northwest Ontario. One climate region, southern Ontario and Quebec, experienced its second wettest year (17.6% above normal); no climate region ranked among its 10 driest years. The southern prairies provinces experienced the driest value, –5.8% (22d driest).

*(iii) Notable events*

Vancouver, British Columbia, set a couple of records in January: the most rainfall for the month (283.6 mm, the normal is 154 mm) and the most number of days with rain (29). The warm season had the opposite effect, with a dearth of rain across much of Vancouver Island. The resort town of Tofino, on the west coast of the island and normally one of the wettest spots in Canada, received no significant rain between 14 July and 16 September. Consequently, the town's reservoir fell to record-low levels. November brought three notable storms to British Columbia's coast. The first, on 5 and 6 November, brought intense rains, at times 10–15 mm of rain an hour for 15 hours. A storm on the 15 November brought heavy rains to the Vancouver area, causing so much turbidity in the drinking water that an estimated two million people were advised to boil their tapwater before drinking. Then, on 25 November, a storm brought 40 cm of snow to Vancouver and Victoria, the amount they normally receive in a year. Three wind storms (greater than 100 km $h^{-1}$), all aimed at Vancouver Island and the lower mainland, were the hallmark of December.

Several tornadoes were reported across central Canada, resulting in one death and costing thousands in property damage. The death was the result of a tornado that hit Gull Lake, Manitoba, on a stormy day on 5 August. One storm system on 17 July generated a series of tornadoes and microbursts that affected areas from Lake Huron through Quebec, one of the longest storm tracks in Ontario's history. Another storm system hit Ontario in early August affecting cottage country, north of Toronto. Remarkably, nobody was killed in the 14 tornadoes that were generated, two of which had winds speeds greater than

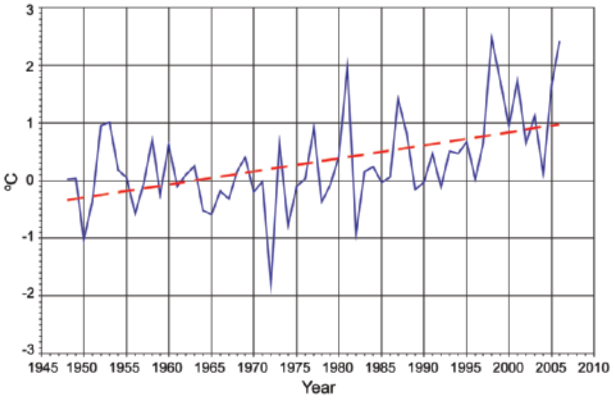


**Fig. 6.11. Annual average air temperature anomalies (°C; blue; 1951–80 base) and the 1948–2006 linear trend showing a +1.3°C increase (red). [Source: Environment Canada.]**

180 km $h^{-1}$. The Canadian Interagency Forest Fire Centre reported an active wildfire season. At the end of the fire season, 1 October, the center reported a total of 9,482 fires (27% more than normal), covering an area of 2,031,705 ha (4% more than normal) for all of Canada.

2) United States—R. R. Heim Jr., D. H. Levinson, N. B. Guttman, and A. M. Sanchez-Lugo

*(i) Overview*

Reliable monthly, seasonal, and annual weather records for the United States exist since 1895, enabling the climate of 2006 to be placed in a 112-year context. The nationally averaged temperature for 2006 was 12.72°C, ranking this year as the second warmest on record. The 2006 annual average temperature was only 0.04°C cooler than the record that occurred in 1998, and ~0.01°C warmer than 1934, making these three years nearly identical in rank (Fig. 6.12). These rankings are based on version 2 of the U.S. Historical Climatology Network. Note that ties are not indicated in figures; ties are labeled as duplicates of the more extreme ranking (e.g., a tie for ranking two and three is listed as two for both).

Nationally, annual precipitation was near the long-term mean, giving 2006 a rank of 55th driest year in the 112-year record. Considerable variability in precipitation occurred across the country and throughout the year. Florida had the driest March–December season on record in 2006, while Indiana ranked as the wettest on record for the same season. Significant drought expanded during the first half of the year, affecting ~52% of the country at its peak in July. The dry conditions were accompanied by a record wildfire season, with almost 10 million acres (~4 million ha) burned during 2006.

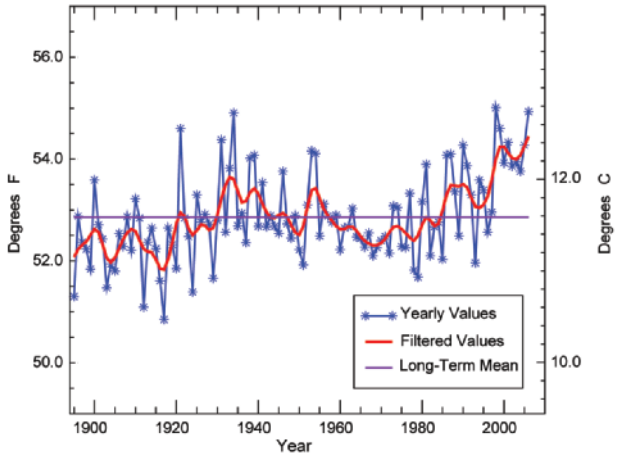


**Fig. 6.12. Annual temperature (°F and °C) averaged across the contiguous United States from 1895 to 2006.**

*(ii) Temperature*

For the contiguous United States, 2006 marked the ninth consecutive year with temperatures much warmer than the long-term average (Fig. 6.12). The past nine years have all been among the 25th warmest years on record, a streak that is unprecedented in the historical record. The long-term warming trend for annual temperatures is approximately 0.56°C (1.0°F) warmer than at the start of the twentieth century. National temperatures persisted at warm or record warm levels throughout 2006 with only two months (September and October) that were cool exceptions.

The 2005/06 winter season (December–February) temperatures were above average across most of the nation with near-average temperatures limited to parts of the Northwest and Southeast and no state ranking below average. The warmer-than-average winter season was due in part to record-warm temperatures that affected the nation in January. The nationally averaged temperature for January 2006 was 3.9°C, which is 1°C warmer than the previous January record set in 1953. All states within the contiguous United States were warmer than average during January, with 13 states, mostly located in the central and northern plains and Great Lakes, ranking as their record warmest.

Cold-air outbreaks affected the western states during March and the Southeast during May, but warm temperatures dominated the nation during the 2006 spring season (March–May). Much warmer-than-average temperatures affected most of the central states, with Texas and Oklahoma having the warmest spring on record. April ranked second warmest in the 1895–present record for the nation, with an average temperature of 13.4°C.

The summer (June–August) months were characterized by an intense and long-lasting heat wave that began in mid-July in the northern plains and upper Midwest, breaking records that stood since the Dust Bowl years in some locations. The heat spread across the plains and moved into the West before returning to the northern plains by late July, then spreading to the East Coast by the first week of August. More than 2,300 daily temperature records were broken in the United States during the last two weeks of July and several more during the first half of August; more than 50 records for the highest temperatures in any July were established. Many locations from the West Coast to the central plains broke records for the most

days above 32.2° (90°F) and 37.8°C (100°F). The month of July 2006 ranked as the second hottest month ever in the 112-year record, with a nationally averaged temperature of 25.1°C, only 0.24°C cooler than the record-hottest month—July 1936. Nationally averaged temperatures gave summer 2006 a rank of second warmest on record just behind 1934 (second warmest) and 1936 (warmest).

The persistent widespread warmth for much of the year resulted in the warmest January–August period on record. Colder weather during September and October brought a brief respite before unusual warmth returned to much of the country during November and December. December 2006 ranked fourth warmest on record.

For the year as a whole, New Jersey, Vermont, Oklahoma, and Texas were second warmest on record (Fig. 6.13a). Another 13 states had one of their top-five warmest years. All of the 48 contiguous states were either record warmest, warmer, or much warmer than average. No state ranked near or below average during 2006. This contrasts with the spatial pattern during the warmest and third warmest years, 1998 and 1934, when at least one state ranked colder than average for the year (Figs. 6.13b,c). The 2006 annual temperature for Alaska ranked near the 1918–2006 average, breaking a string of persistently warm years dating back to 2000. Winter temperatures in 2006 were above average for the seventh consecutive year. Both spring and summer were slightly cooler than average and fall was slightly warmer.

*(iii) Precipitation and drought*

Precipitation in the contiguous United States during 2006 was variable throughout much of the country, with periods of excessive rainfall, especially across the Northwest, Great Lakes, and Northeast, and persistent and developing drought in other areas. Winter storms in the Northwest contributed to the ranking of 10th wettest winter for the region. The Southwest had its second driest winter, with Arizona and New Mexico having their driest winters on record. Precipitation averaged across the nation was below average during spring. Regionally, the Southeast had the third driest spring, whereas the West ranked as the sixth wettest. The Northeast had its wettest summer, exceeding the previous record by more than 25.4 mm (1 in.), while the region consisting of the Northern Great Plains and northern Rockies states had its ninth driest summer. Three states (New Hampshire, New York, and Rhode Island) had the wettest summer on record. Fall was generally wet across the contiguous United States, resulting in a rank of 15th wettest for the nation. Regionally, the Northwest and Northeast ranked as having the 10th and 4th wettest autumn periods, respectively.

Five of the first seven months of the year were drier than average for the contiguous United States as a whole. Combined with unusually warm temperatures, this exacerbated drought across much of the country. By late July, half of the contiguous United States was in moderate to exceptional drought.

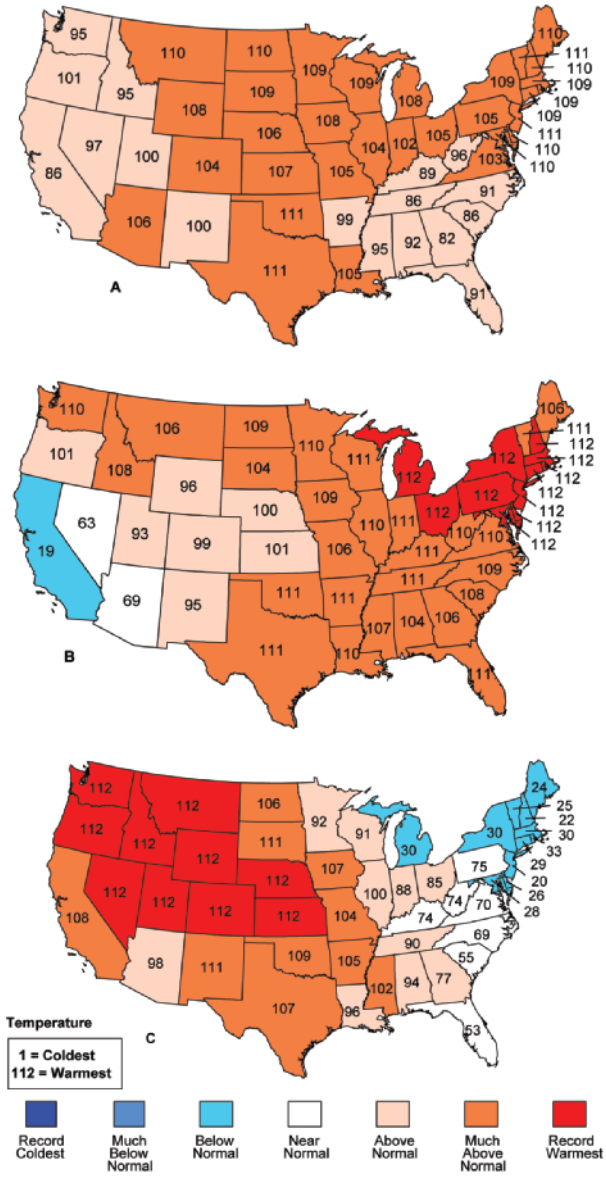


**Fig. 6.13. Statewide rankings (as of 2006) of annual temperature as measured across the contiguous United States for (a) 2006, (b) 1998, and (c) 1934. A rank of 112 (1) in the record represents the warmest (coldest) year in the 1895–2006 period. Ties are included as duplicates of the more extreme ranking. [Source: NOAA/NCDC.]**

Annual precipitation ranks ranged from third driest in Florida and fifth driest in Wyoming and Georgia, to second wettest in New Hampshire and third wettest in Indiana. The Northeast had another wet year, ranking sixth wettest in 2006 and marking the fifth consecutive year with above-average precipitation. In fact, the top two wettest annual periods in New Hampshire occurred during the past two years. Nationally, annual precipitation was near the long-term mean, ranking as the 55th driest year on record.

The year began drier than average across a broad swath of the country from the Southwest to the Great Plains, across much of the Gulf Coast, and into the coastal Southeast. Above-average precipitation continued to erode the drought areas in the Pacific Northwest. This pattern continued throughout the spring and into the summer (Fig. 6.14). By fall, drought was concentrated in the plains, especially in Texas and Oklahoma. By the end of the year, drought subsided in much of the Southeast, but was prominent across parts of the plains.

Several short-lived dry episodes occurred in other regions throughout the year, notably in the mid-Atlantic in February and March, the Northeast coast in March, the Pacific Northwest in July and August, and Florida for much of the year. The percent area of the contiguous United States experiencing moderate to extreme drought (as defined by the Palmer Drought Index) grew steadily from 20% in January, to a peak of about 52% by July, and then declined during the second half of the year. Impacts from the 2006 droughts were felt especially hard by the agricultural and hydrological communities. The South Platte River was nearly dry during the summer, low water levels in the Mississippi and Missouri Rivers forced an early end to barge transportation, several municipalities imposed water use restrictions, livestock was prematurely sold, and crops died before harvest. In some areas, such as in South Dakota and Nebraska, recovery of grazing lands from drought is not expected for at least two years.

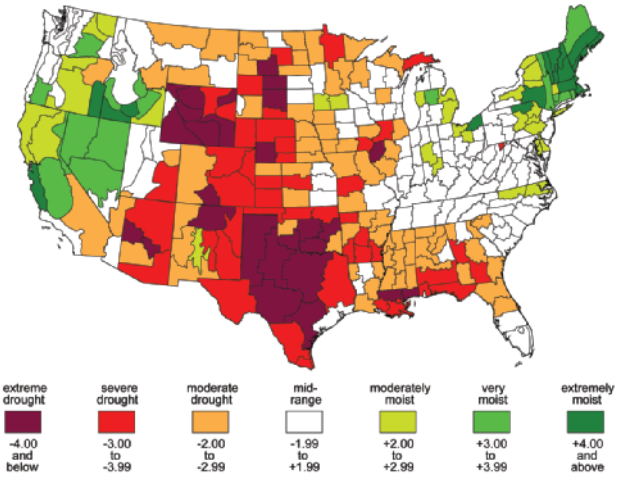


**Fig. 6.14. Palmer Hydrological Drought Index showing the spatial pattern of drought across the contiguous United States during July 2006. [Source: NOAA/NCDC.]**

*(iv) Snowpack*

The 2005/06 snow season was generally above average across parts of the Northwest and below average across the Southwest. The snow cover extent was below average for the North American continent as a whole during the winter season, in which January 2006 had the second lowest snow cover extent behind 1981, as well as during the spring season. This is consistent with a trend toward reduced spring snow cover for North America since 1986. By the end of the spring season, snowpack was above average across the western mountains from the Sierra Nevada in California to the Washington Cascades, and into the interior Northwest.

Notable snow storms in 2006 include a blizzard during the month of February that affected areas of the Mid-Atlantic and the Northeast on 11–12 February. This storm produced 68.3 cm (26.9 in.) of snow in New York City's Central Park. This amount broke the all-time storm total record of 67.1 cm (26.4 in.) set during the 26–27 December 1947 storm. The NESIS classified the February blizzard as a category 3 (major) storm and ranked it as the 20th most intense on record for the Northeast. In Hartford, Connecticut, a snowfall total of 55.6 cm (21.9 in.) broke the old storm total record of 53.3 cm (21 in.), set in 1983. Many locations in the region reported 25–51 cm (10–20 in.) during this event.

An active Pacific storm track during the winter and spring brought a steady supply of snow to the West, Northwest, and Intermountain West. On the other hand, snowfall across Arizona and New Mexico was exceptionally low throughout the season, with most basins reporting less than 40% of normal snowpack at the end of spring.

The 2006/07 snow season started with above-average snowfall across parts of the West. Snowfall accumulations of up to 60 cm (2 ft) fell across the Cascades in late November. During December 2006, two major winter snow storms impacted Colorado and parts of the High Plains. Denver, Colorado, had its third snowiest December on record and endured a major blizzard, which brought the city to a standstill during the holiday travel season. Snowfall in excess

of 90 cm (3 ft) fell across portions of the Colorado Front Range and western High Plains during these two events.

*(v) Wildfires*

Continuing a pattern of increased large fire activity that extends back to the early 1990s, wildland fires reached record levels in 2006. According to the NIFC, preliminary estimates of the area burned exceeded 9.8 million acres (~4 million ha) across the United States this past year. In contrast to the total acreage burned, the annual number of wildfires has decreased steadily since the 1980s; over 96,000 fires were reported in 2006, which was the sixth consecutive year that the annual number of fires for the entire United States has been below 100,000. As discussed by Westerling et al. (2006), there has been an increasing trend of larger wildfires across the West, where the inverse relationship between increasing area burned and decreasing number of fires has been the most pronounced.

There were several notable aspects to the record fire season in 2006, in terms of its timing and severity. Wildfires that initially began across the southern plains in December 2005 persisted into early 2006. Below-normal precipitation and extreme drought conditions aided in the development of numerous wildfires across Oklahoma, Texas, and Arkansas, with over 1.5 million acres (~600,000 ha) burned over the first three months of the year in the southern area (which encompasses 13 states, Puerto Rico, the Virgin Islands, and the District of Columbia). During the spring, fire activity spread to the Southwest, with the most severe activity concentrated in New Mexico and southern California. By summer, wildfires had spread into the Great Basin and Pacific Northwest, with large fires affecting most of the West by the end of July. Large fire activity spread northward, because the Pacific Northwest was the focal area in August and early September, while during the fall, activity shifted again into southern California.

*(vi) Severe extratropical storms*

Several severe extratropical cyclones affected the United States in 2006. The first of these occurred early in the year on 18 January, when a powerful winter storm brought heavy rainfall, strong winds, and heavy snowfall to sections of the East Coast. During the spring peak in severe weather, several tornado outbreaks occurred in the southern plains, as well as the Tennessee and Ohio valleys, which produced over 500 tornadoes and nearly 50 fatalities during March and April combined. Northwestern Tennessee was the hardest hit region, with 23 fatalities attributed to the storms. According to preliminary statistics compiled by NOAA's Storm Prediction Center, there were 1333 tornadoes reported across the United States in 2006, with April having the most of any month (324). The most severe day of the year was 12 March when 142 tornadoes were reported.

Two large extratropical storms of note occurred toward the end of 2006. On 21–22 November, a strong extratropical cyclone developed off the southeastern coast of the United States, producing a variety of severe weather events in the Southeast and Mid-Atlantic. Heavy rainfall and strong winds were reported along the coastline from South Carolina northward through Virginia. Winds gusting over 115 km $h^{-1}$ (70 mph) were reported along the coast of North Carolina. On 13–15 December, a powerful storm system came ashore along the Pacific Northwest coast and generated strong winds, heavy rainfall, and high-elevation snows. Wind gusts reaching hurricane force caused power outages across Washington and Oregon.

**3) Mexico—V. Davydova Belitskaya and A. Douglas**

Mexico was on average 5% wetter than normal in 2006, with much warmer than normal temperatures. Mexico's SMN reported a national precipitation average of 808 mm, compared with an historical average of 771 mm (1941–2000). The nationwide annual mean temperature was 21.9°C, which was a 1.2°C above the long-term climate average. However, it should be noted that most of the stations used to create the nationwide temperature values are in large urban centers. In light of inherent heat island biases in the underlying data, which are currently unaccounted for, care should be taken in interpreting the 1.2°C climate anomaly.

The rainfall distribution was not homogeneous throughout the year or across large sections of the country. The year started abnormally dry but it quickly recovered with a good rainy season from May to October (total rain or warm-season precipitation was 111% of normal according to the SMN; see Fig. 6.15). The summer of 2006 was typified by widespread and consistent monsoon rainfall through much of the country; this helped to raise reservoir levels throughout the western states following a long series of dry winters in that region.

Some states reported major rainfall deficits for the year. These include Baja California (46% below the long-term mean), San Luis Potosí (25% below), México and Yucatan (19% below), Oaxaca and Sonora (16% below), Hidalgo (15% below), Zacatecas and Tamaulipas (12% below), Quintana Roo (10%

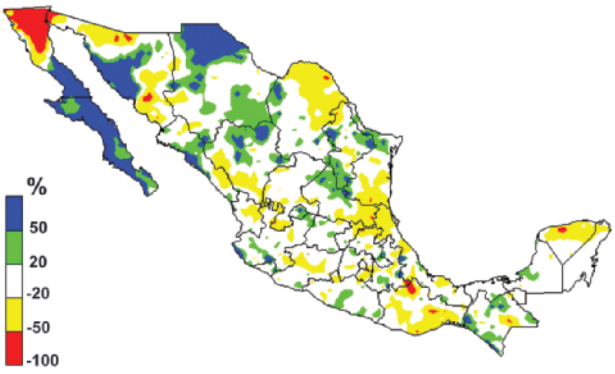


**Fig. 6.15. Precipitation anomalies (%) during the May–October 2006 rainy season in Mexico.**

below), and Sinaloa (7% below). The deficits in the northwest were associated with a poor winter rainy season in early 2006 and again in late 2006. The development of El Niño conditions during the later half of the year was associated with four east Pacific tropical storms that recurved toward the west coast of Mexico: John, Lane, Norman, and Paul. In contrast, there were no landfalling tropical storms on the east coast of Mexico; this helped to contribute to the observed dryness in the Yucatan Peninsula and northeast Mexico.

Despite the very warm annual mean temperature; a notable cold outbreak occurred in northern Mexico on 17 January when Temosachic and La Rosilla recorded –15°C, Yecora recorded –10°C, Pabillon recorded –7°C, and Saltillo recorded –4.5°C. An exceptionally early winter cold outbreak occurred in the northwest on 1 December, with La Rosilla falling to –13.5°C and Temosachic to –12°C. One of the most significant and highly unusual meteorological events occurred during the last week of the year in the states of Chihuahua and Durango when very heavy snows covered the western section of the these two states, with mountainous areas exceeding well over 10 in. of snow.

*d. Central America and the Caribbean*—P. Ramírez and J. Peréz Fernández

1) Precipitation

Most of the Central American isthmus and the Caribbean experienced drier-than-normal conditions in 2006 (Fig. 6.16). Precipitation deficits were severe and more persistent over what is known as the "dry corridor" of Central America (western Guatemala, central Honduras, northern and central Nicaragua, and western El Salvador). August had the highest precipitation deficits compared to the 1971–2000 period. Precipitation deficits continued during September and October along the dry corridor. In parts of Nicaragua and Honduras, deficits between 35% and 55% of the long-term mean were observed in September and October. October is when most tropical cyclones form close to Central America, generating very intense rains or "temporales" on the Pacific side of the isthmus. The temporales were lacking in autumn 2006, because El Niño conditions were observed in the tropical Pacific. In November, the Caribbean side of Central America was affected by a cold front that brought strong rains to the northern Honduras coast and central Panama. Late-year rains, associated with the divergent phase of the MJO, were observed on the Pacific side of Central America through the middle of December.

2) Temperature

Annual mean surface temperature in 2006 was above normal across much of Central America and parts of the Caribbean (Fig. 6.17). Positive anomalies of between 0.3° and 0.4°C were found over Central America (south and west of Honduras and El Salvador, Nicaragua, and northern Costa Rica), and were near normal across Panama. Temperatures that were near normal predominated the first two months of the year. In March, resulting from a late intrusion of cold fronts into the region, below-normal monthly means were observed in Belize, western Guatemala and Honduras, and western Panama. At the same time, positive anomalies were registered in Costa Rica and Nicaragua. Positive anomalies dominated along the whole region from May to October. The warmest

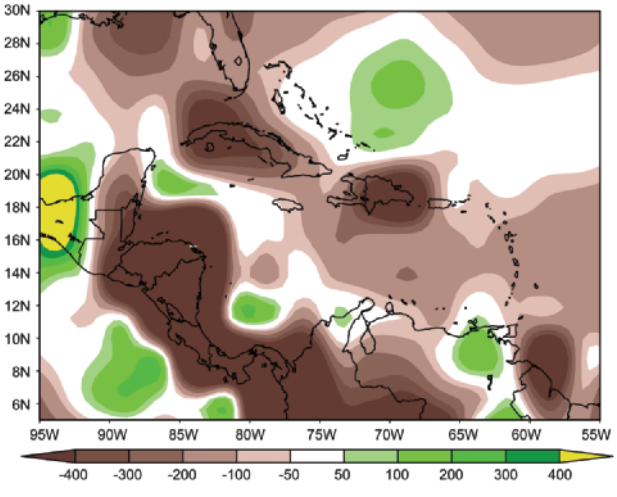


**Fig. 6.16. Central American and Caribbean 2006 annual precipitation anomalies (mm, 1979–2000 base) from CAMS-OPI.**

conditions, relative to climatology, were observed in July and August, when monthly departures from the 1971–2000 mean exceeded 0.5°C. In November, mean temperatures in northern Central America (northern Guatemala and Belize) showed negative anomalies. In the southern extreme of the Central American isthmus (eastern Panama), temperatures remained above normal. The whole region showed positive anomalies once again in December.

3) Notable events

In 2006, the reduced hurricane activity in the Caribbean (consistent with the development of a weak El Niño event) spared Central America from heavy rainy events, creating a stark contrast between 2006 and 2005, when tropical cyclones had a significant impact on the region. Also consistent with El Niño, Central America experienced drier-than-normal conditions in the latter half of 2006. Cold surges in November impacted the region with low temperatures in the north and stronger-than-normal winds and rainfall in southern Costa Rica and Panama. The surges caused significant damage to vegetable crops in the Guatemala Plateau. Along with high humidity values, heavy flooding events produced floods in the Caribbean plains of Honduras and central Panama, where more than 450 mm of rain fell in some parts between 20 and 28 November.

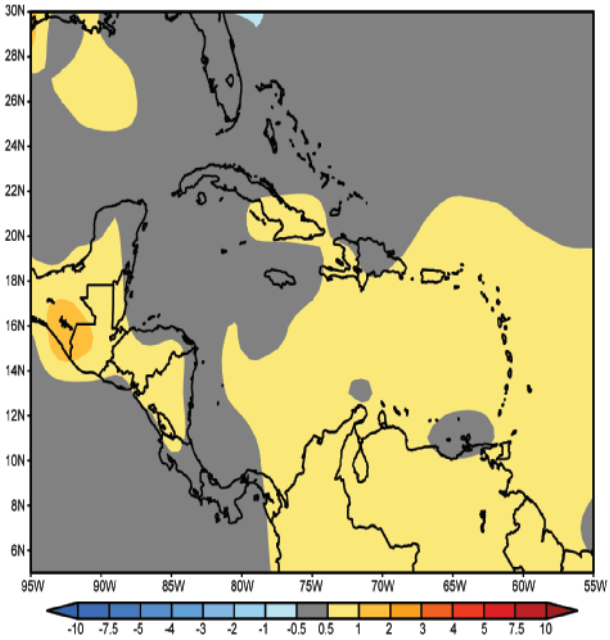


**Fig. 6.17. Central American and Caribbean 2006 annual temperature anomalies (°C, 1971–2000 base) from CAMS-OPI.**

## *COUNTRY SPOTLIGHT:* CUBA—R. Peréz Suárez, C. Fonseca Rivera, B. Lapinel Pedroso, V. Cutié Cansino, A. M. Carrión Romero, M. Hernández Souza, and D. Boudet Roco

The Cuban climate in 2006 was affected by the weak El Niño, primarily from September through December. Precipitation was lower than normal in September and October. In November and December, precipitation was above normal as cold fronts reached the Caribbean, and the subtropical jet was southeast of its usual position (consistent with El Niño). December was a particularly warm month across Cuba.

The year 2006 as a whole was very warm (11th warmest since 1951), with an average temperature of 25.85°C, 0.36°C above normal (Fig. 6.18). January and December contributed most to the warm anomaly. January, the coldest month, brought positive anomalies of 0.5°–1°C across Cuba, whereas December was the second warmest since 1951 (just behind 1986). Many Cuban stations broke maximum or minimum temperature records in 2006, especially during a cold outbreak in late November.

Rainfall deficits affected parts of western and central Cuba. Eastern parts received abundant rainfall, including Holguín y Guantánamo (comparing against the 1971–90 normal). Tropical cyclones Alberto and Ernesto both impacted Cuba. In June, Alberto brought intense rains to western Cuba, especially in Pinar del Río and Isla de la Juventud.In August, Ernesto brought torrential rains to central and eastern Cuba. Despite these two storms, the 2006 hurricane season was relatively quiet for Cuba, considering the activity witnessed this decade.

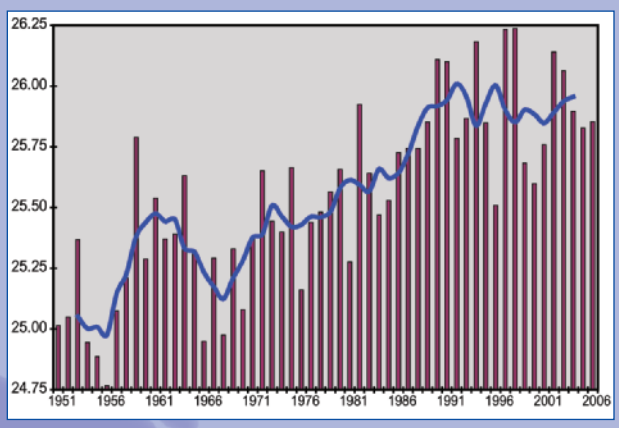


**Fig. 6.18. Annual average temperatures (°C) over Cuba from 1951 to 2006.**

e. *South America*

1) Overview—M. Rusticucci and J. L. Camacho

The overall weather in South America in 2006 was very dry or wet in parts (Fig. 6.19), but largely warmer-than-normal (Fig. 6.20). La Niña conditions prevailed in the central equatorial Pacific for a few months at the start of the year. A weak-to-moderate El Niño event developed by the middle of the year; it reached its maximum strength by late November. Modulation by the MJO also played a role. Some extreme rainfall events occurred in Colombia and Ecuador. In July–August, ENSO shifted to the warm phase. In the second part of the year, some classical teleconnections were active, especially in central or Atlantic areas. Most notably, there were no reports of hurricane activity in the north. However, the teleconnections over the Pacific side were less clear and the ITCZ in the eastern Pacific was not as intense as expected.

For temperature, the most important feature was the overall positive anomaly. Consistent with the overall warming pattern since 1950 (Fig. 6.21), 2005 and 2006 were warmer than average, though not reaching the peak of 1998. Some areas of Brazil experienced record-breaking temperatures in austral summer, for example, the 44.6°C record for Bom Jesus on 31 January. A belt from northern Argentina, Paraguay, Uruguay, and southern Brazil showed a marked warm anomaly in July. In contrast, fall (April–May) was cold in the tropical Andes and in southern areas due to marked cold-air advection. Extreme temperature variability on weekly or monthly time periods was noteworthy in Brazil.

Rainfall anomalies were highly variable across the region. The Andean territory of Colombia and Venezuela was in general above average. Neighboring areas of Orinoco and Amazonian basins were below average. There was yet another year of drought, adding to the long-term event that southern Brazil, Uruguay, and parts of Argentina have been enduring. Much of southern Peru, a relatively arid zone, had rainfall clearly above normal. South-central Chile (near 40°S), the rainiest area in the country, received more rain than normal, as did Patagonia. A combination of extreme events and passage of fronts more frequent than normal in the second half of the year could explain this fact.

2) Northern South America and the southern Caribbean—J. D. Pabón, G. Hurtado, and M. Henriquez

During the first half of 2006, the climate over northern South America was influenced by La Niña conditions. Precipitation was above normal over Caribbean and Andean sectors of Colombian territory and western Venezuela. In May–June, these conditions were accentuated by the effects of a strong convective phase of the MJO. Consequently, heavy rainfall events produced landslides, flash floods in mountain regions, and lowland floods, killing over 100 and affecting over 100,000.

Monthly mean air temperature during the first six months in the region was between near normal and slightly below normal, with the exception of February when isolated regions recorded slight positive anomalies. Negative anomalies of monthly precipitation

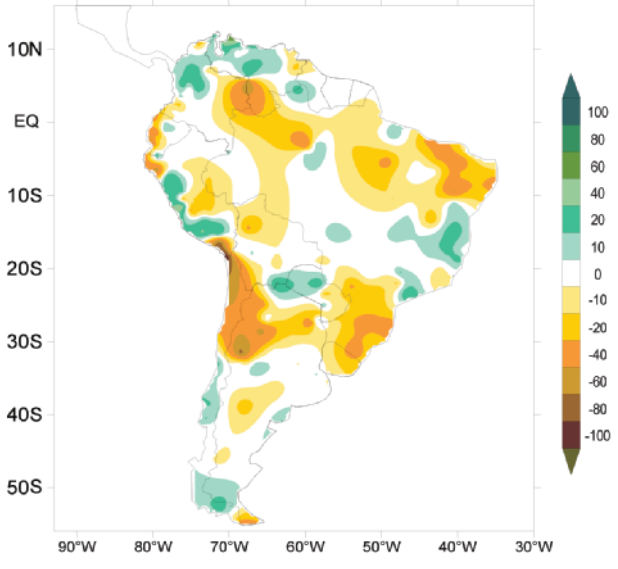


**Fig. 6.19. South American 2006 annual precipitation anomalies (mm, 1979–2000 base) from CAMS-OPI.**

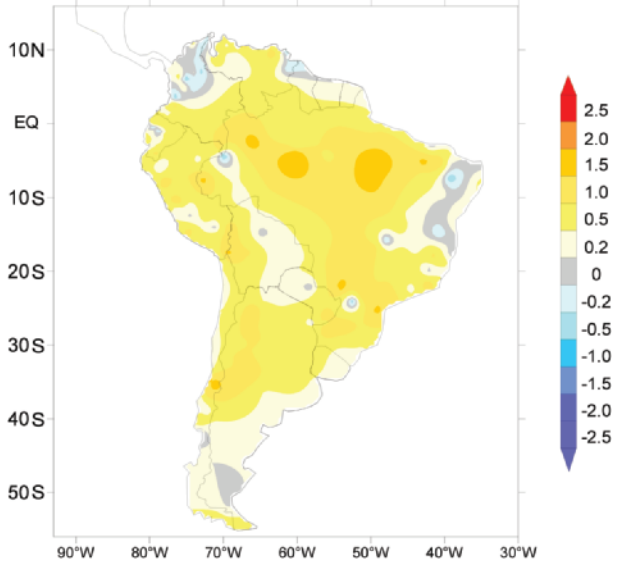


**Fig. 6.20. South American 2006 annual temperature anomalies (°C, 1971–2000 base) from CAMS-OPI.**

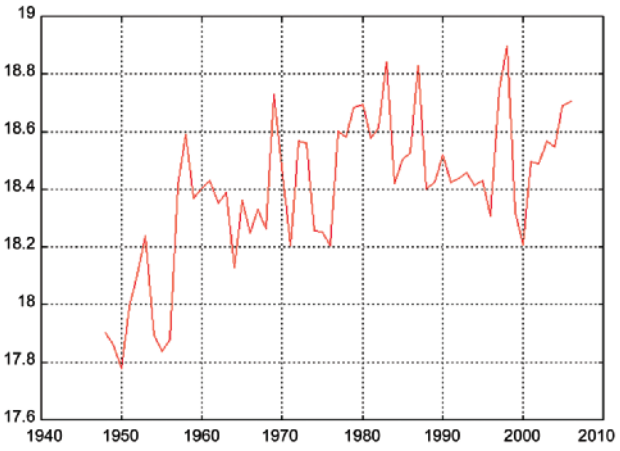


**Fig. 6.21. Time series of annually averaged air temperature (°C), spatially averaged from 15°N to 55°S and 30° to 90°W, for the 1948–2006 period. [Source: NCEP–NCAR reanalysis at www.cdc.noaa.gov/cgi-bin/Composites/.]**

dominated over the region from July to October. The rainfall deficit was strong in September–October thanks in part to a subsidence phase of the MJO (Fig. 6.22). A very strong convective phase of the MJO was observed in November over northern South America; this phase reactivated rainfall over the region and above-normal precipitation was reported for November–December.

In the period from July to September, monthly mean air temperatures were near to below normal. In October, some sectors recorded slight positive air temperature anomalies, and during November–December, consistent with El Niño, positive anomalies dominated the region. As in the tropical Atlantic, the tropical cyclone season in the Caribbean Sea was not active. Only some tropical waves (easterly waves) observed over the Caribbean Sea influenced the weather of the Caribbean sector of this region.

3) Tropical Andean region—E. Jaimes and R. Martínez

During January and February, the South Pacific anticyclone was between normal to slightly more intense. The frequency of inverted troughs brought warmer conditions to the Peruvian coast. The ITCZ and the ET were located slightly north of their normal position. However, the Bolivian high was located to the west of its normal position, favoring significant rains over the central and southern mountain regions in Peru and affecting the mountain region of Bolivia with some scattered rains. Conversely, the periodic formation of the Atlantic convergence zone contributed frequent rains over the Amazonian region in Brazil, Bolivia, and Peru. In March, the formation of a second band of the ITCZ in the eastern Pacific Ocean was observed, close to 5°S with moderate activity. The ET formed near 8°S with convective activity in the Amazonian region of Brazil, causing rains and storms with an intensity ranging between moderate and strong. Conversely, some migratory highs caused instability in the atmosphere, forming convective complexes in the jungles and highlands of Bolivia.

For the April–May period, the South Pacific anticyclone started to show some intensification, typical of the season; however, a second band of the ITCZ persisted, though smaller than in March, favoring rains along the Peruvian coast. In some days in April, migratory highs were generated (up to 1030 hPa) that favored the presence of strong winds from the south, affecting northern Argentina, Paraguay, Bolivia, and south-central Peru with cold and dry air. This led to significantly lower temperatures in the southern jungles of Peru. Early meteorological frosts occurred in many parts of the southern mountainous region in Peru and in the highlands of Bolivia.

The South Pacific anticyclone and ITCZ moved to the north during austral winter, as expected. In July, a thermal orographic low was observed at 1005 hPa and contributed to the convergence of humidity and to the increase of air temperatures in Paraguay, the

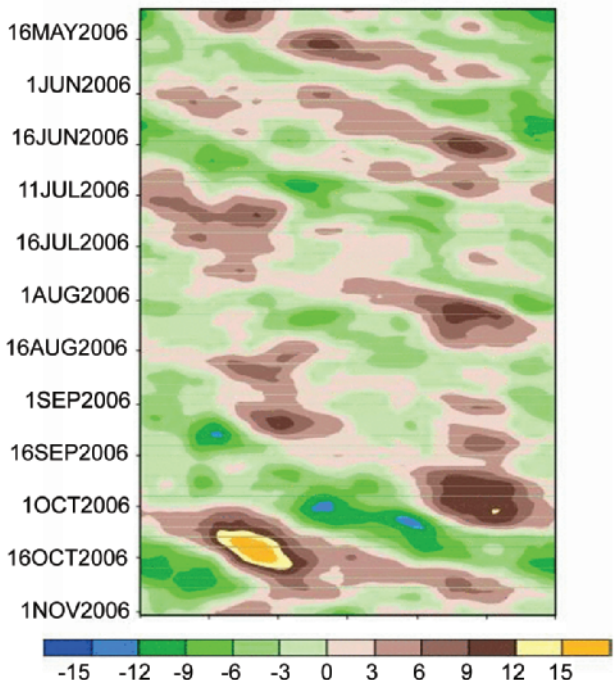


**Fig. 6.22. Hovmöller diagram, averaged from 5°S to 5°N, of 200-hPa velocity potential anomalies. [Source: www.cpc.ncep.noaa.gov/products/.]**

southern jungles of Bolivia, and the north and central parts of Argentina. In August and September, the migratory highs systems in the continent were very frequent (though not very intense), keeping the skies clear. Frosts occurred in many areas located near 2500 m above sea level in the Amazonian regions of Bolivia, Peru, and Brazil. In November, there were some circulation patterns considered to be characteristics of (an early) austral summer, such as the behavior of the Bolivian high. This caused heavy precipitation over Huanuco, San Martin, and Ucayali; it later affected Bolivia with strong winds from the north.

#### 4) Tropical South America, east of the Andes—J. Marengo

In general, the most important feature of summer rainfall for 2006 was the occurrence of rainfall extremes that produced floods and avalanches, claiming lives and resulting in huge economic losses. During the summer of 2006 (December 2005—March 2006), and following a drought situation that affected southwestern Amazonia during most of 2005 (Marengo et al. 2007, manuscript submitted to *J. Climate*), the Brazilian state of Acre experienced abundant rainfall. Below-normal precipitation was observed in southeastern South America, featuring a drought situation in southern Brazil and neighboring Uruguay, which has lasted at least 3 years. Changes in Southern Hemisphere circulation may be the cause of this extended drought. Meanwhile, most of northern South America and Bolivia saw above-average amounts of rainfall. In January, Bolivia was affected by destructive flooding and landslides.

Intense rainfall during the end of 2005 and beginning of 2006 caused flooding along rivers and coastal areas of Guyana, including the capital, Georgetown. Thousands of acres of farmland in Barima Waini and Mahaica Berbice were lost due to flooding. In the state of Bahia in the southern section of northeast Brazil, drought affected the agricultural production with losses of about 30% in corn and 29% in bean production. By the end of summer and the beginning of the fall season (March–May 2006), abnormally heavy rainfall of about 200 mm above normal in the Brazilian state of Para caused flooding along the Tocantins, Xingu, and Tapajos Rivers, all of which are Amazon River tributaries. Meanwhile, heavy rainfall triggered new flooding and landslides in Colombia, particularly along the Pacific coast and in central sections of the country during January and February, with values between 100 and 150 mm month$^{-1}$ above normal.

Consistent with the weakening of the cold episode in the Pacific in 2006, northeastern Brazil, northern Argentina, and southern Peru experienced above-average rainfall, while Uruguay, southeastern Brazil, and much of Colombia had a deficit of rainfall during April. The rainy season in northeast Brazil that extends from February to May was near normal. In July–September 2006, dry anomalies characterized northern and southeastern South America, from northern Colombia to Venezuela, with deficits of about 200 mm month$^{-1}$ below normal. September and October featured abundant rainfall (about 200 mm month$^{-1}$ above normal) from the transition region between Amazonia and northeast Brazil, extending up to southeastern Brazil. The latter region (especially the region off the coast) experienced above-normal rainfall until December 2006, due to the penetration of frontal systems coming from the south.

Most of tropical South America, east of the Andes experienced a warm 2006, with anomalies between 2° and 3°C warmer than normal, especially during summer between the Andes and eastern Amazonia. Temperature records were broken in the austral summer in Brazil. Record highs above 41°C were also detected in other cities in southern Brazil in January 2006. Associated with the extended drought, these were among the highest temperatures during the last 40 years. In May, in a notable departure from recent trends, many Southern Hemisphere land areas saw temperatures well below average, including much of western Brazil, and southward to Uruguay, Paraguay, and northeastern Argentina. During September, extreme cold weather affected southern Brazil. During the austral winter season, air temperatures in tropical South America east of the Andes were very high, sometimes about 3°C warmer than normal. The city of São Paulo reached a maximum of 30.2°C on 24 July (a record for the last 63 years), accentuating the notion that the Brazilian winter of 2006 was highly irregular, being warmer than normal in most of Brazil even though extreme cold days occurred.

#### 5) Southern South America—P. Aceituno, M. Bidegain, J. Quintana, and M. Rusticucci

Temperature anomalies were positive in 2006 over most the region. Anomalies between 0.5° and 1.5°C were observed in northern Argentina, northern Chile, Paraguay, and northwest Uruguay. The beginning of 2006 was anomalously warm in northwest Argentina and Chile. In southern Uruguay and the province of Buenos Aires, mean temperature was slightly below normal. Autumn in southern South America was characterized by below-normal temperatures along

Uruguay and eastern Argentina (+0.2° to –1.0°C), particularly during May, when the negative anomalies extended into Paraguay, southern Brazil, Bolivia, and the southern portion of the Amazon basin. The winter season was warm over the entire region with temperatures from +1.0° to +2.0°C over the climatological mean. June and July were exceptionally warm in Paraguay, northern Argentina, Uruguay, and southeast Brazil. In July, mean temperature anomalies exceeding +4.0°C were observed over Paraguay and the surrounding regions, while the area with anomalies above +2.0°C included most of the continental territories between 6° and 38°S. The warm spell ended abruptly by the end of the month due to a powerful cold-air incursion than also affected southern and western Brazil, Bolivia, Peru, and southern Colombia. In Uruguay, the daily mean temperature dropped around 10°C between 26 and 27 July, while frost was observed in central Argentina and daily minimum temperatures below –10°C occurred in the southern part of the country (Patagonia).

The spring season showed positive anomalies of the order of +0.5° to +1.0°C. Significant weather events occurred in Argentina during July. During the first half of the month, a high pressure system located on the eastern side of the continent favored the advection of warm and moist air from the Amazon basin. An extreme Zonda event occurred between 11 and 12 July, producing significant property damage. At the same time, a powerful winter storm hit central Chile and caused significant flooding. On 26 July, a warm and wet air mass affected the central and northern portion of the country, provoking rain showers and intense thunderstorms.

Across northeast Uruguay and southern Brazil, the moderate-to-exceptional drought that persisted during 2006 contributed to a record low in the Uruguay River level. Nevertheless, on 23 March, the most intense rainfall episode in the last 50 years (232 mm in 24 h) affected southeast Uruguay and the adjacent territory in southern Brazil. During another intense rainfall episode that affected the Uruguayan coast of the La Plata River on 17 December, 200 mm were measured at Nueva Palmira during a 24-h period. In contrast, a seasonal rainfall deficit of about 40% characterized the eastern Uruguayan territory of the Laguna Merin basin (along the border with Brazil).

The rainfall regime along the extratropical west coast of South America is determined by the frequency and intensity of cold fronts moving eastward in the southeast Pacific. The year 2006 ended with a rainfall surplus between 10% and 20% at most of the stations south of 30°S. However, the rainy season started late in central Chile (30°–35°S), with a rainfall deficit at the end of May that was nearly –70%. The anomalously intense frontal activity in June produced a quick recovery from the deficit. Very wet conditions continued during July along the west coast of the continent, southward from 30°S. A powerful extratropical winter storm hit the region from 9 to 12 July, producing landslides, flooding, and damage associated with strong winds. The 107 mm of rainfall measured at Concepción (37°S) on 10 July was the second highest daily rainfall reported at this station since 1950. The region of Bio-Bio in central Chile (around 37°S) suffered the greatest damage and was declared a disaster zone. The passage of this frontal system, with associated strong westerlies in the middle troposphere, was the origin of a severe episode of Zonda winds along the eastern side of the Andes on 11 July. Although August was relatively dry in central Chile (30°–35°S) an extraordinary rainfall episode occurred along the extremely arid region of northern Chile during the night of 29 August, associated with the arrival of an extratropical cyclonic disturbance. Precipitation (7.7 mm at Antofagasta, 23°S) and strong winds produced considerable damage in urban areas of this region where it very seldom rains.

### 6) Notable events

*(i) Drought in southern Brazil*—J. Marengo

Southern Brazil exhibited a regular pattern of precipitation, with maxima in austral spring and autumn. An analysis of rainfall since January 2003 to June 2006 shows that precipitation was below the climatological mean during most of the period (especially during the peak season) with above-normal rainfall outside the rainy season. During 2004 and the period between December 2005 and June 2006, rainfall has been below normal. This drought especially impacted the hydroelectric sector, with precipitation below 60% of the long-term mean over the basins of the Uruguay, Jacui, and Iguaçu Rivers. During the 2006 winter, the reservoir levels along these basins reached values lower than 20% of their averages. The drought produced severe impacts in the state of Rio Grande do Sul in southern Brazil during the first six months of 2006, with losses of 11% and 48% reported for the soybean and wheat harvest, respectively. Rainfall deficits were also observed in neighboring northern Uruguay during this time of year. Rainfall in Rivera/Santana do Livramento, near the Uruguay/Brazil border, was about 60% of the normal. Discharge of the Uruguay (Fig. 6.23) and Negro Rivers reached their lowest values since 1968,

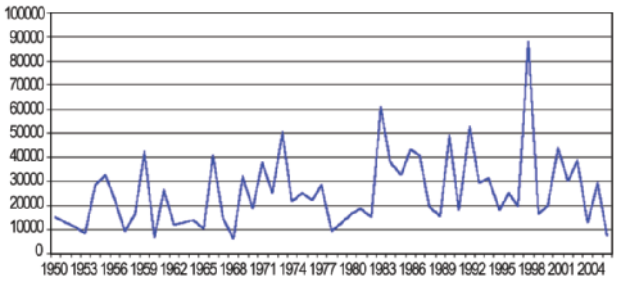


**Fig. 6.23. Seasonal January–June discharge ($m^3 s^{-1}$) of the Uruguay River at Salto Grande during 1950–2006.**

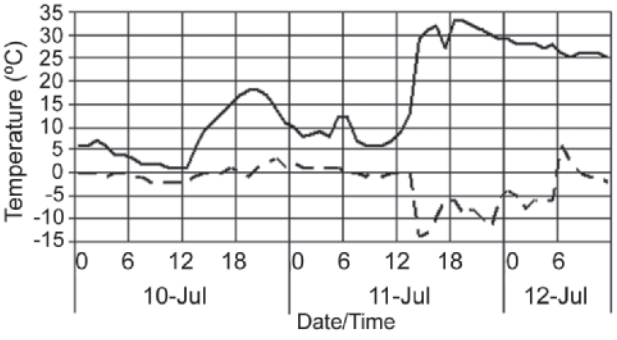


**Fig. 6.24. Hourly evolution of surface temperature (°C) and dewpoint temperature (°C) in San Juan, Argentina.**

producing shortages in hydroelectric power in the whole country.

The SPI, as defined by McKee et al. (1993, 1995), quantifies the drought in southern Brazil. The SPI accounts for the various time scales at play during drought and subsequent rains. For the last four years, the SPI values were lower than the moderate (–1.0) to very dry (–1.5) threshold. The drought situation affecting southern Brazil is not just the consequence of the rainfall deficit in 2006, but is due to a rainfall deficit that has accumulated during the last three years.

The causes of this extended drought have been linked to variability in the regional circulation. Cold fronts represent the main rainfall-producing mechanisms in southern Brazil. An assessment of the number of cold fronts during January 2003–June 2006 affecting the region shows that this number was below normal. This behavior is consistent with an increase in the frequency of blocking systems in southern South America and a reduction in wavenumber in the higher latitudes of the Southern Hemisphere.

*(ii) The Zonda event in Argentina*—F. Norte, G. Ulke, S. Simonelli, and M. Viale

The Zonda is a strong, warm, and very dry wind associated with adiabatic compression upon descending the eastern slopes of the Andes, preferentially in winter and spring. It is the Argentine version of katabatic winds, which are also called mistral, chinook, Santa Ana, and foehn winds in different parts of the world. Although this phenomenon occurs across the entire length of the extratropical Andes, it is most frequently detected near the cities of Mendoza (33°S) and San Juan (31.5°S), which are the most populated cities in western Argentina (1.5 million inhabitants).

Four categories define the strength of the Zonda. The top two categories, "severe" (Z3) and "extremely severe" (Z4), respectively, account for less than 8% of Zonda events (Norte 1988). The event of 11 July reached categories Z3 and Z4 in the surrounding area of Mendoza and San Juan, where wind speeds reached over 120 km $h^{-1}$ during a 2–3-hour period without interruption.

The synoptic surface and upper-air conditions were the typical ones associated with a severe Zonda wind occurrence: 1) a surface cold front approaching the central coast of Chile driven by a 500-hPa-level trough, 2) a deep low pressure surface system approximately over 55°S and 65°W, and 3) a strong upper-level jet stream. The main feature of the event is the sharp polar air advection from the south and an intense meridional 500–1000-hPa thickness gradient. The occurrence of the Zonda episode was characterized by a marked increase in temperature and a decrease in humidity. Thus, in Mendoza, the temperature reached 28.2°C while the dewpoint dropped to –6°C. At San Juan, the air temperature rose to 33.0°C, and the dewpoint fell to –15.0°C (Fig. 6.24). The Zonda caused severe impacts in the region, including fires, power outages, fallen trees, and destroyed buildings.

*f. Asia*

1) West and central Asia—O. Bulygina, N. N. Korshunova, and V. N. Razuvaev

The year 2006 in Russia showed near-normal rainfall (Fig. 6.25), while much of the country was quite warm (Fig. 6.26). The anomaly of the mean annual air temperature averaged over the Russian territory was 0.5°C. In early 2006, most of the Russian territory experienced severe frosts. Record-breaking low mean monthly temperatures were recorded in western Siberia. In both the Yamalo-Nenets Autonomous Area and the Khanty-Mansisk Autonomous Area, the minimum air temperature dropped as low

as –58°C. Six meteorological stations in the Tomsk region recorded temperatures that were 0.1°–0.4°C below the absolute minimum. Daily anomalies exceeded –25°C.

In the Kemerovo region, thermometers dropped to –53°C. In the second and third 10-day periods, record-breaking anomalies were recorded in the Tomsk and Kemerovo regions and in the Krasnoyarsk Territory. This winter, the Siberian anticyclone moved far to the west of its usual position over Yakutia. The anticyclone center was over the southern part of the Krasnoyarsk Territory. Therefore, severe frosts persisted there for a long time. At the station of Bor, frosts below –30°C lasted 22 days—a new record. The same pattern was observed in the northern part of the Tomsk region at Aleksandrovskoe, where severe frosts persisted for 24 days, with frosts below –30°C persisting for 23 days.

Record-breaking low minimum air temperatures were recorded in the second 10-day period of January in the eastern parts of the central Chernozem region. By 24 January, severe frosts reached southern regions; in Krasnodar and Adygeia, the recorded air temperatures were –34° and –29°C, respectively. Even on the Black Sea coast, in the vicinity of Anapa-Novorossisk, the air temperature dropped as low as –25°C. The Astrakhan region (Verkhny Baskunchak) experienced the record-breaking low minimum air temperature of –33.3°C. The lowest minimum air temperatures for the whole period of record were observed in Krasnodar (–30.6°C) and Stavropol (–24.3°C). On 30 January, temperatures in Krasnoyarsk dropped to –41.3°C, dropping below the previous daily record of –40°C. In some of the settlements in the Krasnoyarsk Territory, the air temperature dropped as low as –50°C. The lowest temperature in Russia was registered on 30 January in the Evenki Autonomous Area (–58.5°C in the Kerbo Settlement). For comparison, in Oimyakon, the town in Yakutia that is the "cold pole" in the Northern Hemisphere, thermometer readings did not drop below –45.4°C.

In most of European Russia, it was also cold in February. Severe frosts persisted in the southern part of the Evenki Autonomous Area and in the central Krasnoyarsk Territory (1°–2°C below normal). In western Siberia, particularly in the north, February was warm. In the north of the Yamalo-Nenets Autonomous Area, mean monthly temperature anomalies were 6°–8°C. In northeastern Siberia, mean monthly air temperature in February was 3°–5°C above normal. February was also warmer than normal in the Tyva Republic. Maximum positive anomalies (more than 4°C) were recorded in the northwest of the Yakutia-Sakha Republic and in the east of the Chukotka Autonomous Area. In Chukotka, warm weather was accompanied by a large amount of precipitation, frequent snow storms with wind speeds attaining 23–28 and 35–40 m $s^{-1}$ on the coast, and poor visibility. Above-average precipitation was also recorded in the eastern Amur Region, central Khabarovsk Territory, and Maritime Territory, and on the western coast of Kamchatka.

In March, a substantial part of European Russia experienced cold weather: the entire Northwestern Federal District and nearly all of the Central Federal District, except for the Voronezh, Belgorod, and Kursk regions. At the cold center, the anomalies were –6°C. In Ural, warmer weather was accompanied by substantial precipitation (200%–300% of monthly

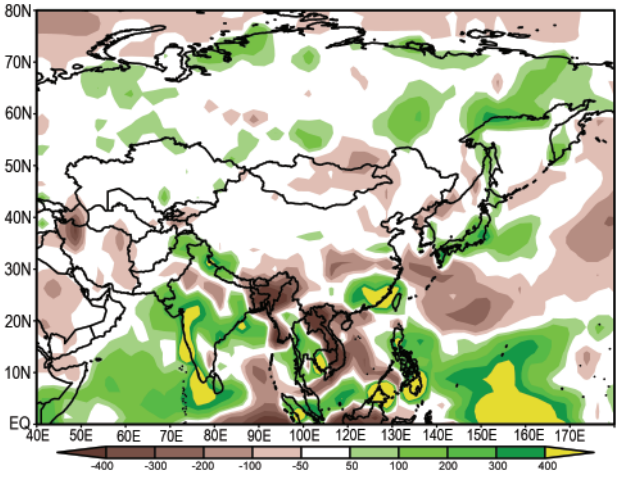


**Fig. 6.25. Asian 2006 annual precipitation anomalies (mm, 1979–2000 base) from CAMS-OPI.**

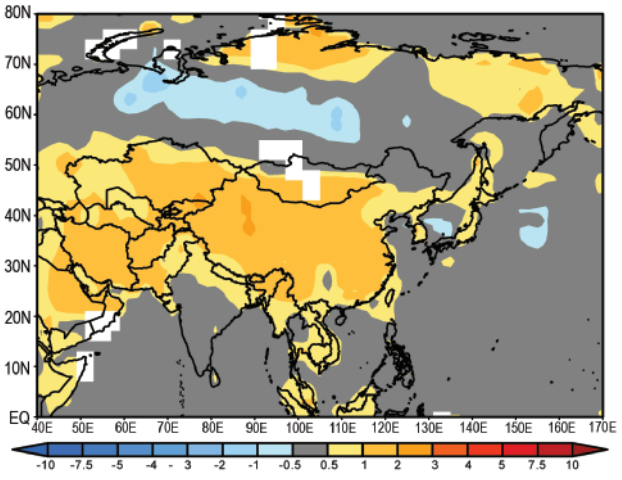


**Fig. 6.26. Asian 2006 annual temperature anomalies (°C, 1971–2000 base) from CAMS-OPI.**

norms). A monthly precipitation norm was also considerably exceeded in the Volga-Vyatka and central Chernozem regions (250%–300%). Very large amounts of precipitation (250%–330% of monthly norms) were recorded in the southern Far East. Particularly intensive precipitation was recorded in Sakhalin and the Maritime Territory in the third 10-day period.

In April, positive temperature anomalies were recorded in most of European Russia. East of Ural, the air temperature was below normal, with temperature anomalies –6° to –8°C in the Yamalo-Nenets Autonomous Area and in the vicinity of the Ob Bay. In southwestern Siberia, cool weather was accompanied by high precipitation (170%–230% of the monthly norm), which, combined with intensive snow melting, caused torrential spring floods in the Kemerovo region and Altai Territory. Particularly serious hydrological conditions were noted on the Biya River near Biysk: about 500 houses were impounded in the town and people had to be evacuated.

Summer began with hot weather. In nearly the entire Russian territory, mean monthly air temperatures in June were above normal. Although temperature anomalies were no higher than 5°C, positive anomalies over most of the Russian territory resulted in 2006 having the warmest June on record (1936–2006). In July, the mean monthly temperature in the west of European Russia was 0.5°–1.0°C above normal. In the northwestern region, from 8 to 12 July, mean daily air temperatures attained 24°–27°C (anomalies of 7°–10°C).

A significant precipitation deficit in the north of the north Caucasus region caused soil drought in most of the Rostov region and the steppe zone of the Kabardino-Balkaria Republic, and allowed soil drought to persist in the southern and Volga areas of the Volgograd region. Soil drought was also recorded in individual regions of the republics of Mordovia, Chuvashia, and Udmurtia. The southern Khabarovsk Territory received more than two monthly precipitation norms, which caused high rainfall floods on the territory's rivers that had not been recorded since 1961.

In August, very hot weather set in the southern Federal District. Mean monthly air temperature anomalies were 5°–6°C. In the first half of the month, air temperatures rose as high as 37°–43°C. On 10 August, air drought started in the steppe regions of north Osetia; the dry period lasted 25–35 days, during which the maximum air temperature exceeded 30°C. Air drought was aggravated by soil drought. On 23–24 August, rains in the north and southeast of the Rostov region stopped soil drought. August in central European Russia proved to be very rainy. The Kaluga, Tula, Oryol, and Ryazan regions received more than two monthly precipitation norms. In Kaluga, August of 2006 was the most humid in the past century.

In the Far East, warm weather prevailed in August. Mean monthly air temperature anomalies in the southern Khabarovsk Territory and in Sakhalin exceeded 3°C. The southeast of the Yakutia-Sakha Republic and the north of the Magadan region and the Khabarovsk Territory experienced very warm weather. However, frequent rains were observed in these regions; some places received more than three monthly precipitation norms. Okhotsk, for example, received 72 mm of precipitation in 12 hours on 15–16 August. September, like in the previous year, proved to be warm in most of the country, though mean monthly air temperature anomalies were lower than those in September 2005.

In the first 10-day period of October, cold weather occurred abruptly in the north of the Irkutsk Region, causing frost conditions. Strong winds and snow caused damage of power transmission lines and power supply failures. For all of October, the northeast of the Far East region experienced a strong heat center, where mean monthly temperature anomalies exceeded 6°C. In November, Russia experienced two large heat foci, divided by a sufficiently intensive cold zone. On the Arctic coast and on the islands, as well as in most of the Far East, November was very warm. The center of this focus was over continental zones of the Magadan region and the Chukotka Autonomous Area. At the center, mean monthly air temperature anomalies were 13°–15°C. In the east and south of Yakutia, the Amur region, the northern Khabarovsk Territory, the north of the Chita region, and the southwest of the Magadan region, warm weather was accompanied by a large amount of precipitation. This is not typical for this season, when the Siberian anticyclone is normally prevailing in these regions. As a result, monthly precipitation norms were exceeded by up to 100%–300% in many places. This November in Magadan, for example, following two very low-snow months of November, 161 mm of precipitation (358% of the monthly normal) was recorded, which is only 5 mm lower than the 1995 absolute maximum.

The end of the year proved to be abnormally warm over most of the Russian territory (Fig. 6.27). The mean monthly air temperature averaged over the territories of the quasi-homogeneous regions (region IV in the center and the south of European Russia

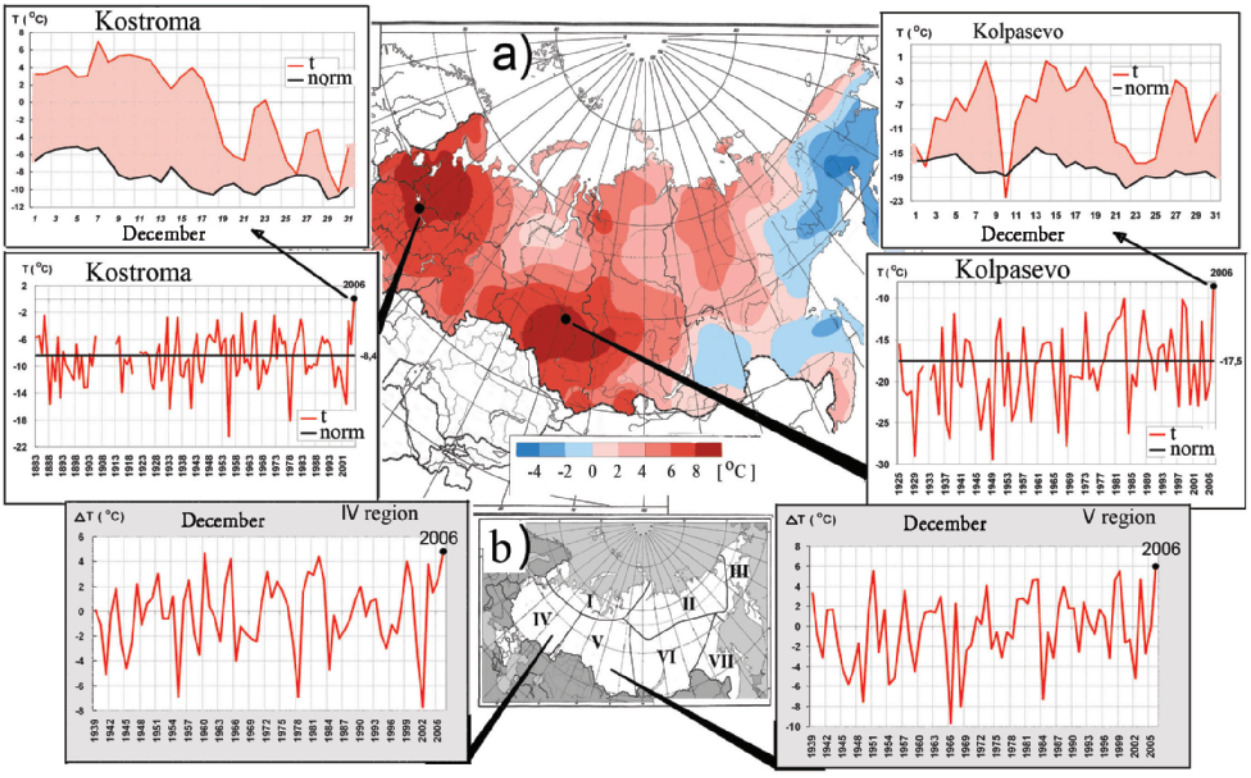


**Fig. 6.27. Russian air temperature anomalies (°C) in December 2006. The middle side panels (a) show December mean monthly air temperature series at meteorological stations Kostroma (1883–2006) and Kolpasevo (1925–2006). The upper side panels depict daily air temperature values during December 2006 for these two stations. The lower panels (b) show the December mean monthly air temperatures averaged over quasi-homogeneous regions IV and V.**

and region V in the center and the south of western Siberia) was the warmest on record (Fig. 6.27b). Meteorological stations at the places of positive anomalies registered record-breaking mean monthly air temperatures (Fig. 6.27a). In Moscow, for more than 100 years of observations, the mean December air temperature did not reach such values as in 2006. It was 1.2°C. Mean daily air temperatures were above normal during the whole month, except for 26 December. Daily air temperatures that are maximal for the whole period of record were exceeded 11 times. On 15 December, the maximum air temperature reached 9°C.

2) China—Ling Wang and D. Ye

*(i) Temperature*

The annual mean temperature of China in 2006 was 9.9°C, which was 1.1°C above the climatology (1971–2000 mean value). The year 2006 was the warmest year since 1951 (see Fig. 6.28). The seasonal mean temperature was also above the climatology in all four seasons, and reached the hottest peak since 1951 in both summer and autumn.

Above-normal temperatures were observed almost throughout the whole country. In the northwest, southwest, western parts of north China, Huanghuai region, the middle and lower reaches of the Yangtze River, and western parts of inner Mongolia, the temperature anomalies were 1°–2°C above normal (see Fig. 6.29). In the winter of 2005/06 (December–February), warmer-than-normal temperatures were observed in most areas of the Tibetan Plateau, where the temperature was 2°–5°C above normal. In summer (June–August), a record-breaking heat wave affected Chongqing and eastern parts of Sichuan. In Chongqing, from mid-July to late August, the number of "broil days" in which the daily maximum temperature was greater than 38°C was 21. This was significantly above the normal of 3.2 days, and reached the maximum in records. In autumn (September–November), above-normal temperatures were observed in most regions of China.

*(ii) Precipitation and droughts*

In association with the higher temperature, China experienced a deficient rainfall year. Below-

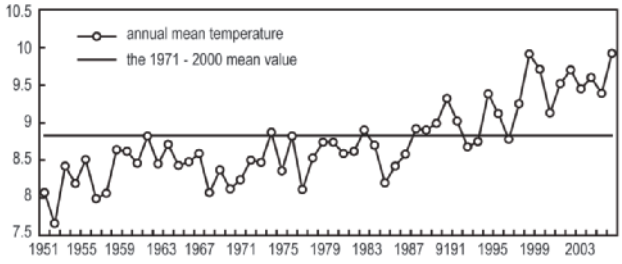


**Fig. 6.28. Time series of annual average air temperature (°C) in China, 1951–2006.**

normal precipitation was observed in most areas of the Yangtze River valley, north China, and western parts of northeast and eastern parts of Inner Mongolia. Rainfall was 10%–50% less than normal in these regions. From June to the first half of November, the Yangtze River valley endured dry conditions, and the average precipitation was the second lowest since 1951, making the river drop to record low levels.

A severe drought occurred in Sichuan Province and Chongqing City during the summer. From June to August, the precipitation over these regions was about 67% of normal, and was the lowest since 1951. Meanwhile, due in part to the heat wave, Chongqing and Sichuan endured the worst drought since 1951: about 3.38 million ha of crops were damaged. Total losses were estimated at 19.3 billion RMB.

Eastern parts of China experienced warmer and drier conditions during autumn. The precipitation was 50%–80% less than normal in north China, Huanghuai region, and western parts of south China during September to the first half of November. In addition, higher temperatures were observed almost

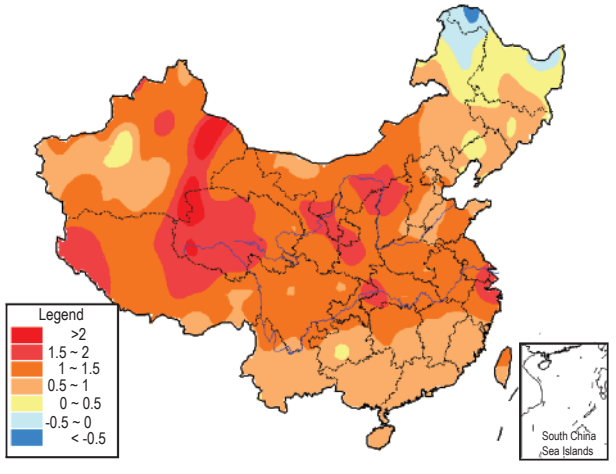


**Fig. 6.29. Annual air temperature anomalies (°C) over China in 2006.**

throughout the country. This condition enhanced the soil water evaporation and caused a large-scale drought over eastern China. More than 6.4 million ha of crops were affected, particularly in Shandong and Guangxi Provinces.

*(iii) Floods and heavy rainstorms*

Heavy rainstorms during 2–10 June affected southern China, where the accumulated precipitation was about 100–300 mm. It reached 500 mm on Shanwei, on the eastern coast of Guangdong Province. During 12–13 June, extremely heavy rain occurred in Wangmo County in the southern part of Guizhou Province. The 4-hour accumulated precipitation reached 196 mm, causing severe mountain torrents and mudslides, leading to 30 deaths. During 5–13 October, heavy rain continued to control the south-central parts of Yunnan Province, and brought 100–300 mm of precipitation, which is 100%–200% more than the October normals.

*(iv) Tropical cyclones*

In 2006, there were 24 tropical cyclones with at least tropical storm intensity in the western North Pacific, this was below the 1971–2000 average of 27. Six of them made landfall in China (the average of seven). The first landfalling typhoon, Chanchu, was earlier than normal by 40 days. It is the earliest typhoon to directly strike Guangdong since 1949. From July to August, five tropical cyclones made landfall in China one after another, with strong intensity, causing devastation. In autumn, no tropical cyclones made landfall, which is also a rare occurrence. There were 1522 deaths caused by tropical cyclones in China during 2006 (the most deaths in 10 years). Associated with the southwesterly monsoon, Tropical Storm Bilis killed 843 people. Supertyphoon Saomai was the most powerful typhoon to strike China since 1949; it directly struck Zhejiang Province with a maximum wind near the center of 60 m $s^{-1}$ and a minimum pressure of 920 hPa, resulting in 483 fatalities.

*(v) Dust storms*

In spring of 2006, 18 dust weather events occurred, including 5 strong dust storms. The number of dust events reached the maximum since 2000. The strongest dust storm occurred on 9–11 April, affecting 13 provinces in northern China; Tulufan Basin in Xinjiang Province witnessed the most intense dust storm in the past 22 years. Another dust storm happened on 16–18 April, which affected about 1.2 million $km^2$, with large impacts in Beijing.

3) Southeast Asia—W. Li and Y. Zhu

*(i) East Asian monsoon*

The East Asian summer monsoon onset commenced over the SCS in the fourth pentad of May, which is near normal, and the flow remained southwesterly over regions from South China to the Jiangnan area before the third pentad of June. During the fourth pentad of June, with the subtropical high skipping northward, southwesterly flow advanced to the Huanghuai area. Meanwhile, the 340-K isoline of potential pseudoequivalent temperature moved northward and remained north of 35°N from July to the first decad of August. During the fourth pentad of August, the 340-K isoline retreated southward quickly to 30°N, and to 20°N during the first decad of September. During the second pentad of October, the 340-K isoline withdrew from the SCS, which indicated that the warm and humid air had withdrawn from the SCS. Meanwhile, at the 850-hPa level, wind flow over the SCS changed 180° to become northeasterly. This indicated that the SCS summer monsoon came to an end during the second pentad of October 2006, which was later than normal.

The SCS summer monsoon index was –0.79 in 2006, which was weaker than average. Pentad intensities of the SCS summer monsoon were weaker than normal during most of the time (Fig. 6.30). During the summer of 2006, rainfall totals were more than normal in South China, Huanghuai area, and mid-northern northeast China, while they were less than normal in the mid–lower reaches of the Yangtze River.

*(ii) Temperature*

Generally, monthly mean surface air temperatures were slightly above normal (1971–2000 mean) in most regions of Southeast Asia during December 2005–November 2006. Seasonal mean surface air temperatures were above normal in most of Southeast Asia during winter (December 2005–February 2006) and autumn (September–November), with departures exceeding 1°C in the northern Indo-China peninsula during boreal winter and in the eastern Indo-China peninsula during boreal autumn. Generally, temperatures were near normal across Southeast Asia throughout the remainder of the year.

*(iii) Precipitation*

Generally, precipitation was above normal across the western Indo-China peninsula and below normal in the eastern Indo-China peninsula from December 2005 to November 2006. During winter, rainfall totals were 50%–100% above average in the western Indo-China peninsula. Meanwhile, heavy amounts of rain associated with the northeast monsoon contributed to significant flooding across the central Philippines and parts of the Malay peninsula. In spring, precipitation was ~50%–100% above average in the northwestern Indo-China peninsula. June–August precipitation was close to normal, though heavy rainfall associated with the monsoon affected Vietnam, Cambodia, and the Philippines. During autumn, rainfall totals were 30% to 50% below average in the eastern Indo-China peninsula, and near normal elsewhere.

*(iv) Notable events*

In the Philippines, heavy rainfall induced deadly landslides in southeastern Philippines during the second decad of February 2006; there were at least 139 confirmed fatalities. Typhoon Chanchu crossed the Philippines during 11–13 May and produced torrential rain, causing 41 deaths and leaving thousands homeless. Typhoon Xangsane crossed the Philippines during 27–28 September and was blamed for 110 deaths. Typhoon Durian struck the northern Philippines on 30 November, with at least 406 fatalities. Across eastern Indonesia, landslides and floods caused by torrential rain on 21 February killed at least 33 people in the city of Manado. Monsoon-related rainfall produced flooding in east Java during mid-April, and was blamed for at least 23 deaths. Floods and landslides ravaged eastern Indonesia on 19–20 June, causing about 200 fatalities. In Malaysia during the mid-December 2005, flooding killed at least 9 people, and over 17,000 people were driven into relief shelters.

During the third decad of May, heavy rainfall brought devastating flooding and mudslides to parts of northern Thailand. More than 100 people may have died in flash floods. In Thailand during early October, heavy rainfall in the wake of the remnants of Typhoon Xangsane was responsible for 32 deaths across the country, and affected 1.8 million people. Monsoon-related flooding in central and northern

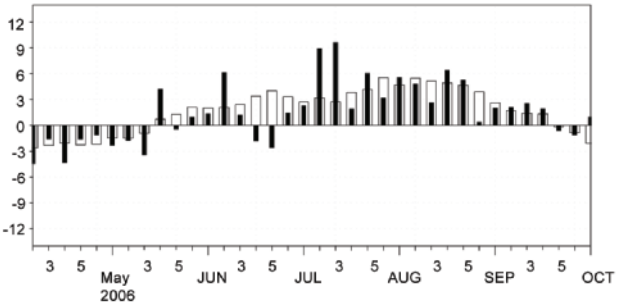


**Fig. 6.30. Variation of the zonal wind index over the South China Sea (m s$^{-1}$).**

regions of Vietnam was blamed for 42 deaths during August. Typhoon Xangsane made a final landfall in central Vietnam in October; there were 68 deaths and nearly 320,000 homes were destroyed or submerged.

4) South Asia—M. Rajeevan and Jayashree Revadekar

The year 2006 was marked by extreme weather across South Asia, both in terms of precipitation and temperature. In January, many parts of South Asia experienced severe cold wave conditions with minimum temperatures dipping below normal by more than 4°C. Minimum temperatures hovered around the freezing point at some stations like Amritsar (–2°C on 7 January), Srinagar (–7°C on 11 January), and Ganganagar (–1°C on 8 January). Frost was observed in New Delhi for the first time in 70 years as cold air sweeping in from the Himalayas produced a low temperature of 0.2°C on 8 January. Over north India, more than 150 deaths were attributed to cold weather conditions. In neighboring Bangladesh, unusually cold weather also claimed some lives during the same period. However, in February, many parts of South Asia experienced unusually warm temperatures, which severely affected the winter crops over this region. During the month, mean temperatures were 5°–6°C warmer than normal over northern parts of India and adjoining Pakistan and Afghanistan. More than 30 stations reported the highest maximum temperatures ever recorded for the month of February, even some 100-year records. At Allahabad, the monthly mean maximum temperature in February was 36.3°C, breaking the previous record set in 1896.

Before the southwest monsoon sets in, heat waves are common in May and June over northern parts of India and Pakistan. During the second week of May, severe heat wave conditions prevailed over northwestern parts of India, with daily maximum temperatures above normal by 6°C, claiming more than 50 lives. At some stations, temperatures reached 45°C. Over India, mean temperatures were consistently above normal during all the months, except in June. The year 2006 was the warmest year on record since 1901, with the annual mean temperature above normal (1961–90) by 0.59°C. In January, snowstorms and flooding affected major parts of Afghanistan, claiming many lives. Badakhstan was among the worst hit provinces when snowstorms moved over this region. During April, flooding due to snowmelt and seasonal rainfall affected numerous provinces of Afghanistan-like Faryab and Baghlan. On the other hand, drought conditions and severe water stress prevailed over some parts of Pakistan, especially in Balochistan, due to inadequate rainfall during the winter and spring seasons.

*(i) South Asian summer monsoon (June–September)*

The summer monsoon season (June–September) is the main rainy season over a major portion of South Asia, contributing 60%–90% of annual rainfall. The onset phase of the 2006 monsoon season was characterized by an early monsoon onset over the south peninsula (26 May). However, after the first active spell associated with monsoon onset, there was a prolonged hiatus of about 16 days, due to southward intrusion of stronger midlatitude westerlies and enhanced convection over the equatorial Indian Ocean. During this period, the advance of the monsoon over northern and northwestern parts of India was delayed. The monsoon revived during the last week of June and it finally covered northwestern parts of India and Pakistan during the last week of July, about 10 days later than its normal date.

Breaking the declining trends observed over the past few years, a revived occurrence of low pressure systems typical of the summer monsoon was observed this year. As many as 16 low pressure systems formed over the Indian region, 12 over the Bay of Bengal, 1 over the Arabian Sea, and 3 over land. Of these 16 low pressure systems, 8 (the highest since 1997) intensified into monsoon depressions and 1 into a cyclonic storm (Mukda). In August, four monsoon depressions formed over the Bay of Bengal, which is a record since 1891. The monsoon depressions formed over the Bay of Bengal moved more in a west-to-northwesterly direction, very much south of the normal track position, thus giving copious amounts of rainfall over central India. The remnants of these systems then moved over extreme northwest India and adjoining Pakistan.

The all-India summer monsoon seasonal rainfall was near normal (100% of its long period average). However, rainfall was not well distributed over space and time. After the first spell of active rainfall activity associated with the onset phase, the monsoon was more or less subdued over the country until the third week of July. As of 26 July, cumulative all-India seasonal rainfall departure was only 87% of its long period average. However, the monsoon revived rapidly during the last week of July and remained active over India and Pakistan almost until the end of September. In August, all-India rainfall was 6% above its long period average and in September, it was 2%.

During this season, out of 36 meteorological subdivisions of India, 6 received excess rainfall, 21 re-

ceived normal rainfall, and the remaining 9 received deficient rainfall. About 60% of the 533 meteorological districts received excess/normal rainfall and the remaining 40% received deficient or scanty rainfall. About 25% of the districts experienced moderate drought and 30 districts (6%) experienced severe drought conditions on a seasonal scale. During the second half, the seasonal trough (monsoon trough) was confined mainly south of its normal position and all the low pressure systems moved across central India along the monsoon trough. Due to this, central India received excess rainfall by 16%, while seasonal rainfall over northeastern parts of India and adjoining Bangladesh was below normal by more than 15%. However, northwest and southern parts of India received normal rainfall during the season (Fig. 6.31). Over Nepal, rainfall activity was below normal by more than 20% in July and August. Rainfall activity picked up only in September, during which the monthly rainfall was above normal.

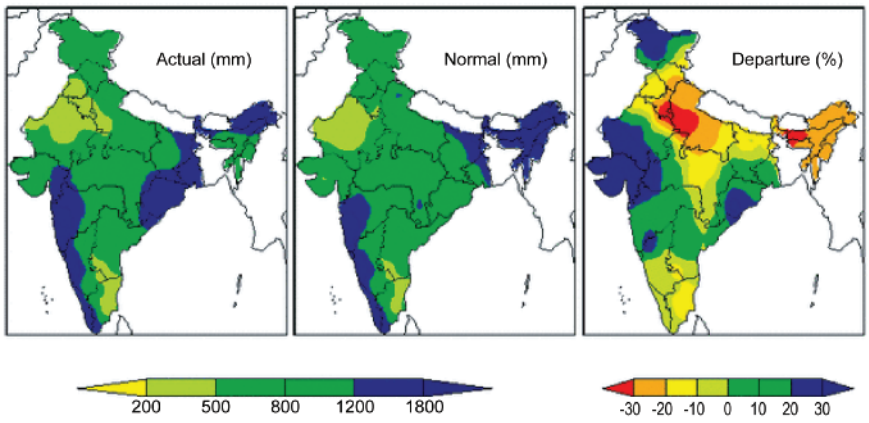


**Fig. 6.31. Seasonal rainfall patterns during the 2006 summer monsoon season. [Source: http://soman.tropmet.res.in/mol.]**

Pakistan experienced moderately above normal rainfall (27.2%) during the monsoon season (July–September). The province of Punjab received normal rainfall (1.5%) and the provinces of NWFP and Balochistan experienced slightly above normal rainfall (22.0% and 12.4%, respectively). The province of Sindh had received largely above normal rainfall (116.6%). Another interesting aspect of this season was the occurrence of extreme rainfall events. In many places, many heavy rainfall events occurred, causing localized but severe flooding. The unprecedented heavy rains and destructive flooding across much of South Asia, including Afghanistan, Pakistan, India, and Nepal, affected more than 5 million people and resulted in more than 1000 deaths. During the third week of August, unusually heavy rainfall in the Thar Desert over northwest India caused devastating floods. During the period 16–25 August, 549 mm of rainfall was recorded over this region, which destroyed thousands of hectares of standing crops.

*(ii) Northeast monsoon*

The northeast monsoon (October–December) contributes 30%–50% of annual rainfall over southeastern parts of India and Sri Lanka. During the 2006 northeast monsoon season, heavy rainfall continued unabated over these regions especially during October and December. In India, the states of Tamil Nadu and Andhra Pradesh were the worst affected. However, the season known for tropical cyclone activity, witnessed only one tropical cyclone (Ogni), which affected parts of Tamil Nadu and Andhra Pradesh. Most of the rainfall activity during the season was associated with the movement of easterly waves. The associated floods in southeast India and Sri Lanka affected more than 1 million people with at least 100 fatalities and had a considerable socioeconomic impact. Over these regions, the northeast monsoon seasonal rainfall was above normal by more than 15%.

### 5) Southwest Asia—F. Rahimzadeh and M. Khoshkam

Anomalously warm and cold seasonal temperature was observed across the region this year. Temperature patterns varied in time and space. Warmer-than-average temperatures occurred in winter and spring (about 1°–2°C above average). Cooler-than-average and wetter-than-average conditions occurred in the western half of Iran during autumn.

*(i) Winter*

Temporal and spatial temperature variability was intense in winter (2005/06). Iran experienced anomalously warm temperatures in February. On average, winter temperatures were 2°C above that of the long-term. Parts of central and northeastern Iran were 2°–3°C cooler than normal. The areas with precipitation amounts near normal or above were the west, southwest, northwest, and Alborz Mountains, while the rest of the area had precipitation amounts of 75% of normal or less. The range of

winter precipitation was 1250 mm. The largest amount of precipitation was observed near the Zagros Mountains (Koohrang 1250 mm) in western Iran, and the lowest (5.9 mm) in southeastern Iran. Winter precipitation was 28% less than 2005, and 6% less than the long-term average. Much of the precipitation falls as snow, especially in December and January. Heavy rainfall brought flooding to parts of the southern provinces during February 2006, creating serious transportation problems for the mountain and cold provinces.

*(ii) Spring*

Spring temperatures were mostly 0°–2°C above normal over most parts of Iran. A few exceptions were Fars, Kerman, Yazd, and the south, which was 2°C cooler, as well as a few places that were up to 4°–6°C warmer than the long-term spring averages. The seasonal mean temperatures ranged from 10°C in the northwest to 35°C in the southeast. Precipitation totals across the southeast of the country were only 0%–25% of the long-term mean, whereas wetter-than-average conditions prevailed over the central region, which received 100%–260% of its long-term average precipitation. The northwest region received 50%–100% of normal rainfall. In general, precipitation increased with respect to 2005, but was 14% lower than the long-term mean in spring.

*(iii) Summer*

Summer was cooler than average over one-fourth of Iran (in the central and eastern provinces) while above-average temperatures were observed in the rest of the country, with averaged departures 2°C above normal. Many parts including central, eastern, and some parts of the southwest received no measurable rainfall. Averaged precipitation was below normal in the summer of 2006, 5% lower than 2005, and 24% lower than the long-term mean. Areas with precipitation amounts of 75% normal to near normal were parts in south, southeast, northeast, and northwest. Dust and sandstorms occurred in the Sistan and Balochestan provinces in southeastern Iran, western Afghanistan, and Pakistan.

*(iv) Autumn*

In autumn, cooler-than-average conditions persisted across southern and central Iran; warmer-than-average conditions were limited to parts in the eastern provinces. Cold temperatures affected many areas during autumn, with many locations breaking their all-time record minimum temperatures for the season. Averaged across the nation as a whole, it was one of coldest autumns in decades. A severe cold wave, which arrived during early December, brought some of the coldest temperatures to the region in decades. Parts of Iran were up to 8°C cooler than normal during

## *COUNTRY SPOTLIGHT:* TURKEY—S. Sensoy

The annual surface temperature anomaly averaged over Turkey in 2006 was 0.9°C above the 1971–2000 average (Fig. 6.32). Only one station (Solhan) in the eastern part of Turkey had annual temperatures below average (–0.59°C). Generally, western parts of the country had annual temperatures near average while eastern parts were above the mean. Positive temperature anomalies have been reported since 1994 (except 1997). The number of summer days ($T_{max} \geq 25$°C) have been increasing all over Turkey while ice days and frost days have decreased. Temperatures in January, November, and December were below average. Between February and October, temperatures were near and above average. Significant positive temperature anomalies ($p \leq 0.05$) occurred during the summer season (JJA).

Due to Turkey's topography, rain clouds seldom penetrate the country's interior. Rain clouds drop most of their water on the slopes opposite the sea. For this reason, the central Anatolia does not have very much precipitation. While Rize receives 2200 mm of precipitation annually, Konya receives only 320 mm. Average annual total precipitation for Turkey is 632 mm according to the 1971–2000 base periods (Sensoy 2004). The average total precipitation in 2006 was 606 mm, slightly below average. Western parts of Turkey and the Çukurova Plateau had been suffering prolonged drought conditions. Approximately 150 stations received less precipitation than average in the winter, spring, and summer seasons. Despite these dry conditions, flood events occurred in some places. Ten people died in Diyarbakir in October from flooding.

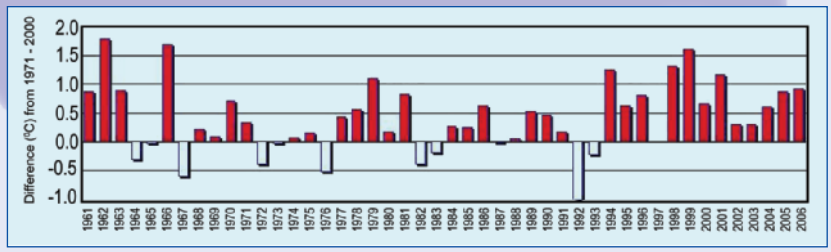


**Fig. 6.32. Time series of Turkish annual average air temperature anomalies (°C; 1971–2000 base) from 1961–2006.**

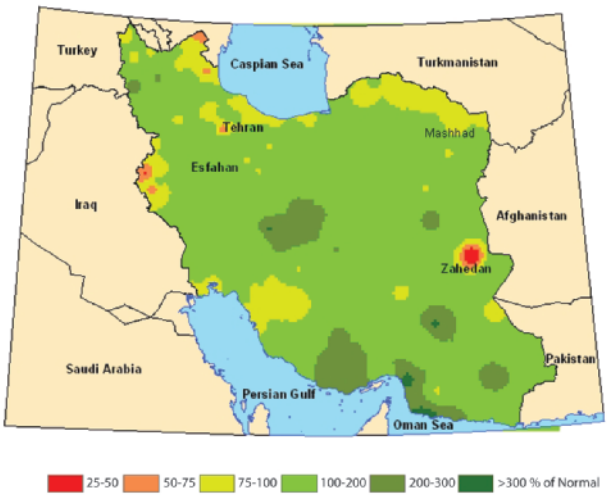


**Fig. 6.33. Autumn precipitation anomalies (%) over Iran. [Source: I.R. of the Iran Meteorological Organization.]**

December. Snow and cold weather penetrated northern Iran, with heavy rainfall in eastern and southern Iran. For the country, the average of precipitation in autumn was 83 mm. The largest anomalies were recorded in Hormozgan Province, with 2.2 times the normal precipitation (Fig. 6.33). From a seasonal perspective, precipitation totals were normal to above normal in much of Iran during autumn 2006.

*(v) Significant weather events*

Significant weather events included drought, heat and cold waves, flooding, and dust and sandstorms. Floods occurred in northern Iraq in February and November, in Turkey in July, in Pakistan from late July through mid-August, in Afghanistan in August and November, and in Iran's Ardebil Province in May. Heavy rain triggered mudslides in Tajikistan in May and in northern Pakistan on 3 July. In addition, significant drought continued throughout some parts of the region. For example, significant drought across Afghanistan occurred in July as rainfall had been lacking since April 2006. Dust storms blew and spread out over a wide area, covering some parts of Afghanistan, southeastern Iran, and western Pakistan during summer and autumn. Other extreme events, such as a severe winter storm accompanied by heavy snowfall in some provinces of Afghanistan, and near Dushanbe in Tajikestan, caused economic losses.

## g. *Europe and the Middle East*

### 1) Overview—A. Obregón, P. Bissolli, and J. J. Kennedy

CAMS-OPI precipitation and air temperature anomalies over Europe are shown in Figs. 6.34 and 6.35, respectively. Europe experienced above-normal temperature anomalies across nearly the entire continent in 2006.[6] For the 35°–75°N and 10°W–30°E region the annual average land surface temperature was 1.15° ±0.08°C above the 1961–90 average (based on CRU TEM3; Brohan et al. 2006). The annual average near-surface temperature, incorporating land and sea surface temperatures, was 0.93 ±0.05°C above the 1961–90 mean (Fig. 6.36). The highest positive annual anomalies of more than +4°C were found in northern parts of Greenland and around Svalbard.

[6] Contributing countries (national meteorological and hydrological services) to this section are Armenia, Austria, Bulgaria, Cyprus, Denmark, Finland, France, Germany, Iceland, Italy, Kazakhstan, Lithuania, Norway, Portugal, Romania, Russia, Spain, Sweden, and the United Kingdom.

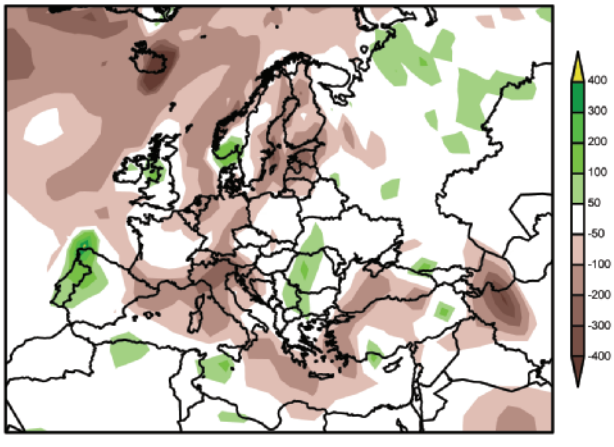


**Fig. 6.34. European 2006 annual precipitation anomalies (mm, 1979–2000 base) from CAMS-OPI.**

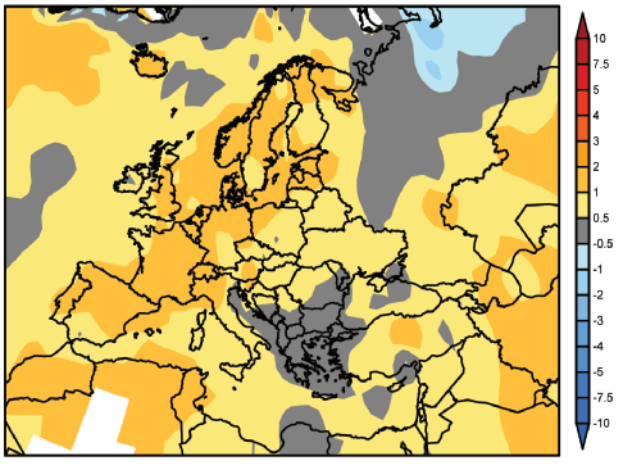


**Fig. 6.35. European 2006 annual temperature anomalies (°C, 1971–2000 base) from CAMS-OPI.**

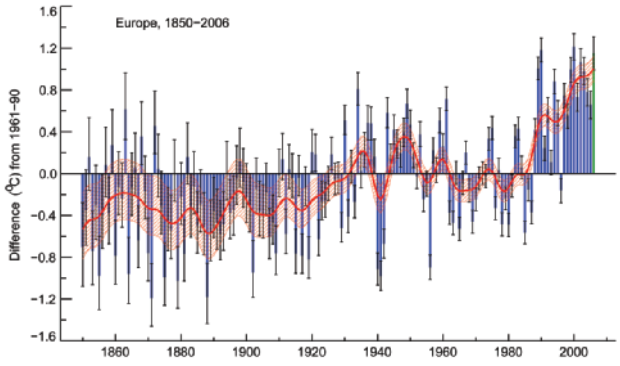


**Fig. 6.36. Time series of area average land surface temperatures over Europe (35°N–75°N, 10°W–30°E) from 1850 to 2006 (data are from Brohan et al. 2006). The blue bars show the individual annual values and the thin gray bars indicate the two standard error range on the annual values. The value for 2006 is shown in green. The smooth red curve and shaded area show the annual values after smoothing with a 21-point binomial filter and represent roughly the interdecadal variability in the data and its uncertainty.**

Large parts of Scandinavia, northwestern, western, and central Europe, and even most parts of the Iberian Peninsula experienced anomalies above +1°C, exceeding the 90th percentile in many areas, and the 98th percentile in more limited areas in the HadCRUT3 dataset. The United Kingdom, Spain, and the Netherlands reported their warmest years in recorded history. The eastern parts of Europe had smaller anomalies of less than +1°C. Slight negative anomalies (down to about –0.5°C) were only registered locally in southern and southeastern Europe. Seasonal temperature anomalies in Europe increased throughout the year from winter 2005/06 through to autumn 2006.

Precipitation amounts for the climatological year of 2006 (December 2005–November 2006) were generally above average in eastern and southeastern parts of Europe, with anomaly maxima over the Arctic islands, and in Greece and southern Italy, while wide areas over the western part of Europe received below-average rainfall. Areas receiving less than 80% of normal precipitation amounts were restricted to the region between the Alps and the Pyrenees, and southern Spain, as well as some coastal regions in the north. Precipitation anomalies averaged over 2006 were generally lower than those in 2005. However, the seasonal variation throughout the year was quite high.

2) Nordic region—C. Achberger, J. E. Box, and D. Chen

Weather and climate conditions in the Nordic region (comprising Sweden, Norway, Denmark, Finland, Iceland, and Greenland) are characterized by a continued pattern of warm anomalies in observational records for 2006 as compared to recent decades. The Fennoscandinavian countries (Norway, Sweden, Finland, and Denmark) and Iceland experienced a warm summer and an extremely warm autumn. Surface climate conditions in this area are to a large extent controlled by the atmospheric circulation over northern Europe and the North Atlantic region. Synoptic weather typing, according to the scheme by Lamb (1950), has been used to estimate the impact of the large-scale atmospheric circulation on the surface weather conditions in this region (e.g., Chen 2000). Compared to the 1961–90 mean, the frequency of daily southwesterly and westerly weather types were above normal, which can explain the warmer-than-normal conditions in 2006. Positive deviations from the normal weather-type distribution are especially obvious during autumn, with stronger-than-normal large-scale flow from westerly and southerly directions and increased number of anticyclonic days. These flow conditions in autumn are consistent with the warm and wet weather that prevailed in extended parts of Fennoscandinavia.

*(i) Fennoscandinavia and Iceland*

Annual temperatures in Fennoscandinavia and Iceland were, on average, well above the long-term means for 1961–90: 1°–2.5°C depending on the region (Fig. 6.37). For Denmark, 2006 was the warmest year since 1874. The annual mean temperature was 1.7°C above the 1961–90 mean. For Norway, 2006 was one of the three warmest years in the country's tempera-

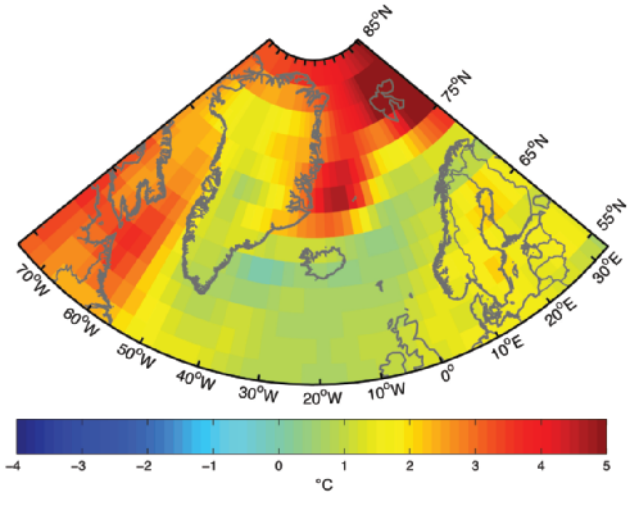


**Fig. 6.37. 2006 annual air temperature anomalies (°C; 1961–90 base) across Fennoscandinavia, the North Atlantic, and Greenland. [Source: NCAR–NCEP reanalysis.]**

ture record (behind 1934 and 1990). Some Norwegian regions experienced their largest positive deviations from the long-term mean (1961–90), such as Svalbard (+5°C) as well as parts of the county of Trøndelag and the southern regions of northern Norway (+2°–3°C). In Sweden, 2006 was also a very warm year. The annual mean temperature was only 0.3°C below the warmest year, as 2006 ranked as the sixth warmest year during 1860–2006. The Finnish annual mean temperatures were among the 10th–15th highest since 1900. Iceland experienced a warm year. Several selected Icelandic stations reported annual mean temperatures placing 2006 among the 5th to 13th warmest year since about 1870.

Iceland and Norway experienced a rather mild start to the year, with temperatures above the 1961–90 mean, in contrast to Denmark, Sweden, and Finland. Spring was characterized by unusually cold weather in March, occurring almost everywhere in the region. Summer temperatures were well above the long-term mean nearly everywhere. Many very hot days (air temperature > 30°C) were reported in Finland. Norway had its fourth warmest summer since 1900. July temperatures in Denmark were nearly 4°C higher than normal. Swedish summer temperatures were also higher than normal. Temperatures at Svalbard airport were more than 2°C above normal, which made 2006 the second warmest summer since measurements commenced in 1912. The warm summer was followed by an unusually warm autumn in most parts of the Nordic region, especially in Denmark where the monthly mean temperatures from September to December were 3°–5°C above normal, reaching new records. Finland experienced unusually warm weather from the second half of November through the end of 2006. In Helsinki, the monthly mean temperature in December was 4°C, the highest since 1929. In Sweden, September and December were extremely warm.

In some parts of the region, precipitation conditions deviated considerably from the 1961–90 average, especially in western Norway and the Norwegian west coast, which were drier than normal. In contrast, precipitation in Sweden and Denmark were well above normal values. For Sweden, 2006 became the sixth wettest year since 1860. Finland's annual precipitation was close to normal or slightly above. Iceland got rather normal amounts of precipitation, though the southwest of the island had somewhat wetter-than-normal conditions. In several areas, the summer was either rather dry and/or rainfall was unequally distributed over the summer months. Southern and western Finland experienced their driest summers ever recorded. In Sweden, farmers had problems because of the lack of rain in June and July, but heavy thunderstorms and strong showers in August led to serious flooding in many places in southern and middle Sweden. Conditions in Denmark were similar, with only half of its normal rainfall amount in July, but August had 100% above-normal precipitation. Norwegian summer precipitation was below normal for most of the country, but strong showers led to damage from flooding at some places. The Icelandic summer was rather wet with stormy weather during July. Wet conditions continued during autumn in many regions. For example, southern Norway received precipitation well above the normal. Heavy thunderstorms in October brought large amounts of rain to many coastal areas in Sweden, while strong and extended rainfall events in December caused serious flooding in southwestern Sweden. Finland got part of its autumn precipitation as snow, leading to all-time high values of snow cover in southeastern parts of Finland in the beginning of November.

*(ii) Greenland*

(a) *Upper-air temperatures*

Upper-air soundings available from the IGRA (Durre et al. 2006) indicate a complex vertical pattern of warm tropospheric and stratospheric cold temperature anomalies surrounding Greenland (not shown), compared to the 1971–2000 base period. The general pattern of lower-tropospheric warm anomalies accompanied by cold anomalies near the maximum height of the observations (< 100 hPa) is consistent with overall 1964–2005 warming trends (Box and Cohen 2006). In the lower troposphere, still well above the surface at the 850-hPa level (1.1–1.5-km altitude), for example, annual temperature anomalies were between +0.9° and +3.1°C at six sites surrounding the island. Over east-central and southeastern Greenland at Ittoqqortoormiit/Scoresby Sund and Tasiilaq, respectively, a general pattern of lower-tropospheric warm anomalies is evident with the exception of spring, perhaps influenced by above-normal sea ice concentration (see section 5b). At the upper limit of mandatory observational levels (20 hPa), relatively large (–7.1° to –8.6°C) cold anomalies are evident in the balloon observations but are not abnormal considering relatively large lower-stratospheric temperature variability (e.g., Christy and Drouilhet 1994). What else stands out are +2.4° to +6.6°C warm anomalies centered at 200 hPa in winter for all sites surrounding but Narsarssuaq in the extreme south. Other regional patterns of note include warm anomalies below 500 hPa in Autumn (September–Novem-

**Table 6.1. Greenland station surface air temperature statistics: 2006 versus 1971–2000.**

| Station Region | Latitude/ longitude | Statistic | Winter | Spring | Summer | Autumn | Annual |
|---|---|---|---|---|---|---|---|
| **Aasiaat/ Egedesminde** | 68.7°N | Anomaly (K) | 3.9 | **4.8** | **1.2** | 1.0 | **2.7** |
| West | 52.8°W | Rank | 7 | 2 | 6 | 8 | 4 |
| **Nuuk** | 64.2°N | Anomaly (K) | 2.1 | **2.7** | 0.9 | 0.8 | **1.6** |
| Southwest | 51.8°W | Rank | 11 | 3 | 7 | 11 | 5 |
| **Prins Christian Sund** | 60.0°N | Anomaly (K) | 1.5 | **1.5** | **1.1** | 0.6 | **1.2** |
| South | 43.2°W | Rank | 7 | 3 | 4 | 11 | 4 |
| **Tasiilaq** | 65.6°N | Anomaly (K) | 1.8 | 0.4 | 0.6 | 0.0 | 0.7 |
| Southeast | 37.6°W | Rank | 4 | 16 | 10 | 22 | 11 |
| **Danmarks-havn** | 76.8°N | Anomaly (K) | **3.6** | **2.9** | **-0.5** | 1.4 | **1.8** |
| Northeast | 18.7°W | Rank | 4 | 3 | 32 | 8 | 2 |

**Bold** values indicate *Z* scores that meet or exceed one absolute magnitude.

ber) at Pituffik/Thule AFB, including apparently extreme, but probably erroneous, +7.9°C at 850 hPa for September–November 2006, given disagreement with MSU4 data (J. Christy 2007, personal communication). Another relatively large (+8.5°C) December 2005–February 2006 anomaly at Aasiaat/Egedesminde may also result from observational error. The potentially erroneous seasonal anomalies at these two sites also affect the annual anomalies.

(b) *Coastal air temperatures*

During the last 56 years (1951–2006), when continuous surface air temperature records are available from a collection of stations around the island (Cappelen et al. 2007), the only significant annual anomalies indicate higher-than-normal surface air temperatures (Table 6.1). In 2006, seasonally, for western and southern sites, like in 2005, spring stood out as being warmer than normal. At eastern sites, cold spring anomalies are evident and are significant seasonally, but not enough to effectively cancel the warmer annual anomalies. Eastern winter anomalies were positive, yet eastern summer temperatures were much lower than normal. Eastern glacier melt rates are likely to have been below recent years in 2006, apparently owing to the eastern coastal cooling effect of April–June positive sea ice anomalies. Western and southern summer temperatures imply continued enhanced glacial melting as sea ice is absent in southwestern Greenland at this time of year. Considering the past century at sites around Greenland where long-term records are available (such as Nuuk and Tasiilaq), the 1930s–40s air temperatures rival recent warm temperatures and suggest that recent extreme melt rates are not without precedent.

3) Iberia—R. M. Trigo, R. Garcia-Herrera, D. Paredes, and A. Ramos

*(i) Temperature*

The Iberian Peninsula registered temperatures above the average throughout the year, with the exception of winter (Fig. 6.38). The annual average 850-hPa temperature across Iberia in 2006 was 1.14°C above normal (with respect to the 1961–90 period average). This significant positive annual anomaly occurred despite the early negative anomaly for the winter (–1.16°C) that was followed by an extremely hot spring (+2.38°C), and a warm summer (+1.50°C) and fall (+1.84°C). It should be stressed that the annual average temperature for 2006 was the hottest in Madrid (since 1900) and Barcelona (since 1925). The corresponding analysis of the associated upper-level 500-hPa geopotential height anomaly field in winter shows intense positive anomalies between the Azores archipelago and northern Europe, while southern Europe is characterized by lower-than-usual values (Fig. 6.38; DJF). Southwestern Europe and northern Africa were under the influence of strong cold-air advection from higher latitudes. Several cold spells affected Iberia in January and February.

In particular, a strong cold break was observed in late January affecting all of Iberia, as well as France and central Europe. This cold plume reached Lisbon, Portugal, on the western coast of Iberia, producing a number of days with both maximum and minimum temperatures below the 10th percentile of daily long-term records. On 29 January the cold break was responsible for the first snow episode in Lisbon since 2 February 1954!

Unlike winter, the remaining seasons were characterized by warmer-than-normal temperature values, particularly between late May and November, where parts or the entire Iberian Peninsula were affected by five intense heat waves between May and September. These three seasons were generally characterized by high values of 500-hPa geopotential height, with maximum anomalies located in southern (spring), northern (summer), and eastern (fall) Europe. These patterns contributed to the advection of warm air masses with origins from overheated Eurasia and/or northern Africa. Moreover, these intense anticyclonic patterns can induce subsidence over Iberia associated with further heating of the surface layers through enhanced adiabatic heating (Trigo et al. 2005).

*(ii) Precipitation*

Most of the Iberian Peninsula experienced drier-than-normal conditions during the winter of 2006, as is clearly shown by the seasonal precipitation percentages computed with respect to the 1961–90 base period average. Based on the monthly precipitation dataset from GPCC (Rudolf et al. 2005) it is possible to see that such winter drought conditions affected a much larger European region, with the exception of the western Mediterranean (and northern Africa). From an atmospheric circulation perspective, the 2006 winter was characterized by positive (negative) SLP anomalies north (south) of the Azores–Iberia latitudinal band, inducing the negative (positive) precipitation anomalies mentioned. It should be stressed that the Iberian Peninsula registered one of the worst droughts ever recorded during 2005, particularly in its southern half (Garcia-Herrera et al. 2006). The dryness of yet another winter season had a strong impact on water resources, hydroelectric production, and agriculture. However, the remaining seasons of the year unfolded very differently from winter, with western Iberia characterized by normal (spring), above-normal (summer), and extremely high values (fall) of precipitation. In fact, Portugal, located in western Iberia, registered the third wettest fall since 1931 (Espirito-Santo 2006), with most of the country showing values above 200% of the seasonal average. The spring and fall seasons correspond to the two most important rainfall seasons for northern and eastern Iberia (Trigo and Palutikof 2001). Interestingly, both spring and fall seasons were characterized by negative anomalies of SLP over the Atlantic Ocean and northern Europe. However, the amplitude of these negative anomalies was deeper during fall (compared to spring), and covered the entire Iberian Peninsula, which is related to the intense positive precipitation observed. Nevertheless, the Mediterranean coastal sector, including southern France, eastern Spain, and northern Africa, remained mostly dry between spring and fall. Therefore, at the end of 2006, several Spanish provinces located close to the Mediterranean coast were extremely dry as a consequence of more than two consecutive years with precipitation below the 1961–90 average.

4) Central Europe and the Alpine region—A. Obregón, P. Bissolli, and J. J. Kennedy

*(i) Temperature*

Annual average temperatures in the region were significantly above average (upper decile of the 1961–90 distribution). Central Europe and the Alpine region experienced one of its warmest years on record with several record-breaking months and seasons. The annual mean temperature of Germany was 9.5°C, which is 1.3°C above normal. Annual average temperature anomalies in Switzerland varied be-

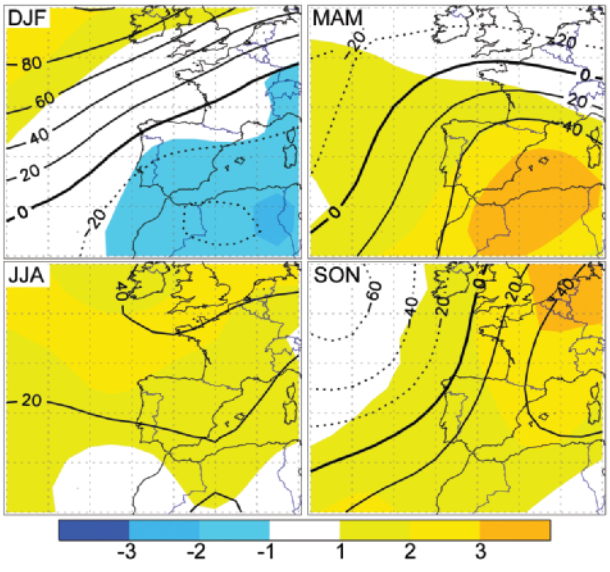


**Fig. 6.38. Seasonal anomalies of 500-hPa geopotential height contours and corresponding 850-hPa temperature anomaly field (color, °C) compared to 1961–90 base period. [Source: NCAR–NCEP reanalyses.]**

tween 1° and 1.7°C above average, placing 2006 as the fifth warmest year in the records since 1864. In most areas of Austria, temperature anomalies in 2006 ranged between 0.2° and 1.0°C above average. Poland and the Czech Republic also experienced above-average temperatures ranging between 1° and 2°C above the mean temperatures of the reference period (1961–90).

Temperatures in Germany, Poland, and the Czech Republic were significantly below the long-term average at the beginning of the year. In Germany, mean January temperatures were 2.1°C below the long-term mean. In Poland and the Czech Republic, temperatures were even lower and Warsaw reported an average temperature anomaly of –5.0°C for January. Temperatures in February also remained below average over the whole region. March was the coldest in Germany for 10 years (anomaly of –2.0°C).

The alpine region experienced below-average temperatures from January to March with anomalies ranging from –0.5° to –1.5°C. In some regions of Austria temperatures were between –2° and –3°C and temperatures down to –24°C were measured during the first 20 days of March in Tyrol, with the lowest value on 13 March. These lower temperatures are consistent with NAO's negative phase (Casty et al. 2005); the NAO had a reading of –0.82 over the December 2005 to March 2006 winter.

In April and May, temperature anomalies rose to slightly above average (up to +1.5°C). Temperatures in the summer months (JJA) showed an extreme contrast. August was well below average in all regions. July was dominated by an extended anticyclone over the Azores, which was stationary over Europe for a long time. This led to an extreme heat wave in central Europe and adjacent areas (Fig. 6.39). The average temperature in Germany was 21.8°C, the warmest in the 106-year record, with an anomaly of 4.9°C above the 1961–90 mean. Temperature anomalies in July in the Czech Republic were 4°–5°C above average. In Vienna, Austria, where observations started in 1775, a new July record for monthly mean temperature (23.9°C) was set. The warmest areas, with anomalies above 5°C, were found in the northern parts of the Alps. August was somewhat cooler than normal across the region.

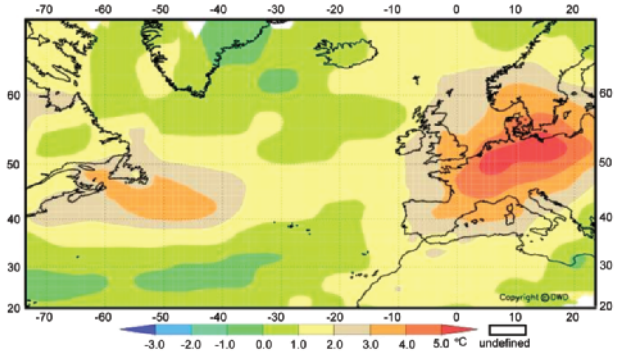


**Fig. 6.39. Monthly average near-surface air temperature anomalies (°C; 1961–90 base) for July 2006. [Source: DWD via CLIMAT messages and ship data.]**

Autumn was extraordinarily warm in central Europe and neighboring areas. It was by far the warmest autumn in central Europe since meteorological measurements began. Seasonal temperature averages in Germany were 3.2°C above the long-term mean. Remarkably, September average temperatures (16.8°C, +3.5°C anomaly) across the region were even higher than in August (15.4°C, –1.1°C anomaly). These extreme temperature anomalies are mostly explained by the anomalous southwesterly flow. In Germany, December was the warmest it has been for 32 years (3.4°C above normal). Northern Germany, the Czech Republic, and Poland experienced anomalously high temperatures exceeding the 90th percentile in places. The highest anomalies occurred in northeastern Poland (> 4°C).

*(ii) Precipitation*

Precipitation in central Europe in 2006 was close to average. Northern Germany and parts of Poland were drier than average while southern Germany and the Czech Republic experienced slightly above-average precipitation. Annual precipitation anomalies averaged over the entire area of Germany were 93% of normal. Austria experienced below-average precipitation (70%–90%) in the southern provinces, eastern Tyrol, Carinthia, and southern Styria, but totals were above average (110%–130%) in the north. In Switzerland, negative precipitation anomalies were restricted to southwestern regions and most parts of Switzerland experienced 110%–140% of their normal precipitation amount in March and April and the significantly wet months of May and August.

In winter, the region was drier than normal with 74% of the normal precipitation amount in Germany. January was particularly dry with only 39% of normal rainfall. Precipitation during the winter mostly fell as snow. February saw the heaviest snowfall in southern Germany for more than 10 years. Rainfall amounts in spring were significantly above average in many parts of central Europe. Germany received 130% of its normal rainfall. In April, melting of the large amounts of lying snow coupled with above-average precipitation resulted in one of the largest

spring floods in the past 50 years in southern and eastern Germany. The Elbe River rose to record levels in parts of northern Germany, breaking the records set during the 2002 flood.

Summer precipitation was correlated with temperature; the warm June and the extraordinarily hot July were also remarkably dry (50% and 65% of the normal in Germany). In July, areas of the Czech Republic, eastern Germany, and the Bavarian forest received less than one-fifth of the normal average rainfall for the month. Prague (Karlov) reported only 12.5% of its normal precipitation. August was unusually wet. Autumn saw drier-than-normal conditions in Germany (80% of the normal rainfall), and some areas along the Danube River received only about 30% of the average. In southern and eastern Austria, anomalies ranged between 40% and 80%. Rainfall totals in September were significantly below average over large parts of Germany, Austria, Poland, and the Czech Republic.

*(iii) Notable events*

On the evening of 31 October–1 November, a severe storm occurred over northern Germany. Wind gusts of more than 150 km $h^{-1}$ were registered over the northern German islands. On the island of Borkum, the water level reached that of the historical flooding event of 1962.

5) Western and northwestern Europe—A. Obregón, P. Bissolli, and J. J. Kennedy

*(i) Temperature*

Temperatures in northwestern Europe in 2006 were above average in all areas, with parts exceeding the 98th percentile of the 1961–90 distribution. The United Kingdom and the Netherlands, which have some of the longest weather records in the world, reaching back to 1659 and 1706, respectively, reported their warmest years in history. Annual average temperatures were 1.42°C above the 1961–90 average in the United Kingdom. In Ireland, it was the warmest year for at least nine years with annual mean air temperatures reaching up to 1°C above the normal. The mean annual temperature of 10.6°C in Dublin was the highest value since reliable measurements began there in 1855. The CET is the oldest continuous temperature dataset in the world (Parker and Horton 2005; Parker et al. 1992). The mean CET for 2006 was 1.35° ±0.09°C above the 1961–90 average and exceeded all values in the series going back to 1659.

Across Ireland and large parts of the United Kingdom, March was the only month with widespread below-average temperatures. The Low Countries and France experienced an unusually cold winter. Temperatures in spring were close to or slightly above average in the Netherlands and France, while summer temperatures were considerably above average in June and July. August was, by contrast, rather cool. July 2006 was the warmest month on record for the Netherlands and Belgium, where records began in 1830. The mean temperature for July was around 5°–7°C above the 30-year meteorological average. Temperature anomalies in July in France were above 4°C in most parts of the country, where it was the hottest July in the 57-year record and the second hottest month overall behind August 2003.

The warmest September in the CET series (16.8° ±0.2°C, +3.2°C anomaly) contributed to the warmest autumn (12.6° ±0.12°C). Indeed, in central England, autumn 2006 was nearly seven standard errors warmer than the next warmest autumns recorded in 1730 and 1731 (11.8°C). Autumn was also the warmest ever in the De Bilt (Netherlands) series, which started in 1706. The mean temperature of 13.6°C in De Bilt was exceptionally high even compared to the previous record temperature of 12.0°C. September was the warmest ever recorded in the Netherlands. France experienced temperatures above the 90th percentile in October and November. October 2006 was the second warmest month in France since records began in 1950 with an anomaly relative to 1971–2000 of +3.3°C.

*(ii) Precipitation*

Annual average precipitation was close to the long-term mean for the northwestern European countries. However, there was significant seasonal and regional variability. The United Kingdom as a whole registered 107% of normal annual rainfall (1961–90). With 112% of normal rainfall, Scotland was the wettest British region in 2006. In Ireland, annual rainfall totals were above normal over most of the country.

The United Kingdom had its driest winter since 1964. France, Belgium, and the Netherlands experienced their highest negative rainfall anomalies in January and June, with totals in large parts of the country below the 10th percentile. Spring precipitation was slightly above normal in most of the region, with the highest anomalies in Northern Ireland, Wales, and western parts of England. May was a significantly wet month in Belgium, Ireland, England, and Wales, where monthly precipitation totals were above the 90th percentile (w.r.t. 1979–2000) and the England and Wales region reported its wettest May for 23 years.

## *COUNTRY SPOTLIGHT:* BOSNIA AND HERZEGOVINA—*Z. Majstorovic*

Bosnia and Herzegovina can be divided into three climate regions, which are covered by 13 professional meteorological stations. The lowest air temperature in 2006 was recorded in January: –24.7°C in Bjelasnica. The highest air temperatures was recorded in June in Mostar (41.2°C) Annual precipitation ranged from a high of 1218 mm in Bihac to a low of 716 mm in Zenica. The lowest monthly precipitation total was recorded in October: 11 mm in Jajce. The highest monthly precipitation total occurred at Ivan Sedlo (197 mm) in August. Overall, Bosnia and Herzegovina was 0.4°C warmer normal in 2006, while annual precipitation was slightly lower than normal.

Winter 2005/06 was slightly colder than average. December was near normal, January was significantly colder, and February was slightly colder than average. Precipitation was slightly higher than normal, mostly due to December rains, but the sums in January and February were below normal. Spring 2006 had near-normal temperatures: March was colder than normal, April was slightly warmer, and May was near normal. Precipitation was wetter than average, especially in March when the largest snow cover on record was reported in Bjelasnica: 345 cm. Average summer temperatures were near normal, but there were several periods of extremely high temperatures (especially in June), and some with temperatures below the LTM. Precipitation was slightly wetter than normal; some eastern locations reported their wettest August on record. Mean temperature during autumn (all 3 months; OND) were above normal, especially in October when the mean monthly temperature anomaly was +2°C. Fall precipitation was below normal.

Summer rainfall in England and Wales was the lowest for a decade. Eastern Scotland, South Wales, and the southwest were particularly dry. Extremely dry conditions occurred in the Netherlands in June and July with very low rainfall amounts (only 39% of the normal in July), especially in the western part, which had less than 10 mm of rainfall. In contrast, August was extremely wet (above the 90th percentile) in the Netherlands, Belgium, and northern France. The Netherlands reported 297% of normal values in August.

Autumn was dry in the Low Countries and northern France, while conditions in Ireland, the United Kingdom, and western France were much wetter (150% of the normal in Ireland). The Netherlands received only 16% of the monthly average rainfall in September. Precipitation in France was lower only in its northern part, while wetter conditions occurred in the south of the country. Northern Ireland registered its second wettest September since 1985. Scotland experienced its wettest November (155% of the normal with some stations in the west receiving more than double the monthly average) and December in a rainfall series that began in 1914.

*(iii) Notable events*

At the end of September, the extratropical remnants of Hurricane Gordon brought strong winds and rain to the United Kingdom, particularly to Northern Ireland and Scotland. The remnants of Gordon produced widespread and sustained rainfall across Northern Ireland and Scotland, with winds gusting to 130 km $h^{-1}$ in Northern Ireland. The southwest of England was also affected by high winds.

6) Baltic States and eastern Europe—A. Obregón, P. Bissolli, and J. J. Kennedy

*(i) Temperature*

In 2006, the region experienced above-average temperatures nearly everywhere, with anomalies increasing with latitude. The highest positive anomalies were observed in the Baltic States (e.g., Lithuania 0.9°–1.7°C). Temperature anomalies in eastern Europe were mainly between 0.5° and 1.0°C.

The year started with unusually low temperatures in January across the whole region, except northern parts of Estonia. Temperature anomalies during the first month were lowest in Belarus and Ukraine. The Baltic States were affected by the cold wave and experienced similarly low temperatures. In Serbia, a new record-low temperature of –39.0°C was measured in Karajukica Bunari on 26 January. February and March were also cold throughout most of the region.

The rest of the year saw mostly above-average temperatures throughout the region. The heat wave in July affected the western part of eastern Europe. Serbia experienced a remarkable heat wave between 20 and 29 July with temperatures of 5°C above the long-term mean. August showed a dipole pattern in temperature anomalies. The Baltic States and eastern regions of Belarus and Ukraine experienced high temperatures, exceeding the 90th percentile, while temperatures in Hungary, Slovenia, western Slovakia, parts of Croatia, Serbia, and Bosnia and Herzegovina were below the long-term mean. Autumn temperatures were generally well above average, especially in the Baltic States, Slovakia, and Hungary. The year ended with extremely high mean temperatures. Temperatures in December mostly exceeded the 90th

percentile. The capitals of Lithuania and Estonia reported mean temperature anomalies around +7°C. The influence of the Siberian air masses was significantly reduced by cyclones from the North Atlantic region.

*(ii) Precipitation*

In 2006, wide areas of eastern Europe experienced normal or above-average precipitation, while the Baltic States were mostly drier than normal. Precipitation in Lithuania was near normal due to an extremely wet August; Vilnius received more than 180% of its August average. The wettest regions were generally found in eastern Europe, with highest rainfall anomalies in Bulgaria.

Winter 2005/06 was drier than average in the Baltic States and wetter than average in eastern Europe. Spring precipitation totals were higher than usual in most areas, with the exception of the Baltic States. The distribution of summer rainfall across the whole region was similar to that seen in the spring with negative anomalies in the Baltic States and positive anomalies in eastern Europe. During the last months of the year, drier-than-normal conditions were to be found in Croatia and Bosnia and Herzegovina.

*(iii) Notable events*

An extraordinarily swift thaw in April produced extensive flooding along the Danube, which reached its highest level in more than a century. Areas in Hungary, Serbia, Romania, and Bulgaria were most affected. In Budapest, the water level of the Danube exceeded the record set in 2002. Romania was affected by several extreme weather events during the summer: a deadly mudslide in northern Romania in June and flooding in July within the same region.

### 7) Southeastern Europe—A. Obregón, P. Bissolli, and J. J. Kennedy

*(i) Temperature*

Temperatures in southern Europe were above average in 2006 through much of the region. Greece and the European part of Turkey experienced slightly above average temperatures. In the western regions of southern Europe, temperature anomalies were considerably higher. Italy had annual anomalies on the order of +1°C in the northern and central regions and about +0.5°C in the south.

In early 2006, Greece, Turkey and southern regions of Italy were also unusually cold. The monthly average maximum temperature in Athens was 2.1°C below the climatological norm. Temperatures in the European part of Turkey were below the 10th percentile. However, some areas on the Italian islands (Sicily and Sardinia) were also warm in the spring (anomalies up to 4°C), exceeding the 90th percentile.

Summer temperatures were generally above average. In Italy, June was characterized by warming in the north and in some points in the south (anomalies up to 3°–4°C). In July, most of Italy experienced temperatures above the 90th percentile. Monthly average maximum temperatures in the northeast of Italy reached new records in some regions. Temperatures in southern parts of Greece were above the 90th percentile in August, while regions in northern Italy were colder than the 10th percentile. Southern Italy, particularly Sicily, experienced unusually high temperatures in August. In Messina, an historical high temperature of 41.8°C was recorded. In Bologna, it was the second hottest autumn since 1948. December was colder than normal over Greece. Temperatures in large parts of Italy were above the 90th percentile during this month.

*(ii) Precipitation*

Most parts of northern Italy experienced drier-than-normal conditions, while central and southern Italy, Greece, and Turkey received positive rainfall anomalies. In the Po Valley in northern Italy, the low precipitation amounts caused drought conditions with reduced water availability. Spring was generally drier than average in Italy and Greece, due mainly to an unusually dry May. Summer conditions were generally wetter than normal in southern Italy and Greece, while northern Italy remained dry, especially in June. During this month, most of northern Italy experienced precipitation below the 10th percentile (1979–2000 base period).

Lower-than-average precipitation was also observed in Italy as a whole during autumn. Greece was significantly wet in September (rainfall above the 90th percentile), but precipitation was well below average in November (below the 10th percentile) in most regions. Rainfall on the Greek Aegean island of Samos was 920% of the average October value. December was dry across most of southeastern Europe, especially in southern Greece, although southern Italy and Sicily were very wet.

### 8) Middle East—A. Obregón, P. Bissolli, and J. J. Kennedy

*(i) Temperature*

Annual average temperatures were above average over nearly the whole region. The anomalies were mostly between 0° and +1°C and partly above +1°C

in the eastern parts (Georgia, Armenia, Azerbaijan, and western Kazakhstan). The cold spell that dominated Europe in January also affected the Caucasian countries and western Kazakhstan, where temperatures were lower than the 10th percentile with anomalies between –6° and –10°C. In February, warmer air from the southeast extended into the region and temperatures exceeded the long-term average during most of the spring season. The summer, too, was generally above average, with high anomalies in June and August, while July was mostly near average. A heat wave occurred in Cyprus between 19 August and 28 August, with maximum and minimum temperature anomalies of 2°–5°C above normal. The autumn was mostly warmer than normal. Significant anomalies occurred in October when eastern parts of the region were 3°C above average.

*(ii) Precipitation*

Precipitation totals from December 2005 to November 2006 were mainly near normal. Cyprus and Azerbaijan were the exceptions in that they were very dry, with some areas receiving less than 50% of the annual precipitation average. The annual average for Cyprus was 77% of the normal, although October and November were particularly wet.

*h. Oceania*

1) Australia—A. Watkins and B. Trewin

Despite only weak-to-moderate El Niño conditions in the Pacific, Australia, as in 2002, experienced above-normal pressures during the year, which suppressed convection and kept cold fronts south of the continent. As a result, significant dry conditions were experienced over much of the country by the second half of 2006. For many of these areas the drought of 2006 added to significant longer-term rainfall deficiencies, with large regions having experienced little recovery from the droughts of 1997/98 and 2002/03, resulting in severe hydrological drought throughout much of eastern and southwestern Australia.

However, a vigorous wet season across northern Australia, as well as the inland penetration of tropical cyclones into remote areas of western Australia early in the year, largely offset the acute dry in the country's

## *COUNTRY SPOTLIGHT:* ARMENIA—A. Hovsepyan

The year 2006 was 1.2°C warmer than normal all over Armenia (Fig. 6.40). It was the seventh warmest year in Armenia since 1929. Annual precipitation totals were close to the 1961–90 normal. The northeastern and southern parts were very dry, while central parts received above-average precipitation. Winter 2005–06 was rather warm, with seasonal temperatures 1°C above the 1961–90 mean. The summer was the hottest in 70 years; seasonal temperatures exceeded the 1961–90 mean by 2.7°C. Mean summer precipitation was only 60% of normal.

January was colder than normal by 1.5°C all over Armenia. Precipitation exceeded the normal by about 40%. Temperatures in February were higher than normal by 1°–1.5°C, except in the Ararat valley, where negative anomalies reached –1.5°C. March was very warm (anomalies of 2°–3°C) and dry (60%–70% of normal precipitation) over the country. April was warm and rainy across Armenia. Precipitation totals exceeded the normal by 60%–70%. Climatologically, April–May is the wettest period of the year in Armenia, but in 2006, some regions reported no rain in May. Severe drought developed across the country in June. Mean monthly temperature was above normal by 4°–4.5°C. August was very hot and dry, as monthly temperature anomalies reached 3.5°–4°C. During a heat wave (6–15 August) maximum temperatures reached up to 42°C.

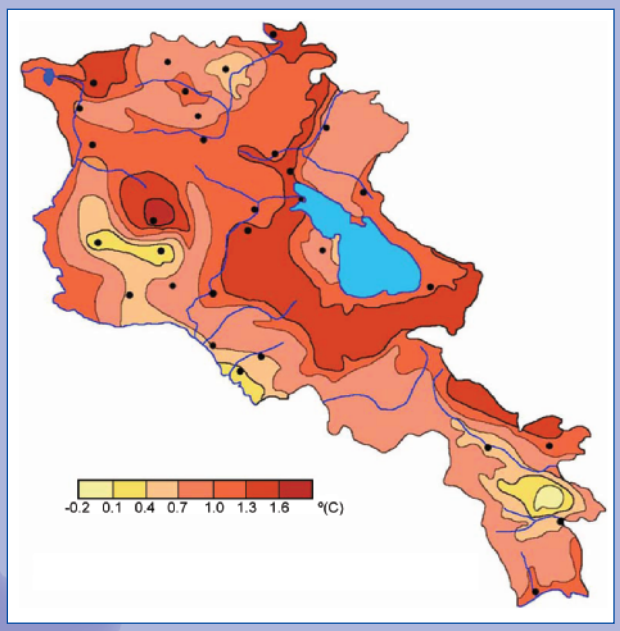


**Fig. 6.40. Annual average air temperature (°C) anomalies for Armenia.**

In September, the monthly mean temperature was 2°–4°C higher than normal. October was quite warm (2.7°C higher than normal) and wet (precipitation totals exceeded the normal by 150%–250%). December was very cold. The monthly mean temperature was 2.2°C below normal. Precipitation was generally about 60% of normal.

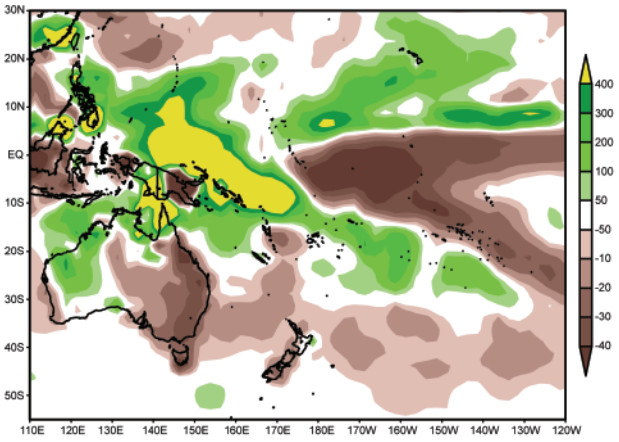


**Fig. 6.41. 2006 annual precipitation anomalies (mm, 1979–2000 base) for Oceania from CAMS-OPI.**

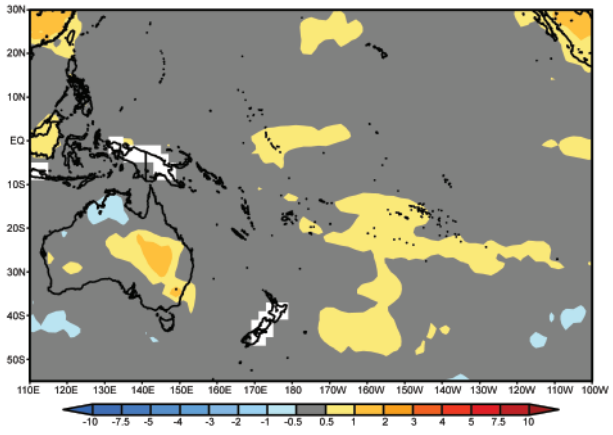


**Fig. 6.42. 2006 annual temperature anomalies (°C, 1971–2000 base) for Oceania from CAMS-OPI.**

main population and agricultural areas of the south and east (Fig. 6.41). The wetter-than-average conditions in the north and northwest of the continent earlier in the year reduced daytime maximum temperatures in these areas, while high pressures brought clear skies and cold nights to the southeast and a cool winter in the Tropics. Overall, much of eastern Australia had above-average temperatures in 2006, while a small patch in the north was cooler than average (Fig. 6.42).

For eastern and southwestern Australia, the big drought of 2006 was exacerbated in the latter months of the year by very warm conditions. Spring 2006 was Australia's warmest since seasonal records commenced in 1950. The driest and warmest 5-year period on record in the major Australian cropping zones, in addition to a general failure of rainfall during the 2006 April–October crop and pasture growing season, contributed to extremely large downturns in agricultural production.

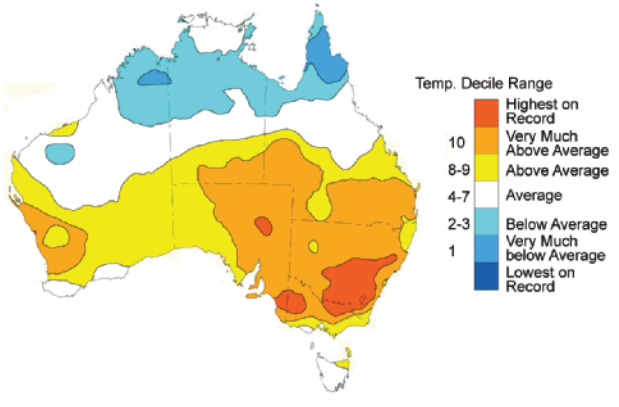


**Fig. 6.43. Australian maximum temperature deciles for 2006 (1950–2006 base).**

*(i) Temperature*

Maximum temperatures for 2006 were mostly above normal for areas south of the Tropics, resulting in 33% of the continent experiencing daytime temperatures in the top decile (Fig. 6.43). New South Wales, Victoria, and the Murray Darling Basin (Australia's "food basket") all recorded their second warmest annual maximum temperatures (behind 2002) on record[7] (1.55°, 0.97°, and 1.54°C above average, respectively). Overall, Australia's maximum temperatures were the ninth warmest on record, with an anomaly of +0.60°C.

In some contrast, minimum temperatures for the year were cooler than normal in the southeast, as well as in the top end of the Northern Territory and the Kimberly region of western Australia. However, inland regions were generally warm at night despite the reduced cloud cover, with temperatures ~0.5°C above normal. South Australia and Queensland both had their 10th warmest nighttime temperatures on record (+0.65° and +0.56°C above the 1961–90 average, respectively), and with 40% and 36% of the states in decile 10. The Australian minimum temperature anomaly for 2006 was +0.34°C, the 17th warmest. Australia's mean temperature for the year was 0.47°C

[7] High-quality *annual* Australia-wide temperature anomalies have been calculated for all years since 1900 (Della-Marta et al. 2004), while high-quality *monthly* anomalies are available from 1950. High-quality nationwide rainfall measurements commenced in 1900 (Lavery et al. 1997). Anomalies are calculated with respect to the 1961–90 average, in accordance with World Meteorological Organization guidelines.

above the 1961–90 mean, making it the 11th warmest year on record.

*(ii) Precipitation*

With only January, April, and July bringing widespread near- or above-average rainfall to Australia, 2006 proved to be an extremely dry year for most regions south of the Tropics (Fig. 6.44). Aside from Darwin, Australia's northern-most major city, all of the densely populated regions of Australia, as well as the vast majority of Australian agricultural areas, experienced significantly below normal rainfall for the year. Victoria, New South Wales, and Tasmania had 96%, 45%, and 72% of their state in decile 1, giving them their third (366 mm), ninth (349 mm), and third (877 mm) driest years, respectively. For southeastern Australia, this was the second-driest year (367 mm) after 1982 (355 mm), while in the southwest of the continent, it was sixth driest (476 mm). It was the driest year on record for the cities of Perth and Hobart, and the second driest for Adelaide. The agriculturally vital Murray Darling Basin experienced its third-driest year on record, after 1902 and 1944. When added to the long-term dry, the resulting inflows to Australia's second-longest river, the Murray, were lower than that of the previously lowest inflows, which occurred in the Federation drought of 1902. Rainfall anomalies were particularly extreme in the highlands of eastern Victoria, southern New South Wales, and northern Tasmania. Stations such as Burnie in northwestern Tasmania (408 mm, previous record 670) and Harrietville in northeastern Victoria (504 mm, previous record 710) were more than 200 mm below their driest recorded year.

The dry conditions blanketing the major population and agricultural regions added to long-term rainfall deficiencies. By the end of 2006, New South Wales had experienced dry conditions for over five years; southeast Queensland, seven years; Victoria, northern Tasmania, and eastern south Australia, 10 years; and in southwest western Australia, some 30 years.

In contrast, the wet season (October 2005–April 2006) over northern Australia was the fifth wettest since high-quality rainfall records commenced in 1900, with an average of 674 mm falling over the period. This was despite an initially weak and late start to the Australian monsoon. At Darwin, the monsoon onset did not occur until around 13 January, about two weeks later than the usual timing of 28–29 December (Drosdowsky 1996). Overall, Australia recorded 490 mm (long-term average 472 mm) for the year, making it the 32d wettest year of the 107 years of record. However, such a relatively wet year would be contrary to the experience of most Australians, with the vast majority living within the 39% of the continent, which received rainfall in the lowest three deciles.

*(iii) Notable events*

Tropical Cyclone Larry (see section 4) was category 5 shortly before it crossed the coast as category 4, the most intense system at landfall in Queensland since 1918. Similarly, during the passage of Tropical Cyclone Monica along the Northern Territory coast, it became a category 5 system and the strongest ever observed in the Northern Territory region.

A major unseasonal cold outbreak affected southeastern Australia from 15 to 17 November (late spring). Snow fell near sea level in southern Tasmania, above 400 m in central Victoria, through large parts of the NSW tablelands, including the nation's capital Canberra, and as far north as Queensland. Numerous record low maximum temperatures were set. A Queensland State November record of 0.0°C was set at Stanthorpe and Applethorpe, and Sydney (8.3°C) had its coldest November night since 1905.

Persistent extreme heat affected much of eastern inland Australia from late December 2005 through early March 2006, with many records being set for average temperatures or consecutive days above thresholds. At Windorah (Queensland), there were 55 consecutive days above 37.8°C (100°F) from 30 December to 22 February, and 63 consecutive days above 35°C ending on 2 March. Birdsville's January mean monthly minimum of 30.0°C was the first time an Australian station had recorded a monthly average minimum of 30°C or above.

A severe early spring heat wave occurred in southeastern Australia in early October, with many locations setting early season records. On 12 October Adelaide

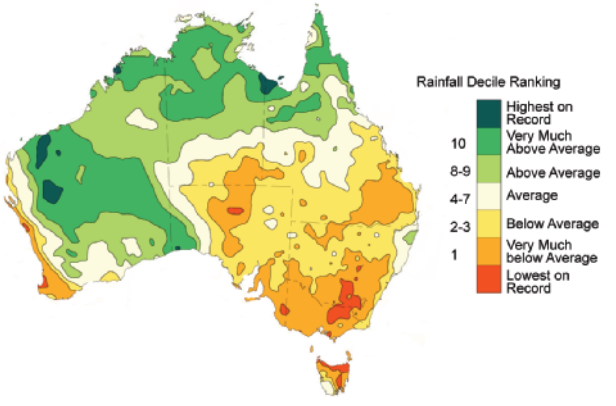


**Fig. 6.44. Australian rainfall deciles for 2006 (1900–2006 base).**

reached 37.9°C, Melbourne 36.6°C, and Hobart 33.1°C, all early season records. This was Melbourne's earliest postwinter 35°C+ day on record (records commence 1856), which followed its earliest postwinter 30°C+ day which had occurred only the month before (30.1°C on 19 September 2006). October was the hottest on record for New South Wales and Victoria.

Persistent extreme heat affected much of central and inland eastern Australia during the second half of November. November record highs were set over much of southwestern Queensland, and Birdsville reached 48.5°C on 30 November, which was 0.2°C below the Australian November record set there in 1990. Many locations set records for extended November hot spells, including Canberra (11 days above 30°C) and Alice Springs (12 days above 37.8°C, or 100°F).

Numerous major bushfires occurred in Victoria during January 2006. There were also significant fires during this period in Tasmania. With dry and hot conditions, major fires in South Australia, New South Wales, Victoria, and Tasmania occurred far earlier than in previous years. Lightning strikes on 1 December sparked an immense blaze in Victoria's Gippsland and northeast regions. The fire lasted over two months and burned approximately 1.1 million ha.

With clear skies and very low soil moisture, a number of major frost episodes occurred in the southern half of Australia during late May and June. One extreme event occurred on 30 May, when state records for the month were set for Queensland (–6.8°C at Stanthorpe) and Tasmania (–10.5°C at Liawenee). In western Australia, a state record for June (–6.0°C) was set at Collie East on 17 June, the same day the city of Perth recorded its first subzero minimum (–0.7°C). A succession of frost events also caused damage in southeastern Australia during late September and October. The most damaging event occurred on 25 September, when widespread subzero temperatures in northern Victoria led to major losses in the Goulburn Valley fruit crop (estimated at $70 million Australian). A new Australian record low temperature for October was set on the 29th when Charlotte Pass (New South Wales) reached –12.0°C.

### 2) New Zealand—J. Salinger

#### *(i) General conditions*

Erratic and sometimes extreme, New Zealand's climate for 2006 featured one of the severest winter snowstorms in decades, a very windy spring, and a rather cool start to summer in December 2006. The national average temperature of 12.4°C in 2006 was 0.2°C below the 1971–2000 normal. Thus, 2006 ended up very close to the 1971–2000 normal, as a compromise between very warm months (April and September) and very cold months (March, June, December). April was the warmest and June the coldest in the last 30 years, September was the third warmest on record, and December one of the coldest in the last 60 years. Temperatures were above normal in the northeast of both islands, but below normal in inland areas of the South Island. Well-below-normal rainfall occurred throughout parts of central Otago (southeast of South Island), with totals less than 75% of normal, as well as in Awatere Valley in Marlborough. Rainfall was well above normal in the southern North Island and Christchurch areas, with totals at least 120% of normal. The year was dominated by more anticyclones in the Australian Bight/Tasmania area, with stronger westerlies in the Southern Oceans, giving windier southwesterlies over New Zealand.

#### *(ii) Notable events*

The highest recorded extreme temperature of the year occurred during a heat wave in central Otago toward the end of January. Alexandra recorded maximum temperatures of 36°C for three consecutive days from 27–29 January (unheard of in their historical record, commencing in 1930).

The lowest air temperature for the year was –14.0°C recorded at both Tara Hills, Omarama, on 14 June, and Fairlie on 28 June. The minimum air temperatures were –10°C or lower in parts of inland south Canterbury and/or north Otago, on nine days between 14 and 29 June.

The highest recorded wind gust for the year was 180 km $h^{-1}$ and was recorded from the northwest, at Southwest Cape (Stewart Island) on 2 September, which is a new record for a wind gust at that site. Mean wind speeds reached 128 km $h^{-1}$.

The driest rainfall recording locations were Alexandra in central Otago with 266 mm of rain for the year, followed by Clyde with 286 mm.

Of the regularly reporting gauges, the Cropp River gauge in Westland, inland in the headwaters of the Hokitika River, recorded the highest rainfall with a 2006 annual total of 11,370 mm.

Nelson was the sunniest center in 2006, recording 2580 hours, followed by Blenheim with 2528 hours, and Tauranga with 2507 hours.

Invercargill recorded its sunniest year on record with 1853 hours, and Kaitai, Tauranga, and Dunedin their second sunniest.

The year began with significant soil moisture deficits in the north and east of the North Island and eastern South Island, which persisted in these regions

until March. March was cold, and an ex–tropical cyclone produced high rainfall in the north of the North Island. Flood-producing rainfall events occurred in north and east Otago and in the Hauraki–Coromandel region during April. As a result, the month's rainfall was very high in these regions. Rainfall in north and east Otago totalled 300%–400% of normal, and totals in the Hauraki–Coromandel region were at least 200% of normal. It was the eighth warmest April on record. May produced well-above-average rainfall in the north of the North Island, and east of the South Island, with low rainfall in parts of the south of the South Island. Two severe winter snowstorms accompanied by bitterly cold conditions, and later heavy frost, contributed to a particularly cold June. Temperatures were 2°C below average in some regions. It was much sunnier than normal in all western and southern regions, with record high June totals in the north of the North Island, and coastal Otago. In contrast, July was warmer than June, going against the usual trend. It was very wet in the south and west of the North Island, with twice the normal rainfall in Wairarapa with flooding. July was rather dry in other areas with rainfall totals a mere 25%–50% or less of normal in the north of the North Island and Otago. High rainfall continued in August in the south and west of the North Island, but it was dry in much of the South Island, and extremely sunny in the south. September was a month of climate extremes with record low rainfall and high mean temperatures at many locations. Rainfall was low throughout much of New Zealand, especially in the east, with some locations recording 10% or less of normal rainfall. In some areas temperatures were 2°C above average, with windy conditions in the south. It was windier than usual over most of the South Island and southern half of the North Island in October, with several locations in Marlborough and Otago recording their windiest October in over a decade. November produced stormy westerlies over the South Island: it was particularly warm in the east of the North Island, yet cold in the southwest of the South Island. Significant soil moisture deficits existed in Northland and central Marlborough by the end of the year. December ended the year on a cool note, with one of the coldest Decembers in the last 60 years, as more frequent southerlies brought temperatures 2°C below average.

Notable climate features in various parts of the country included numerous heavy rainfall events of which 18 produced floods. Snowfall events occurred on 11 occasions, mainly in high country areas from midautumn to late winter, with ski areas having an extended season. Other climate extremes included a summer heat wave, seven tornado-like incidents, three severe hailstorms, and many damaging windstorms. The most significant extreme event of the year was the winter snowfall event over the night of 11/12 June in Canterbury, especially in the south, with snow settling to sea level. The worst flooding events during 2006 were those of 25–26 April in Otago and 4–6 July in Wairarapa. In the Otago flood, rivers ran extremely high, and much of the Taieri Plains including Mosgiel were flooded, with some evacuations. Floodwaters also affected the towns of Oamaru and Waitati. The Wairarapa flood occurred during a 3-day period of high rainfall, also affecting Wanganui and Wellington.

### 3) Southwest Pacific—J. Salinger

This year saw a change from a La Niña to an El Niño climate pattern in the Pacific. The first quarter of the year was dominated by weak La Niña–like (cold episode) characteristics, followed by a neutral period. Weak-to-moderate El Niño conditions in the tropical Pacific were in place by September, which peaked in December. A higher frequency of surface equatorial westerlies occurred near the date line from August through November (the highest persistence since the 2002 El Niño event when surface westerlies were much stronger). Trade winds generally were near normal in strength at other times of the year. The SPCZ was farther south than usual from January through May (typical for La Niña), but was near its normal location throughout much of the remainder of the year. Below-average equatorial SSTs occurred around western and eastern Kiribati with the cold episode (–1°C anomalies), returning to normal by April. Positive SST anomalies (+0.5°C) became apparent near the date line in the equatorial Pacific in June. These warmed to a constant +1.5°C above average in the seas around western and eastern Kiribati from August/September onward. Negative SST anomalies occurred around New Caledonia from August through December, more than 1°C below average in October. These features were also consistent with El Niño development. From January through June, OLR anomalies showed enhanced convection over the Solomon Islands and Papua New Guinea. Suppressed convection occurred over western and eastern Kiribati from January through May, with a reversal to enhanced convection from August through December. For much of the year, mean SLP was below average east of the date line. However, positive anomalies prevailed in the western Pacific over Australia and the Tasman Sea from May onward.

For 2006 as a whole, above-average SSTs occurred throughout much of the tropical southwest Pacific.

These were at least +0.7°C above average throughout central and southern French Polynesia, extending to the southern Cook Islands and Pitcairn Island. Some locations experienced above-average SSTs for 11 months of the year. SSTs were at least +0.5°C above average in many other tropical island nations, especially those near and east of the date line. SSTs were near average in the region between Papua New Guinea and New Zealand, including New Caledonia. Southwest Pacific island surface air temperature anomalies for 2006 were consistent with the SST anomalies throughout the region. It was an extremely warm year in Fua'amotu, Tonga, where the mean temperature of 24.6°C was 0.8°C above the historical average and was highest since measurements commenced in 1980. Tahiti Faa'a, in French Polynesia was also much warmer than usual, with a mean temperature of 26.9°C (0.7°C above the 1971–2000 normal).

OLR anomalies (Fig. 6.45) showed a region of enhanced convection over Papua New Guinea and the Caroline Islands to the north, extending southeast to the Solomon Islands and northern part of Vanuatu. Another area of enhanced convection, although not as strong, occurred over Niue and the southern Cook Islands. Convection was suppressed in a horseshoe-like pattern in 2006 over eastern Kiribati and parts of western Kiribati, extending to the northern Cook Islands and southeast over the Tuamotu Islands of French Polynesia and to Pitcairn Island.

The year's rainfall anomalies were similar to those of the OLR, with above-average (at least 110% of normal) rainfall over much of the Solomon Islands, northern Vanuatu, Niue, and the Southern Cook Islands, as well as parts of central and southern French Polynesia. Rainfall was below average (less than 90% of normal) in the North Tasman and over New Caledonia, as well as parts of eastern Kiribati and the northern Cook Islands. One location, Rotuma Island, Fiji, recorded an extremely high 2006 rainfall of 4378 mm (128% of normal). Two locations recorded well-below-average annual totals. These were Noumea, New Caledonia, with 735 mm (75% of normal), and Raoul Island, New Zealand, with 948 mm (61% of normal).

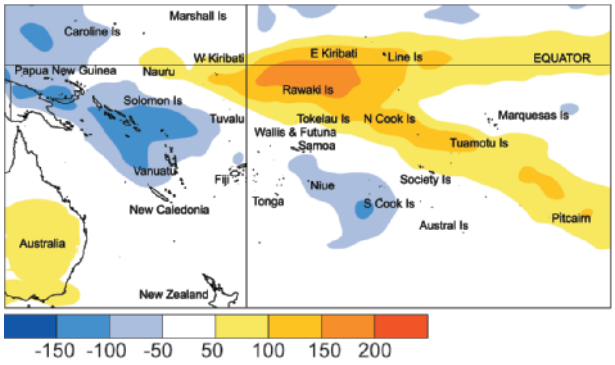


**Fig. 6.45. Annual South Pacific OLR anomalies (W m$^{-2}$). High radiation levels (yellow or orange) are typically associated with clearer skies and lower rainfall, while low values (blue) often indicate cloudy conditions and more rain for the region.**

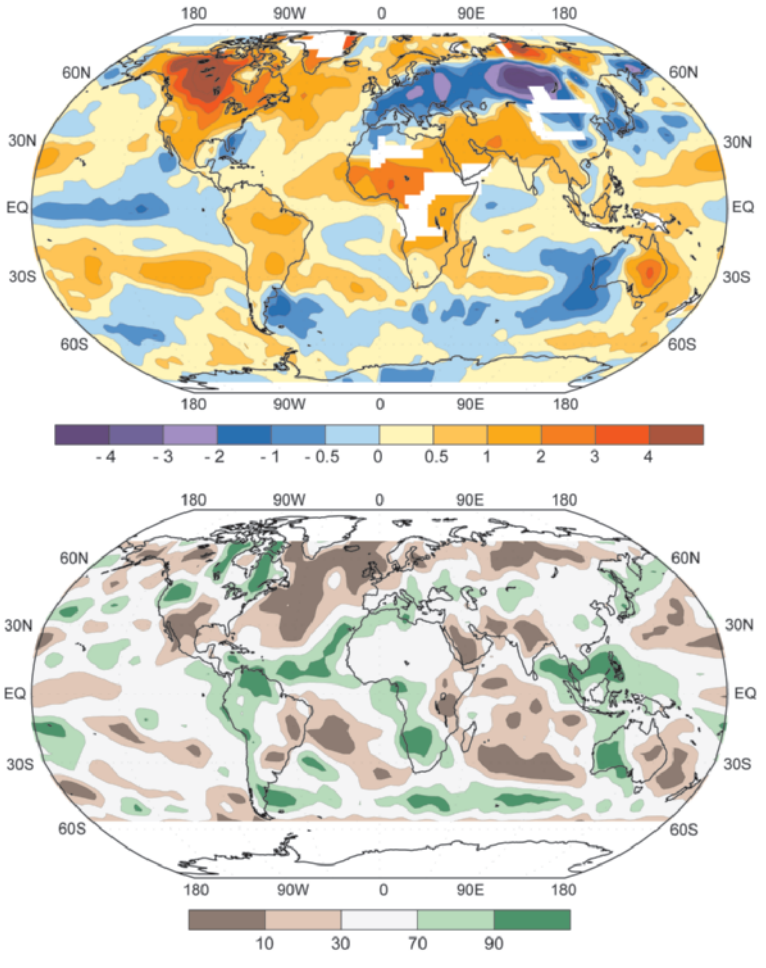


**Fig. 7.1. December 2005–February 2006 (top) surface temperature anomalies (°C) and (bottom) precipitation percentiles based on a gamma distribution fit to the 1979–2000 base period. Temperature anomalies (1971–2000 base period) are based on station data over land and sea surface temperature over water. Precipitation data were obtained from a combination of rain gauge observations and satellite-derived estimates (Janowiak and Xie 1999). Analysis was omitted in data-sparse regions (white areas).**

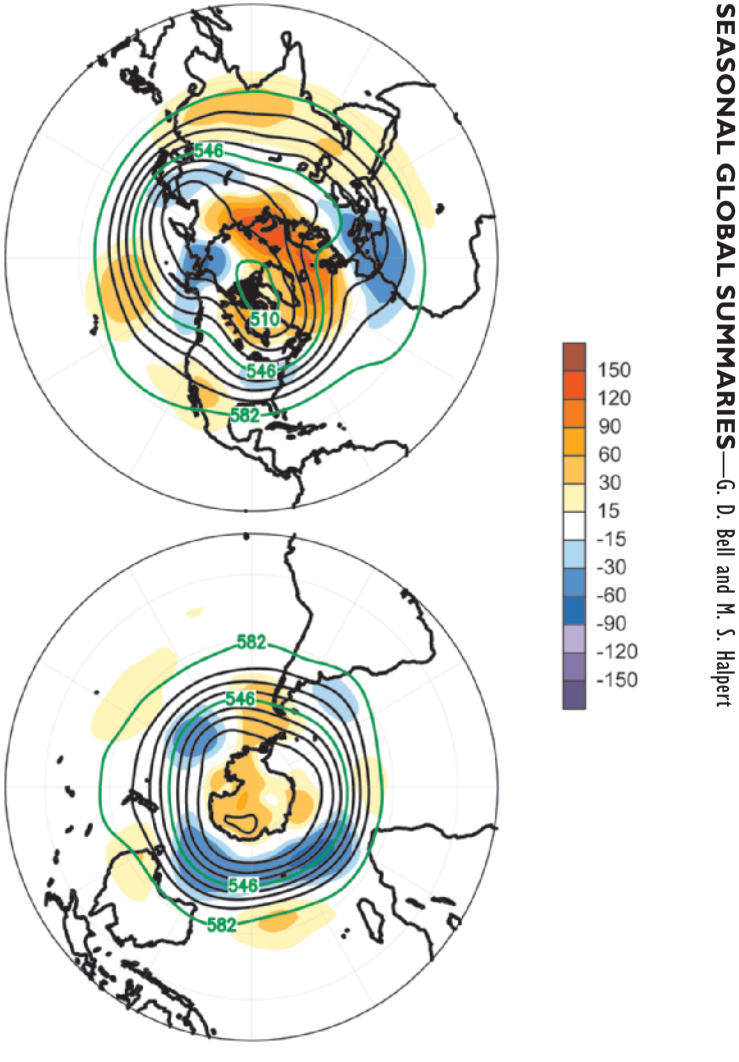


**Fig. 7.2. December 2005–February 2006 (top) Northern Hemisphere and (bottom) Southern Hemisphere 500-hPa geopotential heights (9-dam contour interval) and anomalies (shading) from the 1979–2000 base period mean.**

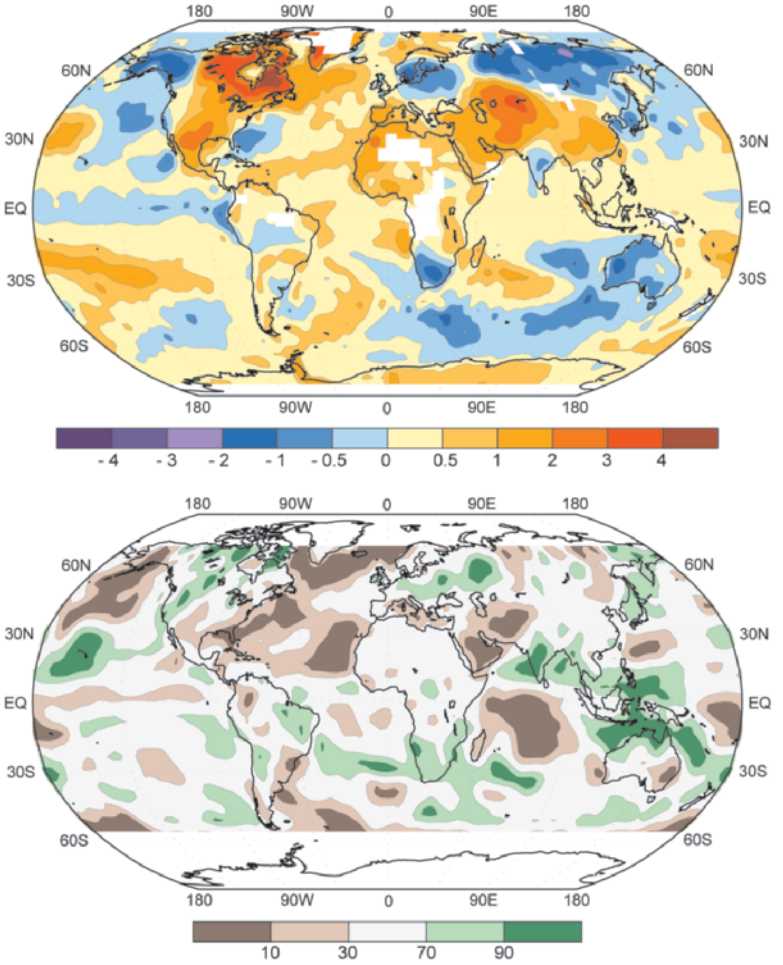


**FIG. 7.3. March–May 2006 (top) surface temperature anomalies (°C) and (bottom) precipitation percentiles based on a gamma distribution fit to the 1979–2000 base period. Temperature anomalies (1971–2000 base period) are based on station data over land and sea surface temperature over water. Precipitation data were obtained from a combination of rain gauge observations and satellite-derived estimates (Janowiak and Xie 1999). Analysis was omitted in data-sparse regions (white areas).**

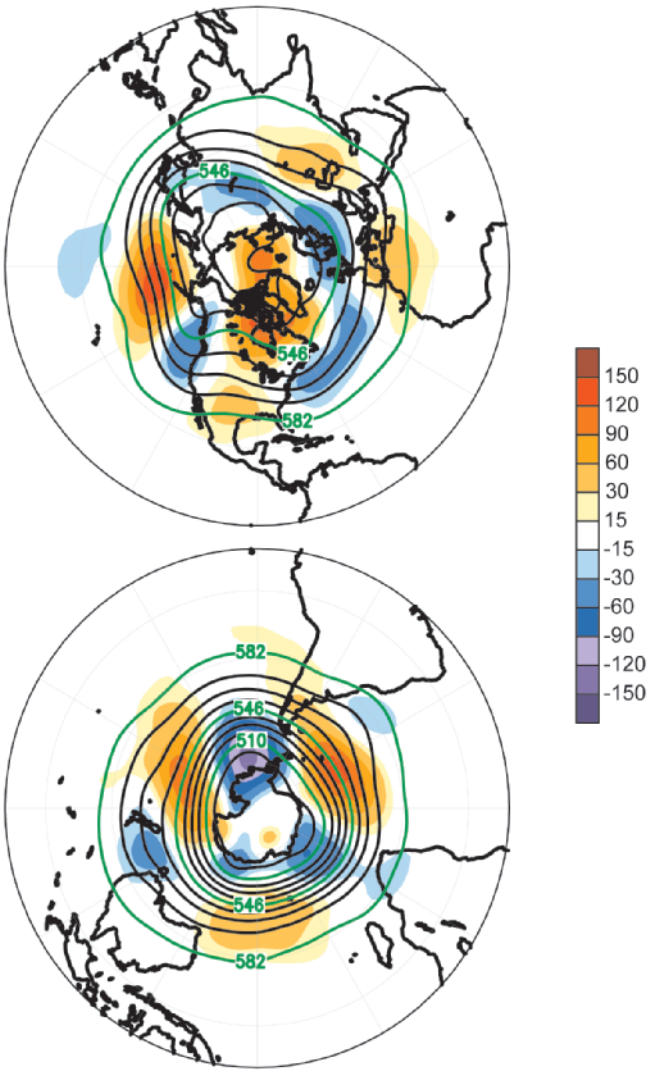


**FIG. 7.4. March–May 2006 (top) Northern Hemisphere and (bottom) Southern Hemisphere 500-hPa geopotential heights (9-dam contour interval) and anomalies (shading) from the 1979–2000 base period mean.**

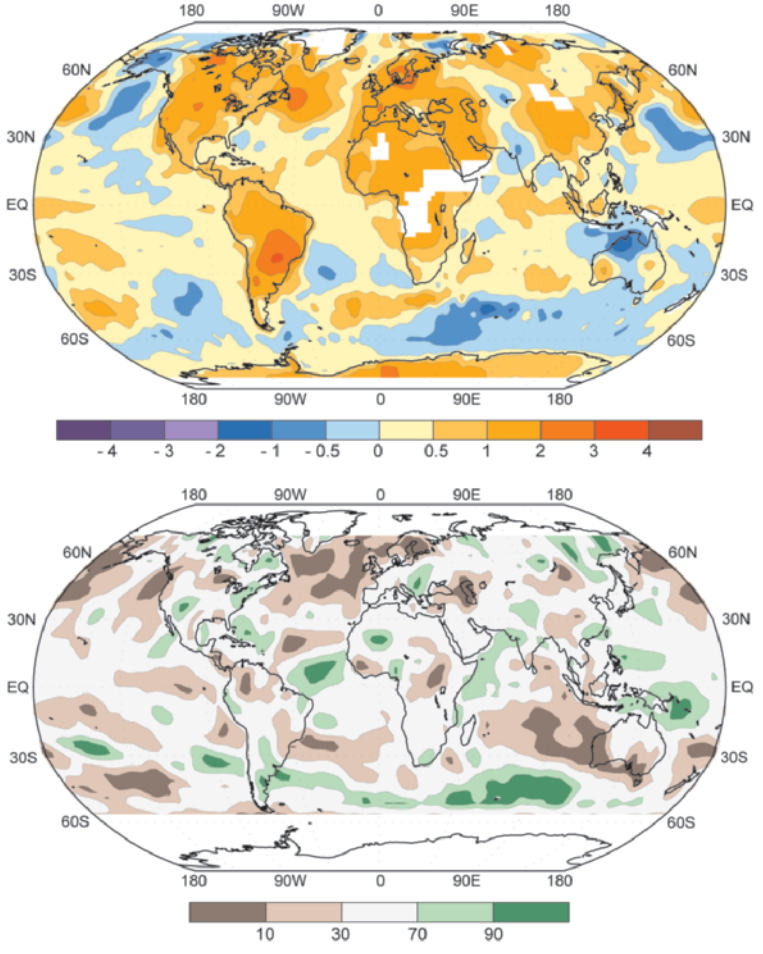


**Fig. 7.5. June–August 2006 (top) surface temperature anomalies (°C) and (bottom) precipitation percentiles based on a gamma distribution fit to the 1979–2000 base period. Temperature anomalies (1971–2000 base period) are based on station data over land and sea surface temperature over water. Precipitation data were obtained from a combination of rain gauge observations and satellite-derived estimates (Janowiak and Xie 1999). Analysis was omitted in data-sparse regions (white areas).**

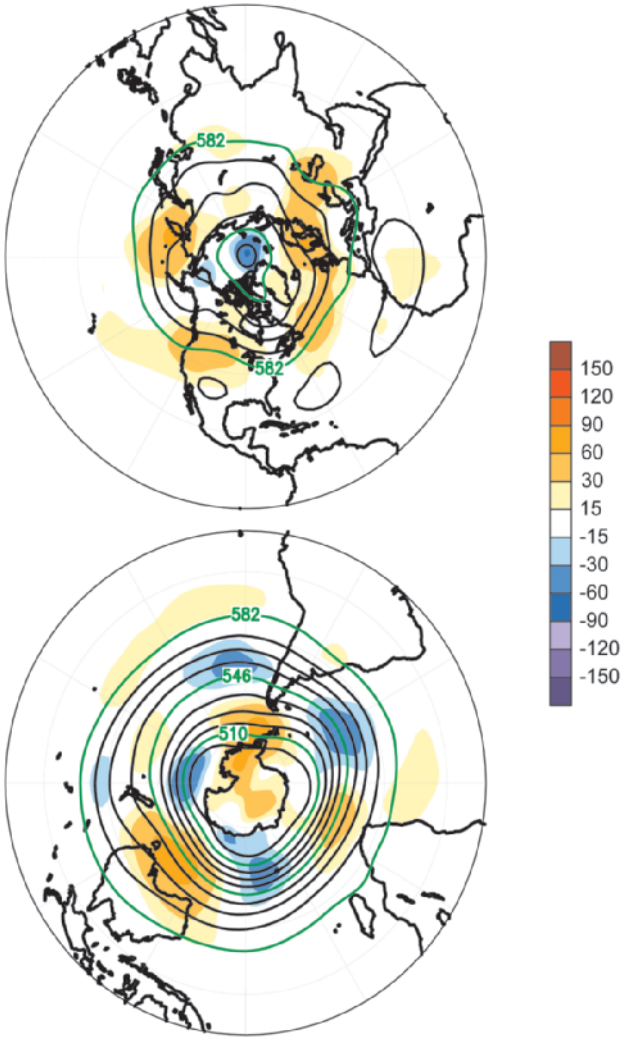


**Fig. 7.6. June–August 2006 (top) Northern Hemisphere and (bottom) Southern Hemisphere 500-hPa geopotential heights (9-dam contour interval) and anomalies (shading) from the 1979–2000 base period mean.**

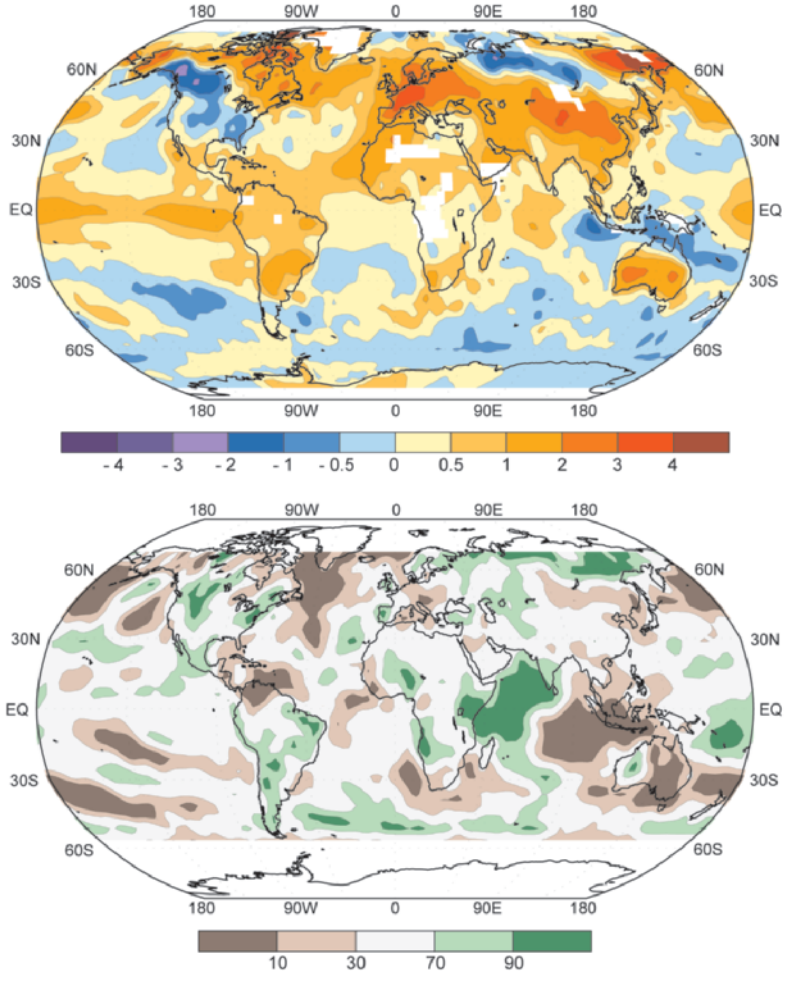


**Fig. 7.7. September–November 2006 (top) surface temperature anomalies (°C) and (bottom) precipitation percentiles based on a gamma distribution fit to the 1979–2000 base period. Temperature anomalies (1971–2000 base period) are based on station data over land and sea surface temperature over water. Precipitation data were obtained from a combination of rain gauge observations and satellite-derived estimates (Janowiak and Xie 1999). Analysis was omitted in data-sparse regions (white areas).**

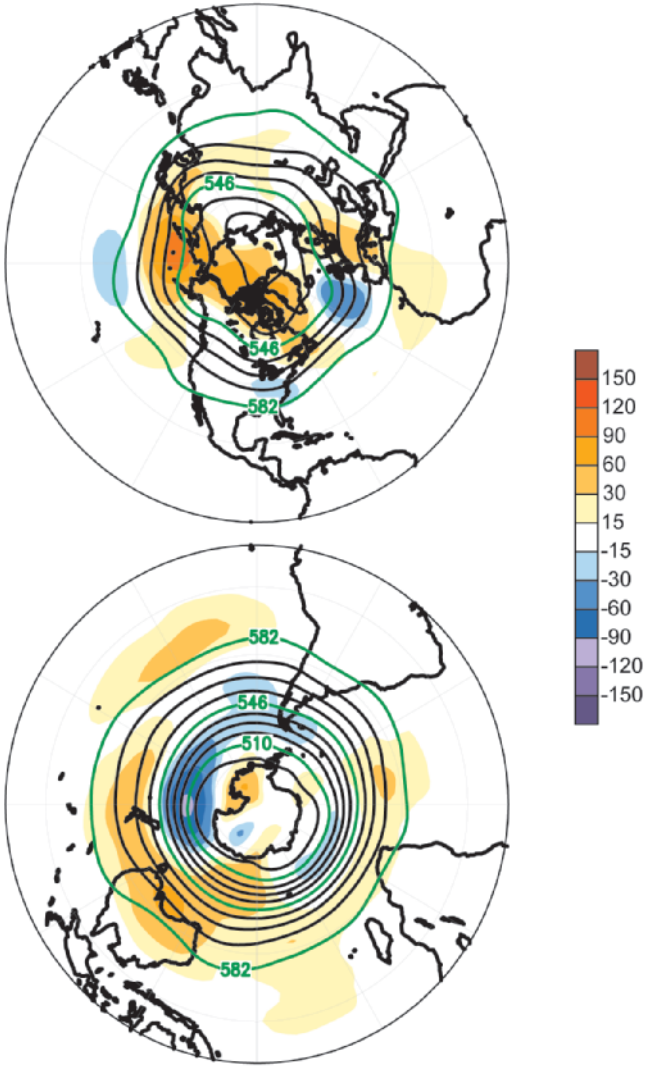


**Fig. 7.8. September–November 2006 (top) Northern Hemisphere and (bottom) Southern Hemisphere 500-hPa geopotential heights (9-dam contour interval) and anomalies (shading) from the 1979–2000 base period mean.**

**ACKNOWLEDGMENTS.** Over 200 individuals from 33 countries participated in this report, including authors, reviewers, graphics specialists, and various facilitators. The editors acknowledge the graphics team at NOAA's NCDC for their devotion to the report: Glenn Hyatt, Sara Veasey, Anne Markel, and Deborah Riddle. Acknowledgments are also given to past editors for their wise counsel: Jay Lawrimore, Karsten Shein, Anne Waple, and David Levinson. Richard Thigpen (WMO), Omar Baddour (WMO), and Ken Knapp (NOAA's NCDC) are appreciated for helping to identify authors. John Kennedy is supported by the U.K. Department for Environment, Food and Rural Affairs under contract PECD 7/12/37. The research carried out at the Jet Propulsion Laboratory, California Institute of Technology, was supported by the National Space and Aeronautics Administration (Cryospheric Sciences Program). This report was partially supported by the NOAA Climate Program Office Climate Change Data and Detection Program Element.

We also gratefully acknowledge the following individuals:

- Phillip Arkin, Earth System Science Interdisciplinary Center, University of Maryland
- Jessica Blunden, North Carolina State University
- Glenn Carter, University of Hawai'i at Manoa
- Michael Changery, STG, Inc., NOAA's NCDC
- Kathleen Crane, NOAA Climate Program Office
- Imke Durre, NOAA's NCDC
- Wayne Faas, NOAA's NCDC
- Shane Forsythe-Newell, STG, Inc., NOAA's NCDC
- Melissa Free, NOAA
- Byron Gleason, NOAA's NCDC
- Andy Goss, NOAA's NCDC
- Valentina Grigoryan, Armenian State Hydro-Meteorology and Monitoring Service
- Wendy Gross, NOAA's NCDC
- Greg Hammer, NOAA's NCDC
- Leopold Haimberger, University of Vienna, Austria
- Bryan Hanssen, American Meteorological Society
- Tamara Houston, NOAA's NCDC
- Philip Jones, STG, Inc., NOAA's NCDC
- Bryant Korzeniewski, STG, Inc., NOAA's NCDC
- Sharon Leduc, NOAA's NCDC
- Marjorie McGuirk, NOAA's NCDC
- Carl Mears, Remote Sensing Systems
- Chris Miller, NOAA Climate Program Office
- Deb Misch, STG, Inc., NOAA's NCDC
- Brian Nelson, NOAA's NCDC
- Diana O'Connell, STG, Inc., NOAA's NCDC
- Karen Owen, NOAA's NCDC
- Ana Pinheiro, STG, Inc., NOAA's NCDC
- Fumin Ren, China Meteorological Administration
- Hilawe Semunegus, NOAA's NCDC
- Lei Shi, NOAA's NCDC
- Mike Squires, NOAA's NCDC
- Scott Stephens, NOAA's NCDC
- Peter Thorne, Hadley Centre, United Kingdom
- Holly Titchner, Hadley Centre, United Kingdom
- Rod Truesdell, NOAA's NCDC
- Konstatin Vinnikov, University of Maryland
- Russell Vose, NOAA's NCDC
- Xungang Yin, NOAA's NCDC
- Huai-Min Zhang, NOAA's NCDC

## REFERENCES

Armstrong, R. L., and M. J. Brodzik, 2001: Recent Northern Hemisphere snow extent: A comparison of data derived from visible and microwave sensors. *Geophys. Res. Lett.*, **28**, 3673–3676.

——, and ——, 2005: Northern Hemisphere EASE-Grid weekly snow cover and sea ice extent version 3. National Snow and Ice Data Center, Boulder, Colorado, digital media. [Available online at http://nsidc.org/data/nsidc-0046.html.]

——, B. Raup, S. J. S. Khalsa, R. Barry, J. Kargel, C. Helm, and H. Kiefer, 2005: GLIMS glacier database. National Snow and Ice Data Center, Boulder, Colorado, digital media. [Available online at http://nsidc.org/data/nsidc-0272.html.]

——, M. J. Brodzik, K. Knowles, and M. Savoie, 2005: Global monthly EASE-Grid snow water equivalent climatology. National Snow and Ice Data Center, Boulder, Colorado, digital media. [Available online at http://nsidc.org/data/nsidc-0271.html.]

Atkinson, G. D., 1971: Forecasters' guide to tropical meteorology. U.S. Air Force Tech. Rep. 240, 360 pp.

Baquero-Bernal, A., M. Latif, and S. Legutke, 2002: On dipolelike variability of sea surface temperature in the tropical Indian Ocean. *J. Climate*, **15**, 1358–1368.

Barnston, A. B., and R. E. Livezey, 1987: Classification, seasonality and persistence of low-frequency atmospheric circulation patterns. *Mon. Wea. Rev.*, **115**, 1083–1126.

Barnston, A. G., M. Chelliah, and S. B. Goldenberg, 1997: Documentation of a highly ENSO-related SST

region in the equatorial Pacific. *Atmos.–Ocean*, **35**, 367–383.

Behrenfeld, M. J., and Coauthors, 2001: Biospheric primary production during an ENSO transition. *Science*, **291**, 2594–2597.

Behringer, D. W., M. Ji, and A. Leetmaa, 1998: An improved coupled model for ENSO prediction and implications for ocean initialization. Part I: The ocean data assimilation system. *Mon. Wea. Rev.*, **126**, 1013–1021.

Bell, G. D., and M. Chelliah, 2006: Leading tropical modes associated with interannual and multidecadal fluctuations in North Atlantic hurricane activity. *J. Climate*, **19**, 590–612.

——, and Coauthors, 2000: Climate assessment for 1999. *Bull. Amer. Meteor. Soc.*, **81**, S1–S50.

——, and Coauthors, 2005: Atlantic hurricane season. *State of the Climate in 2004,* D. H. Levinson, Ed., *Bull. Amer. Meteor. Soc.*, **86** (6), S26–S29.

——, and Coauthors, 2006: The record breaking 2005 Atlantic hurricane season. *State of the Climate in 2005,* K. A. Shein, Ed., *Bull. Amer. Meteor. Soc.*, **86** (6: supplement), S44–S45.

Bopp, L., C. Le Que´re´, M. Heimann, A. C. Manning, and P. Monfray, 2002: Climate-induced oceanic oxygen fluxes: Implications for the contemporary carbon budget. *Global Biogeochem. Cycles*, **16**, 1022, doi:10.1029/2001GB001445.

Bousquet, P., and Coauthors, 2006: Contribution of anthropogenic and natural sources to atmospheric methane variability. *Nature*, **443**, 439–443.

Box, J. E., and A. E. Cohen, 2006: Upper-air temperatures around Greenland: 1964–2005. *Geophys. Res. Lett.*, **33**, L12706, doi:10.1029/2006GL025723.

Boyer, T. P., C. Stephens, J. I. Antonov, M. E. Conkright, R. A. Locarnini, T. D. O'Brien, and H. E. Garcia, 2002: *World Ocean Atlas 2001, Salinity. Vol. 2.* S. Levitus, Ed., NOAA Atlas NESDIS 50, 165 pp.

——, S. Levitus, J. I. Antonov, R. A. Locarninin, and H. E. Garcia, 2005: Linear trends in salinity for the World Ocean, 1955–1998. *Geophys. Res. Lett.*, **32**, L01604, doi:10.1029/2004GL021791.

Bretherton, F. P., R. E. Davis, and C. Fandry, 1976: A technique for objective analysis and design of oceanographic instruments applied to MODE-73. *Deep-Sea Res.*, **23**, 559–582.

Brodzik, M. J., R. L. Armstrong, E. C. Weatherhead, M. H. Savoie, K. W. Knowles, and D. A. Robinson, 2006: Regional trend analysis of satellite-derived snow extent and global temperature anomalies. *Eos, Trans. Amer. Geophys. Union*, **87,** Abstract U33A-0011.

Brohan, P., J. J. Kennedy, I. Harris, S. F. B. Tett, and P. D. Jones, 2006: Uncertainty estimates in regional and global observed temperature changes: A new data set from 1850. *J. Geophys. Res.*, **111**, D12106, doi:10.1029/2005JD006548.

Bromwich, D. H., 1988: Snowfall in high southern latitudes. *Rev. Geophys.*, **26**, 149–168.

——, Z. Guo, L. Bai, and Q.-S. Chen, 2004a: Modeled Antarctic precipitation. Part I: Spatial and temporal variability. *J. Climate*, **17**, 427–447.

——, A. J. Monaghan, and Z. Guo, 2004b: Modeling the ENSO modulation of Antarctic climate in the late 1990s with Polar MM5. *J. Climate*, **17**, 109–132.

Brown, J., K. M. Hinkel, and F. E. Nelson, 2000: The Circumpolar Active Layer Monitoring (CALM) program: Research designs and initial results. *Polar Geog.*, **24**, 163–258.

Bryden, H. L., H. R. Longworth, and S. A. Cunningham, 2005: Slowing of the Atlantic meridional overturning circulation at 25°N. *Nature*, **438**, 655–657.

Budyko, M. I., 1969: The effect of solar radiation variations on the climate of the Earth. *Tellus*, **21**, 611–619.

Callendar, G. S., 1938: The artificial production of carbon dioxide and its influence on temperature. *Quart. J. Roy. Meteor. Soc.*, **64**, 223–237.

——, 1961: Temperature fluctuations and trends over the Earth. *Quart. J. Roy. Meteor. Soc.*, **87**, 1–12.

Camargo, S. J., and A. H. Sobel, 2005: Western North Pacific tropical cyclone intensity and ENSO. *J. Climate*, **18**, 2996–3006.

——, A. W. Robertson, S. J. Gaffney, P. Smyth, and M. Ghil, 2007: Cluster analysis of typhoon tracks. Part II: Large-scale circulation and ENSO. *J. Climate,* in press.

Cappelen, J., E. V. Laursen, P. V. Jørgensen, and C. Kern-Hansen, 2007: DMI monthly climate data collection 1768–2006, Denmark, The Faroe Islands and Greenland. DMI Tech. Rep. 07-06, in press.

Casty, C., J. Luterbacher, H. Wanner, J. Esper, and R. Böhm, 2005: Temperature and precipitation variability in the European Alps since 1500. *Int. J. Climatol.*, **25**, 1855–1880.

Chan, J. C. L., 1985: Tropical cyclone activity in the northwest Pacific in relation to El Niño/Southern Oscillation phenomenon. *Mon. Wea. Rev.*, **113**, 599–606.

——, cited 2007: Verification of forecasts of tropical cyclone activity over the western North Pacific in 2006. Laboratory for Atmospheric Research, City University of Hong Kong. [Available online at http://aposf02.cityu.edu.hk/~mcg/tc_forecast/2006_Verification.htm.]

——, and K. S. Liu, 2004: Global warming and western North Pacific typhoon activity from an observational perspective. *J. Climate*, **17**, 4590–4602.

Chavez, F. P., P. G. Strutton, and M. J. McPhaden, 1998: Biological-physical coupling in the central equatorial Pacific during the onset of the 1997–98 El Niño. *Geophys. Res. Lett.*, **25**, 3543–3546.

——, ——, G. E. Friederich, R. A. Feely, G. Feldman, D. Foley, and M. J. McPhaden, 1999: Biological and chemical response of the equatorial Pacific Ocean to the 1997–1998 El Niño. *Science*, **286**, 2126–2131.

Chen, D., 2000: A monthly circulation climatology for Sweden and its application to a winter temperature case study. *Int. J. Climatol.*, **20**, 1067–1076.

Chia, H. H., and C. F. Ropelewski, 2002: Interannual variability in the genesis location of tropical cyclones in the northwest Pacific. *J. Climate*, **15**, 2934–2944.

Christy, J. R., and S. J. Drouilhet, 1994: Variability in daily, zonal mean lower-stratospheric temperatures. *J. Climate*, **7**, 106–120.

——, R. W. Spencer, W. B. Norris, W. D. Braswell, and D. E. Parker, 2003: Error estimates of Version 5.0 of MSU/AMSU bulk atmospheric temperatures. *J. Atmos. Oceanic Technol.*, **20**, 613–629.

Chu, P.-S., and J. Wang, 1997: Tropical cyclone occurrences in the vicinity of Hawaii: Are the differences between El Niño years significant? *J. Climate*, **10**, 2683–2689.

Clark, J. D., and P.-S. Chu, 2002: Interannual variation of tropical cyclone activity over the central North Pacific. *J. Meteor. Soc. Japan*, **80**, 403–418.

Cogley, G. J., 2005: Mass and energy balances of glaciers and ice sheets. *Encyclopedia of Hydrological Sciences*, M. Anderson, Ed., John Wiley & Sons, 2555–2573.

Conway, T. J., P. P. Tans, L. S. Waterman, K. W. Thoning, D. R. Kitzis, K. A. Masarie, and N. Zhang, 1994: Evidence for interannual variability of the carbon cycle from the NOAA CMDL global air sampling network. *J. Geophys. Res.*, **99**, 22 831–22 855.

Cosca, C. E., R. A. Feely, J. Boutin, J. Etcheto, and M. J. McPhaden, 2003: Seasonal and interannual $CO_2$ fluxes for the central and eastern equatorial Pacific Ocean as determined from $fCO_2$–SST relationships. *J. Geophys. Res.*, **108**, 3278, doi:10.1029/2000JC000677.

Couture, R., S. Smith, S. D. Robinson, M. M. Burgess, and S. Solomon, 2003: On the hazards to infrastructure in the Canadian North associated with thawing of permafrost. *Proc. Geohazards 2003, Third Canadian Conf. on Geotechnique and Natural Hazards*. Edmonton, AB, Canada, Canadian Geotechnical Society, 97–104.

Cunnold, D., and Coauthors, 2007: Long-lived compounds. Scientific Assessment of Ozone Depletion: 2006, WMO Global Ozone Research and Monitoring Project Rep. 50, 1.1–1.63.

Curry, R. G., and M. S. McCartney, 2001: Ocean gyre circulation changes associated with the North Atlantic oscillation. *J. Phys. Oceanogr.*, **31**, 3374–3400.

——, and C. Mauritzen, 2005: Dilution of the northern North Atlantic in recent decades. *Science*, **308**, 1772–1774.

Dai, A., K. E. Trenberth, and T. Qian, 2004: A global data set of Palmer Drought Severity Index for 1870–2002: Relationship with soil moisture and effects of surface warming. *J. Hydrometeor.*, **5**, 1117–1130.

Daniel, J. S., and S. Solomon, 1998: On the climate forcing of carbon monoxide. *J. Geophys. Res.*, **103**, 13 249–13 260.

Davis, C. H., Y. Li, J. R. McConnell, M. M. Frey, and E. Hanna, 2005: Snowfall-driven growth in East Antarctic ice sheet mitigates recent sea-level rise. *Science*, **308**, 1898–1901.

Della-Marta, P. M., D. A. Collins, and K. Braganza, 2004: Updating Australia's high-quality annual temperature dataset. *Aust. Meteor. Mag.*, **53**, 75–93.

Dlugokencky, E. J., S. Houweling, L. Bruhwiler, K. A. Masarie, P. M. Lang, J. B. Miller, and P. P. Tans, 2003: Atmospheric methane levels off: Temporary pause or new steady state? *Geophys. Res. Lett.*, **30**, 1992, doi:10.1029/2003GL018126.

Drosdowsky, W., 1996: Variability of the Australian summer monsoon at Darwin: 1957–1992. *J. Climate*, **9,** 85–95.

Durre, I., R. S. Vose, and D. B. Wuertz, 2006: Overview of the Integrated Global Radiosonde Archive. *J. Climate*, **19**, 53–68.

Dyurgerov, M., and M. F. Meier, 2006: Glaciers and changing earth system: A 2004 snapshot. INSTAAR University of Colorado Occasional Paper 58, 118 pp.

Emanuel, K. A., 2005: Increasing destructiveness of tropical cyclones over the past 30 years. *Nature*, **436**, 686–688.

Espirito-Santo, F. E., V. Pires, A. Silva, S. Moita, T. Cota, and L. Mendes, 2007: Characterization of the climate in Portugal during 2006 (in Portuguese). Instituto de Meteorologia, 41 pp.

Evan, A. T., A. K. Heidinger, and M. J. Pavolonis, 2006: Development of a new over-water Advanced Very High Resolution Radiometer dust detection algorithm. *Int. J. Remote Sens.*, **27**, 3903–3924.

Feely, R. A., R. Wanninkhof, C. E. Cosca, P. P. Murphy, M. F. Lamb, and M. D. Steckley, 1995: $CO_2$ distributions in the equatorial Pacific during the 1991–1992 ENSO event. *Deep-Sea Res. II*, **42**, 365–386.

——, C.L. Sabine, T. Takahashi, and R. Wanninkhof, 2001: Uptake and storage of carbon dioxide in the oceans: The global $CO_2$ survey. *Oceanography*, **14**, 18–32.

——, T. Takahashi, R. Wanninkhof, M. J. McPhaden, C. E. Cosca, and S. C. Sutherland, 2006: Decadal variability of the air–sea $CO_2$ fluxes in the equatorial Pacific Ocean. *J. Geophys. Res.*, **111**, C08590; doi:10.1029/2005JC003129.

Fetterer, F., and K. Knowles, 2004: Sea ice index. National Snow and Ice Data Center, Boulder, Colorado, digital media. [Available online at http://nsidc.org/data/g02135.html.]

Fiore, A. M., L. W. Horowitz, E. J. Dlugokencky, and J. J. West, 2006: Impact of meteorology and emissions on methane trends, 1990–2004. *Geophys. Res. Lett.*, **33**, L12809, doi:10.1029/2006GL026199.

Follows, M., and S. Dutkiewicz, 2002: Meteorological modulation of the North Atlantic spring bloom. *Deep-Sea Res. II*, **49**, 321–344.

Frauenfeld, O. W., T. Zhang, R. G. Barry, and D. Gilichinsky, D., 2004: Interdecadal changes in seasonal freeze and thaw depths in Russia. *J. Geophys. Res.*, **109**, D05101, doi:10.1029/2003JD004245.

Free, M., D. J. Seidel, J. K. Angell, J. Lazante, I. Durre, and T. C. Peterson, 2005: Radiosonde Atmospheric Temperature Products for Assessing Climate (RATPAC): A new dataset of large-area anomaly time series. *J. Geophys. Res.*, **110**, D22101, doi:10.1029/2005JD006169.

Frei, A., and D. A. Robinson, 1999: Northern Hemisphere snow extent: Regional variability 1972–1994. *Int. J. Climatol.*, **19**, 1535–1560.

Ganachaud, A., and C. Wunsch, 2003: Large-scale ocean heat and freshwater transports during the World Ocean Circulation Experiment. *J. Climate*, **16**, 696–705.

Garcia-Herrera, R., D. Paredes, R. M. Trigo, I. F. Trigo, H. Hernández, D. Barriopedro, and M. T. Mendes, 2006: The outstanding 2004/05 drought in the Iberian Peninsula: Associated atmospheric circulation. *J. Hydrometeor.,* in press.

Garrison, T., 2005: *Oceanography: An Invitation to Marine Science.* 5th ed. Thomson Brooks/Cole, 522 pp.

Genthon, C., 2004: Space-time Antarctic surface mass balance variability from climate models. *Ann. Glaciol.*, **39**, 271–275.

——, G. Krinner, and M. Sacchettini, 2003: Interannual Antarctic tropospheric circulation and precipitation variability. *Climate Dyn.*, **21**, 289–307.

GLOBALVIEW-CO2, 2006: *Cooperative Atmospheric Data Integration Project—Carbon Dioxide.* NOAA GMD, CD-ROM. [Available online via anonymous FTP to ftp.cmdl.noaa.gov, Path: ccg/co2/GLOBALVIEW.]

Goetz, S. J., A. G. Bunn, G. J. Friske, and R. A. Houghton, 2005: Satellite-observed photosynthetic trends across boreal North America associated with climate and fire disturbance. *Proc. National Acad. Sci.*, **102**, 13 521–13 525.

Goldenberg, S. B., and L. J. Shapiro, 1996: Physical mechanisms for the association of El Niño and West African rainfall with Atlantic major hurricane activity. *J. Climate*, **9**, 1169–1187.

——, C. W. Landsea, A. M. Mestas-Nuñez, and W. M. Gray, 2001: The recent increase in Atlantic hurricane activity: Causes and implications. *Science*, **293**, 474–479.

Gray, W. M., 1984: Atlantic seasonal hurricane frequency: Part I: El Niño and 30-mb quasi-bienniel oscillation influences. *Mon. Wea. Rev.*, **112**, 1649–1668.

Grebmeier, J. M, and Coauthors, 2006: A major ecosystem shift in the northern Bering Sea. *Science*, **311**, 1461–1464.

Groisman, P. Ya., T. R. Karl, D. R. Easterling, B. Sun, and J. H. Lawrimore, 2004: Contemporary changes of the hydrological cycle over the contiguous United States: Trends derived from in situ observations. *J. Hydrometeor.,* **5**, 64–85.

Gu, G., R. F. Adler, and A. H. Sobel, 2005: The eastern Pacific ITCZ during the boreal spring. *J. Atmos. Sci.*, **62**, 1157–1174.

Haas, C., 2004: Late-summer sea ice thickness variability in the Arctic Transpolar Drift 1991–2001 derived from ground-based electromagnetic sounding. *Geophys. Res. Lett.*, **31**, L09402, doi:10.1029/2003GL019394.

Haimberger, L., 2007: Homogenization of radiosonde temperature time series using innovation statistics. *J. Climate*, **20,** 1377–1403.

Hansen, J., and S. Lebedeff, 1987: Global trends of measured surface air temperature. *J. Geophys. Res.*, **92,** 13 345–13 372.

——, R. Ruedy, M. Sato, M. Imhoff, W. Lawrence, D. Easterling, T. Peterson, and T. Karl, 2001: A closer look at United States and global surface temperature change. *J. Geophys. Res.*, **106**, 23 947–23 963.

——, and Coauthors, 2005: Earth's energy imbalance: Confirmation and implications. *Science*, **308**, 1431–1435.

Harris, C., and W. Haeberli, 2003: Warming permafrost in European mountains. *Global Planet. Change*, **39**, 215–225.

Hátún, H., A. B. Sandø, H. Drange, B. Hansen, and H. Valdimarsson, 2005: Influence of the Atlantic subpolar gyre on the thermohaline circulation. *Science*, **309**, 1841–1844.

Heidinger, A. K., C. Y. Cao, and J. T. Sullivan, 2002: Using Moderate Resolution Imaging Spectrometer (MODIS) to calibrate advanced very high resolution radiometer reflectance channels. *J. Geophys. Res.*, **107**, 4702, doi:10.1029/2001JD002035.

Held, I. M., and B. J. Soden, 2006: Robust response of the hydrological cycle to global warming. *J. Climate*, **19**, 5686–5699.

Hofmann, D. J., J. H. Butler, E. J. Dlugokencky, J. W. Elkins, K. Masarie, S. A. Montzka, and P. Tans, 2006: The role of carbon dioxide in climate forcing from 1979–2004. *Tellus*, **58B**, 614–619.

Holland, G. J., 1993: Ready reckoner. Global Guide to Tropical Cyclone Forecasting, World Meteorological Organization WMO/TC–No. 560, Rep. TCP–31. [Available online at http://www.bom.gov/au/bmrc/pubs/tc–guide/global_guide_intro.htm.]

Hurrell, J. W., 1995: Decadal trends in the North Atlantic Oscillation: Regional temperatures and precipitation. *Science*, **269**, 676–679.

Ignatov, A., and L. Stowe, 2002a: Aerosol retrievals from individual AVHRR channels. Part I: Retrieval algorithm and transition from Dave to 6S radiative transfer model. *J. Atmos. Sci.*, **59**, 313–334.

——, and ——, 2002b: Aerosol retrievals from individual AVHRR channels. Part II: Quality control, probability distribution functions, information content, and consistency checks of retrievals. *J. Atmos. Sci.*, **59**, 335–362.

IPCC, 2007: Observations: Changes in snow, ice and frozen ground. *Climate Change 2007: The Physical Science Basis,* IPCC, 337–383.

Isaksen, K., D. Vonder Mühll, H. Gubler, T. Kohl, and J. L. Sollid, 2000: Ground surface temperature reconstruction based on data from a deep borehole in permafrost at Janssonhaugen, Svalbard. *Ann. Glaciol.*, **31**, 287–294.

Janowiak, J. E., and P. Xie, 1999: CAMS–OPI: A global satellite–rain gauge merged product for real-time precipitation monitoring applications. *J. Climate*, **12**, 3335–3342.

Jauregui, E., 2003: Climatology of landfalling hurricanes and tropical storms in Mexico. *Atmosfera*, **16**, 193–204.

Jia, G. J., H. E. Epstein, and D. A. Walker, 2003: Greening of arctic Alaska, 1981–2001. *Geophys. Res. Lett.*, **30**, 2067, doi:10.1029/2003GL018268.

Johannessen, O. M., and Coauthors, 2004: Arctic climate change: Observed and modeled temperature and sea ice variability. *Tellus*, **56A**, 328–341.

Joint, I., and S. B. Groom, 2000: Estimation of phytoplankton production from space: Current status and future potential of satellite remote sensing. *J. Exp. Mar. Biol. Ecol.*, **250**, 233–255.

Jones, P. D., S, C. B. Raper, R. S. Bradley, H. F. Diaz, P. M. Kelly, and T. M. L. Wigley, 1986a: Northern Hemisphere surface air temperature variations: 1851–1984. *J. Climate Appl. Meteor.*, **25**, 161–179.

——, ——, and T. M. L. Wigley, 1986b: Southern Hemisphere surface air temperature variations: 1851–1984. *J. Climate Appl. Meteor.*, **25**, 1213–1230.

Kalnay, E., and Coauthors, 1996: The NCEP/NCAR 40-Year Reanalysis Project. *Bull. Amer. Meteor. Soc.*, **77**, 437–471.

Kasischke, E. S., and Coauthors, 2000: Contributions of 1998 fires in the boreal forest to atmospheric concentrations of carbon monoxide and methane. *Eos, Trans. Amer. Geophys. Union*, **81**, 260.

Keppler, F., J. T. G. Hamilton, M. Brass, and T. Rockmann, 2006: Methane emissions from terrestrial plants under aerobic conditions. *Nature*, **439**, 187–191.

Koltermann, K. P., A. V. Sokov, V. P. Tereschenkov, S. A. Dobroliubov, K. Lorbacher, and A. Sy, 1999: Decadal changes on the thermohaline circulation of the North Atlantic. *Deep-Sea Res. II*, **46**, 109–138.

Kousky, V. E., and M. T. Kayano, 1994: Principal modes of outgoing longwave radiation and 250-mb circulation for the South American sector. *J. Climate,* **7**, 1131–1143.

Kwok, R., H. J. Zwally, and D. Yi, 2004: ICESat observations of Arctic sea ice: A first look. *Geophys. Res. Lett.*, **31**, L16401, doi:10.1029/2004GL020309.

Lamb, H. H., 1950: Types and spells of weather around the year in the British Isles. *Quart. J. Roy. Meteor. Soc.*, **76**, 393–438.

Lander, M. A., 1994: Description of a monsoon gyre and its effects in the western North Pacific during August 1991. *Wea. Forecasting*, **9**, 640–654.

——, 1995: The merger of two tropical cyclones. *Mon. Wea. Rev.*, **123**, 2260–2265.

——, and C. P. Guard, 1998: A look at global tropical cyclone activity during 1995: Contrasting high Atlantic activity with low activity in other basins. *Mon. Wea. Rev.*, **126**, 1163–1173.

Landsea, C. W., and W. M. Gray, 1992: The strong association between Western Sahel monsoon rainfall and intense Atlantic hurricanes. *J. Climate*, **5**, 435–453.

——, G. D. Bell, W. M. Gray, and S. B. Goldenberg, 1998: The extremely active 1995 Atlantic hurricane season: Environmental conditions and verification of seasonal forecasts. *Mon. Wea. Rev.*, **126**, 1174–1193.

——, R. A. Pielke Jr., A. M. Mestas-Nuñez, and J. A. Knaff, 1999: Atlantic basin hurricanes: Indices of climatic changes. *Climatic Change*, **42**, 89–129.

Langenfelds, R. L., R. J. Francey, B. C. Pak, L. P. Steele, J. Lloyd, C. M. Trudinger, and C. E. Allison, 2002: Interannual growth rate variations of atmospheric $CO_2$ and its $\delta_{13}C$, $H_2$, $CH_4$, and CO between 1992 and 1999 linked to biomass burning. *Global Biogeochem. Cycles*, **16**, 1048, doi:10.1029/2001GB001466.

Lavery, B., G. Joung, and N. Nicholls, 1997: An extended high-quality historical rainfall dataset for Australia. *Aust. Meteor. Mag.*, **46**, 27–38.

Laxon, S., N. Peacock, and D. Smith, 2003: High interannual variability of sea ice thickness in the Arctic Region. *Nature*, **425**, 947–950.

Lee, K., R. Wanninkhof, T. Takahashi, S. Doney, and R. A. Feely, 1998: Low interannual variability in recent oceanic uptake of atmospheric carbon dioxide. *Nature*, **396**, 155–159.

Lejenas, H., and H. Okland, 1983: Characteristics of Northern Hemisphere blocking as determined from a long time series of observational data. *Tellus*, **35A**, 350–362.

Leuliette, E. W., R. S. Nerem, and G. T. Mitchum, 2004: Calibration of TOPEX/Poseidon and Jason altimeter data to construct a continuous record of mean sea level change. *Mar. Geodesy*, **27**, 79–94.

Levitus, S., J. I. Antonov, and T. P. Boyer, 2005: Warming of the World Ocean, 1955–2003. *Geophys. Res. Lett.*, **32**, L02604, doi:10.1029/2004GL021592.

Lietzke, C. E., C. Deser, and T. H. Vonder Harr, 2001: Evolutionary structure of the eastern Pacific double ITCZ based on satellite moisture profile retrievals. *J. Climate*, **14**, 743–751.

Liu, H., L. Wang, and K. Jezek, 2005: Wavelet-based edge detection approach to derivation of snow-melt onset, duration and extent from satellite passive microwave measurements. *Int. J. Remote Sens.*, **26**, 4639–4660.

——, ——, and ——, 2006: Spatio-temporal variations of snow melt zones in Antarctic ice sheet derived from satellite SMMR and SSM/I data (1978–2004). *J. Geophys. Res.,* **111**, F01003, doi:10.1029/2005JF000318.

Liu, W. T., and X. S. Xie, 2002: Double intertropical convergence zones—A new look using scatterometer. *Geophys. Res. Lett.,* **29,** 2072, doi:10.1029/2002GL015431.

Lucht, W., and Coauthors, 2002: Climate control of the high-latitude vegetation greening and Pinatubo effect. *Science*, **296**, 1687–1689.

Lumpkin, R., and S. L. Garzoli, 2005: Near-surface circulation in the tropical Atlantic Ocean. *Deep-Sea Res. I*, **52**, 495–518.

——, and K. Speer, 2007: Global Ocean Meridional Overturning. *J. Phys. Oceanogr.*, in press.

——, ——, and K. P. Koltermann, 2007: Transport across 48°N in the North Atlantic Ocean. *J. Phys. Oceanogr.*, submitted.

Luo, C., N. Mahowald, and C. Jones, 2004: Temporal variability of dust mobilization and concentration in source regions. *J. Geophys. Res.*, **109**, D20202, doi:10.1029/2004JD004861.

Madden, R. A., and P. R. Julian, 1971: Detection of a 40–50 day oscillation in the zonal wind in the tropical Pacific. *J. Atmos. Sci.*, **28**, 702–708.

——, and ——, 1972: Description of global-scale circulation cells in the tropics with 40–50 day period. *J. Atmos. Sci.*, **29**, 1109–1123.

——, and ——, 1994: Observations of the 40–50 day tropical oscillation—A review. *Mon. Wea. Rev.*, **122**, 814–837.

Maes, C., K. Ando, T. Delcroix, W. S. Kessler, M. J. McPhaden, and D. Roemmich, 2006: Observed correlation of surface salinity, temperature and barrier layer at the eastern edge of the western Pacific warm pool. *Geophys. Res. Lett.*, **33**, L06601, doi:10.1029/2005GL024772.

Mahowald, N., C. Luo, J. del Corral, and C. Zender, 2003: Interannual variability in atmospheric mineral aerosols from a 22-year model simulation and observational data. *J. Geophys. Res.*, **108**, 4352, doi:10.1029/2002JD002821.

Massom, R. A., and Coauthors, 2006: Extreme anomalous atmospheric circulation in the west Antarctic Peninsula region in austral spring and summer 2001/02, and its profound impact on sea ice and biota. *J. Climate*, **19**, 3544–3571.

Matsumoto, K., and Coauthors, 2004: Evaluation of ocean carbon cycle models with data-based metrics. *Geophys. Res. Lett.*, **31**, L07303, doi:10.1029/2003GL018970.

McKee, T. B., N. J. Doesken, and J. Kleist, 1993: The relationship of drought frequency and duration to time scales. *Proc. Eighth Conf. of Applied Climatology,* Anaheim, CA, Amer. Meteor. Soc., 179–184.

——, ——, and ——, 1995: Drought monitoring with multiple time scales. *Proc. Ninth Conf. of Applied Climatology,* Dallas, TX, Amer. Meteor. Soc., 233–236.

McNeil, B. I., R. J. Matear, R. M. Key, J. L. Bullister, and J. L. Sarmiento, 2003: Anthropogenic $CO_2$ uptake by the ocean based on the global chlorofluorocarbon data set. *Science*, **299**, 235–239.

Mears, C. A., and F. J. Wentz, 2005: The effect of diurnal correction on satellite-derived lower tropospheric temperature. *Science*, **309**, 1548–1551.

——, M. C. Schabel, and F. J. Wentz, 2003: A reanalyses of the MSU channel 2 tropospheric temperature record. *J. Climate*, **16**, 3650–3664.

Meinen, C. S., M. O. Baringer, and S. L. Garzoli, 2006: Variability in deep western boundary current transports: Preliminary results from 26.5°N in the Atlantic. *Geophys. Res. Lett.*, **33**, L17610, doi:10.1029/2006GL026965.

Melling, H., D. A. Riedel, and Z. Gedalof, 2005: Trends in the draft and extent of seasonal pack ice, Cana-

dian Beaufort Sea. *Geophys. Res. Lett.*, **32**, L24501, doi:10.1029/2005GL024483.

Miller, C. B., 2004: *Biological Oceanography.* Blackwell Publishing, 402 pp.

Mitchell, J. M., Jr., 1963: On the world-wide pattern of secular temperature change. *Changes of Climate: Proceedings of the Rome Symposium Organized by UNESCO and the World Meteorological Organization*, UNESCO Arid Zone Research Series, Vol. 20, Paris, 161–181.

Mo, K. C., 2000: The association between intraseasonal oscillations and tropical storms in the Atlantic basin. *Mon. Wea. Rev.*, **128**, 4097–4107.

——, and V. E. Kousky, 1993: Further analysis of the relationship between circulation anomaly patterns and tropical convection. *J. Geophys. Res.*, **98**, 5103–5113.

Monaghan, A. J., D. H. Bromwich, and S.-H. Wang, 2006: Recent trends in Antarctic snow accumulation from Polar MM5. *Philos. Trans. Roy. Soc. London*, **364**, 1683–1708.

Morison, J., M. Steele, T. Kikuchi, K. Falkner, and W. Smethie, 2006a: Relaxation of central Arctic Ocean hydrography to pre-1990s climatology. *Geophys. Res. Lett.*, **33**, L17604, doi:10.1029/2006GL026826.

——, J. Wahr, R. Kwok, and C. Peralta-Ferriz, 2006b: Change in the Arctic Ocean as observed with GRACE and in situ bottom pressure measurements. *Eos, Trans. Amer. Geophys. Union*, **87**, Abstract G12A-03.

Mote, P. W., A. F. Hamlet, M. P. Clark, and D. P. Lettenmaier, 2005: Declining mountain snowpack in western North America. *Bull. Amer. Meteor. Soc.*, **86**, 39–49.

Münnich, M., and J. D. Neelin, 2005: Seasonal influence of ENSO on the Atlantic ITCZ and equatorial South America. *Geophys. Res. Lett.*, **32**, L21709, doi:10.1029/2005GL023900.

Murtugudde, R. G., S. R. Signorini, J. R. Christian, A. J. Busalacchi, C. R. McClain, and J. Picaut, 1999: Ocean color variability of the tropical Indo-Pacific basin observed by SeaWiFS during 1997–1998. *J. Geophys. Res.*, **104**, 18 351–18 366.

Myneni, R. B., C. D. Keeling, C. J. Tucker, G. Asrar, and R. R. Nemani, 1997: Increased plant growth in the northern high latitudes from 1981–1991. *Nature,* **386,** 698–702.

——, C. J. Tucker, G. Asrar, and C. D. Keeling, 1998: Interannual variations in satellite-sensed vegetation index data from 1981 to 1991. *J. Geophys. Res.*, **103**, 6145–6160.

Neumann, C. J., B. R. Jarvinen, C. J. McAdie, and J. D. Elms, 1993: *Tropical Cyclones of the North Atlantic Ocean, 1871–1992.* NOAA National Climatic Data Center, in cooperation with the National Hurricane Center, 193 pp.

Newman, P. A., E. R. Nash, S. R. Kawa, S. A. Montzka, and S. M. Schauffler, 2006: When will the ozone hole recover? *Geophys. Res. Lett.*, **33**, L12814, doi:10.1029/2005GL025232.

Nghiem, S. V., and G. Neumann, 2007: Arctic sea-ice monitoring. *2007 McGraw-Hill Yearbook of Science and Technology*, McGraw-Hill, 12–15.

——, M. L. Van Woert, and G. Neumann, 2005: Rapid formation of a sea ice barrier east of Svalbard. *J. Geophys. Res.*, **110**, C11013, doi:10.1029/2004JC002654.

——, Y. Chao, G. Neumann, P. Li, D. K. Perovich, T. Street, and P. Clemente-Colon, 2006: Depletion of perennial sea ice in the East Arctic Ocean. *Geophys. Res. Lett.*, **33**, L17501, doi:10.1029/2006GL027198.

Nicholls, N., 2004: The changing nature of Australian droughts. *Climatic Change*, **63**, 323–336.

Niiler, P. P., N. A. Maximenko, G. G. Panteleev, T. Yamagata, and D. B. Olson, 2003: Near-surface dynamical structure of the Kuroshio Extension. *J. Geophys. Res.*, **108**, 3193, doi:10.1029/2002JC001461..

Nixon, F. M., C. Tarnocai, and L. Kutny, 2003: Long-term active layer monitoring: Mackenzie Valley, northwest Canada. *Proc. Eighth Int. Conf. on Permafrost*, Vol. 2, Zurich, Switzerland, International Permafrost Association, 821–826.

Nobre, P., and J. Shukla, 1996: Variations of sea surface temperature, wind stress and rainfall over the tropical Atlantic and South America. *J. Climate*, **9**, 2464–2479.

NOAA/NESDIS/OSDPD/SSD, 2004: IMS daily Northern Hemisphere snow and ice analysis at 4 km and 24 km resolution. National Snow and Ice Data Center, Boulder, Colorado, digital media. [Available online at http://www.nsidc.net/data/g02156.html.]

Norte, F. A., 1988: Características del Viento Zonda en la Región de Cuyo (Zonda wind characteristics over Cuyo Region). Ph.D. dissertation, University of Buenos Aires, 223 pp.

Novelli, P. C., K. A. Masarie, P. M. Lang, B. D. Hall, R. C. Myers, and J. C. Elkins, 2003: Reanalysis of tropospheric CO trends: Effects of the 1997–1998 wildfires. *J. Geophys. Res.*, **108**, 4464, doi:10.1029/2002JD003031.

Oberman, N. G., 2007: Some peculiarities of up-to-date degradation of cryolithozone in the Pechora-Ural region. *Proc. Int. Conf.: Cryogenic Resources of Polar Regions,* Salekhard, Russia, Russian Academy of Sciences.

——, and G. G. Mazhitova, 2001: Permafrost dynamics in the northeast of European Russia at the end of the 20th century. *Norweg. J. Geogr.*, **55**, 241–244.

Oludhe, C., P. Ambenje, and L. Ogallo, 2006: Eastern Africa. *State of the Climate in 2005,* K. A. Shein, Ed., *Bull. Amer. Meteor. Soc.,* **87** (6; supplement), S56–S57.

Osterkamp, T. E., 2003: A thermal history of permafrost in Alaska. *Proc. Eighth Int. Conf. on Permafrost,* M. Phillips, Vol. 2, Zurich, Switzerland, International Permafrost Association, 863–868.

——, 2005: The recent warming of permafrost in Alaska. *Global Planet. Change*, **49**, 187–202.

——, and V. E. Romanovsky, 1999: Evidence for warming and thawing of discontinuous permafrost in Alaska. *Permafrost Periglacial Process.*, **10**, 17–37.

Overland, J. E., and M. Wang, 2005: The third Arctic climate pattern: 1930s and early 2000s. *Geophys. Res. Lett.*, **32**, L23808, doi:10.1029/2005GL024254.

Padgett, G., cited 2007: Monthly global tropical cyclone summary. [Available online at http://www.typhoon2000.ph.]

Park, G.-H., K. Lee, R. Wanninkhof, and R. A. Feely, 2006: Empirical temperature-based estimates of variability in the oceanic uptake of $CO_2$ over the past 2 decades. *J. Geophys. Res.*, **111**, C07502, doi:10.1029/2005JC003090.

Parker, D. E., and E. B. Horton, 2005: Uncertainties in the central England temperature series 1878–2003 and some improvements to the maximum and minimum series. *Int. J. Climatol.*, **25**, 1173–1188.

——, T. P. Legg, and C. K. Folland, 1992: A new daily central England temperature series, 1772–1991. *Int. J. Climatol.*, **12**, 317–334.

Pavlov, A. V., 1994: Current changes of climate and permafrost in the Arctic and Sub-Arctic of Russia. *Permafrost Periglacial Process.*, **5**, 101–110.

——, and N. G. Moskalenko, 2002: The thermal regime of soils in the north of Western Siberia. *Permafrost Periglacial Process.*, **13**, 43–51.

Pérez, V., E. Fernández, E. Marañón, P. Serret, and C. García-Soto, 2005: Seasonal and interannual variability of chlorophyll a and primary production in the Equatorial Atlantic: In situ and remote sensing observations. *J. Plankton Res.*, **27**, 189–197.

Peterson, B. J., R. M. Holmes, J. W. McClelland, C. J. Vörösmarty, R. B. Lammers, A. I. Shiklomanov, I. A. Shiklomanov, and S. Rahmstorf, 2002: Increasing river discharge to the Arctic Ocean. *Science*, **298**, 2171–2173.

Peterson, T. C., and R. S. Vose, 1997: An overview of the Global Historical Climatology Network temperature database. *Bull. Amer. Meteor. Soc.*, **78**, 2837–2849.

Polyakov, I., and Coauthors, 2003: Long-term ice variability in arctic marginal seas. *J. Climate*, **16**, 2078–2085.

Prather, M. J., 1996: Natural modes and time scales in atmospheric chemistry: Theory, GWPs for $CH_4$ and CO, and runaway growth. *Geophys. Res. Lett.*, **23**, 2597–2600.

Prentice, I. C., and Coauthors, 2001: The carbon cycle and atmospheric carbon dioxide. *Climate Change 2001: The Scientific Basis,* J. T. Houghton et al. Eds., Cambridge University Press, 183–237.

Proshutinsky, A. Y., and M. A. Johnson, 1997: Two circulation regimes of the wind-driven Arctic Ocean. *J. Geophys. Res.*, **102**, 12 493–12 514.

——, I. M. Ashik, E. N. Dvorkin, S. Häkkinen, R. A. Krishfield, and W. R. Peltier, 2004: Secular sea level change in the Russian sector of the Arctic Ocean. *J. Geophys. Res.*, **109**, C03042, doi:10.1029/2003JC002007.

Prospero, J. M., and P. J. Lamb, 2003: African droughts and dust transport to the Caribbean: Climate change implications. *Science*, **302**, 1024–1027.

——, D. L. Savoie, and R. Arimoto, 2003: Long-term record of nss-sulfate and nitrate in aerosols on Midway Island, 1981–2000: Evidence of increased (now decreasing?) anthropogenic emissions from Asia. *J. Geophys. Res.*, **108**, 4019, doi:10.1029/2001JD001524.

Quadrelli, R., and J. M. Wallace, 2004: A simplified linear framework for interpreting patterns of Northern Hemisphere wintertime climate variability. *J. Climate*, **17**, 3728–3744.

Ramsay, B. H., 1998: The Interactive Multisensor Snow and Ice Mapping System. *Hydrol. Processes*, **12**, 1537–1546.

Raphael, M. N., 2004: A zonal wave 3 index for the Southern Hemisphere. *Geophys. Res. Lett.*, **31**, L23212, doi:10.1029/2004GL020365.

Remer, L. A., and Coauthors, 2005: The MODIS aerosol algorithm, products and validation. *J. Atmos. Sci.*, **62**, 947–973.

Reynolds, R. W., and T. M. Smith, 1994: Improved global sea surface temperature analyses using optimum interpolation. *J. Climate*, **7**, 929–948.

——, N. A. Rayner, T. M. Smith, D. C. Stokes, and W. Wang, 2002: An improved in situ and satellite SST analysis for climate. *J. Climate*, **15**, 1609–1625.

Richter-Menge, J., and Coauthors, 2006: Arctic. *State of the Climate in 2005,* K. A. Shein, Ed., *Bull. Amer. Meteor. Soc.,* **87** (6; supplement), S46–S53.

Rigor, I., and J. M. Wallace, 2004: Variations in the age of Arctic sea-ice and summer sea-ice extent. *Geophys. Res. Lett.*, **31**, L09401, doi:10.1029/2004GL019492.

Robinson, D. A., K. F. Dewey, and R. R. Heim, 1993: Global snow cover monitoring: An update. *Bull. Amer. Meteor. Soc.*, **74**, 1689–1696.

Roemmich, D., S. Riser, R. Davis, and Y. Desaubies, 2004: Autonomous profiling floats: Workhorse for broadscale ocean observations. *J. Mar. Technol. Soc.*, **38**, 31–39.

——, J. Gilson, R. Davis, P. Sutton, S. Wijffels, and S. Riser, 2007: Decadal spin-up of the South Pacific subtropical gyre. *J. Phys. Oceanogr.*, **37**, 162–173.

Romanovsky, V. E., M. Burgess, S. Smith, K. Yoshikawa, and J. Brown, 2002: Permafrost temperature records: Indicator of climate change. *Eos, Trans. Amer. Geophys. Union*, **83**, 589, 593–594.

——, S. S. Marchenko, R. Daanen, D. Nikolsky, D. O. Sergeev, and D. A. Walker, 2006: Soil climate and frost heave along the Permafrost/Ecological North American Arctic Transect. *Eos, Trans. Amer. Geophys. Union*, **87** (Fall Meeting Suppl.), Abstract C44A-06.

——, T. S. Sazonova, V. T. Balobaev, N. I. Shender, and D. O. Sergueev, 2007: Past and recent changes in permafrost and air temperatures in Eastern Siberia. *Environ. Global Change*, in press.

Ropelewski, C. F., and M. S. Halpert, 1987: Global and regional scale precipitation patterns associated with the El Niño/Southern Oscillation. *Mon. Wea. Rev.,* **115,** 1606–1626.

——, J. E. Janowiak, M. S. Halpert, 1985: The analysis and display of real-time surface climate data. *Mon. Wea. Rev.*, **113**, 1101–1106.

Rothrock, D. A., Y. Yu, and G. A. Maykut, 1999: Thinning of the Arctic sea-ice cover. *Geophys. Res. Lett.*, **26**, 3469–3472.

Rudolf, B., C. Beck, J. Grieser, and U. Schneider, 2005: Global precipitation analysis products. Global Precipitation Climatology Centre (GPCC), DWD, 8 pp. [Available online at http://www.dwd.de/en/FundE/Klima/KLIS/int/GPCC/Reports_Publications/QR/GPCC-intro-products-2005.pdf.]

Ryan, J. P., P. S. Polito, P. G. Strutton, and F. P. Chavez, 2002: Unusual large-scale phytoplankton blooms in the equatorial Pacific. *Progress in Oceanography,* Vol. 55, Pergamon, 263–285.

Sabine, C. L., and Coauthors, 2004a: The oceanic sink for anthropogenic $CO_2$. *Science*, **305**, 367–371.

——, and Coauthors, 2004b: Chapter 2: Current status and past trends of the global carbon cycle. *The Global Carbon Cycle: Integrating Humans, Climate, and the Natural World, Scope 62*, C. B. Field and M. R. Raupach, Eds., Island Press, 17–44.

Santer, B. D., and Coauthors, 2006: Forced and unforced ocean temperature changes in Atlantic and Pacific tropical cyclogenesis regions. *Proc. Nat. Acad. Sci.*, **103**, 13 905–13 910.

Scambos, T., M. Fahnestock, C. Shuman, and T. Haran, 2006: Impact of megadunes and glaze areas on estimates of East Antarctic mass balance and accumulation rate change. *Eos, Trans. Amer. Geophys. Union*, **87**, Abstract C11A-1130.

Schott, F. A., R. Zantopp, L. Stramma, M. Dengler, J. Fischer, and M. Wibaux, 2004: Circulation and deep-water export at the western exit of the subpolar North Atlantic. *J. Phys. Oceanogr.*, **34**, 817–843.

Seidel, D. J., and J. R. Lanzante, 2004: An assessment of three alternatives to linear trends for characterizing global atmospheric temperature changes. *J. Geophys. Res.,* **109,** D14108, doi:10.1029/2003JD004414.

Sensoy, S., 2004: The mountains influence on Turkey climate. *BALWOIS 2004 Conf.,* Ohrid, Macedonia, European Commission, 37–38.

Shapiro, L. J., and S. B. Goldenberg, 1998: Atlantic sea surface temperatures and tropical cyclone formation. *J. Climate*, **11**, 578–590.

Shein, K. A., and Coauthors, 2006: State of the climate in 2005. *Bull. Amer. Meteor. Soc.,* **87** (6; supplement), S6–S102.

Shimada, K., F. McLaughlin, E. Carmack, A. Proshutinsky, S. Nishino, and M. Itoh, 2004: Penetration of the 1990s warm temperature anomaly of Atlantic water in the Canada basin. *Geophys. Res. Lett.*, **31**, L20301, doi:10.1029/2004GL020860.

——, T. Kamoshida, M. Itoh, S. Nishino, E. Carmack, F. A. McLaughlin, S. Zimmermann, and A. Proshutinsky, 2006: Pacific Ocean inflow: Influence on catastrophic reduction of sea ice cover in the Arctic Ocean. *Geophys. Res. Lett.*, **33**, L08605, doi:10.1029/2005GL025624.

Simpson, R. H., 1974: The hurricane disaster potential scale. *Weatherwise*, **27**, 169–186.

Skvarca, P., F. Rau, T. Scambos, H. Sala, Y. Yermolin, and J. Thom, 2006: Effects of ongoing climatic warming on the cryosphere of the Antarctic Peninsula. *Extended Abstracts, Int. Symp. on Cryospheric Indicators of Global Climate Change,* Cambridge United Kingdom, International Glaciological Society, Abstract 46A070.

Smith, S. L., M. M. Burgess, and A. E. Taylor, 2003: High Arctic permafrost observatory at Alert, Nunavut—Analysis of 23 year data set. *Proc. Eighth Int. Conf. on Permafrost,* Vol. 2, Zurich, Switzerland, International Permafrost Association, 1073–1078.

Smith, T. M., and R. W. Reynolds, 1998: A high-resolution global sea surface temperature climatology for the 1961–90 base period. *J. Climate*, **11**, 3320–3323.

——, and ——, 2005: A global merged land–air–sea surface temperature reconstruction based on historical observations (1880–1997). *J. Climate*, **18**, 2021–2036.

Sommerville, R., H. Le Treut, U. Cubasch, Y. Ding, C. Mauritzen, A. Mokssit, T. C. Peterson, and M.

Prather, Eds., 2007: Historical overview of climate change science. *Climate Change 2007—The Physical Science Basis: Working Group I Contribution to the Fourth Assessment Report of the IPCC,* Cambridge University Press, 93–127.

Spencer, R. W., J. R. Christy, W. D. Braswell, and W. B. Norris, 2006: Estimation of tropospheric temperature trends from MSU channels 2 and 4. *J. Atmos. Oceanic Technol.,* **23,** 417–423.

Stabeno, P. J., N. B. Kachel, M. Sullivan, and T. E. Whitledge, 2002: Variability of physical and chemical characteristics along the 70-m isobath of the southeast Bering Sea. *Deep-Sea Res. II*, **49**, 5931–5943.

Stohl, A., and Coauthors, 2006: Arctic smoke-record high air pollution levels in the European Arctic due to agricultural fires in Eastern Europe. *Atmos. Chem. Phys. Discuss.*, **6**, 9655–9722.

Stroeve, J. C., M. C. Serreze, F. Fetterer, T. Arbetter, W. Meier, J. Maslanik, and K. Knowles 2005: Tracking the Arctic's shrinking ice cover: Another extreme September minimum in 2004. *Geophys. Res. Lett.*, **32**, L04501, doi:10.1029/2004GL021810.

Takahashi, T., and Coauthors, 2002: Global sea-air $CO_2$ flux based on climatological surface ocean $pCO_2$, and seasonal biological and temperature effects. *Deep-Sea Res. II*, **49**, 1601–1623.

Talley, L. D., 2003: Shallow, intermediate, and deep overturning components of the global heat budget. *J. Phys. Oceanogr.*, **33**, 530–560.

Tang, B. H., and J. D. Neelin, 2004: ENSO influence on Atlantic hurricanes via tropospheric warming. *Geophys. Res. Lett.*, **31**, L24204, doi:10.1029/2004GL021072.

Tarnocai, C., F. M. Nixon, and L. Kutny 2004: Circumpolar-Active-Layer-Monitoring (CALM) sites in the Mackenzie Valley, Northwestern Canada. *Permafrost Periglacial Process.*, **15**, 141–153.

Tegen, I., P. Hollrig, M. Chin, I. Fung, D. Jacob, and J. Penner, 1997: Contribution of different aerosol species to the global aerosol extinction optical thickness: Estimates from model results. *J. Geophys. Res.*, **102**, 23 895–23 915.

Thompson, D. W. J., and J. M. Wallace, 1998: The Arctic Oscillation signature in the wintertime geopotential height and temperature fields. *Geophys. Res. Lett.*, **25**, 1297–1300.

Thorne, P. W., D. E. Parker, S. F. B. Tett, P. D. Jones, M. McCarthy, H. Coleman, P. Brohan, and J. R. Knight, 2005: Revisiting radiosonde upper-air temperatures from 1958 to 2002. *J. Geophys. Res.*, **110**, D18105, doi:10.1029/2004JD005753.

Tibaldi, S., and F. Molteni, 1990: On the operational predictability of blocking. *Tellus*, **42A**, 343–365.

Timokhov, L., and F. Tanis, Eds., 1997: *Environmental Working Group Joint U.S.–Russian Atlas of the Arctic Ocean–Winter Period.* Arctic Climatology Project, Environmental Research Institute of Michigan in association with the National Snow and Ice Data Center, CD-ROM.

——, and ——, 1998: *Environmental Working Group Joint U.S.-Russian Atlas of the Arctic Ocean–Summer Period.* Arctic Climatology Project, Environmental Research Institute of Michigan in association with the National Snow and Ice Data Center, CD-ROM.

Trigo, R. M., and J. P. Palutikof, 2001: Precipitation scenarios over Iberia: A comparison between direct GCM output and different downscaling techniques. *J. Climate*, **14**, 4422–4446.

——, R. García-Herrera, J. Díaz, I. F. Trigo, and A. Valente, 2005: How exceptional was the early August 2003 heatwave in France? *Geophys. Res. Lett.*, **32**, L10701, doi:10.1029/2005GL022410.

Turner, J., 2004: The El Niño–Southern Oscillation and Antarctica. *Int. J. Climatol.*, **24**, 1–31.

——, T. Lachlan-Cope, S. Colwell, J. Marshall, and M. Connolley, 2006: Significant warming of the Antarctic winter troposphere. *Science*, **311**, 1914–1917.

Van de Berg, W. J., M. R. van den Broeke, C. H. Reijmer, and E. van Meijgaard, 2005: Characteristics of the Antarctic surface mass balance (1958–2002) using a regional atmospheric climate model. *Ann. Glaciol.*, **41**, 97–104.

van der Werf, G. R., J. T. Randerson, G. J. Collatz, L. Giglio, P. S. Kasibhatla, A. F. Arellano, S. C. Olsen, and E. S. Kasischke, 2004: Continental-scale partitioning of fire emissions during the 1997 to 2001 El Niño. *Science*, **303**, 73–76.

Varlamov, S. P., 2003: Variations in the thermal state of the lithogenic base of landscapes in Central Yakutia.*Proc. Int. Conf. on "The Role of Permafrost Ecosystems in Global Climate Change,"* Yakutsk, Russia, Permafrost Institute for Biological Problems of Cryolithozone Siberian Division of the Russian Academy of Sciences, 52–56.

——, Y. B. Skachkov, P. N. Skryabin, and N. I. Shender, 2001: Thermal response of the lithogenic base of permafrost landscapes to recent climate change in Central Yakutia. *Proc. Int. Conf. on "The Role of Permafrost Ecosystems in Global Climate Change,"* Yakutsk, Russia, Permafrost Institute for Biological Problems of Cryolithozone Siberian Division of the Russian Academy of Sciences, 44–45.

Velicogna, I., and J. Wahr, 2006: Measurements of time-variable gravity show mass loss in Antarctica. *Science*, **311**, 1754–1756.

Vinnikov, K. Y., and Coauthors, 2006: Temperature trends at the surface and in the troposphere. *J. Geophys. Res.*, **111**, D03106, doi:10.1029/2005JD006392.

Vose, R. S., R. L. Schmoyer, P. M. Steurer, T. C. Peterson, R. Heim, T. R. Karl, and J. Eischeid, 1992: The Global Historical Climatology Network: Long-term monthly temperature, precipitation, sea level pressure, and station pressure data. Carbon Dioxide Information Analysis Center (CDIAC), Oak Ridge National Laboratory, ORNL/CDIAC-53, NDP-041, 324 pp.

Waliser, D. E., and C. Gautier, 1993: A satellite-derived climatology of the ITCZ. *J. Climate*, **6**, 2162–2174.

Wallace, J. M., 2000: North Atlantic Oscillation/Northern Hemisphere annular mode: One phenomenon, two paradigms. *Quart. J. Roy. Meteor. Soc.*, **126**, 791–805.

——, 2001: Storage and transport of excess CO2 in the oceans: The JGOFS/WOCE Global CO2 Survey. *Ocean Circulation and Climate: Observing and Modeling the Global Ocean,* G. Siedler, J. Church, and J. Gould, Eds., Academic Press, 489–521.

——, and D. S. Gutzler, 1981: Teleconnections in the geopotential height field during the Northern Hemisphere winter. *Mon. Wea. Rev.*, **109**, 784–812.

Wang, B., and J. C. L. Chan, 2002: How strong ENSO events affect tropical storm activity over the western North Pacific. *J. Climate*, **15**, 1643–1658.

Wang, M., J. E. Overland, V. Kattsov, J. E. Walsh, X. Zhang, and T. Pavlova, 2007: Intrinsic versus forced variation in coupled climate model simulations over the Arctic during the twentieth century. *J. Climate*, **20,** 1084–1098.

Wanninkhof, R., 1992: Relationship between gas exchange and wind speed over the ocean. *J. Geophys. Res.*, **97**, 7373–7381.

Westerling, A. L., H. G. Hidalgo, D. R. Cayan, and T. W. Swetnam, 2006: Warming and earlier spring increases western U.S. forest wildfire activity. *Science*, **313**, 940–943.

White, W. B., and Y. He, 1986: Interannual variability in the heat content of the Kuroshio Extension associated with the 1982 ENSO event. *J. Phys. Oceanogr.*, **16**, 309–321.

Whitney, L. D., and J. S. Hobgood, 1997: The relationship between sea surface temperatures and maximum intensities of tropical cyclones in the eastern North Pacific Ocean. *J. Climate*, **10**, 2921–2930.

Wijffels, S. E., R. W. Schmitt, H. L. Bryden, and A. Stigebrandt, 1992: Freshwater transport by the ocean. *J. Phys. Oceanogr.*, **22**, 155–162.

Willett, H. C., 1950: Temperature trends of the past century. *Centen. Proc. Roy. Meteor. Soc.*, 195–206.

Willis, J. K., D. Roemmich, and B. Cornuelle, 2004: Interannual variability in upper ocean heat content, temperature, and thermosteric expansion on global scales. *J. Geophys. Res.*, **109**, C12036, doi:10.1029/2003JC002260.

Wilson, C., and D. Adamec, 2001: Correlations between surface chlorophyll and sea surface height in the tropical Pacific during the 1997–1999 El Niño–Southern Oscillation event. *J. Geophys. Res.*, **106**, 31 175–31 188.

Woodworth, P. L., T. Aarup, M. Merrifield, G. T. Mitchum, and C. Le Provost, 2003: Measuring progress of the Global Sea Level Observing System. *Eos, Trans. Amer. Geophys. Union*, **84**, 565.

Xie, P., and P. A. Arkin, 1997: Global precipitation: A 17-year monthly analysis based on gauge observations, satellite estimates, and numerical model outputs. *Bull. Amer. Meteor. Soc.*, **78**, 2539–2558.

——, and ——, 1998: Global monthly precipitation estimates from satellite-observed outgoing longwave radiation. *J. Climate*, **11**, 137–164.

Xue, Y., T. M. Smith, and R. W. Reynolds, 2003: Interdecadal changes of 30-yr SST normals during 1871–2000. *J. Climate*, **16**, 1601–1612.

Yoder, J. A., and M. A. Kennelly, 2003: Seasonal and ENSO variability in global ocean phytoplankton chlorophyll derived from 4 years of SeaWiFS measurements. *Global Biogeochem. Cycles*, **17**, 23.1–23.14.

Yu, L., and R. A. Weller, 2007: Objectively analyzed air–sea heat fluxes for the global ice-free oceans (1981–2005). *Bull. Amer. Meteor. Soc.*, **88**, 527–539.

Zebiak, S. E., 1989: Oceanic heat content variability and El Niño cycles. *J. Phys. Oceanogr.*, **19**, 475–486.

Zhang, C., 2001: Double ITCZs. *J. Geophys. Res.*, **106**, 11 785–11 792.

——, H. Hendon, W. Kessler, and A. Rosati, 2001: A workshop on the MJO and ENSO. *Bull. Amer. Meteor. Soc.*, **82**, 971–976.

Zhang, T., and Coauthors, 2005: Spatial and temporal variability of active layer thickness over the Russian Arctic drainage basin. *J. Geophys. Res.*, **110**, D16101, doi:10.1029/2004JD005642.

Zhou, L., C. J. Tucker, R. K. Kaufmann, and D. Slayback, 2001: Variations in northern vegetation activity inferred from satellite data of vegetation index during 1981 to 1999. *J. Geophys. Res.*, **106**, 20 069–20 083.

## ACRONYMS

| | |
|---|---|
| ACC | Antarctic Circumpolar Current |
| ACE | NOAA's Accumulated Cyclone Energy Index |
| AEJ | African Easterly Jet |
| AGGI | NOAA's Annual Greenhouse Gas Index |
| ALT | Active layer thickness |
| AMM | Atlantic Multidecadal Mode |
| AMO | Atlantic Multidecadal Oscillation |
| AO | Arctic Oscillation |
| AOD | Aerosol optical depth |
| ASO | August–September–October |
| ATLAS | Autonomous Temperature Line Acquisition System |
| AVHRR | Advanced Very High Resolution Radiometer |
| AVISO | Archiving, Validating, and Interpretation of Satellite Oceanographic data |
| BC | British Columbia |
| BGOS | Beaufort Gyre Observing System |
| Br | Bromine |
| CAMS | Climate Anomaly Monitoring System |
| CET | Central England Temperature |
| CFC | Chlorofluorocarbon |
| CFC-11 | Trichlorofluoromethane |
| CFC-12 | Dichlorodifluoromethane |
| $CH_4$ | Methane |
| Cl | Chlorine |
| CLIVAR | Climate Variability and Predictability |
| ClO | Chlorine monoxide |
| CO | Carbon monoxide |
| $CO_2$ | Carbon dioxide |
| CPC | Climate Prediction Center |
| CRU | Climate Research Unit |
| DIC | Dissolved inorganic carbon |
| DISC | Data and Information Services Center |
| DJF | December–January–February |
| DU | Dobson units |
| DWBC | Deep western boundary current |
| EASE | Equal-Area Scalable Earth |
| ECL | Equivalent chlorine |
| EECL | Effective equivalent chlorine |
| EESC | Effective equivalent stratospheric chlorine |
| ENP | Eastern North Pacific (basin) |
| ENSO | El Niño–Southern Oscillation |
| EOF | Empirical orthogonal function |
| ESRL | Earth System Research Laboratory |
| ET | Equatorial trough |
| ETC | Extratropical cyclone |
| EWG | Environmental Working Group |
| GCOS | Global Climate Observing System |
| GES | Goddard Earth Sciences |
| GHA | Greater Horn of Africa |
| GHCN | Global Historical Climatology Network |
| GHG | Greenhouse gas |
| GIA | Glacial isostatic adjustment |
| GISS | NASA's Goddard Institute of Space Studies |
| GLOSS | Global Sea Level Observing System |
| GMD | Global Monitoring Division |
| GPCC | Global Precipitation Climatology Centre |
| GRACE | Gravity Recovery and Climate Experiment |
| H | Hurricane |
| HadAT2 | Hadley Centre gridded free-atmosphere temperatures from radiosondes dataset |
| HadCRUT3 | Hadley Centre/CRU gridded monthly temperatures dataset |
| HCFC | Hydrochlorofluorocarbon |
| HFC | Hydrofluorocarbon |
| hPa | Hectopascal (1 mb) |
| HTC | Hurricanes/typhoons/cyclones |
| HURDAT | Atlantic Hurricane Database |
| IGRA | Integrated Global Radiosonde Archive |
| INPO | International Network of Permafrost Observatories |
| IOD | Indian Ocean Dipole |
| IPCC | Intergovernmental Panel on Climate Change |
| IPCC AR4 | IPCC Fourth Assessment report (due to be published in 2007) |
| IPCC FAR | IPCC First Assessment Report (published in 1996) |
| IPY | International Polar Year |
| IR | Infrared |
| ITCZ | Intertropical convergence zone |
| JAMSTEC | Japan Agency for Marine–Earth Science and Technology |
| JASO | July–August–September–October |
| J-CAD | JAMSTEC Compact Arctic Drifter |
| JGOFS | Joint Global Ocean Flux Study |
| JJA | June–July–August |
| JMA | Japanese Meteorological Agency |
| JTWC | U.S. Navy's Joint Typhoon Warning Center |
| LHF | Latent heat flux |

| | |
|---|---|
| LS | Lower stratosphere |
| LT | Lower troposphere |
| MAM | March–April–May |
| MCC | Mesoscale convective complex |
| MDR | Main Development Region |
| MEI | Multivariate ENSO Index |
| MH | Major hurricane |
| MJO | Madden–Julian oscillation |
| MLO | Mauna Loa Observatory |
| MLS | Microwave Limb Sounder |
| MOC | Meridional overturning current |
| MODIS | Moderate Resolution Imaging Specroradiometer |
| MPI | Maximum potential intensity |
| MSU | Microwave Sounding Unit |
| MT | Midtroposphere |
| MTC | Major tropical cyclone |
| $N_2O$ | Nitrous oxide |
| NAM | Northern Annular Mode |
| NAO | North Atlantic Oscillation |
| NARR | North American Regional Reanalysis |
| NASA | National Aeronautics and Space Administration |
| NBC | North Brazil Current |
| NCAR | National Center for Atmospheric Research |
| NCDC | National Climatic Data Center |
| NCEP | National Center for Environmental Prediction |
| NDVI | Normalized Difference Vegetation Index |
| NESIS | Northeast Snowfall Impact Scale |
| NH | Northern Hemisphere |
| NHC | National Hurricane Center |
| NIFC | National Interagency Fire Center |
| NIO | Northern Indian Ocean |
| NN2 | NOAA/NWS/NCEP/DOE Reanalysis II |
| NO | Nitric oxide |
| NOAA | National Oceanic and Atmospheric Administration |
| NOMADS | National Operational Model Archive and Distribution System |
| NPEO | North Pole Environmental Observatory |
| NS | Named storm |
| NSIDC | National Snow and Ice Data Center |
| NSW | New South Wales, Australia |
| NWS | National Weather Service |
| $O_3$ | Ozone |
| OAFlux | Objectively Analyzed Air–Sea Fluxes |
| OBPG | Ocean Biology Processing Group |
| ODGI | Ozone Depleting Gas Index |
| ODS | Ozone-depleting substance |
| OH | Hydroxide anion |
| OHCA | Ocean Heat Content Anomaly |
| OI | Optimal interpolation |
| OLR | Outgoing longwave radiation |
| OMI | Ozone Monitoring Instrument |
| OPI | OLR precipitation index |
| PATMOS (-x) | Pathfinder Atmospheres (Extended Product) |
| $pCO_2$ | Carbon dioxide partial pressure |
| PDO | Pacific Decadal Oscillation |
| PDSI | Palmer Drought Severity Index |
| Pg | Petagram (1015 g) |
| PNA | Pacific–North American pattern |
| PPB | Parts per billion |
| PPBV | Parts per billion by volume |
| PPM | Parts per million |
| PPT | Parts per trillion |
| PSC | Polar stratospheric cloud |
| PSS | Practical salinity scale |
| QBO | Quasibiennial oscillation |
| QuikSCAT | Quick Scatterometer |
| QSCAT | QuikSCAT satellite |
| RAOBCORE | Radiosonde Observation Correction |
| RATPAC | Radiosonde Atmospheric Temperature Products for Assessing Climate |
| RMB | Renminbi |
| RPCA | Rotated principal component analysis |
| RSL | Relative sea level |
| RSS | Remote Sensing Systems |
| SAM | Southern Hemisphere Annular Mode |
| SCA | Snow-covered area |
| SCE | Snow cover extent |
| SCS | South China Sea |
| SeaWiFS | Sea-viewing Wide Field of View |
| SEC | South Equatorial Current |
| $SF_6$ | Sulfur hexafluoride |
| SH | Southern Hemisphere |
| SHF | Sensible heat flux |
| SIO | Southern Indian Ocean |
| SITCZ | Southern intertropical convergence zone |
| SLA | Sea level anomaly |
| SLE | Sea level equivalent |
| SLP | Sea level pressure |
| SMN | Mexico's National Meteorological Service |
| SON | September–October–November |

| | | | |
|---|---|---|---|
| SPCZ | South Pacific convergence zone | UAH | University of Alabama Huntsville |
| SPI | Standardized Precipitation Index | UKMO | Met Office |
| SSM/I | Special Sensor Microwave Imager | UMD | University of Maryland |
| SSS | Sea surface salinity | USD | U.S. dollars (2006) |
| SST | Sea surface temperature | USDA | U.S. Department of Agriculture |
| Sv | Sverdrups (1 Sv $\equiv 10^6$ m$^3$ s$^{-1}$) | WBC | Western boundary current |
| SWI | Summer warmth index | WHOI | Woods Hole Oceanographic Institute |
| TC | Tropical cyclone | | |
| TD | Tropical depression | WMO | World Meteorological Organization |
| TOMS | Total Ozone Mapping Spectrometer | WOA | World Ocean Atlas |
| TRMM | Tropical Rainfall Measuring Mission | WOCE | World Ocean Circulation Experiment |
| TS | Tropical storm | WP | West Pacific (teleconnection pattern) |
| TSP | Thermal state of permafrost | | |
| TY | Typhoon | WPO | West Pacific Ocean |